Investigation of the Smart Tooling System and Dynamics in Ultraprecision Machining of Freeform Surfaces and its Implementation Perspective

Ali Khaghani

Supervisor: **Professor Kai Cheng**

Department of Mechanical and Aerospace Engineering

College of Engineering, Design and Physical Sciences

Brunel University London

This thesis is submitted for the degree of

Doctor of Philosophy in Micro-Nano Manufacturing

August 2020

Abstract

The concept of the smart tooling system for ultraprecision machining of freeform surfaces compromises the high intensity of developing adaptable technologies towards innovative holding the workpiece and cutting tool mechanisms. This is in line with the emerging development of smart applications in precision engineering and industrial-scale ultraprecision production. Furthermore, due to rapidly growing requirement for three-dimensional micro and miniature components or products in high precision, the ultraprecision and micromanufacturing are getting increasingly applied in aerospace, automotive, medical engineering, optics, and microelectronics in particular. Over the last decade or so, ultraprecision machining has become a key enabling technology for machining complex freeform surfaced components and products in an industrial scale. From the dynamics point of view, freeform surface with a large depth machining using diamond turning machine can be difficult challenging and in some cases. Despite substantial research and investigation were employed in this field, there are some critical issues remained and needing to be addressed desperately. Nowadays, ultraprecision machining is gradually progressing or maturing over time to meet the full range of requirements for exceptional accuracy and desirable surface quality for freeform surface applications.

In current precision engineering, actuation systems for precise positioning and motion control of spindles and direct-drive slideways are profoundly reliant on using rotary and linear encoders. Notwithstanding, in the dynamic machining process, the positioning and control are somehow 'passive' and unable to directly monitor and control the tool and workpiece statuses. The machining system is hypothetically rigid, and the cutting dynamics are stable. Nevertheless,

machining dynamics and the dynamic synchronization of the cutting tool and workpiece positioning have compelled the challenges on the machining system, which should be carefully considered versus conforming requirements of high productivity for the fulfilment of high precision products in particular. It is also imposing the question in the driving and development of next-generation ultraprecision machining systems operating towards higher or even pico-precision. Overall, this PhD research is focused on the fundamentals and implementation perspectives, as discussed above. In this research work, an innovative dynamic cutting force orientated approach is presented for motion control and positioning in ultraprecision machining of freeform surfaces mainly using either slow tool servo or fast tool servo mode machining techniques. This novel method is developed using seamless integration of cutting forces and machining dynamics with the aid of multi-body dynamics analysis. The positioning and dynamic motion between the workpiece freeform surface and cutting tool are achieved under interfacial interactions at the tooltip and workpiece surface. Necessarily, the interfacial cutting dynamics and physics are the foundation for developing the higher-level of positioning and motion control for the next generation ultraprecision machining system. Thus, the critical interfacial areas were identified and researched accordingly. A novel and dynamics-orientated freeform surface toolpath generation were developed to enable the detection of the dynamic effects of the interfacial cutting forces in the process. Also, an innovative smart chuck for freeform surface workpiece holding was designed and developed to fulfil the requirements of positioning and motion control for next-generation ultraprecision machining systems.

The approach is further described using analytical and comparative methodology with an in-depth investigation on employing light material such as MMC material for designing the hydrostatic bearing supported direct-drive slideway. The investigation is supported with simulations and experimental trials for evaluation and validation. The results are auspicious and remarkably promising in overcoming the conventional limitation in positioning and motion

control. The research concludes with a further discussion on an extensive application case study using this methodology, and its manufacturing and industrial associations and beyond.

To,

This thesis is dedicated to "My loving parents, My brothers and sister"

Hope you are proud of me.

Declaration

I declare that this thesis is my own work and is submitted for the first time to the Post-Graduate Research Office. The study was originated, composed and reviewed by myself and my supervisors in the College of Engineering Design and Physical Sciences, Department of Mechanical and Aerospace Engineering, Brunel University London, UK. All the information derived from other work has been properly referenced and acknowledged.

<div align="right">

Ali Khaghani

August 2020

</div>

Acknowledgements

I would like to express my sincere thanks and appreciation to the people who have helped and supported me in working to accomplish this research project. First and foremost, I would like to sincerely thank the UK Government, Engineering and Physical Sciences Research Council (EPSRC) and Brunel University London for their support in scholarship and funding of this research study.

I would like to thank my dear supervisor, Professor Kai Cheng, for his patience, assistance, and motivation. His guidance helped me throughout my research, during the publishing of journal papers, and the writing of this thesis. Without his time, support and consideration, it would not be possible to conclude a research of this magnitude.

I would also like to show endless appreciation for my loving parents, who always surrounded me with love and emotional support. Moreover, I am forever indebted to my brothers and sister for supporting me and believing that I could overcome any challenges in my life. I am also grateful to my other family members and friends who have backed me along this journey.

On a professional level, I would also like to express my deepest gratitude to my dearest friend and advisor, Dr Atanas Ivanov, for his valuable support and assistance. A very special thanks also goes out to Dr Mazin Ghazi Al-wswasi, for giving excellent support and inspiration, who has over time become a brother more than a friend over the last three years. My special thanks go to Gavin Chapman from Moor Nanotechnology Ltd for his help and advice, which was quite valuable to finish my research project. On the same note thanks are due to Liang

Table of contents

List of figures

List of tables

Nomenclature

Roman Symbols

$[C]$ stiffness matrix

$[K]$ stiffness matrix

$[M]$ mass matrix

$\ddot{u}(t)$ vector for acceleration at time (t)

$\dot{u}(t)$ vector for velocity at time (t)

λ Lagrange multiplier vector

Φ_q constraint equations Jacobian matrix

$C\dot{u}$ damping constant

$F(t)$ force vector variation at each time step

Ku stiffness constant

$M\ddot{u}$ mass acceleration at time (t)

N number of total bodies

q_i generalised coordinate vector

x_i , y_i , *and* z_i Euler angles

$\Phi_q{}^T \lambda$ generalised vector of the reactions

$u(t)$ vector for displacement at time (t)

Q   generalised vectors of the forces

Acronyms / Abbreviations

AFM   Atomic Force Microscopy

API   Application Programming Interface

BDF   Backward Differential Formulating

CAD   Computer Aided Design

CAE   Computer Aided Engineering

CAM   Computer Aided Manufacturing

CCM   Cylindrical Coordinate Machining

CCW   Counter Clock Wise

CW   Clock Wise

DAE   Differential Algebraic Equation

DOC   Depth Of Cut

DTM   Diamond Turning Machine

FAS   Fast Axis Servo

FTS   Fast Tool Servo

GSTIFF Gear Stiff

HRTEM High Resolution Transmission Electron Microscopy

LFTS Long Fast Tool Servo

MBD Multi-Body Dynamics

MMC Metal Matrix Composite

NRS Non Rotational surface

NURBS Non-Uniform Rational B-Splines

OSTS Orthogonal Slow Tool Servo

PDF Probability Density Function

PV Peak-to-Valley

PVT Position-Velocity-Time

PZT Lead Zirconate Titanate

RA Roughness Average

RMSE Root Mean Square Error

SD Standard Deviation

SF Safety Factor

SSE Sum Square Error

SSS Slow Slide Servo

STS Slow Tool Servo

TIR   Total Indicated Reading

TPG   Tool Path Generation

UPM   Ultra Precision Machining

VCM   Voice Coil Motor

WSTIFF Wielenga Stiff

Chapter 1

Introduction

1.1   Background of the Research

The freeform surface can be explained as a surface where its shape has no continuity in rotational or translational symmetry about axes. Freeform surfaces manufacturing towards innovative functionalities and smart applications of the components or products are increasingly emerging in the world of optics manufacturing in particular. Due to rapidly growing requirement for three-dimensional micro and miniature components and products in high precision, the ultraprecision machining systems are getting critical needs, particularly in aerospace, automotive, medical engineering, optics, and microelectronics. Over the last decade or so, ultraprecision machining has become a key enabling technology for machining complex freeform surfaced components or products in an industrial scale. The demands are to be fulfilled by involving the industries research organisations in ultraprecision machining technology, Micro-Nano manufacturing and smart tooling development. The greatest advantage of freeform surfaces is that they can be integrated and designed with multiple surfaces to intensify the functional performance. For instance, vari-focal lenses and contact lenses are the multifunctional applications that can be designed and implemented by integration of freeform surfaces. Ultraprecision machining technology is increasingly applied as a powerful enabler for overcoming the inability of the

complex freeform surface machining and helps developing many recent freeform surfaced applications in optics and precision engineering.

The recent well-known techniques in ultraprecision machining include Fast Tools Servo (FTS) mode machining, Slow Tool Servo (STS) mode machining, Raster Fly-cutting and Micro-milling. However, there are some limitations to those respective technologies which need to address, for instance, Micro-milling machining requires the dynamic and inherent static in ultraprecision machining system and the process of material removal rate is less than turning process. Raster fly-cutting has a disadvantage of relatively long and challenging setup and interference of tool swing diameter. From another perspective, FTS and STS diamond turning process and machining have the highest rate of material removal in comparison with other methods and consequently are widely utilised by researchers and industries. Notwithstanding, in terms of optimisation of FTS and STS methodology, only a few studies have been transferred to fabricate the freeform optical lenses with multi-curvature surfaces. Based on this substance, the optimisation and development of an integrated approach to design and precision manufacturing of freeform optical lenses and its application perspectives need to be carried out.

From the dynamics point of view, the manufacturing of the freeform surface with large depth using diamond turning machine can be difficult and in some cases are challenging. Therefore, the technology of (FTS/STS) diamond turning was developed to address the challenges in the manufacturing process of the freeform optical surface, such as freeform lenses and hybrid surfaces. These techniques can substantially address the limitation of low bandwidth range in the STS and limited range of stroke in FTS. Freeform surface lenses are recognised as freeform optical surface whereby are prevalently non-rotational in a general manner. With comparison to rotational surfaces, the non-rotational surfaces are consisting of a high degree of freeform and are used to decrease the wave-front error and the size. With the aim of manufacturing and machining, the ultraprecision machining technologies such as diamond micro-milling and diamond turning with fast tool servo (FTS) and slow tool servo (STS) are

used extensively with an excellent level of accuracy and superior quality of surface finishing. Nowadays, ultraprecision machining is gradually changing or maturing over time to meet the full range of requirement for exceptional accuracy and desirable extraordinary surface quality for freeform optical surfaces applications.
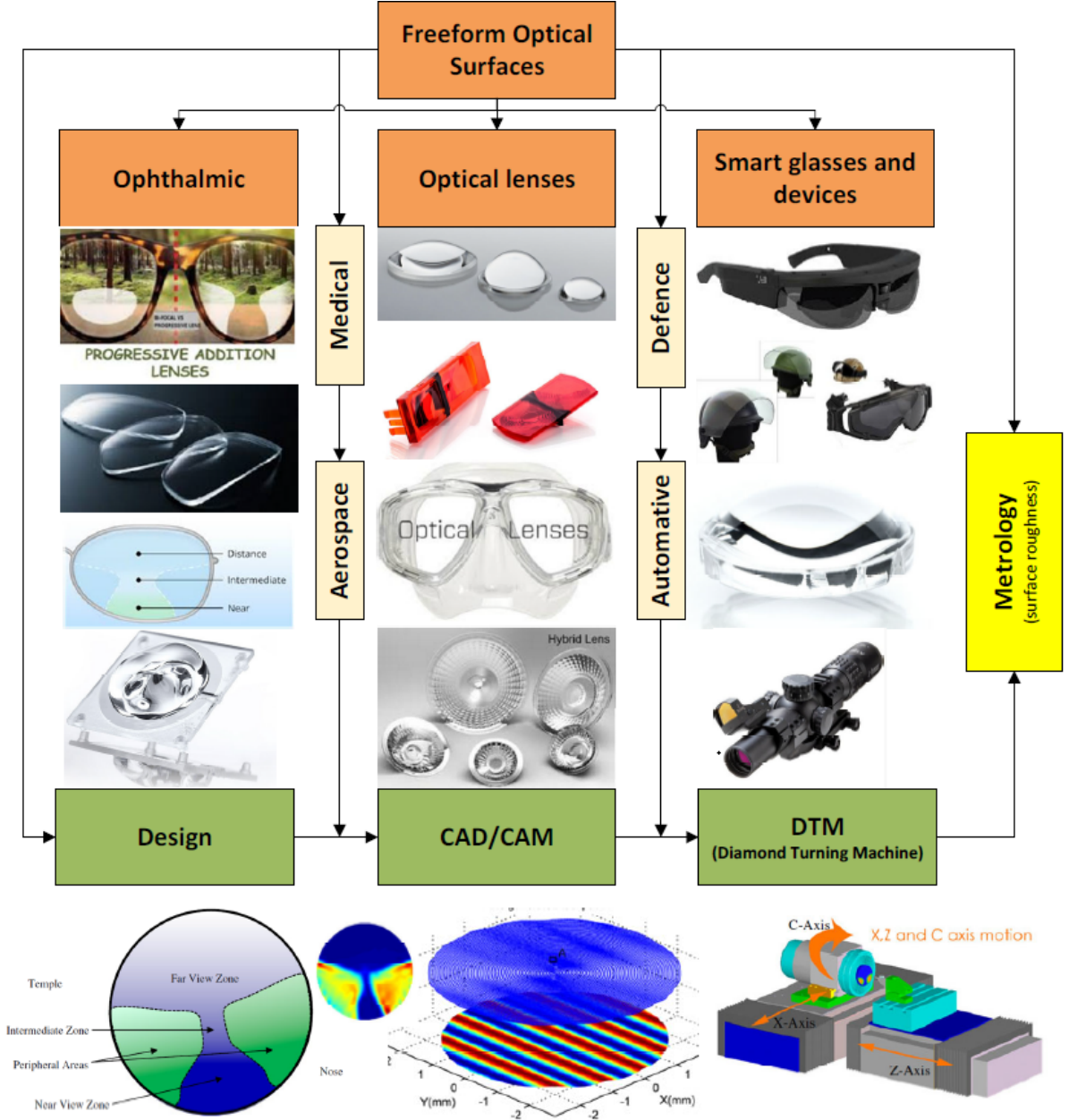
Fig. 1.1 Multi-axes machining and its application trend

Ultraprecision machining with new methodology can lead the market for a significant and progression novel optical design. Although, this new evolution and development have not been fully understood and further explorations are required to discover the un-known potential and knowledge of freeform surfaces. Moreover, it is speculated that the new evolution in ultraprecision machining will be involved with new potential challenges in design, machining and metrology with regards to product development and validation. This research reviews the past critically, presents endeavour and attempts ultraprecision machining techniques for manufacturing freeform optical lenses in a specific manner. Figure 1.1 highlights the freeform surfaces developments and applications in this context.

1.2   Freeform Optical Surfaces

As mentioned in Section 1.1, the freeform surface design has a growing trend in optical production. For instance, progressive additional lenses (PAL) known as vari-focal or multifocal lenses, are designed to focus on the shape of the surface utilisation that is not rotationally symmetric. It provides addition with the variation of focal ray. The power of variation progressive should be met the requirement without aberration [1]. The surfaces such as ophthalmic lenses consist of freeform surfaces that involve with very high and precise resolution. The shape of their surfaces are particularly non-symmetrical and normally from their convex surface are aspherical [2]. The trend of the ophthalmic optic is expanding in demand. The combination of multifocal power in lenses are beneficial for the users where the power is varying on the lenses as the user changes the distances through intermediate power areas to near or far. Ophthalmic surfaces are combined of surfaces as follows: (1) Freeform surfaces + spherical surface, (2) spherical surface + aspherical surface, (3) freeform surface + aspherical surface, and (4) freeform surfaces + freeform surfaces. As for manufacturing point of view, the front surface of vari-focal lenses cannot be machined using traditional diamond turning. It will require a special diamond turning machining techniques such as FTS or STS.

The freeform surface can be described as digital or direct surfacing that applies to the manufacturing process of complex surface geometry. This shape can be defined as the progressive addition surface, aspheric and toric surfaces. The process of manufacturing is numerically controlled and generated by computer. Computer Numerical Control process with typically three axes are used to generate this type of freeform surface. The methodology of single point cutting tool can be employed to produce implicitly any freeform surface shapes include the optical and ophthalmic lenses with a very high level of resolution and accuracy [3].

1.3   Ultraprecision Machining of Freeform Surfaces

Nowadays, the ultraprecision machining technology and its dynamic factors becoming the most reliable and capable precision machining method for fabricating the complex surfaces such as freeform optical lenses [4, 5]. The typical manufacturing ultraprecision machining process for freeform lenses is diamond turning. There are two common methods of ultraprecision machining capable of machining these freeform surfaces which are, (a) Fast Tool Servo (FTS) and (b) Slow Tool Servo (STS). These techniques are robust and highly capable of manufacturing and machining very complex surfaces such as polynomial freeform, aspheric cylinder, NURBS defined freeform surfaces, lens array and bi-conics lenses. Figure 1.2 illustrates the fabrication process chain stating the feasibility of manufacturing methodology for freeform optical surfaces from the earlier stage of the concept to final design and measurement process [6]. According to the process chain, it initially employs the computer-aided design (CAD) software in order to generate the toolpath trajectory and the compensation of freeform surface error with modifying and correcting the tool trajectory. For the last over a decade, diamond turning with FTS mode machining has been widely used for fabrication of the Non-Rotational Symmetrical (NRS) surfaces due to its high resolution and bandwidth [7]. Although STS technique offering a longer stroke in millimetres levels, limitation of its bandwidth constrict the speed of C-axis (in the tool trajectory) for machining of very complex freeform

optic surfaces. Thus, the development of the STS mode technique is becoming an essential task by studying and investigating the dynamics effects of machining efficiency for achieving demanded higher resolution and accuracy in the freeform surfaced applications.
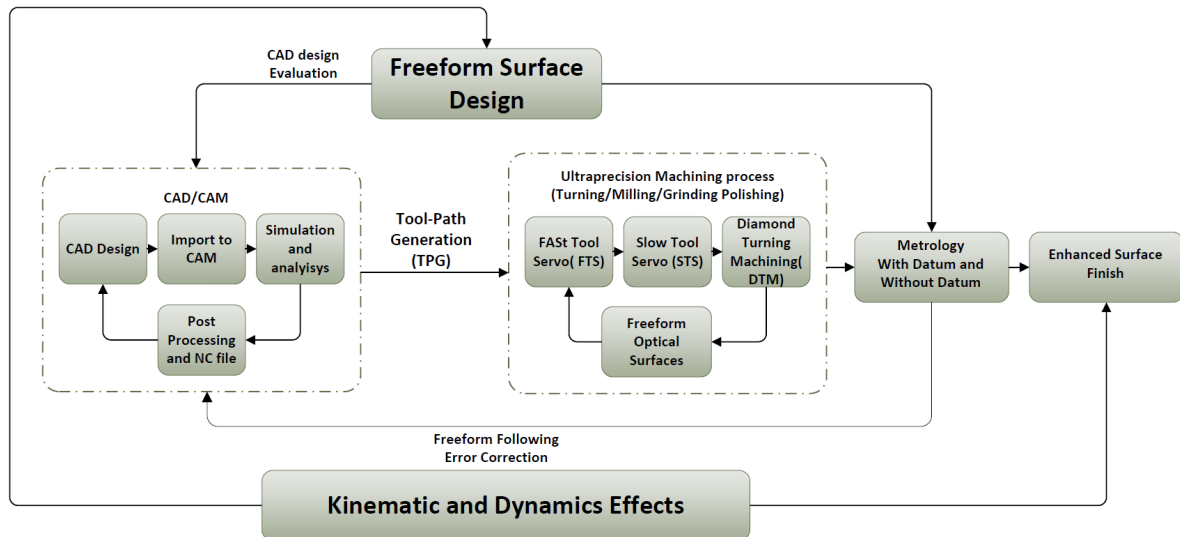
Fig. 1.2 Freeform fabrication process chain

Diamond turning machine (DTM) has a significant impact in the fabrication of optical freeform surfaced applications such as forward-looking infrared radar, contact lenses, infrared spectrometers and smart lenses like google smart contact lenses in both industrial and science sectors. These impacts are not only limited to accuracy and fast-growing fabricated diffractive, refractive and reflective optical surfaces but also for creating reference feature for bounding of the optical surfaces to assist with assembly process [8]. Due to the existence of no rotational symmetry (NRS) components, however, currently, there are some potential challenges are facing towards the fabrication of freeform surfaces using diamond turning machine (DTM). For the creation of a freeform NRS surfaced component, the diamond tool movement should be synchronised as a function of spindle rotation and translation of slideways.

(a)

(b)
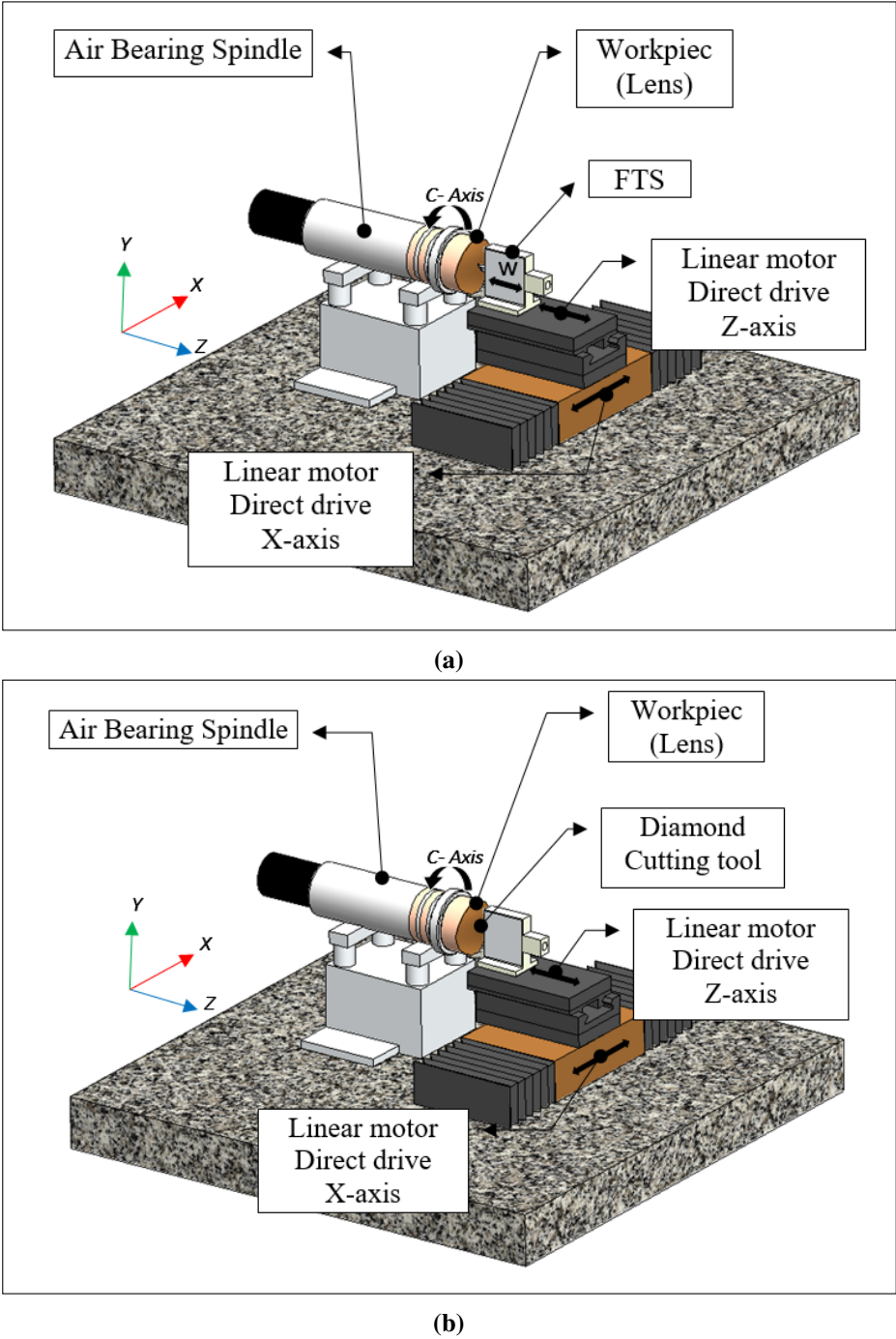
Fig. 1.3 Ultraprecision diamond turning machine and machining configurations: (a) fast tool servo mode; (b) slow tool servo mode

Figure 1.3 shows two typical DTM configurations for FTS and STS technique, with a tool servo that being mounted on their axis of either the X-slide or Z-slide. The work-piece is held

by spindle chuck on C-Axis. Z-Axis or slid is parallel to the spindle axis, and X-axis is the perpendicular direction to Z-axis. Generating the tool motion command as a function of the spindle position and X-slide location will create the multi-axis synchronization.

1.4   Aim and Objectives of the Research

The main aim of this research is to investigate an integrated dynamics-oriented approach and the underlying scientific understanding for design, precision manufacturing of freeform surfaces and its application perspectives. Overall, this research represents a comprehensive but not limited exploration of freeform surfaces machining at a truly industrial scale. To solve the major challenges in manufacturing affordable and high-quality freeform surfaces, it is essential to develop a highly effective and efficient engineering approach. It will integrate the design, precision manufacturing and measurement of the freeform optics such as varifocal lenses in a seamless mass customized industrial manner. This research work is specifically involved with developing key enabling technologies for ultraprecision smart machining of freeform surfaces, including an innovation approach to design of a self-centring clamping devices for freeform components, design and development of hydrostatic linear direct drive motor slideway using MMC (Metal Matrix Composite) material, and developing a novel tool paths generation protocols for machining of freeform surfaced components.

The main objectives of this research include:

1. **Critical review of the state-of-the-art in ultraprecision machining of contact lenses moulds/dies using bespoke machines and universal conventional ultraprecision machines.**

   An extensive investigation will take place to identify the current knowledge in freeform

surface design. Ultraprecision machining characteristics of freeform surfaces such as contact lenses moulds and their application will be identified.

2. **Innovative design of a smart fixture applicable on conventional diamond turning machine through smart flexure structure design further supported by FE analysis.**
   Freeform surface optical lenses design representing the new generation in the optometry, however, there is no effective knowledge contributed to the industry. Most recent development of vision products in this area requires incorporating the newest ideas and features. Identifying the knowledge gap and contribution to knowledge is essential to support and develop the general methodology for the product innovation. A novel smart chuck design applicable to current conventional universal ultraprecision machine will be researched, integrated with newly invented features such as self-centring, self-locking and precise positioning mechanism.

3. **Mechanical engineering design and manufacture of the smart fixture particularly taking account of its reconfigurability, ultraprecision operations and integration with a universal diamond turning machine.**
   The design and development of the smart chuck will be discussed in detail with all CAE verification.

4. **Investigation of the freeform surface features and freeform surface generation in ultraprecision machining using diamond turning machine.**
   Ultraprecision manufacturing is the most important technology for high-precision surface finishing. The technology is also suitable for producing rotationally symmetric geometries and non-rotationally symmetric surface geometries where required. Ultraprecision diamond turning processes can be used in spectacle eyeglasses, mirrors devices and micro-structured surfaces. The method of freeform cutting is enabling the technology to generate very high precision surface in subtle scale, e.g. nano and micro level. At this

stage in this project, further investigation will be carried out to identify the knowledge gap in precision freeform surfaces generation and its related features.

5. **Developing the associated CAD/CAM and CNC toolpath generation method for high precision integrated design and CNC machining.**

   In optometry design and manufacturing, there are some sort of technology currently being capable to machine such a complex surfaces. One of these methods is FTS (Fast Tool Servo) mode machining that can achieve such high precision surface finishing for optical applications. This research aims to develop innovative algorithms that can be used in CAD and CAM and CNC machines to deliver the similar result as FTS methodology. Matlab and Mathcad, LabVIEW and G-Code will be used for this purpose.

6. **Investigation in freeform surface measurement factors with an approach and assessments of the surface accuracy of different type of freeform surfaced components at their optical performances**

   In affordable manufacturing , while very high-quality freeform optics required, it is critical to follow a highly effective and efficient precision engineering approach. In order to achieve such target, seamless precision manufacturing and measurement of the freeform optical surfaces is very significant. At this stage, further investigation and metrology measurement system will be taken place in order to assess the machining accuracy of freeform surface and their optical performance. However, functional approach are significantly important in integrated design–manufacturing measurement.

7. **Investigation on the cutting mechanisms and assessment (e.g. surface roughness and topography, complex micro features, productivity, etc.) in ultraprecision machining of the contact lenses mould insert ultraprecision machining.**

   Integrated approach and specific implementation and application evaluation will be investigated with regards to necessities for ultraprecision production. The essential elements

in manufacturing are the high precision machining with miniature and micro product features, which directly can influence the machining accuracy and efficiency. In this case, the challenges in the implementation is in association with design of precision machine tools, which could play a major factor role in affecting the performance of the precision machining process.

8. **Investigation on ultraprecision machining dynamics by design and development of hydrostatic bearings with Metal Matrix Composite (MMC) material for Slow tool servo mode machining.**

   Linear slideways integrated with either hydrostatic or aerostatic bearings have been widely used in ultraprecision machining systems combined with STS and FTS techniques. Machining the freeform surfaces using STS technique faces some challenges in dynamics related to linear slide motions performance and control system functionality. New Design and analysis for hydrostatic bearings with MMC material will be carry out and the influence of its dynamics will be investigated. The material such as alloy steel widely employed in the hydrostatic bearing. Nevertheless, replacing the lighter material with same mechanical property and stiffness such as MMC expected to enhance the dynamic performance such as motion accuracy in ultraprecision machining.

9. **Undertaking the ultraprecision machining trials and industrial application case study on using the smart fixture developed for contact lenses mould manufacturing as required by the industrial partner.**

   The project will be concluded by a final experimental approach. The project will closely cooperate with one international diamond tooling manufacturing company and undertakes industrial application case study with Brunel facility.

1.5   Outline of the Thesis

The thesis is structured as follows:

Chapter 1 provides a brief background of the research and explains the significant motivations, aims and objectives of the study.

Chapter 2 presents critical literature review on principles, functions, requirements, and different methodologies and approaches for ultraprecision machining including FTS and STS technology. Also, it gives a special emphasis on the fundamental concepts of using light material such as MMC in the system. The key contribution of this work will also be briefly discussed.

Chapter 3 explains the novel multi-body dynamic toolpath generation methodology for ultraprecision machining of freeform surfaces in industrial scale. An ultraprecision machining implementation of a freeform surface component and its surface measurement factors were explained.

Chapter 4 presents the design and development of a novel clamping smart chuck for UPM technology. The design of smart chuck with a compliant flexure mechanism will be discussed, and a solution to precise positioning, self-centring, self-locking will be explained. The collaboration knowledge will be based on the existing ultraprecision machining technology in current market.

Chapter 5 clarifies the experimental work of the smart chuck and explain the freeform surfaces UPM with precision and accuracy analysis. The implementation and case study will be based on collaboration work in contact lenses ultraprecision machining. The workpiece resources are provided by a sponsored company.

Chapter 6 describes an attempt to design hydrostatic bearings with MMC material. A new methodology of using the light material in hydrostatic bearing was discussed. The dynamic and kinematic effect was simulated, and the proper analysis explained.

Chapter 7 includes the simulation analysis of hydrostatic bearing and dynamic charac-
teristics in UPM. The explanation to interfacial forces and higher precision engineering such
pico-precision were explored.

Chapter 8 presents the outlines of the assessment and conclusion of the entire research and
explains the recommendations for possible future directions of the research. It also highlights
the list of publications raised from this research.

1.6   Key Contributions and Novelty of this Research

The key contribution and novelty from this research can be summarised in three items as shown
in Figure 1.4.
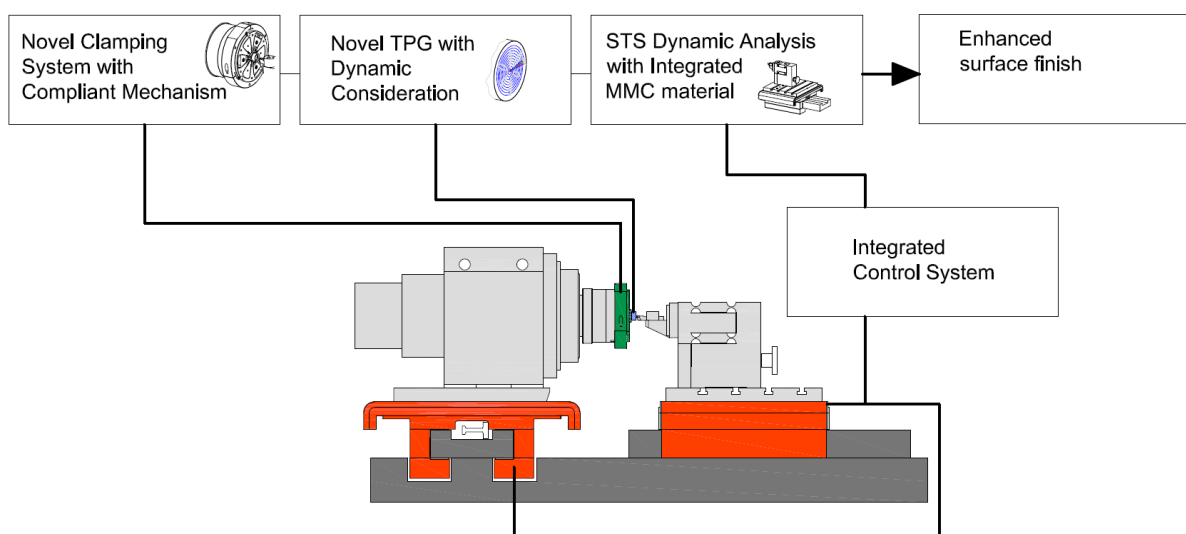
Fig. 1.4 Key contributions and novelty

1.6.1   New Light-weight and High-Stiffness Material

Metal Matrix Composite (MMC), is a new light-weight material that is currently under devel-
opment. Because of its lighter weight and same mechanical properties as other alloy materials,
it could be used in the linear direct-drive motors design to reduce the form error in freeform

surfaces. The excellent properties of MMC's such as strength, weight ratio or high wear resistance make it very high demanded material to use in applications such as aerospace and automotive as it can provide the reinforcement of light metal alloy (e.g, aluminium). However, these type of material can cause poor machinability or surface finishing [9]. In this research work an in-depth investigation made in replacing hydrostatic bearing alloy steel with MMC material. A quantitative and qualitative analysis was made to investigate the dynamics and kinematic effects of the MMC material utilised in linear hydrostatic bearing for STS mode ultraprecision machining. A conventional ultraprecision machining system was modelled a reference for analysing and accuracy evaluation and comparison purposes.

1.6.2 Novel Toolpath Generation Methodology

New toolpath generation methodology was developed using ADAM solver with differential algebra equation (DAE) and WSTIFF and GSTIFF integrators. This novel toolpath generation is not limited to kinematic factors but robustly capable to calculate the dynamic effects in each individual single point at UPM toolpath. It also reliable to detect the interfacial cutting forces, contact and friction forces during the machining process. Recently a paper was written and published in IMechE Proceeding of Manufacturing Engineer Part B. This novel TPG thought to open a new area in Ultraprecision engineering to dynamically analysis the cutting forces in freeform surfaces while the data can be processed in-situ by the controller to implement a fully closed loop feed back system.

1.6.3 Design and Development of the Smart Chuck

In Micro-Nano manufacturing, particularly in optics design and machining, the tooling set up is the most challenging factor. The height position of the diamond tooltip and the centre of the spindle while the workpiece must also accurately be aligned with both spindle axes and tooltip height position. This process could be cost-effective and time-effective. The importance of

Micro-Nano manufacturing in terms of accuracy led the project in this research work to design a new lens holder capable of holding the workpiece in the centre of the spindle while in the machining process. A compliant mechanism was employed to design the flexure hinges for the purpose of precise positioning. Besides, the jaws are designed to be fully functioned by the control system and communicate with PMAC [1] to accurately align the workpiece with the spindle and tooltip height position for future work.

---

[1]PMAC, pronounced Pe'-MAC, stands for Programmable Multi-Axis Controller according to PMAC quick reference guide from Delta Tau, Data Systems, Inc

Chapter 2

Literature Review

This chapter presents the critical literature review on the manufacturing process of freeform surfaces. The main principle, state-of-the-art, current knowledge gaps and limitation of methodology for the manufacturing of freeform surfaces will be discussed including the diamond turning machine process, and other multi-axis precision machining. Finally, the potential development required for manufacturing the freeform surfaces will be covered, and development of new knowledge and methodology will be explained and discussed for the manufacturing of freeform surfaces.

2.1 Ultraprecision Diamond Machining Techniques

2.1.1 Multi-axis Ultraprecision Machining

Complex optical devices are widely used in various applications such as medical imaging, telecommunication, automotive, aerospace and defences industry, where the freeform surface plays the main and characteristic role in the product design and development strategy. Optical designers broadly employ freeform surfaces on their design for achieving novel functions in the products such as metallic and conductive surfaces. Machining of such complex freeform

surfaces require a degree of freedom of motions in multiple axes to form the designed surfaces. Ultraprecision machining of freeform surfaces using multi-axis techniques can fulfil the the needs and brings a high degree of quality and accuracy to optical productions [10]. There are two mainly used and well-known techniques in ultraprecision machining which can satisfy a high level of precision and accuracy and efficiency to the freeform surfaces productions. These techniques are known as fast tool servo (FTS) and slow tool servo (STS) which integrated with diamond turning machine. The multi-axis manufacturing process can precisely control the machining of the freeform surfaces with a high degree level of complexity and make the optical production in extremely high-efficiency and low-cost performances [11].
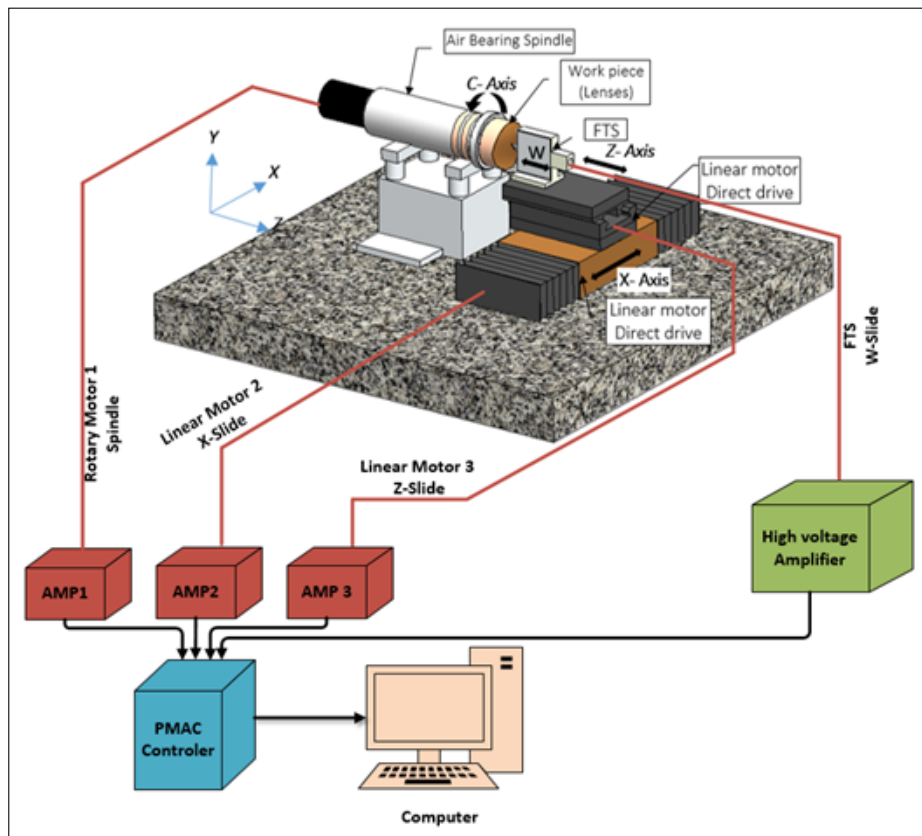
Fig. 2.1 Schematic of multi-axis programmable controlling configuration for ultraprecision diamond turning machine (DTM)

Figure 2.1 shows the conventional configuration of the programmable multi-axis controlling system for ultraprecision diamond turning machine (DTM) with an added-on accessory of

FTS technology. There is a total of four axes in this configuration. X and Z axis are the linear direct-drive motors which are typical in all conventional diamond turning machine, C Axis is the spindle drive that is controlled in a semi closed-loop, which can be commanded to move to a specific degree and angular position. The FTS is mounted in the Z direction and act as a further independent axis. It is also the primary axis (W axis) and can be controlled by the same controller as for other axes [12].

2.1.2   Fast Tool Servo (FTS) Mode Machining

Fast Tool Servo (FTS) technology is widely employed in ultraprecision machining and has key role particularly in optical design and manufacturing of freeform surfaces in optical industry. From this perspective, due to its high resolution and bandwidth, FTS diamond turning is highly capable for fabricating the non-rotational symmetrical surfaces [12–16]. FTS methodology can be described in two different divisions, a) short stroke FTS and b) long stroke FTS.

Short Stroke Fast Tool Servo

The characteristic of FTS is conforming as piezoelectrically driven, and works within a bandwidth range of 200-1,000 Hz and stroke range of 10-400 μm. The main advantage of FTS is that low moving mass of PZT actuators with high stiffness and high bandwidth enabling the control system to operate the tool motion in much robust and efficient status. The lack of stroke is the main disadvantage of using the piezoelectric servos. Also, the strain of 0.1 % or 1 μm per millimetre in length can be produced by Piezoelectric disks (PZT). The range of motion can be extended by using the mechanical amplification piezo motion. Nevertheless, it will remarkably reduce the stiffness and increase the inaccuracy in the tool motion. The earliest FTS technology history back to 1980s, which initially designed by Rakuf and Patterson [13] at Lawrence Livermore National Lab to compensate spindle motions error on diamond turning machine and since then, quickly widened to harvest biconic contact lenses to correct

the astigmatism disorder and zone plates for optical applications, which can achieve 2.5 μm of stroke, 1.3 nm dynamic repeatability and 660 Hz of bandwidth (-3dB).

Back to earlier date 1986, Meinel et al. [17] has successfully tested and manufactured phase corrector plates for wave-front correction. RASMUSSEN et al. [18] designed and implemented a piezoelectric actuated cutting tool to drive thorough a lever assembly for machining asymmetric surfaces with dynamically varying depth. The tool servo generates 50 μm travel and 200 Hz bandwidth. Cuttino et al. [19] developed and implemented an FTS with 100 μm travel and 100 Hz bandwidth which has 13 cm long Piezoelectric stack with 70 N/μm open-loop stiffness. Montesanti et al. [20] has worked and developed a new rotary motor with a maximum travel of 50 μm stroke at 2 kHz bandwidth, and also designed and implanted a hybrid linear/rotary FTS with 70 μm and 10 kHz bandwidth. Precitech, designed and implemented a commercial FTS500 with the capability of 0.5 mm stroke with 1,000 Hz bandwidth. The system is developed with a very linear response curve within 100 Hz, which provided a high form accuracy and performance. Kim et al. [21] carried out in the development of a long-stroke FTS (LFTS) that having maximum travel of 432 μm. Figure 2.2 shows the mechanical mechanism of developed long fast tool servo which presenting several levers and hinges.
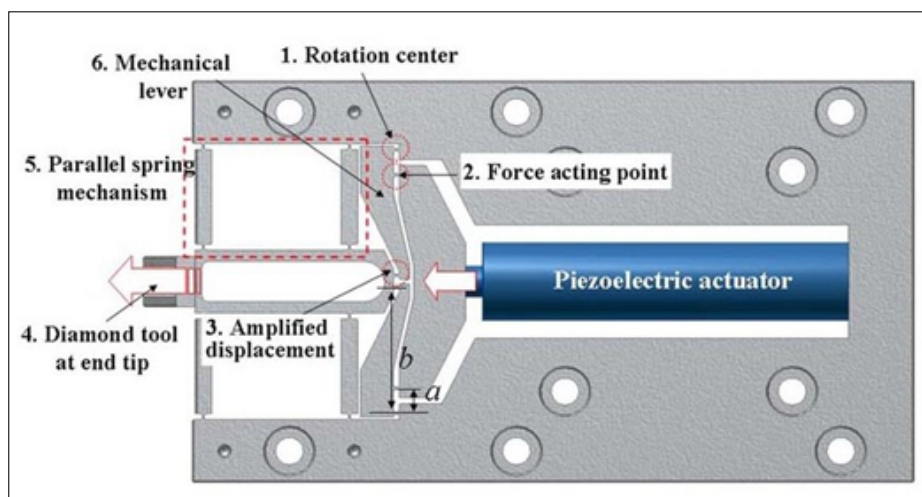
Fig. 2.2 Photography of long fast tool servo mechanism

Buescher et al. [22] designed new fast long-range actuator (FLORA), which using an air-bearing linear slider and linear direct-drive motors to expand the stroke and travel length of up to 4 mm, nevertheless, the design had a bandwidth of 20 Hz which was low with compare to other FTS design. Figure 2.3 shows the FLORA fast tool servo in a diamond turning machine.
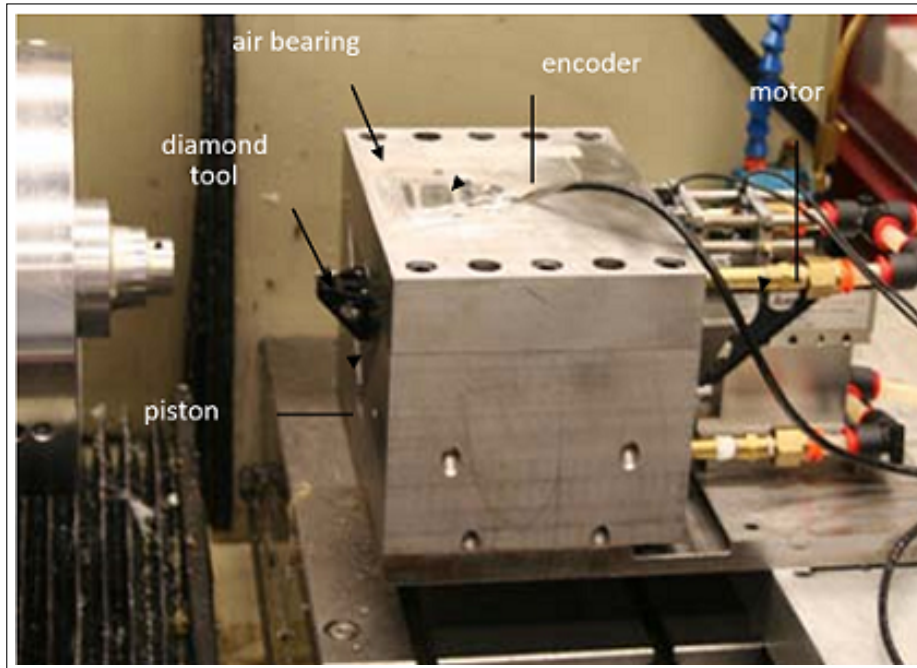
Fig. 2.3 The FLORA Fast Tool Servo in DTM

Yang and Dai [23] have introduced a feasible methodology for FTS machining parameters that can match the FTS dynamics for higher fabricating efficiency but within the limits of the dynamic performance. They have used Simulink model for their controlling system to generate the surfaces. Their quantitative results states that the proposed method was effective and feasible, which could provide valid references for real fabrication. The virtual machining, amplitude and phase lag caused by FTS dynamics proposed quantitatively and described that the optimisation the machining parameters can decrease the effect of FTS dynamics

Long Stroke Fast Tool Servo

The principle of long-range fast tool servo is to function and actuate the tool motion with much extended level of stroke, for instant in millimetre per input Hz. Over the last couple of decade, the demand for producing NRS (Non-Rotational Symmetric Surfaces) which require the tool motion run within millimetre travel level and stroke at high-speed and angular velocity, has driven the technology to develop the long-range stroke fast tool servo device for DTM while providing highest level of quality, resolution and accuracy for the surceases. Lorentz force for actuation, such as brushless linear or rotary motor, and voice coil motor (VCM), has been utilised for this class of actuator. The capability of achieving maximum acceleration is restricted by the maximum heat generated in the coil [24]. The first generation of a linear motor and slid direct drive for fast tool servo, is proposed in 1983 by Douglas in Oak Ridge National Lab [25]. An off-axis part of parabolic mirror has been implemented and machined. Greene and Shinstock [26] developed and implemented a linear servo motor with 6 mm travel and 100 Hz bandwidth. The tool attached to the coil, which is supported by the flexural bearing and a capacitance gauge which used to measure the position. Later on, Ludwick et al. [27] have developed and designed a novel fast tool servo and a rotary servo that excretes the reaction force by a stabilised rotary design, which had a limitation in trajectory generation difficulty. The ophthalmic spectacle lenses have been machined with a max stroke of 30 mm and 200 Hz of bandwidth. The fast tool servo was included in a rotary arm that carrying the cutting tool on a circular path, as opposed to a straight-line path as conventional design. Other standard elements such as an actuator, sensors, and bearings have been used for the experiment. The result was 500 m/s2 instantaneous acceleration at tooltip over a range of 3 cm cutting depth. Figure 2.4 illustrates the schematic diagram of the toolpath generation in their design.
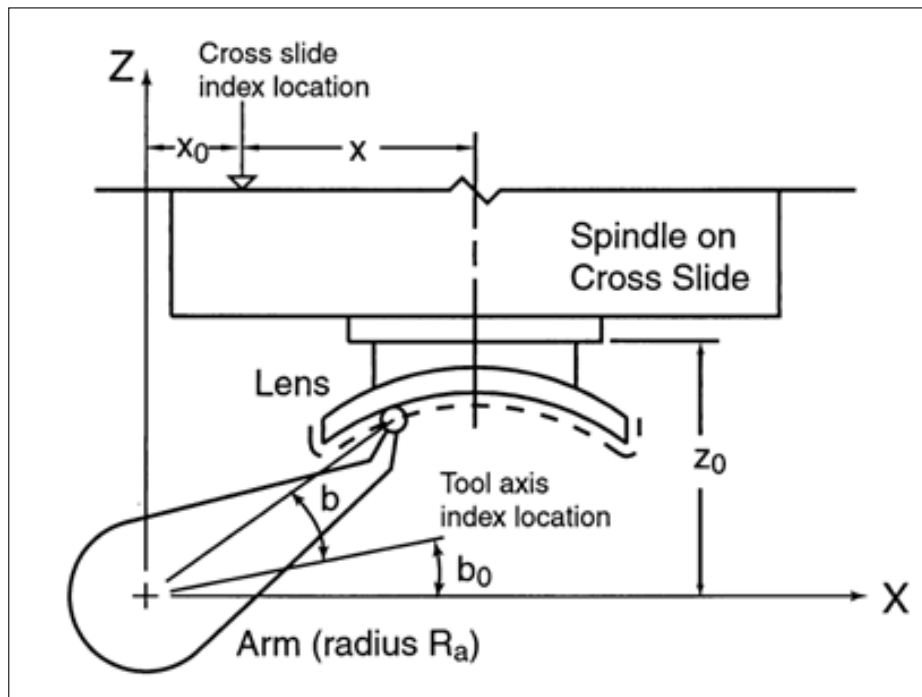
Fig. 2.4 Schematic diagram of the toolpath calculation

Byl [28] designed and developed long linear stroke fast tool servo (FTS) with integral balance mass. This type of FTS made up with a staged air bearing operating with a unique three-phase oiled cooled linear motor. The linear FTS has a maximum stroke range of 25 mm and can achieve 100 m/s2 accelerations. The FTS is fixed and mounted in diamond turning machine (DTM) and attached to a supported in-feed stage hydrostatic bearing which is driven by a secondary linear motor. The in-feed stage is a technology that moves in response to the FTS actuation forces and therefore perform as an integral balance mass. In general, performance of the servo control is restricted by the current loop bandwidth of 2 kHz and slide piston structure's response mode of 1,600 Hz with position measurement error. Figure 2.5 shows the long-range fast tool servo mounted on a Moor Nanotechnology diamond turning machine.
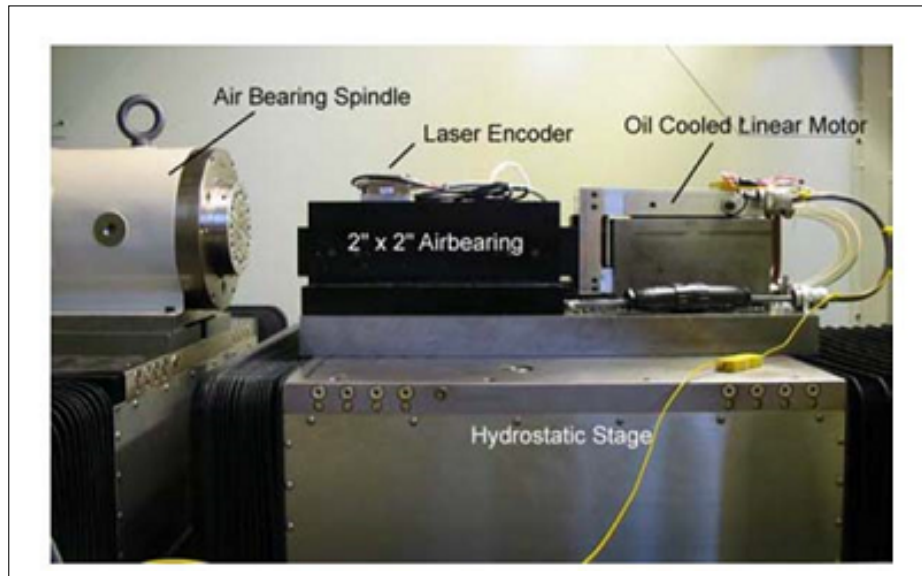
Fig. 2.5 Photograph of the long-range fast tool servo mounted on a Moor Nanotechnology DTM

A long-range, precision fast tool servo (FTS) system was developed by Rakuff et al. [13] that can accurately translate the cutting tool on the DTM with maximum accelerations of 260 m/s2 and bandwidths of up to 140 Hz with the maximum travel range of 2 mm. The FTS utilizes a flexure mechanism that is driven by a voice coil actuator, laser interferometer feedback system and custom linear current amplifier. Commercial NFTS-6000 introduced by Moore Nanotechnology System in 2007 with maximum travel and stroke of 6 mm can achieve 3 mm amplitude at 20 Hz of sinusoidal trajectory. It uses an integrated counterbalance, voice coil motor with constrained porous air bearing, a linear amplifier and a linear scale encoder. An independent DSP controller has been used for its control system. Technical information about this device and its performance is limited. In the direction of this literature review, a few long-range actuators for conventional non-rotational machining were uncovered. The control and design fundamental of those actuators are capable of transferring for diamond turning applications. A hybrid micro and micro-range FTS that enables the machining of freeform surfaces has been proposed by Liu et al. [29]. It has proposed new generation of FTS design that brought new machining methodology using both Voice Coil Motor (VCM), and PZT to drive the micro-range of FTS guided by a flexure hinge. The VCM's output force is

increased by a lever. This method has the capability to machine large and small asymmetrical optical surfaces. A lever enlarges the output force of the VCM. The macro-range FTS can be used to machine large asymmetrical surfaces, and the micro-range FTS machines the small asymmetrical surfaces. Macro-range FTS can achieve the resolution of 34 nm with bandwidth up to 16 Hz. The micro-displacement FTS can reach the resolution of 15 nm and the bandwidth of 200 Hz. Figure 2.6 illustrates the schematic view diagram of a hybrid micro and micro-range utilising FTS mode.
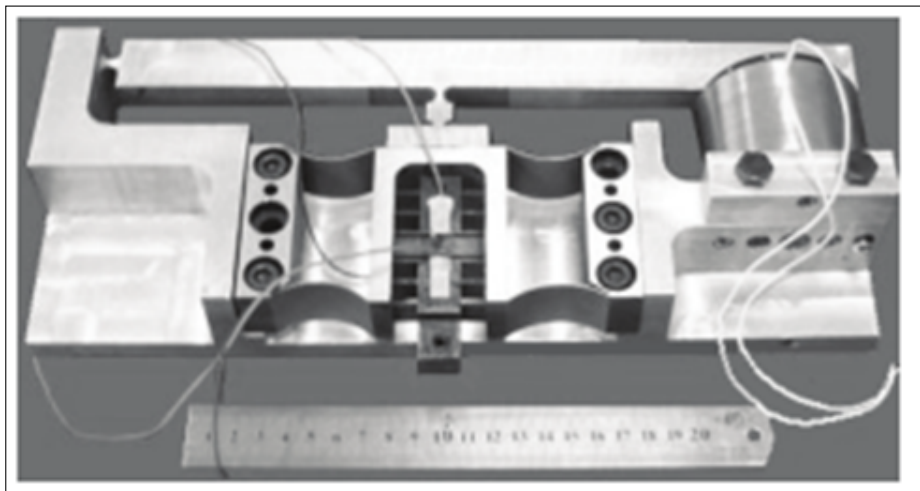
Fig. 2.6 Schematic diagram, hybrid macro and micro-range FTS

VCM technology is growing in the development and design of FTS technology with long-range stroke in ultraprecision and advanced manufacturing. The impact of this methodology making a robust effort to design more precise and high quality freeform surfaces such as optical lenses that include large curvature sag and longer vectors. Following this development philosophy, new fast axis servo (FAS) methodology is introduced by Tian et al. [30], which is incorporated with VCM. They have developed a new long-range fast axis servo which can be used to fabricate the non-rotational symmetric surface with millimetre range of surface depth. Their FAS design consist a light-weight axis includes aerostatic bearing, linear drive slide motor, which can operate with a range of 4 mm at 50 Hz bandwidth and actuate by VCM. The total range of 30 mm of stroke obtained, and the following error of 300nm for a range

of ±2 mm at the frequency of 20 Hz recorded in their experiments. However, some concerns have been identified in the surface resolution and tracking accuracy. They suggested a more advanced control algorithm to control the FAS and overcome those issues. Shang et al. [31] designed and developed a novel voice-coil motor-driven for micro-positioning stage based on flexure mechanism. The design presented a 2-degree of freedom flexure base micro-positioning stage with a flexible decoupling mechanism. Maximum micro-positioning and displacement of 1.8 mm on both X and Y direction have been achieved. Wang et al. [32] developed a new VCM with 6-DOF fine stage of lithographic equipment. The result is proposed to calculate air gap and Lorentz force's magnetic flux density by causing the interaction between the permanent magnet and current. The Lorentz force-displacement of ±4 mm at 48.5 N has been obtained from the experiment. Feng et al. [33] designed and developed a self-developed Long Stroke Fast Tool Servo (LFTS) using Voice coil motor to fabricate a freeform Progressive Addition Lens (PAL). Range of ±4 mm stroke based on VCM actuator-integrated into DTM has been obtained with LFTS methodology that utilized a three-ring cascade control system for the motion trajectory control. From the 3D surface data with freeform features, the numerical control codes was used to generate the tool path. Accuracy of the 6.7 μm (RMS) is obtained from the surface form. Figure 2.7 illustrates the VCM structure of a LFTS using voice coil actuator.
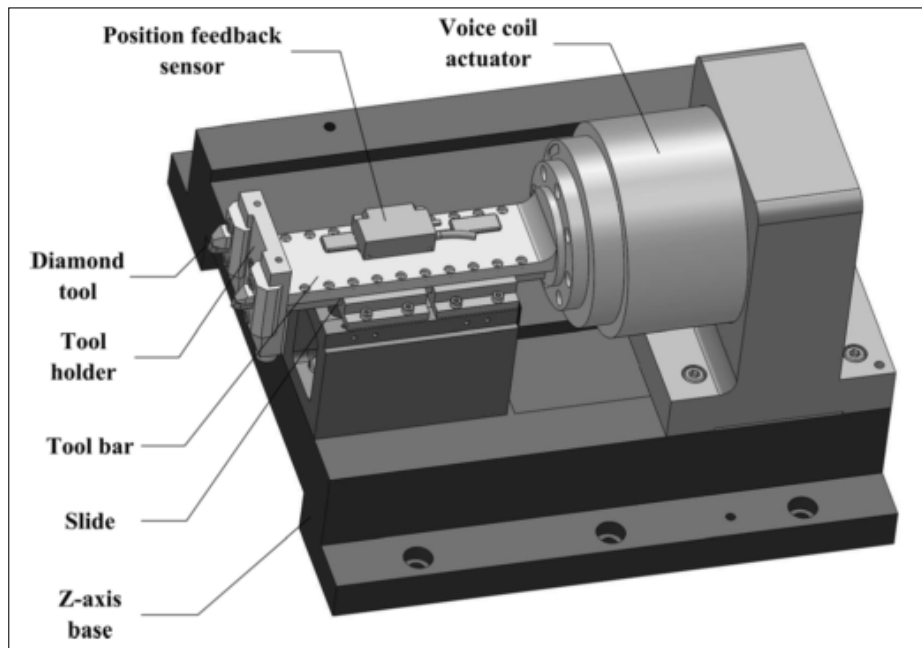
Fig. 2.7 Photography of LFTS mode using voice coil actuator

2.1.3 Slow Tool Servo (STS) Mode Machining

The slow tool servo (STS), also known as slow slide servo (SSS) [34, 35], utilizes diamond tooling machine's Z-Axis which is a direct linear drive slide motor for tool motion to replace the ball screw mechanism. The STS is similar to the FTS in which, the workpiece is fixed on the spindle, but the tools are directly mounted in the linear motor. While the spindle rotates the Z-axis oscillating in and out to generate the trajectory for the designed freeform surface. Other differences between the FTS and STS is C-axis or the position of the spindle. In the DTM with an FTS mode, the spindle is connected to an encoder that feeds the position data into the FTS unit, so the spindle is not in the position control. In the DTM with STS mode, the coordinated positions are fully controlled by all axes. Association to linear direct-drive motor specification, is that the STS can oscillate at significantly longer ranges than FTS, produce very accurate parts, inexpensive system and easy to setup [34]. Despite STS capable of machining the NRS surfaces with motion coordination control of the all axes, the rotatioanl velocity of spindle is significantly low due to fact that the heavyweight slides can not follow

the position commands[36]. By taking the advantages of using the STS methodology, several works and research in optical design and fabrication of freeform surfaces, particularly in freeform surfaces have been carried out and studied the feasibility and capability of the STS technology for production of high accuracy and high-resolution surface finishing [35–37]. Kong at al.[16] experimented manufacturing of progressive addition lenses by using STS technology to replace the traditional manufacturing that usually was done by grinding, polishing one by one, which is cost-effecting and time-consuming. For constructing and fabrication of freeform surfaces, the extended polynomial has been employed. 3S machining, which present diamond turning machining with three axes or STS, have been used for the experiment. The results obtained demonstrate a significant development and improvement in the design process and the optimization of the optic design of the freeform surfaces which could take an enormous benefit and allowance for future mass production in optometric applications. Figure 2.8 shows the schematic of the 3S machining mechanism which is known as Slow Slide Servo (SSS).
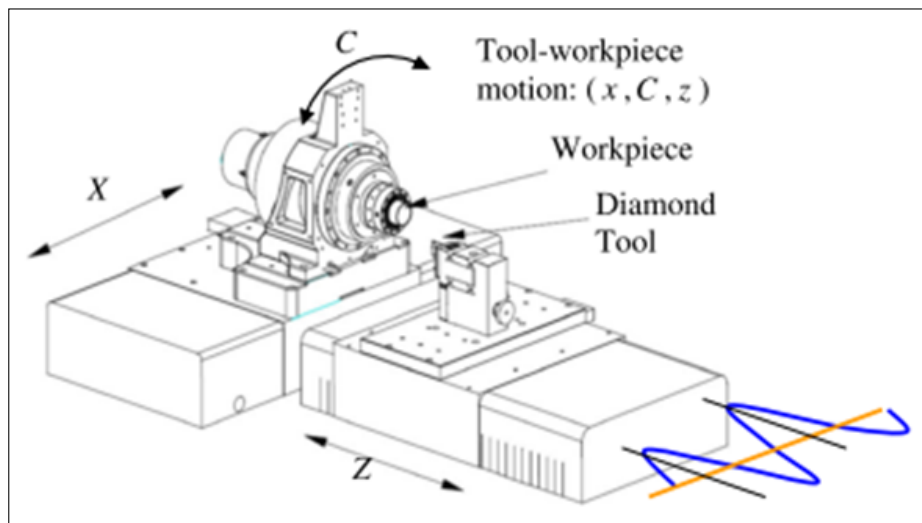
Fig. 2.8 Photography of 3S machining system, Slow Slide Servo mode

Kong et al. [38], experimentally investigated an orthogonal slow tool servo machining of wavy microstructure pattern on the precision roller. For Fabrication of patterned microstructure on the surface of the roller, the ultraprecision machining process is required. Using STS tech-

nology is an enabling and efficient machining method to fabricate this type of microstructure. New development of a toolpath generation methodology for machining wavy microstructure pattern on a precision roller has been presented by using Orthogonal Slow Tool Servo (OSTS). The study proposed a novel machining process for ultraprecision manufacturing of wavy microstructure patterns and therefore, extended the existing machining tools to a new the capacity and capability of ultraprecision machining. Figure 2.9 shows OSTS methodology using STS technology for ultraprecision machining the wavy pattern.
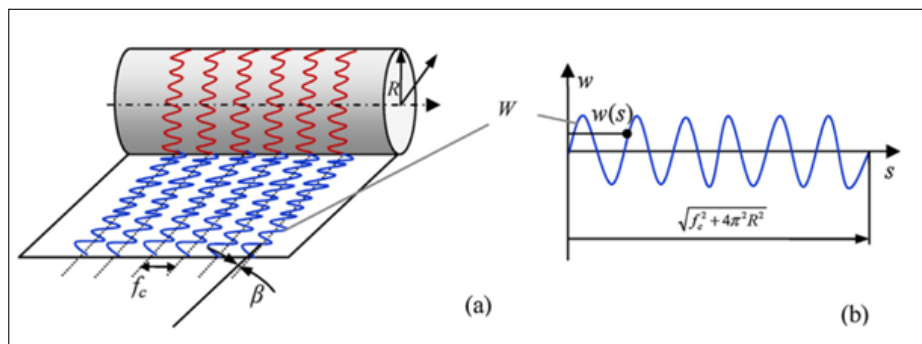
Fig. 2.9 Photograph of wavy structure pattern on roller surface

As a result of this literature review, there are very few works given to account on STS technology. Thus, the impact of the methodology and its influence in the machining of freeform surfaces remains vulnerable. However, there are some unresolved challenges in the STS which need to be addressed. Those challenges include heavy density and mass in the linear axes, and the inertia forces are at a higher level in the STS process, which dynamically slowdowns the motions in the machine axes. Therefore, it is not capable of machining the freeform surfaces with higher frequency. However, this will influence the cutting speed and finally would break down the surface quality and resolution. The percentage of thermal drift is extremely high during the machining process, a similar condition to those traditional manufacturing methods such as polishing, fly-cutting and grinding.

2.1.4 Novel Ultraprecision Machining

Nowadays, the complexity of ultraprecision machining to generate such as high-resolution surfaces, enduring characteristic dimensions that can be led to develop more novel technologies. However, the new techniques such as FTS, STS, fly cutting, diamond milling and diamond turning have demonstrated their capability to fabricate freeform surfaces. Besides, they are still facing the difficulties to achieve very high resolution for complex freeform surfaces in a single machining setup. The UPM complexity associated with loss of symmetry such as NRS surfaces required more axes in the machining process for the motion of the diamond tool to fulfil the expected resolution within the design specification. Figure 2.10 highlights the ultraprecision diamond machining process complexity sequence versus their accuracy resolution [39].
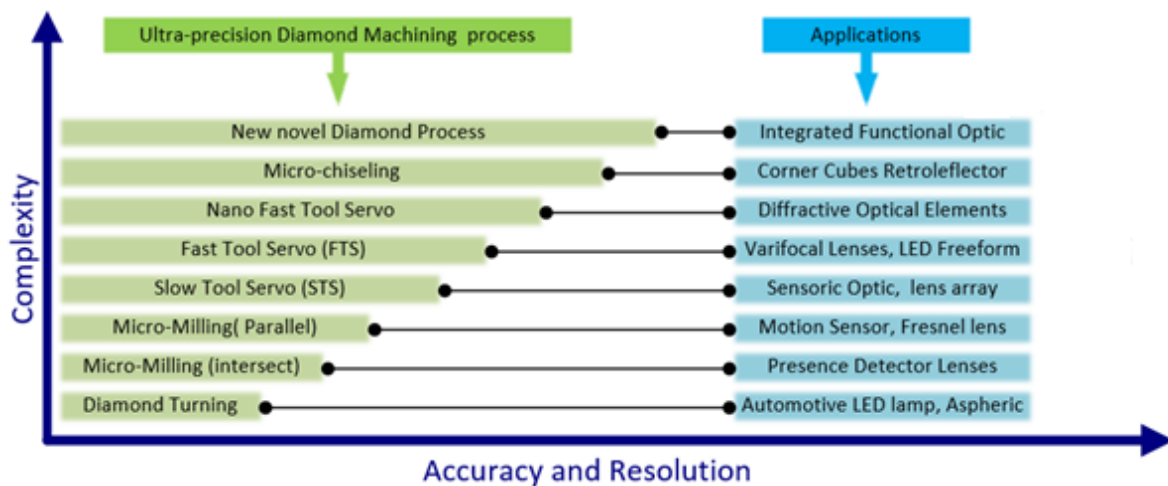
Fig. 2.10 Ultraprecision diamond machining process, complexity vs resolution sequence

Novel manufacturing processes is a growing demand for ultraprecision technologies to overcome potential machining challenges. One of this novel technique is micro-chiselling which is highly capable of fabricating freeform flat-ended microgroove [40–44]. Large-Scale Roll-to-Roll Micro-gravure novel technique can also be used in printing and medical blading [45]. One of the recent novel technique in ultraprecision machining is Atomic Step Formation which can be used on Sapphire Surface in ultraprecision Manufacturing. It uses atomic force microscopy

(AFM) and high-resolution transmission electron microscopy (HRTEM) [46]. Figure 2.11 exemplifies OSTS methodology using STS technology for ultraprecision machining setup in diamond micro chiselling machine.
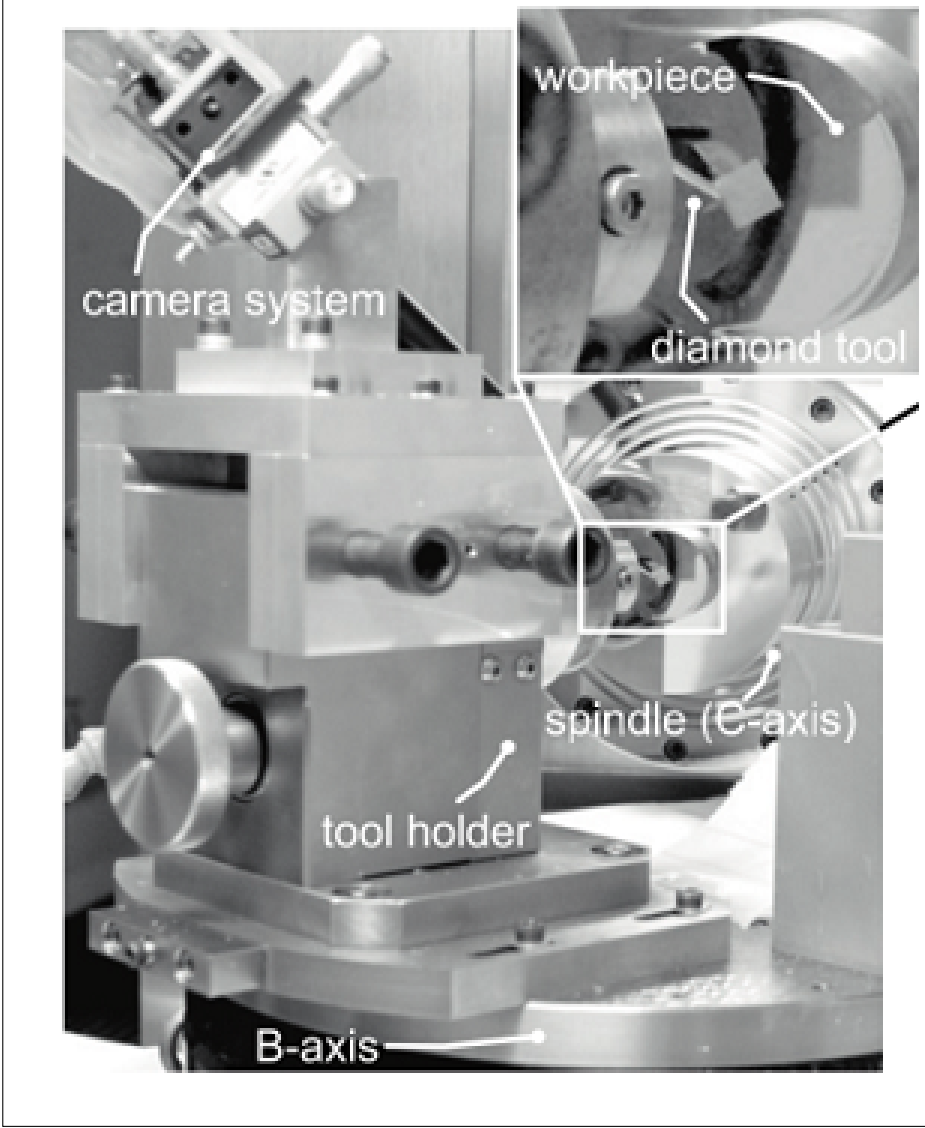
Fig. 2.11 Photograph of ultraprecision machining setup in diamond micro chiselling machine

2.2 State-of-the-Art in UPM

For the last couple of decades, computer-aided design (CAD) methodology is playing a significant role in fabricating the freeform surfaces applications in industrial area. It is efficient and more accessible to design with compare to traditional and tedious mathematical approach. The befit of employing CAD software in the design not limited to designing solution but also offers simulation analysis from digital problem solving to in-depth, organized computer-aided engineering (CAE) reliability and validated result.

2.2.1 Surface Generation Using CAD/CAM

Computer-aided Design (CAD) and modelling could be integrated with Computer-aided Manufacturing (CAM) for Computer Numerical Control (CNC) data post-processing and utilisation in order to make the design fully automated status, taking the full responsibility of the whole design and manufacturing for mass production. Post processor can be described as a software that capable to transfer the CAD/CAM data to specific commands compatible with the CNC machine programming language. In freeform surfaces machining process, those CAM technology can successfully lead the production of ultraprecision applications to the finishing point with a very high level of accuracy and resolutions [47]. The tool path can be generated by CAD/CAM model and sent for data post-processing in the CNC machine. The conventional CAM system has some deficiency in tool path generation for freeform surfaces in Diamond turning machining where the resolution of Nano level is required, and thus, the post-processing system is unable to support FTS/STS technology [48]. Fabrication of freeform surfaced application, utilising UPM with resolution of (<1 nm), is not achievable with conventional CAM system. Hence, customising and integrating those CAM systems with FTS/STS is highly necessary. Nevertheless, there are some solutions made to overcome those issues. For an instance in UPM using diamond turning machine, DIFFSYS and Nano CAM2D/3D software, have been developed to generate the freeform data for post-processing. However, they are still cost-

effective, time-effective and difficult to use and not suitable for mass production application. In a successful manner, by taking advantage of the accuracy of the CAD system and integrating it with new development in advanced software engineering such as application programming interface (API), precise and accurate surface and tool path generation can be exploited for ultraprecision machining of freeform surfaced in optic applications. Paolo [49], introduced reverse engineering methodology integrated with application programming interface (API) into Solidworks to develop the numerical and procedural algorithm. Neo et al. [47], developed a novel method for generating the toolpath for hybrid freeform surfaces. The proposed research was based on finding the solution on CAD software using API to generate spiral tool trajectory for freeform surfaces diamond turning and then extract those trajectory data from CAD without utilising the CAM software. However, according to this literature review, there are still few researches have been employed on the integration of API and reverse engineering methodology in optical freeform surfaces.

2.2.2 Toolpath Generation (TPG)

In ultraprecision machining, one of the critical factors in optical non-rotational surfaces is tool motion control that defines the associated position between the workpiece and diamond tool. Various methodologies and technology have been developed and implemented successfully to determine the tool path for freeform surfaces fabrication. Based on the method that the tool path is generated, the FTS/STS mode, diamond turning can be classified as:

(a) **Diamond turning based on the motion of axes (θ, x, z)**

This methodology of tool path generation usually can be employed for STS where the tool path can be generated by controlling z-axis translation and axial x-axis feed system, with regards to polar spindle rotation θ. The disadvantage of the STS is the lack of efficiency [36].

(b) Diamond turning based on the motion of axis (θ, x, z' + z)

In this method, the tool path can be generated by controlling the position z of axis Z and position z´ of axis Z´, with respect to the spindle's rotation θ and the radial feed on the x-axis of the diamond tool [50]. In this technique, the significant advantage is the allowance for larger deviation for rotationally symmetric surfaces with compare to other techniques, and also the fabrication cycle time is less than other diamond turning methodology. This method has some disadvantages as, a) decomposition for different type NRS surfaces and b) geometrical feature error in NRS surfaces [50].

(c) Diamond turning based on the motion of axes (θ, x, z) or (θ, x, φB)

Dow et al. [51] investigated the motion of diamond turning axes. The tool path can be generated in this method by controlling the translation z´ of a linear motion on the Cartesian coordination plan or the rotation φB on the polar coordination of a rotary FTS, considering rotation θ of the spindle and x radial position of the diamond tool. The disadvantage of this method is that is not capable for fabrication of the non rotational surfaces with high range of convexity or concavity, even though if the surface asymmetry is small. A research carried out by Ludwick [52], in rotary FTS-based DTM on non rotational surfaces which described that the rotary FTS is much capable than linear FTS in bandwidth, acceleration, stroke and backlash force.

2.2.3 Point-to-point Mapping TPG

Fang et al. [10], studied systematically cylindrical coordinate machining (CCM) method for freeform surfaces which the feature points are fitted to typical Non-uniform rational b-splines (NURBS). In their study, all designed points have the mapping coordinates in the variable space with inversion technique, while the NURBS points have their coordinates due to the interpolation technique. The derivation and mathematical features are obtained using the fitting formula. The fitting formula is used to obtain the derivation and compensation features in

the freeform surfaces. Tool geometry compensation and optimisation have been studied, and finally, various typical freeform surfaces have been fabricated using the cylindrical coordinate machining (CCM) method . Yu et al. [12] studied an optimisation approach to micro-structure surface machining that configure a controller for fast tool servo integrated into diamond turning machine . In their study, The controller configuration works with the FTS independently as the primary axis, unlike conventional controller configuration with the auxiliary axis. The simulation has been carried out to predict fabricated surface resolution. In their experiments, the assumption of ideal tracking of the FTS for selecting suitable cutting conditions taken place by calculating the theoretical surface profiles. Based on this methodology, the motion trajectory was generated and corresponding motion programs was defined for all axes. The results have shown an effective and simple approach, impacting on micro-structured surfaces machining. Zhou et al. [11] studied the influence of process parameters on the surface topography in diamond turning of freeform optics. The consideration of tool and the tool nose radius compensation for tool position trajectory generation have been studied in diamond turning process. The influence of the factors such as depth of cut and tool nose radius on surface roughness, feed rate, and spindle speed were studied. Yin et al. [53], studied and implanted off-axis aspheric surfaces using STS. In their study for toolpath generation, the tool position located at the centre point of the diamond tool radius and the position enabling the contact point between the edge of diamond tool and freeform surface workpiece, which can represent the divergent trajectory path between the design surface and single point diamond tooltip. In this methodology for an off-axis freeform surface, the tool path is generated by offsetting the design surface normal to its direction, equal to diamond tool radius. The study was also based on interpolation methodology for slow tool servo such as linear and rotational interpolation. The position-velocity-time (PVT) mode, has been applied for tool path generation (TPG) on which the path created in this mode was a piecewise cubic Hermit spline. The experimental work carried out, and the off-axis paraboloid's form error of tool cantering have been analysed.

The result concluded based on several outcomes such as spiral cutting strategy, PVT mode for tool path generation, investigating the STS burls on the centre of surface and positioning of the tool form error for off-axis aspheric surfaces. Figure 2.12 illustrates the tool path and tool contact path in STS cutting.
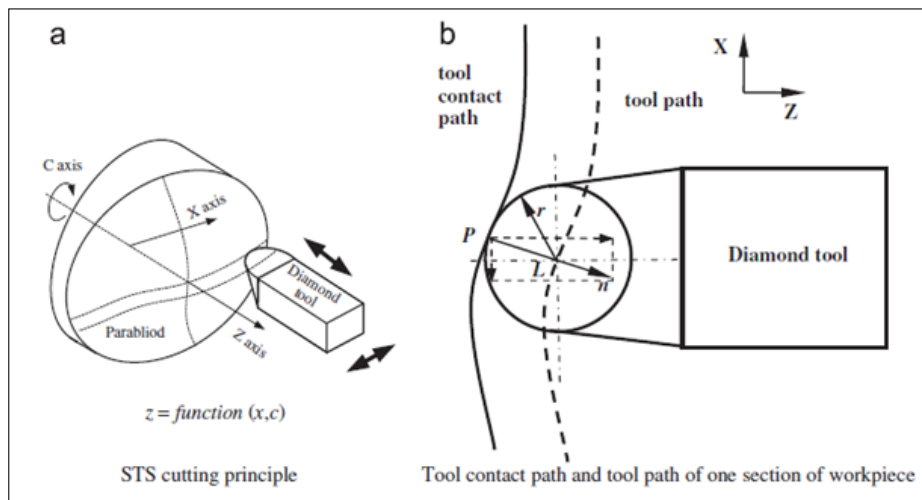
Fig. 2.12 Tool path and tool contact path in STS mode

Gan et al. [12], studied the influence of FTS tool path generation on surface quality and resolution systematically. They presented an optimisation for diamond turning of the micro-structure surface with two both non-uniform rational spline description and analytical description. The optimisation for tool path has been carried out on three aspects as: a) different tool nose compensation methodology to decrease the form error, b) simulation in the perfection of the machined surface profile on which the cutting condition and tool geometry optimised to predict the ideal surface finishing quality, c) the influence of dynamically control machine axes which is neglected in conventional machining. Figure 2.13 shows the schematic diagram of toolpath generation optimisation.
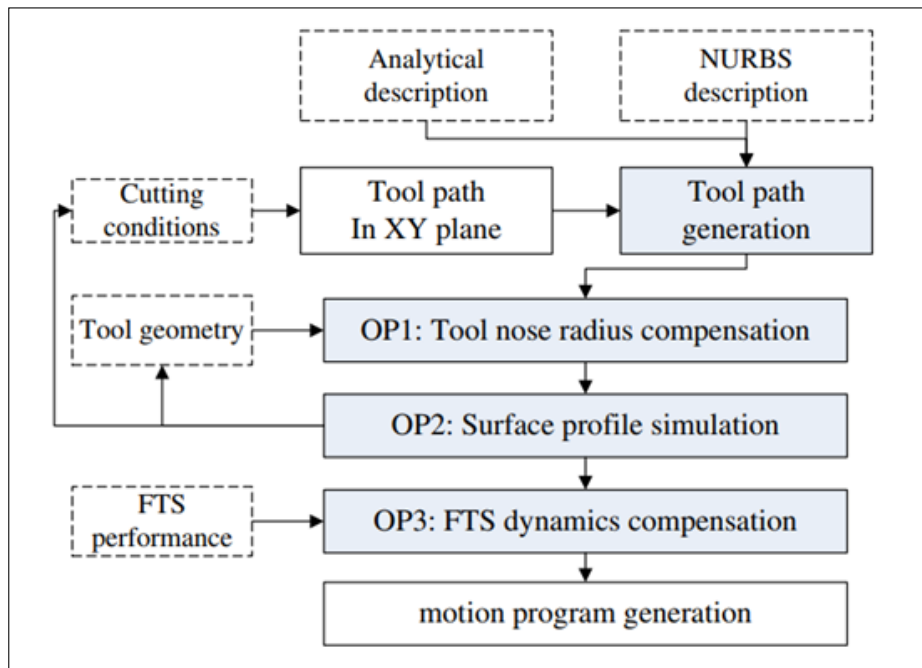
Fig. 2.13 Toolpath generation and optimization schematic diagram

Kong et al. [16], theoretically studied and experimentally analysed the effect of error motion on surface generation for FTS machining. Simulation method has been employed for modelling the FTS, and tool path generation has been employed for identification of the machine's slid error in feed axis and spindle's radial-axial error motion. The result from the experiment was performed and verified with theoretical study and shown an acceptable match between the theoretical prediction and experimental result. The methodology of the proposed research pined the new consideration in FTS and tool path generation to include the motion form errors of the machine axes into the system for much reliable and corresponding optimisation in ultraprecision machining. Figure 2.14 illustrated the form errors in the diamond turning machine axes.
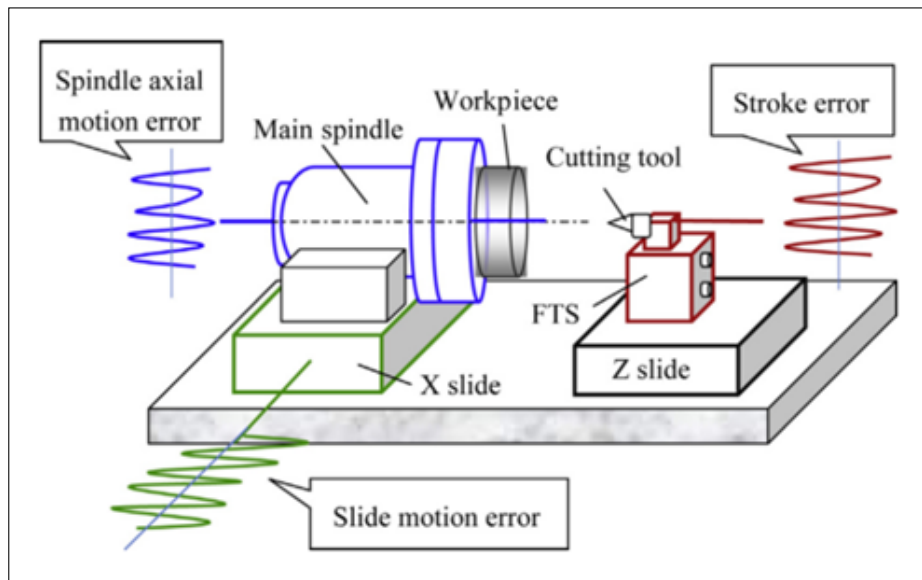
Fig. 2.14 Motion form error identification in diamond turning machine axes

Gong et al. [54], introduced a new technique for spiral tool path generation for diamond turning of freeform surfaces with quasi-revolution. The methodology was proposed based on space Archimedean spiral to the machine and fabricate freeform surfaces with big slop. intheir study, new space Archimedean spiral methodology was explained and theoretical modelling was described and analysed. they also validated their idea by experimental implementation utilising diamond turning machine for quasi-revolution, which can be defined as the surface is near to some surface of revolution. The methodology was obtained on projecting the Space Archimedean spiral onto another base freeform surface along its normal direction rather than its fixed direction, unlike the conventional methods. They concluded the theory that projecting the Archimedean spiral on to designed surface is not a sufficient solutions when the freeform designed surface deals with large slop. They also theoretically verified that, when the surface slope increased, the projected spiral will increase the distance between two adjacent points that passes the vertical projection direction. The result has shown that this technique and methodology is capable of generating the tool path for the freeform surfaces with a significant

slope on 3-axis or 4-axis DTM. Figure 2.15 illustrate the map plane to surface of revolution when the longitude is deformed.
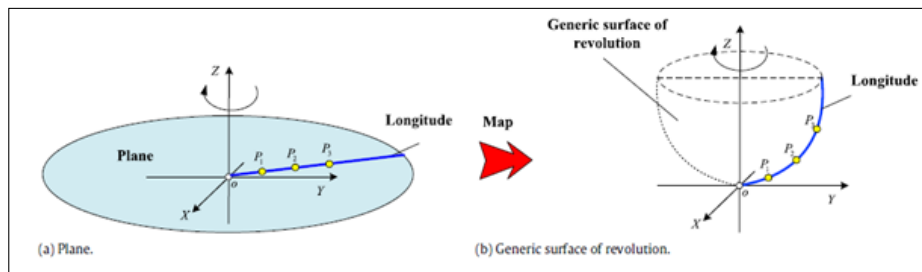
Fig. 2.15 Mapping plane to revolution surface with deformed longitude

Zhou et al. [55] have developed a new freeform surface generation method in diamond turning machine that capable of difficult-to-cut materials. The method is proposed by applying a double-frequency elliptical vibration cutting process. Hence, the elliptical vibration cutting itself is unable to generate the freeform surfaces. The technique provides high-frequency elliptical vibration to cope with difficult-to-cut material removal machining. A new tool path generation method also has been presented, and the final result outcome from the experiment validated the effectiveness of the surface form between the predicted model and the designed model. As illustrated in Figure 2.16, it shows the process of double-frequency elliptical vibration cutting with additional axis of y in diamond turning machine.
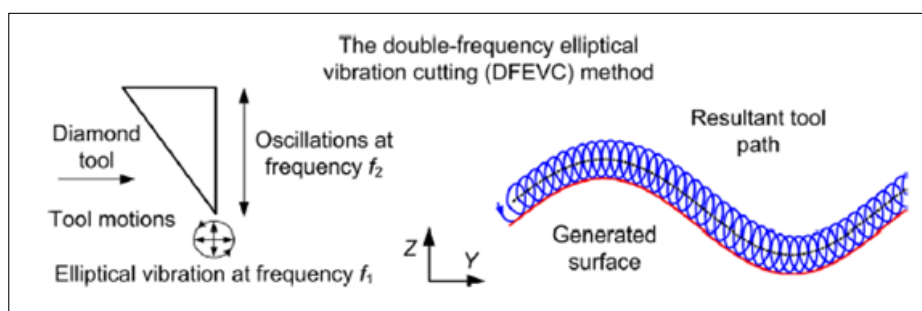
Fig. 2.16 Double-frequency elliptical vibration cutting method

2.2.4   Lens Positioning and Clamping

Nowadays, advanced application such as microscope and lenses integrated with freeform surfaces applies complex systems, particularly when they combining into multiple lenses. Depending on the complexity of the system, the optical performance relies on accurate positioning. Any alterations in linear location or angular position, directly affect the image quality. Mounting those lenses for fabrication and machining by restricting their degree of freedom, play a major role to achieve desirable performance and such high resolution. Hence, any error with respect to the optical axis need to be corrected during the machining. In optical freeform surface lenses such as varifocal contact lenses where the surfaces is NRS and rotationally are not symmetrical, the process of centring and positioning becomes very complex. Therefore the affordable lens holding and positioning design are necessary for their ultraprecision machining. Wood and Springs [56], invented a new single block mounting system for surfacing and edging of a lens blank. This device and lens block assembly were capable of mounting in any surface generating machine without requiring re-blocking the lenses to compensate for axis shift. The control system has been employed in this design. Volken [57] invented and designed a block piece for holding an optical workpiece such as spectacle lens in particular. The block piece consists of a primary body with an end face against the workpiece and can be blocked with a temporarily deformable material, and a clamping face. The body can be directly fixed on the spindle for machining. Bono et al. [58] invented and designed a flexure-based tool holder for sub-μm positioning of a single-point cutting tool on a four-axis lathe. The tool holder adjusts the tool position using flexures. The setting tool in this design simplified, considering the self-correction and positioning with sub-micron accuracy.

Schneider [59] invented preformed block piece with three points of support. "The design was proposed as a block piece for holding an optical lens and a coupling part for holding in a workpiece chuck and with a holding part for fastening the lens. The holding part has a convex or concave holding surface corresponding to a first side of the lens. The holding surface, according

to the shape of the lens to be held, provided in the form of a negative freeform surface, and the block piece is made from a plastic that can be machined." Felten [60], invented and designed new lens blocking and de-blocking method for the optical lens. The design was capable of holding the lens on a heat-conducting unit. The invention was consist of a layer which included an adhesive tape on its upper assembly surfaces and a holding unit which intended to provide a second layer with thermoplastic material arranged on the side of adhesive tape and a third layer on the bottom of the surface with adhesive tape. Breme [61] invented a device for holding and blocking optical spectacle lenses. In particular, the invention is capable for holding a spectacle lens for machining process particularly and individual optical materials such as polycarbonate and mineral glass. The invention also focused in manufacturing methodology for the spectacle lenses machining based on prescribed data from an optician. Following to the need for novel technology and methodology in the ultraprecision machining, Nanotech and Precitech have developed some bespoken technique based on their ultraprecision machining design as a separate accessory. New novel technology recently has been developed in the market to take accountability with much more efficiency of micro-structure manufacturing. Affordable high-tech performance using integrated software-based, in-line measurement and error compensation to fulfil very high-resolution freeform surfaces. IL centric is one of those reliable optical lenses machining in which can provide high precision performance [62]. Langehanenberg et al. [63], at Tioptic, presented the novel technology for directional adhesive and lens alignment for high precision lens mounting for mass production. In their research, they have used the in-line measurement for lens alignment.

Sitzberger and Rascher [64], have investigated the advanced clamping system for freeform surfaces for effectively holding the lenses in very high precision positioning. Due to the high number of individual application in precision optics, they have standardised the workpiece receptions and clamping lens holders and blocker in the optics market. Their standardisation

Fig. 2.17 Photography of bonding station with actuator for alignment of the lenses

can be summarised as: a) vacuum chucks b) collets for single lenses c) precision blocking pieces for spectacle lens manufacturing d) precision blocking pieces with cylindrical fitting.
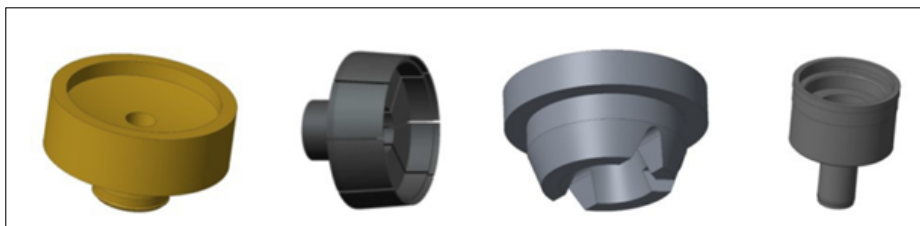
Fig. 2.18 Standardized workpiece receptions for the optics workshop, from the left: vacuum chuck, collet for single lenses, precision blocking piece with cylindrical fitting, precision blocking piece for spectacle lenses

Wenzel et al. [62], introduced a new methodology for lens centring. The novel methodology resulted in new lens centring machine design with a robust capability to automate the in-line lens centring detection and correction the axis according to the spindle axis. The ILCentric which has been developed by Innolite uses the confocal laser reflection measurement sensor and based on a different approach, and there is no need for any alignment of the lens chuck to the mechanical axis of the spindle. Instead, a confocal laser, measures and match the spindle axis references to the absolute position of the optical axis. The design is also configured

and equipped with new clamping technology of NanoGrip zero-point system with 0.5 μm of mechanical repeatability. Using the NanoGrip zero-point clamping system can be used for an individual fixture for different type geometric mounting and can produce a group and be aligned very fast and machined with corresponding programs. Figure 2.19 shows the ILCentric machine with NanoGrip zero-point clamping system.

Fig. 2.19 Photography of ILCentric machine using NanoGrip zero point clamping system

2.3   Summary

The critical review of the research literature reveals that there are some gaps and shortcoming in ultraprecision machining, especially link to freeform surfaces applications. It can be concluded four areas of gaps necessarily should be addressed and overcome in ultraprecision machining, covering:

- Lens design and optimization.

- Lens manufacturing.

- Mounting of the lens mould inserts and tooling setup.

- Development of toolpath generation algorithms.

- Metrology and accuracy assessment for freeform surfaces.

- Effective data analysis for post processing in mass production of freeform surfaced components.

- Control system for ultraprecision machining of freeform surfaces.

Those gaps are focused on freeform surface machining and categorised in the following four areas:

(A) **Machining process of complex freeform surfaces**

Machining and fabrication of optical complex freeform surfaces can be a challenging process. The new ultraprecision machining technologies can fulfil this gap by offering multi-axis controllable, programmable methodology integrated with new techniques such as FTS and STS. However, due to increasing the complexity of optical freeform surfaces geometry, the complexity in the manufacturing of those associated surfaces will be ascending. By meaning that, the machining axes or degree of freedom for the motion purpose, will make the machining process very complex. Although ultraprecision machining system have a noteworthy development trend but few novel techniques and integration in diamond turning of freeform surfaces. The manufacturing process is still not cost-effective and time-effective, and not easy forward task for mass production. Ultraprecision machining processes require a robust strategy to enable the integrating new technology with the machining process and to render mass production in future.

(B) **STS process barrier and limitation for freeform surfaces machining**

The FTS technique has a short-stroke. It depends on the nature of the work and the

system, which is almost not capable of fabricating the freeform surfaces with longer vertex and larger sag. According to the literature review, there have been some researches on FTS developments with a longer range of stroke likewise VCM. However, there are some limitations concerning their bandwidth. For error compensation, the FTS with piezoelectric and lever mechanism system is suitable as it employs low resonance frequency. Although, wide range of researches have been done in ultraprecision machining the freeform surfaces using DTM with FTS technique integrated, the machining processes are costly and not time-effective, thus not suitable for mass production. Applying the slow tool servo (STS) process for machining freeform surfaces can provide much longer stroke length and be capable of machining the freeform surfaces with more considerable sag height. Nevertheless, the limitation of STS is a low bandwidth system where the weight of the slides reduces the performance of the cutting process. The cutting speed is another limitation where the spindle speed cannot be run in a higher range. Therefore this matter raises the probability of lowering surface resolution and quality. However, the low spindle speed can increase the processing time and increase the thermal drift in the surfaces and finally deform the designed surfaces. Hence, both FTS and STS convey some limitations in most cases of freeform surfaces machining, optimisation and innovative integrated technology are required for fabricating the freeform surfaces, particularly for progressive addition lenses.

(C) Post-processing in CAM system for freeform surfaces

Over the last decade, the CAD/CAM system played a major role in the manufacturing of highly precise and complex applications in automotive, aerospace and medical engineering. Moreover, in the area of optical freeform surfaces application, there are also significant developments taking place, and many new novel techniques have been employed. Nevertheless, most of the CAD software is currently unable to accommodate and support those new technologies such as FTS and STS onto diamond turning machines

(DTMs). Some additional special external solutions are integrated into CAD and CAM system to fulfil those gap, but there are some areas yet not fully able to support the DTM technologies. It is believed that those techniques are very complex, expensive and not time-effective. Hence, commercially the CAM developers and manufacturer are investigating for the new solutions to drive the next generation of ultraprecision machines and integrate those technologies with much sustainable and feasible post-processing of freeform surfaces to mass production.

(D) Positioning and clamping for freeform surfaced components

According to the knowledge based on the literature review, some novel systems for lens clamping system are designed and developed for the optical market. However, there are still some areas in freeform surface machining that require high precision positioning. Ultraprecision lens setting up on the machine still requires much operator-effort to have an desirable result of machining with expected surface finishing and resolution. It is a costly process and not time-effective. Since the current methodologies can achieve a very high level of surface resolution, but are still not capable enough for mass production. Hence, new design of a smart chunk for holding and positioning the freeform surfaces for manufacturing is highly expected.

Ultraprecision machining requires for high-tech processing methodology. The machining mechanism is integrated with a vital control system where the components of machining such as the direct-drive slides or the axes and the spindle can be systematically controlled for desirable performance. Hence, in order to fulfil the best result for free surface finishing, development of the ultraprecision control system is necessary. Almost it is impossible to achieve any success in freeform surface manufacturing without employing the control system in ultraprecision machining.
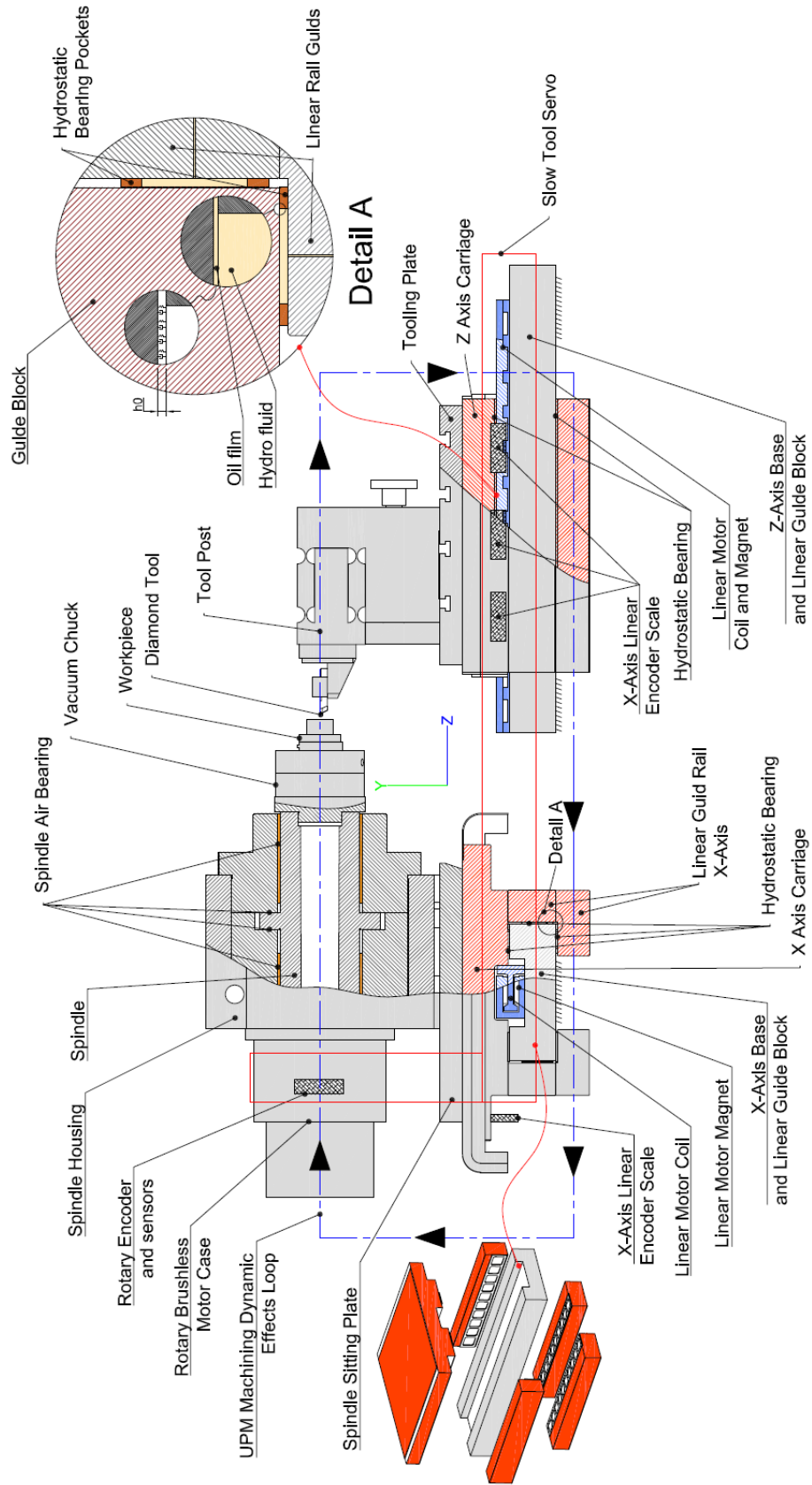
Fig. 2.20 Ultraprecision machining kinematic and dynamics characteristics

The methodology for this research is proposed to improve the performance of the ultrapre-cision machining for freeform surfaces by designing new and novel technology to overcome the issues as explained and identified above with applying an affordable methods that can be in-tegrated with control system of diamond turning machine (DTM). The principle of the research will also be focused on optimisation approach for freeform surfaces using programmable multi-axis control. Figure 2.20 illustrates the close loop of slow tool servo process in ultraprecision machining in which states the association of the parameters and the correlations between them for an enhanced surface finishing.

According to literature review, the dynamics effects in these type of techniques have significant impacts on ultraprecision machining. The areas of development in this research will be focused on investigating new methodology, including:

- New light-weight and high-stiffness material to reduce the following error in FTS/STS using PMAC control system.

- New toolpath generation methodology using multi-body dynamics simulation and analy-sis.

- Novel design and development of a smart chuck for freeform workpiece holding with integrated feature such as self-centring and self-locking features.

Chapter 3

Development of the Novel Multi-body Dynamics Oriented Toolpath Generation

3.1 Introduction

Freeform surfaces can remarkably intensify a system with complex optical feature requirements and deliver integration and simplification of complex engineering systems. They have, thus, been increasingly employed in precision engineering industries, including automotive, defence, aerospace and medical engineering [65]. Ultraprecision machining of freeform optic surfaces through diamond turning is becoming the most reliable and trustworthy enabling process, as it can employ high accuracy and efficiency by integrating with the distinctive techniques of Fast Tool Servo (FTS) and Slow Tool Servo (STS). The integration of those techniques renders the robust capability of ultraprecision machining of complex surfaces such as polynomial freeform, aspheric cylinders, NURBS defined freeform surfaces, lens arrays and bi-conic lenses. According to the fabrication process chain diagram as shown in Figure 1.2, it initially employs 3D CAM software to generate the toolpath trajectory and then, the compensation of surface form error is deployed to modify and correct the tool trajectory [55, 4, 47]. For multi-axis machining of freeform surfaces, toolpath generation methods have been studied and developed

extensively by the academic and industrial communities [66, 67]. Whilst the STS technique provides a longer stroke often at a millimetre level, it has a limitation in its bandwidth, thus constricting the speed of the C-axis (in the tool trajectory) in machining complex freeform optic surfaces. Hence, to achieve very high resolution and accuracy, FTS is often used for freeform surfaces ultraprecision machining [68, 69].

There are potential challenges towards ultraprecision machining of Non-Rotational Symmetry (NRS) surfaces through diamond turning [70]. During the machining process, the diamond tool has to move as a function of the spindle rotation and translation of the machine slide. The methodology above is different from using tool servos separately to generate the tool motion.

Despite all methods above having made significant contributions in the development of ultra-precision machining of freeform surfaces, there are still knowledge gaps, particularly in relation to kinematic and dynamic influence of machining freeform surfaces with high precision and the CAM system alone cannot directly generate the appropriate high precision toolpath without including the dynamic and kinematic factors. This chapter, investigates an innovative integrated approach and the associated scientific understanding of precision engineering design, ultraprecision machining and surface measurement of freeform surfaces. It is focused on a higher level of precision engineering approach that considers all the above mentioned challenges to ultraprecision machining of freeform surfaces. Moreover, is aimed to investigate an affordable method for direct data gathering and communication between CAD modelling and the CAM system in real industrial scale including all machining kinematic and dynamic factors for toolpath generation.

3.2   Slow Tool Servo and Dynamics Effects

Several key characteristic factors should be considered for performing successful STS machining, with most of those being applied to obtain friction free linear and rotary axes. A control system with high-speed data processing plays a key role in accurately running the motors

and all the direct-drive axes. The parameters that influence the precise positioning need to be considered in the system, including the encoder resolution, thermal expansion, high-order trajectory generation, precise data acquisition system and structural stiffness in the control loop. The analysis of the positioning loop is critical in ultraprecision machining using the STS technique as it has a direct effect on the velocity and acceleration based on the freeform surface topology. Regarding which, employing high close position loop bandwidth becomes an essential requirement in STS. Nevertheless, the evaluation of the acceleration and velocity of the system are conditional on the freeform surface curvature feature to maintain adequate bandwidth in an STS system. Thus, analysing the freeform surface geometry for both the tool and workpiece is necessary to specify the electrical and all the associated structural dynamics on the system. The tool trajectory in the conventional ultraprecision toolpath generation methodology is not capable of calculating the dynamics affected by the freeform surface in the system, such as tool velocity and acceleration, tool friction and surface contact force. In the next section, a multi-body dynamic methodology is employed to investigate the dynamic effects in the freeform surface tool trajectory using STS technique in ultraprecision machining. A new methodology for toolpath generation using multi-body dynamics is also presented.

3.2.1   Tool Geometry

For successful ultraprecision machining using STS methodology, the Tool geometries are playing a significant role [71]. The tool feature selection is associated directly to the freeform surfaces topology such as curvature and sag element. As shown in Figure 3.1, typical diamond cutting tool geometrical parameters include the Tool nose radius, Rake angle, Diamond height, Included angle and Clearance angle.
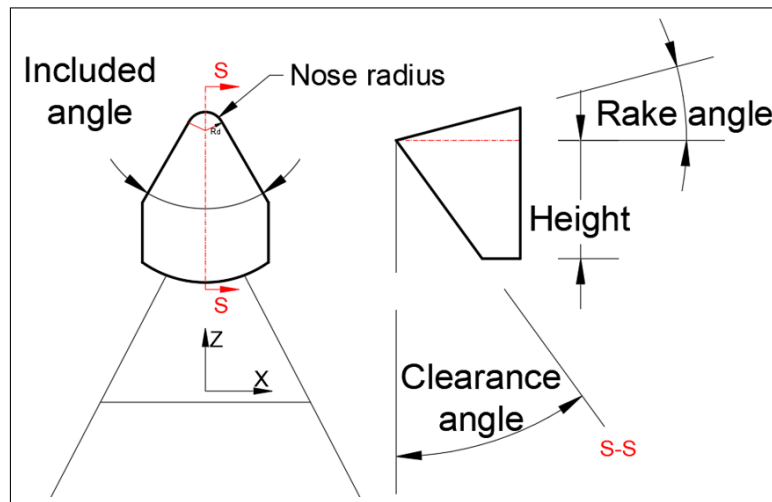
Fig. 3.1 Typical diamond cutting tool geometry

The freeform surface consists of various curvature features that need to be considered very carefully in STS machining. The compatibility between cutting tool nose radius and surfaces maximum and the minimum surface is a key requirement to avoid any interference during the machining process.

As illustrated in Figure 3.2(a), form error can occur when the minimum surface curvature is less than the tool nose curvature, which can be defined as 1/R for both the tool nose and surface. The front clearance angle and tool included angle are dependent and should be less than the maximum surface curvature angle at the tangent point. Figure 3.2(b) shows the correspondence between the tool clearance angle and maximum surface curvature angle in the Z-Y plane. Dynamically, in the larger sagittal curvature of the surface, the tool acceleration and velocity are higher with the STS machining technique. Thus, the dynamic and kinematic effect of the tool on the surface geometry should be considered.
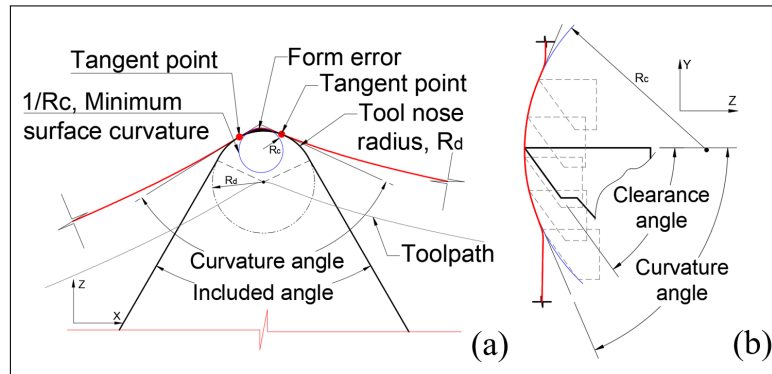
Fig. 3.2 Surface geometry: (a) Included angle and curvature angle effect and form error; (b) clearance angle and curvature effect

3.2.2 Tool Compensation

The geometry feature of the diamond cutting tool nose is circular and has a tilted clearance, being described as a cylindrical or conical. Applying appropriate tool type for UPM using STS mode depends on the surface topology. Nevertheless, due to the circularity of the tooltip, the cutting edge can suffer with the overcut phenomenon on the finished surface when the toolpath generated with large sag slop. Those overcut can impair the surface accuracy causing the final geometry shape will not meet the exact requirements of the proposed surface.
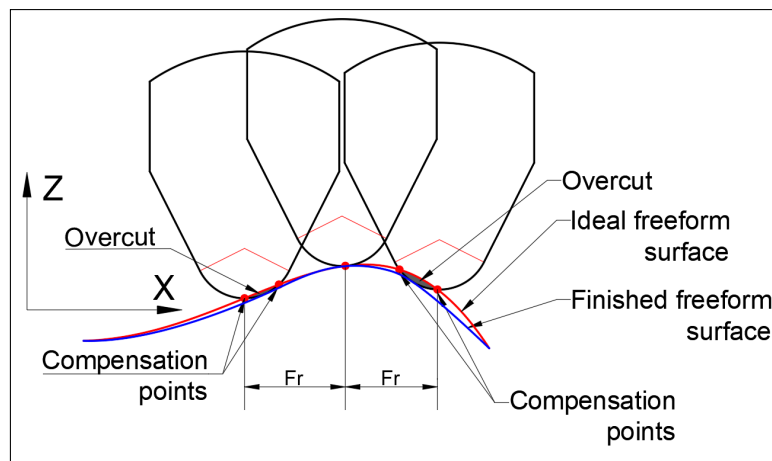
Fig. 3.3 Tool compensation phenomenon

Figure 3.3 illustrates the effect of the overcutting phenomenon on the toolpath. The conventional toolpat generation in the ultraprecision machining, applying a mathematical shifting algorithm to reposition the compensated points to the tangent point between the tooltip and the surface. However, there are issues with this methods, in that the mathematical modelling cannot ideally compensate the overcut in very complex freeform surfaces, and the machining process will fail due to the lack of sufficient data generated points on the surface. With reference to dynamical effects, the stiffness and cutting force is higher in an overcutting position due to material contact penetration, which can lead to a significant mismatch between the machined finished and ideal design surface geometry.

3.3 Multi-body Kinematics and Precision Toolpath Generation

3.3.1 Typical Diamond Turning Toolpath Generation

Figure 3.4 shows the typical STS method and the machine configurations, with a cutting tool being mounted on the axis of either the X-slide or Z-slide. A spindle chuck holds the workpiece on the C-axis. The Z-axis is aligned with the spindle axis, and the X-axis is in the perpendicular direction to the Z-axis. Generating the tool motion command as a function of the spindle position and X-slide location will create the multi-axis synchronisation with the aid of the amplifiers and the Programmable Multi Axis Controller (PMAC). The methodology of toolpath generation, as shown in Figure 3.4, commonly can be employed for STS, whereby the toolpath can be generated by controlling the Z-axis translation and the axial X-axis feed system, concerned with polar spindle rotation θ [36].
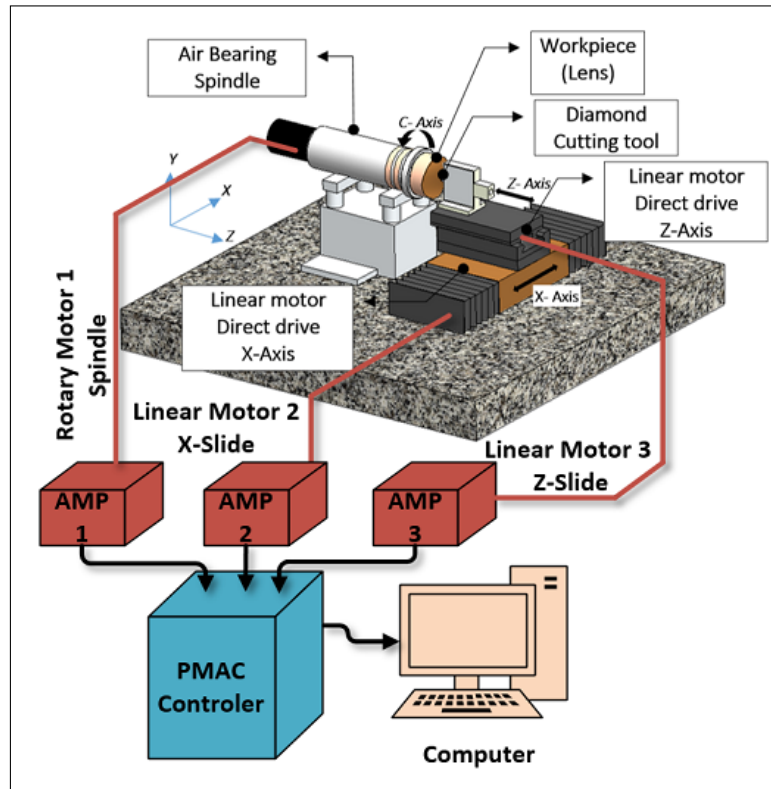
Fig. 3.4 Schematic of the multi-axis control configuration for an ultraprecision diamond turning machine (DTM)

3.3.2   Motion Equations

The system can be considered as a mass-spring-damping system, where the mass (m) is affected by the applied force (F) in the direction of (u). The mass is permitted to have a displacement only in the (u) direction and Newton's second law for this system is the result, whereby the force is equal to the mass times the acceleration at step time (t):

$$\mathbf{M\ddot{u}(t) + C\dot{u}(t) + Ku(t) = F(t)} \tag{3.1}$$

where, *mü* is the mass acceleration at time (t), which is the second derivative of (u), with a specific step time respectively, K is the stiffness constant, and C is the constant for damping induced by the loss of energy friction between the contacts. Regarding the complexity of the

damping phenomenon, it can be presumed that there is viscous damping where the damping force is proportional to the velocity. For toolpath generation, in the diamond turning machine, the system, as shown in Figure 3.5, is considered as multi-body with multi-degrees of freedom. In this case, the mass, damping and stiffness constant will become matrices instead of a single value. The equation of the motion can be expressed as [72]:

$$[\mathbf{M}]\ddot{\mathbf{u}}(\mathbf{t}) + [\mathbf{C}]\dot{\mathbf{u}}(\mathbf{t}) + [\mathbf{K}]\mathbf{u}(\mathbf{t}) = \mathbf{F}(\mathbf{t}) \tag{3.2}$$

where, $[M]$ is the mass matrix, $[K]$ is the stiffness matrix, $[C]$ is the damping matrix, $u(t)$ is the vector for displacement at time (t), $\ddot{u}(t)$ is the vector for acceleration at time (t), $\dot{u}(t)$ is the vector for velocity at time (t) and $F(t)$ is the force vector variation at each time step.
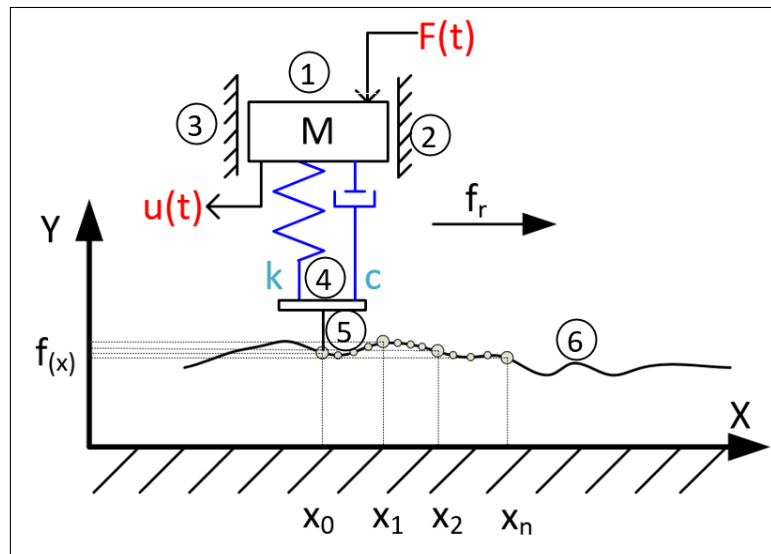
Fig. 3.5 Equations of motion with a multi-body and multi-degrees of freedom

The equation of motion is defined by a set of grouped differential and algebraic equations. Integration of those differential equations can obtain the numerical solution for the system to satisfy algebraic constraint equations at each step size of the motion. Numerically, the set of the differential equations is stiff when there is a full distribution between the low and high-frequency eigenvalues, during the time that the latter is over-damped. In addition, regarding the freeform

surfaces and inconstancy of their tangential vectors, running the stiff solver and integrator can obtain the real dynamical solution for generating the toolpath for the CAM system. For solving the stiff system, the stiff integration method is an efficient computational method, whilst other methods for differential equation solving perform very poorly and slowly. Numerically stiff differential equations ensure stiff integration and compute the solution efficiently [73].

3.3.3   Using ADAMS

Automatic dynamics analysis of mechanical system (ADAMS), is a method that has a robust algorithm to solve the problem for multi-body systems numerically. This methodology has been employed in this work to generate the toolpath for freeform surface directly from the CAD model. It precisely generates the position output coordination at each time step of the tool motion, while it is in 3D contact with the surface of the workpiece in the CAD model. The ADAMS solver widely uses the Newton method to solve the non-linear equation. Nevertheless, the freeform surfaces can be classified as a non-linear system. The Newton-Raphson algorithm can find the roots x^* of a non-linear equation [74].

$$\mathbf{f(x)} = \mathbf{0} \tag{3.3}$$

This phenomenon would be advantageous to employ this methodology for toolpath generation in the STS cutting process. Figure 3.6 shows the principal of the Newton-Raphson methodology, where the function of $f : \mathbb{R} \longrightarrow \mathbb{R}$ is differentiable. Based on this phenomenon, if the initial condition approximation of $x^{(0)}$ of the root is applied to the system, a new configuration of $x^{(1)}$, will be closer to the root of x^* can then be calculated as [74]:

$$\mathbf{x^{(1)}} = \mathbf{x^{(0)}} - \frac{\mathbf{f(x^{(0)})}}{\mathbf{f'(x^{(0)})}} \tag{3.4}$$
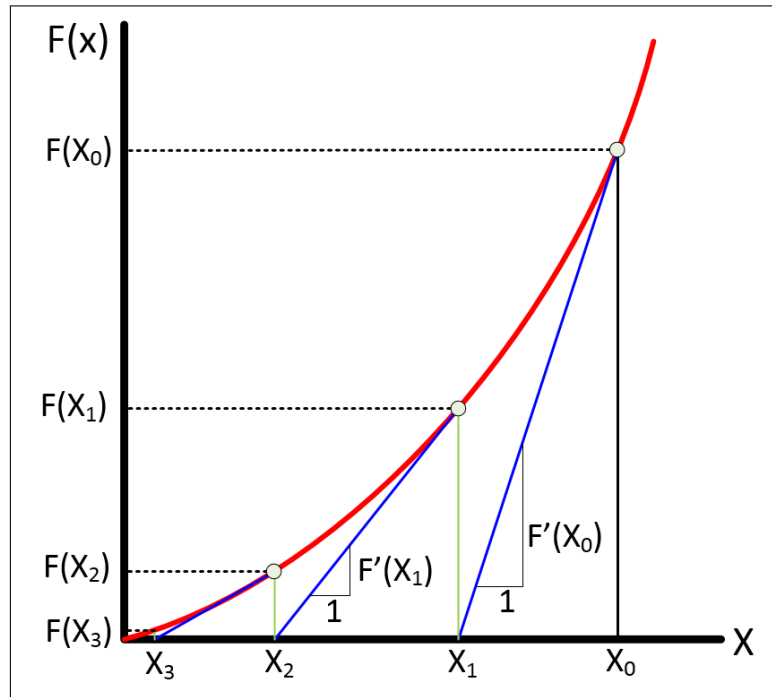
Fig. 3.6 Illustration of the Newton-Raphson method

$$\mathbf{f}(\mathbf{x}) \approx \mathbf{f}(\mathbf{x^{(0)}}) + \mathbf{f'}(\mathbf{x^{(0)}})(\mathbf{x} - \mathbf{x^{(0)}}) \tag{3.5}$$

where, $f'(x)$ is the derivative of the function of the dependent variable and the value of x will be updated by obtaining the linearisation of the function f at the point $x^{(0)}$. Moreover, the new tangent line of the derivative $f(x^{(1)})$ will be computed and a new configuration of $x^{(2)}$ will be obtained. The Newton-Raphson iteration sequence can be defined as:

$$
\begin{aligned}
\mathbf{x^{(1)}} &= \mathbf{x^{(0)}} - \frac{\mathbf{f}(\mathbf{x^{(0)}})}{\mathbf{f'}(\mathbf{x^{(0)}})} \\
\mathbf{x^{(2)}} &= \mathbf{x^{(1)}} - \frac{\mathbf{f}(\mathbf{x^{(1)}})}{\mathbf{f'}(\mathbf{x^{(1)}})} \\
&\quad \text{.......} \\
&= \mathbf{x^{(n)}} - \frac{\mathbf{f}(\mathbf{x^{(n)}})}{\mathbf{f'}(\mathbf{x^{(n)}})}
\end{aligned}
\tag{3.6}
$$

3.3.4   Generalised Coordination Positions

In a dimensional multi-body dynamic system, the position and orientation of the body can be defined by absolute coordinates, which indicate the local reference frame of the origin of the fixed-body and the three local frames of the Euler angles orientation, with the inertial global reference frame, respectively. An additional equation for a constrained multi-body is required to impose the condition of the motion for the system. The generalised coordinate vector for the multi-body can be written as:

$$\mathbf{q_{n \times 1}} = \quad [\mathbf{q_1 q_2 .... q_n}]^\mathbf{T} = \quad [\mathbf{q_1^T q_2^T t ... q_N^T}]^\mathbf{T} \tag{3.7}$$

where, $q_i = [x_i \ y_i \ z_i \ \alpha_i \ \beta_i \ \gamma_i]^T$, and n are the generalised coordinates numbers and N is the number of the total bodies in the system. The x_i , y_i , $and \ z_i$ describe the coordinates of the $i-th$ body translation from the origin of the global reference point to the origin of the $i-th$ body of the local reference frame. The $\alpha_i \ \beta_i \ \gamma_i$ are the Euler angles of the system, as mentioned before. In the case of a multi-body dynamic system the motion equation with respect to Equation 3.2, can be written as [75]:

$$M\ddot{q} + \Phi_q^T \lambda = Q \tag{3.8}$$

where, Q are generalised vectors of the forces, M is the inertia matrix, and $\Phi_q^T \lambda$ is the generalised vector of the reactions, Φ_q is the constraint equations Jacobian matrix, and the Lagrange multiplier vector is the λ. Moreover, the constraint equations need to be fulfilled by generalised coordinate at the position level in each time step:

$$\Phi_{m \times 1} = \Phi(q,t) = 0 \tag{3.9}$$

where, t is the time and m are the constraint numbers. The constraint equations can be expressed by differentiation of Equation 3.9, with respect to the time at the velocity level.

$$\dot{\Phi} = \Phi_q \dot{q} + \Phi_t = 0 \tag{3.10}$$

where the Jacobian matrix can be written as the following arrangement [75].

$$\Phi_{q(m \times n)} = \frac{\partial \Phi}{\partial q} = \begin{bmatrix} \dfrac{\partial \Phi_1}{\partial q_1} \dfrac{\partial \Phi_1}{\partial q_2} & \cdots \dfrac{\partial \Phi_1}{\partial q_n} \\ \dfrac{\partial \phi_2}{\partial q_1} \dfrac{\partial \Phi_2}{\partial q_2} & \cdots \dfrac{\partial \Phi_2}{\partial q_n} \\ \vdots & \vdots \\ \dfrac{\partial \Phi_m}{\partial q_1} \dfrac{\partial \Phi_m}{\partial q_2} & \cdots \dfrac{\partial \Phi_m}{\partial q_n} \end{bmatrix}_{m \times n} \tag{3.11}$$

The Jacobian matrix can be written for deducing and representing the acceleration, forces, reaction forces, and the positions. For the toolpath generation, the unknown position points will be re-evaluated in the Jacobian forces concerning the time and initial condition and will define the curve by integrating those point at each iteration.

3.3.5 Kinematics Analysis and Integration of Position Level

With known initial condition, i.e. position of the system at time t_0, the unknown second-time step at $t_1 > t_0$ is an interesting point. Since the system nature is the non-linear constraint as expressed in Equation 3.9, the Newton-Raphson iterative method is used in ADAMS to find the q_1 at time t_1. Hence, the Taylor-expansion-based linearisation for the non-linear constraint equation can be obtained as:

$$\Phi(q_1, t_1) = \Phi(q_0, t_1) + \Phi_q(q_0, t_1)(q_1 - q_0) \tag{3.12}$$

Using this method, can lead to finding the next step with respect to the time for all unknown-constraints in the system. The integration process of the equations containing the unknown acceleration and Lagrange Multiplier can be resolved at each integration time step. The most common solver in ADAMS is a direct index 3 Differential Algebraic Equation (DAE), in fact, the differential equations of the position kinematic constraint, as shown in Equation 3.9. Two common integrator in ADAMS known as GSTIFF-I3 and WSTIFF have been employed in this research to generate the toolpath. The next section will explain the numerical analysis using the GSTISS-I3/Solver for toolpath generation of freeform optical surfaces.

3.3.6   Multi-Body Dynamic Diamond Turning TPG

As explained in the previous section, ADAMS solver uses the differential algebraic equation to solve the unknown parameters, which is the Z-axis displacement in this case, and defines the toolpath by using a predictor and corrector algorithm, such as the GSTIFF and WSTIFF integrator, based on the initial condition, dynamic constraints and degrees of freedom of the system. The system can be simplified by utilising appropriate constraint only in the interested components. Figure 3.7 shows simplified STS machining schematic bodies and constraints only between the workpiece and the diamond tool for generating the toolpath. Rotary motor present the C-axis and Linear motor are in steady X-axis position. The Z-axis is one of the unknown factors that will be calculated by the ADAMS solver based on the initial force applied to the tool, contact point elastic stiffness, static and dynamic friction coefficient and the maximum damping between the diamond and freeform surface.
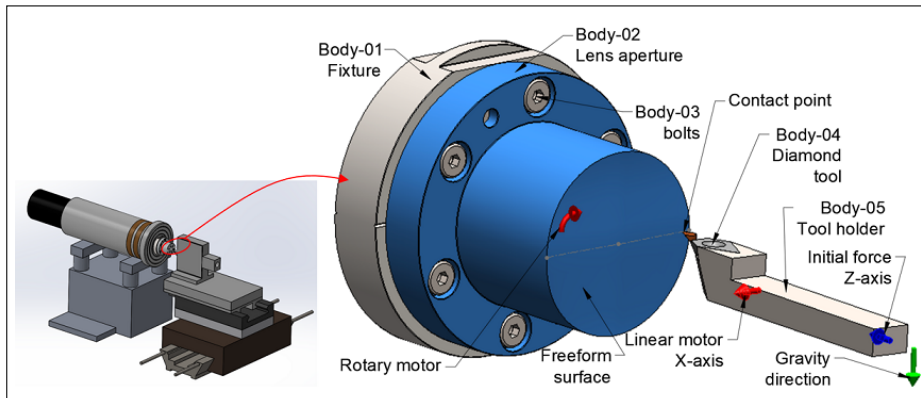
Fig. 3.7 STS machining diagram and it's schematic multi-body constraint

As illustrated in Figure 3.8(a), several constraints such as stiffness, damping, masses, will be marked automatically by the ADAMS solver based on the geometry features. The known-parameters, such as the initial forces, contacts and machinery motors are user-defined ones. The homing point is the critical point that needs to be specified as ADAMS uses those data for defining the initial condition. Figure 3.8(b) shows the exact positioning principle that the ADAMS solver uses to generate a path based on the surface geometry and contact. For instance, at position X_0 and Z_0, at t_0, the homing coordination will be marked by the user as an initial condition. At t_1, according to the equation of motion Equation 3.2, the mass, damping, and stiffness matrices, M, C, and K, respectively, will be defined by the solver and the new coordination point will be generalised according to Equations 3.4. At point n, with respect to t_n time, the same principle will be repeated and at each individual point, whilst the unknown parameters, such as reaction force at the contact point as well as the velocity and acceleration vectors will be calculated by the solver. According to Equation 3.8 to 3.12 the integrator will predict the unknown parameters and the correction of the exact points will be evaluated by the integrator as required. As aforementioned, the system is non-linear dynamic analyses. ADAMS employs a much higher order, up to six order predictors with BDF (Backward Differential Formulating) methods (GSTIFF and WSTIFF) to generate the curves. The effect of step size regarding the surface resolution and path accuracy will be explained in the next section.
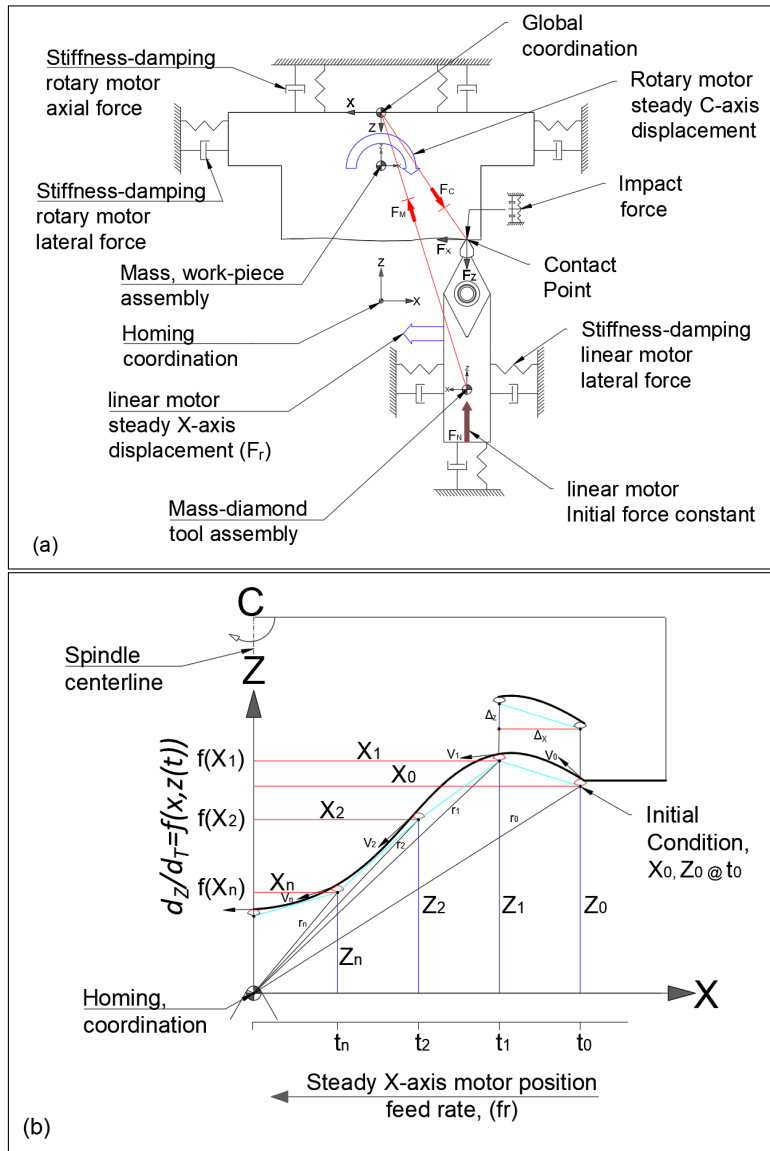
Fig. 3.8 STS multi-body dynamics and ADAMS solver principle of exact positioning: (a) constraints diagram; (b) exact positioning

3.3.7   Definition of the Mass, Damping and Stiffness Using ADAMS

ADAMS uses contact dynamic frictional low for evaluation of mass (M), damping (c) and stiffness (k). The stiffness and damping can be defined as a three-dimensional geometrical solid-to solid contact between tool and workpiece. Geometrical contact also lies in material properties, and thus the direction of the normal contact force can be determined. Dynamic simulation using ADAMS, at the first step, the contact statements identifies the contact is

occurring between the geometry pairs. No force will be identified when there is no contact between the geometries. If contact detected, the location of the individual contact points and the outward normals to the two geometries at the contact point will be calculated by the geometry modelling system. Moreover, Adams Solver (C++) calculates the contact points of the slip and normal velocities from this information. In the next step, Adams Solver (C++) then utilises the velocities to calculate and determine the contact force at each individual contact. ADAMS also uses the IMPACT force model by rearranging the first three auxiliary contact condition using the following expression:

$$F_n = k * (g^e) \tag{3.13}$$

where:

k is the stiffness, scalar penalty parameter. As k approaches infinity, the penalization becomes exact; thus, otherwise permits a small violation of the impenetrability constraint. Considerably, ill-conditioning of the governing equations, and sequentially an integrator failure will result if the stiffness becomes extremely large. Hence, selecting an appropriate value for k is a key point while maintaining the stability for the solutions. The compliance of a body can be determined approximately by associating k to the geometric parameters and bodies material properties. However, to do so, the recall of the earlier remark concerning ill-conditioning should be considered by the user.

In an effort to consolidate general material constitutive relationships for the contacting bodies, and facilitate time integration, Adams Solver (C++) augments the previous expression, Equation 3.13, with nonlinear displacement-dependent and viscous damping terms. The general structure of the IMPACT force function can be express as:

$$F_n = k * (g^e) + Step(g, 0, 0, d_{max}, c_{max}) * \frac{dg}{dt} \tag{3.14}$$

where:

g express the penetration of one geometry into another.

$\dfrac{dg}{dt}$ is the penetration velocity at the contact point

e is a positive real value denoting the force exponent.

d_{max} is a positive real value specifying the boundary penetration to apply the maximum damping coefficient c_{max}.

3.4 Numerical Analysis and Simulation

3.4.1 TPG using a Multi-Body Dynamics Position Point and Integration

As pointed out in previous section 3.3, the benefit of employing the ADAMS Solver for toolpath generation is that it can overcome the potential gap in ultraprecision freeform cutting using a diamond turning machine. As mentioned above, most toolpath generation methodologies in ultraprecision machining use a projection map-point spiral 2D sketch converted into 3D freeform surfaces, which can cause severe problems during the cutting process. ADAMS toolpath generation is not just limited to delivering very high accuracy on complex freeform surfaces, for it can also simulate the dynamical and static parameters within the process, such as contact forces, dynamic friction, static friction, mass distribution for balancing, momentum, angular and linear acceleration, velocity and displacement. Moreover, it could be very beneficial for in-line measurement, where the output data can be directly computed during the cutting process. To fulfil the principal of this new method, Solidworks Motion has been employed in this research, which has an interface with the ADAMS/Solver.

As proposed, the principal idea is to discover a solution by linking the CAD model straight to a CAM system with all dynamic and kinematic parameters included, for an ultraprecision machining process of complex freeform surfaces. For successful fulfilment of this idea, a freeform surface has been modelled, and an ADAMS simulation has been set up with the specification data as listed in Table 3.1. At this early stage of the exploration, the stiffness and

Table 3.1 Motion study simulation input data

Analysis Data	Value	Units
Workpiece speed (S_c)	20	RPM
feed rate (f_r)	0.01	mm/s
initial force (F_N)	1	N
Dynamic Friction Contact (μ_k)	0.25	-
Static Friction (μ_s)	0.3	-
Elastic Impact Stiffness (K)	100000	N/mm
Max Damping (C)	50	$N/(mm/s)$
Penetration	0.0	mm
Integrator	Value	Units
Frames per second ($timestep$)	100	-
3D Contact Resolution	High	-
Accuracy	0.0000001	-
Integrator Type	GSTIFF, WSTIFF	-
Max Iteration	25	-
Initial Integrator Step Size	0.0001	-
Min Integrator Step Size (t_n)	0.000001	-
Max Integrator Step Size	0.01	-
Jacobian Re-evaluation	Every Iteration	-

damping of the material were determined by ADAM's default setting. ADAMS uses a method for estimating contact stiffness and damping parameters for parts with a small mass. the default contact stiffness and damping coefficient in Adams can be defined as:

- Stiffness (k)=1.0E+05 N/mm

- Damping (C)= 10.0 N-s/mm

Adams determines these values of the coefficients for parts with mass order of 1.0Kg and made from steel material. These setting called *"default part"*. For this numerical simulation, damping estimated 50 N-s/mm as tool has expected to have more rigidity in compare to the workpiece. The penetration was chosen as zero; therefore, parts assumed not having any interface penetration but still can be in contact at tangents points between the tooltip and freeform surface. Defining zero penetration will assist in capturing accurate positioning of the tool while it is moving and contacting the surface. The effort of this research in future research

work will be expected to investigate the effects of various material properties and coefficients parameters. The static and dynamic friction coefficient are also determined as a dry steel to steel coefficient.
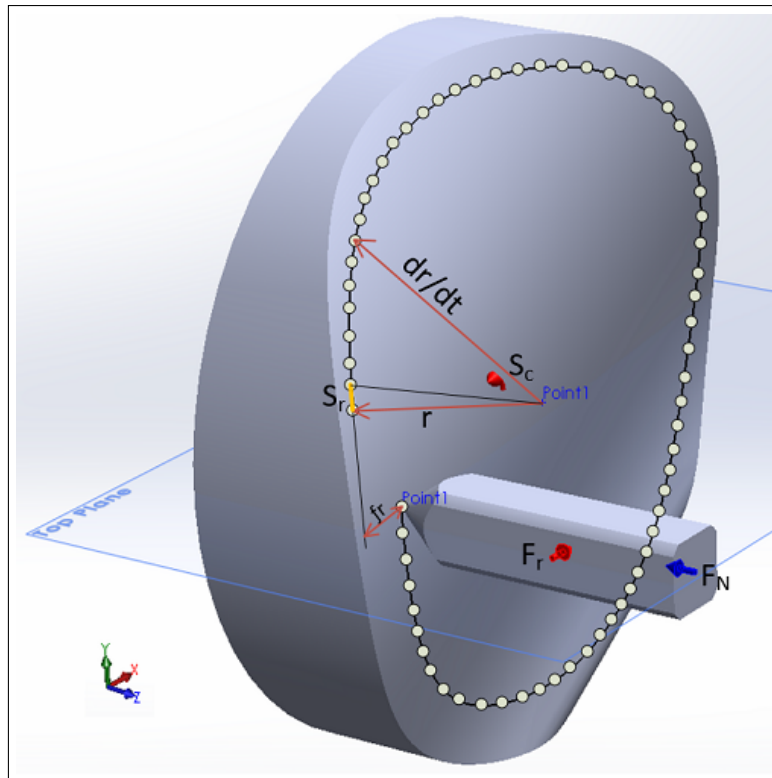
Fig. 3.9 Generalised toolpath points from Jacobian re-evaluation

As per the specification, in the ADAMS solver, the known parameters should be set up as an initial condition, and several unknown factors will be defined automatically by the solver, which in this case, the displacement of the cutting tool with respect to freeform surface topology in the Z direction is interested. Accordingly, the angular velocity of the workpiece, acceleration, linear reaction forces, contact forces, momentum and linear displacement in all degrees of freedom at each step time can be determined as an output.

The assumption can be made in such a way that the tool can be recognised as an indicator of what can be in contact and moved very smoothly across a surface that has intense and high-resolution properties.

Based on this phenomenon, as illustrated in Figure 3.9, the probe, which has a tangential constraint with a freeform surface and normal force F_n, has been applied to the indicator on the Z-Axis. On the X-axis, a linear motor F_r will obtain the feed rate, whilst the angular velocity of S_c will define the spindle speed. As stated in section 3.3, the system is dynamically fully constrained, nevertheless, the contact friction between the tool and freeform surface should be defined. In this case, a dynamic friction of μ_k and static friction μ_s have been included in the system.

The impact stiffness, damping and penetration constraint are also needed as they will compute the displacement at the next time step based on the material contact between the tool and the workpiece. As illustrated in Figure 3.9, after running the solver, the initial condition of both angular velocity of the spindle and linear motor become time dependent and will be computed by ADAMS. At each time step, by employing the Newton-Raphson method, whilst the next position will be calculated. Displacement of the so-called indicator in the Z direction at the X-Z Plane will be defined based on the geometric shape, according to the angular velocity of the spindle on C-axis and linear motor feed rate on the X-Axis from the origin coordination mark. As the spindle rotates, the linear motor moves towards the centre of workpiece, and at each time step, the positioning coordination of that point will be recorded, whilst all stiffness, damping and mass matrix will also be indicated based on the motion equations. The arc distance of S_r is defined by the determination of the differentiation of the polar coordination of r, with respect to time, as $\frac{dr}{dt}$.

Typical TPG methods, with map to map point projection, experience major problems when they need to be compiled in the real cutting environment and machining process. Due to contact and the friction force between the tool and the freeform surface, most of the generated points will be correlated with error on the final finished surface and thus, this approach cannot generate high performance and accuracy resolution in the complex freeform surfaces. The aim is to reduce the level of those errors by including the friction and contact force parameters into the

system and output the computed points based on the dynamic equation of motion. Figure 3.10, shows the diagram of the force distribution for each individual displacement point that ADAMS can include at each step time on the freeform surface, unlike other typical methods that only cope with map to map point projection onto a surface.
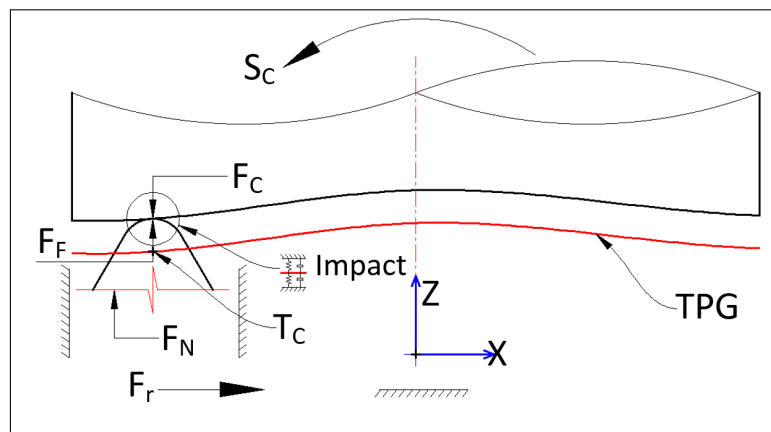
Fig. 3.10 Toolpath generation diagram based on the ADAMS solver strategy

Upon running the system, as aforementioned, the contact between the tool and surface are under impact stiffness and damping forces, which are illustrated as F_c and friction force of F_F. The impact rule and equation are computed at the initial condition based on the ADAMS equation and the position at tool centre T_C is recorded. After generalising the conditions, the Jacobian is re-evaluated and the integrator creates the toolpath at each time step. For much clear visualisation, Figure 3.11 shows a modified setup for the ADAMS toolpath generation as the workpiece speed increases to 50 RPM and the feed rate to 0.5 mm/s. It can be seen that the toolpath is very smoothly generated within the freeform surface geometry. Figures 3.11(b) and 3.11(c) show the displacement at the Z and X axis, respectively. The points are generated at those axes from the selected local coordination point or the homing point towards the centre of the workpiece. The range of the freeform curvature has been calculated between 4 and 10 mm from the coordination points at the Z-Axis. Moreover, the maximum time for simulation has been recorded 38 s, with 0.5 mm/s of linear speed in the X-axis.
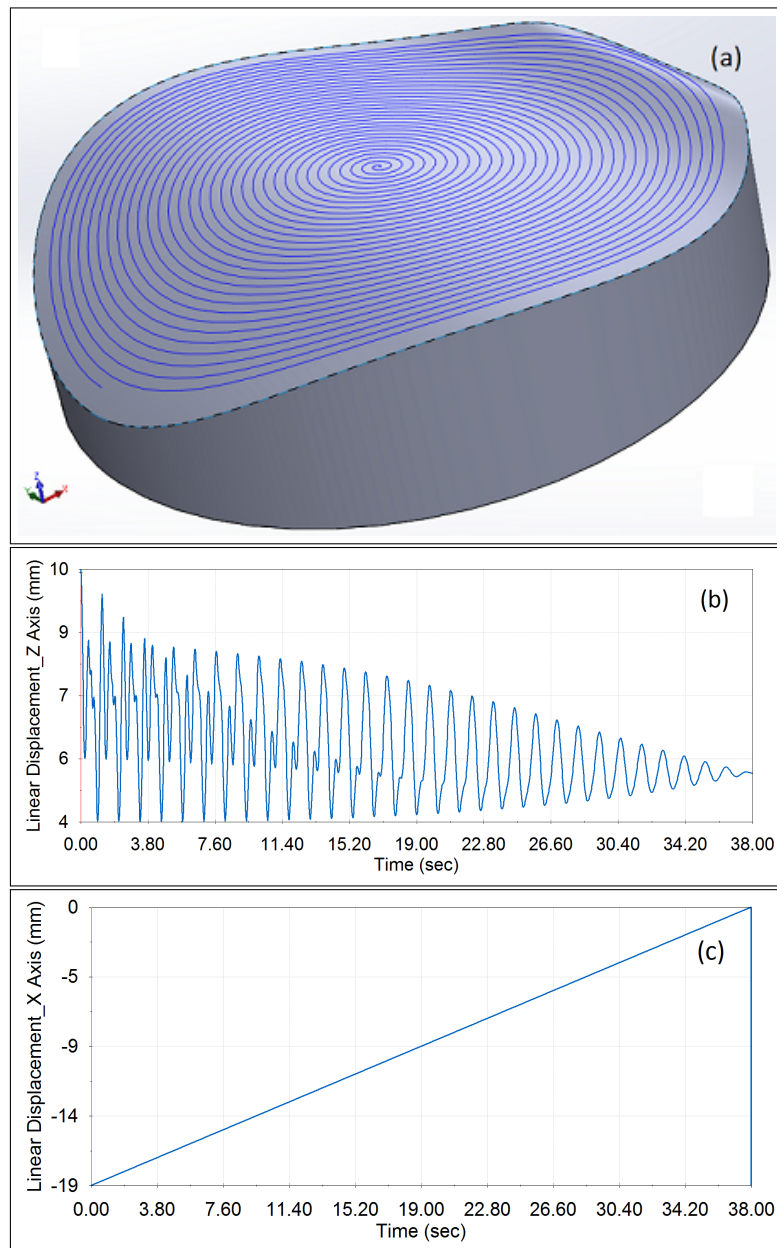
Fig. 3.11 Toolpath-final generalised curve: (a) final and finished curve with 50 *RPM* and 0.5 *mm/s*; (b) tool displacement in the Z-axis; (c) Tool displacement in the X-axis

3.4.2   TPG Principle in Ultraprecision Machining and Efficiency

One of the objective of the research was to overcome the existing issues in toolpath generation for ultraprecision machining. The lack of efficiency is due to the nature of freeform surface complexity and the requirements for high precision and accuracy. Thus, the machining setup

is time-effective. Figure. 3.12, illustrates the principle of ultraprecision machining using multi-body toolpath generation, whereby the CAD model can be directly imported into the CAM system. As can be seen from the diagram, the multi-body dynamics analysis is part of the ultraprecision machining process that can assure the output data of toolpath generation for the freeform surfaces will succeed the machining dynamics in a very efficient way.
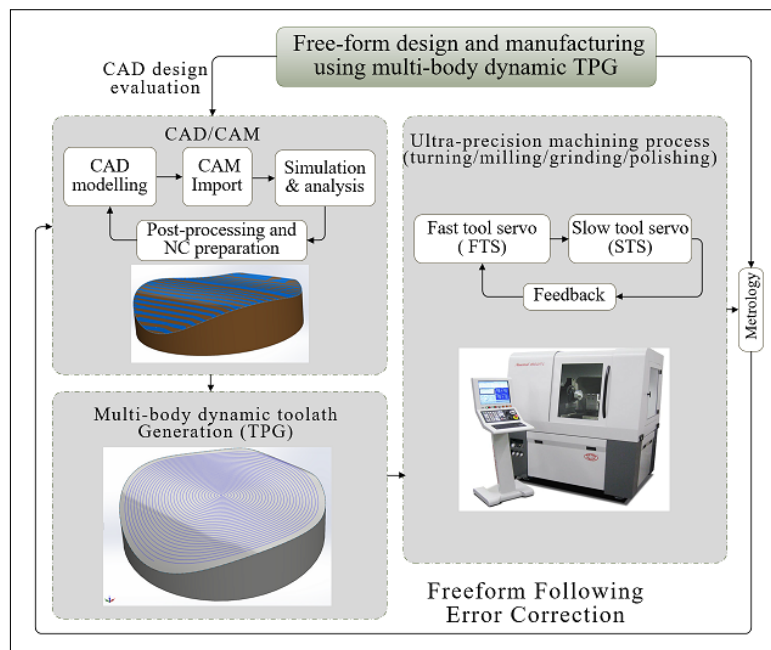
Fig. 3.12 Ultraprecision machining principle diagram using multi-body TPG

3.5 Results, Analysis and Discussion

As specified, the displacement relatively between the tool and workpiece surface in the Z direction can be defined by the ADAMS algorithms and the output data can be computed for a CAM system. In a diamond turning machine, the X and Z axis form the primary plane for tool displacement. Moreover, the points generalised in the X and Z directions with respect to the time step will define the NC-file and G-codes required for STS machining in the CAM system. Either rotational or linear motors with their relevant factors are simulated and the output data points generated can be communicated very precisely with the CAM system. In this

case, to prove the method works, a manual post-processing has been employed by extracting the output data from linear tool displacement in the Z and X directions component. The Y direction linear displacement is counted as zero as it is located at the centre of the workpiece. The post-processing can be atomised by applying an Application Programing Interface (API) in the ADAMS.

3.5.1 Surface and Contact Accuracy

The accuracy of the generated points in the toolpath play a major role in ensuring the feasibility of using this technique for ultraprecision machining.
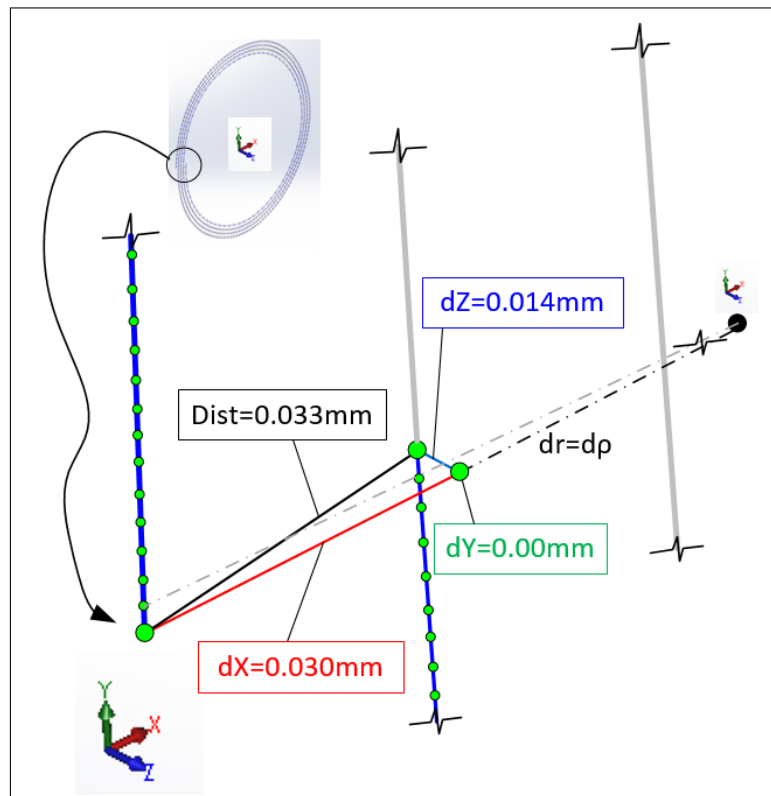
Fig. 3.13 Toolpath generation accuracy per cycle

As aforementioned, precise 3D contact factor between the tool and freeform surface has a significant impact for a successful toolpath generation. With the diamond turning machine using the STS technique, the workpiece has a low velocity, and this can be very beneficial for

providing a high resolution and accurate toolpath along the freeform surface, as the integrator has sufficient time to compute the generalised points from the Jacobean re-evaluation integrator. The more precise surface contact the more accurate will be the generalised of the step points.

According to Table 3.1, for an angular velocity of 20 RPM, and 0.01 mm/s of linear velocity , the tool travels 30 microns along X axis per one rotational cycle. To prove this movement and displacement, Figure 3.13 shows the generated points at the beginning and end of one rotational cycle. From the interpretation point of view of the generated point coordination in X, Y and Z directions, it can be clearly observed that d_x is around 30 microns, which can substantially prove the satisfaction of the linear displacement in the X direction with all constraints included for this direction in the ADAMS motion equations. Moreover, the point generated at the end of the first cycle in the Z direction, d_z, shows 10 microns, which is calculated by ADAMS solver based on the freeform surface geometric topology. The displacement in the Y axis, d_z, is zero as it hypothetically constrained to have no movement in this direction.

3.5.2 Integrator Step Size and its Impact

ADAMS solver work based on points integration at each time step and generate the curves. The impact of the size of the time step is significant for achieving a micro-nano resolution in the toolpath generation. Further simulation and investigation are required to prove the argument. Figure 3.14 shows two different simulations with different step sizes that have been employed to do so.
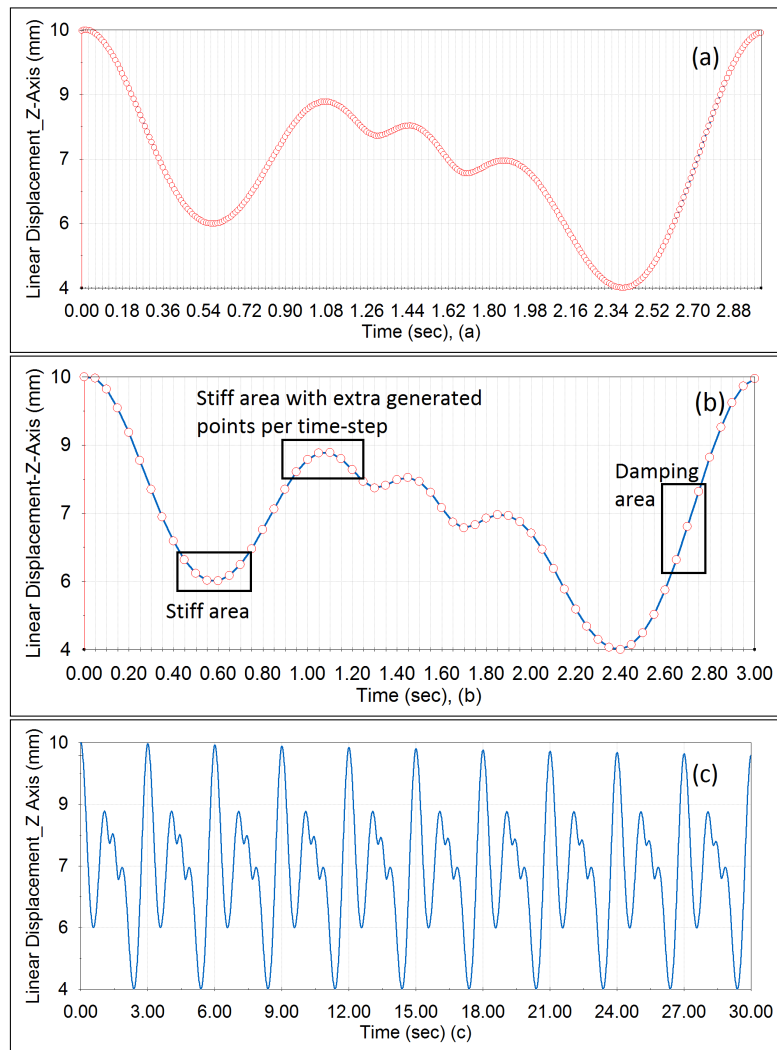
Fig. 3.14 TPG characteristic influence of time step size: (a) time step size of 100 units per second, (0.01 secs); (b) time step size of 20 units per second, (0.05 secs); (c) full cycle of Z-axis displacement after 30 secs with a step size of 100 units per second

As shown in Figure 3.14(a), the step size is set to 0.01s, while Figure 3.14(b) shows the setup for 0.05s. The time domain in simulation (a) is shorter than simulation (b). The diagram illustrated in Figure 3.14(b), shows that more points have been generated in the stiff area and less in the damping area of the freeform surfaces, with respect to the step time. From this point of view, the comparison can be made, thought that, in typically TPG methodology, the points will be generated with constant increment with respect to the step time.

The meaning can be defined that when the step size is short, the computing of the next point

based in Newton-Raphson methodology will be closer to the root. Hence, it can be concluded that variety of the points can be generated within the specified step time based on the freeform shape and geometry. For example, in simulation (a), 100 points have been generated per second, while simulation (b) has calculated 20 points per second. It can be proven that simulation (a) has much more accuracy and resolution in which considerably can provide precise positioning in the ultraprecision machining using STS technique. Finally, Figure 3.14(c) shows the full cycle simulation for running the solver for 30 seconds. As shown, at each cycle the amplitude of the displacement of the curve decreases as it moves towards the centre of the workpiece.

Whilst ultraprecision toolpath generation using the ADAMS solver can take a longer time to generalise the precise coordination points within the surface topology due Jacobian iteration and re-evaluation, the technique can be optimised with additional functions to overcome this disadvantage. The initial integrator step size is the major factor of controlling the speed of simulation. For instant, by increasing this value the simulation can be run much more quickly. Also, increasing the minimum integrator step size to its lowest value can decrease the simulation time as it enters to the lower bound of the integration much instantly. The upper bound of maximum integrator step size is also influential, as it can deal with the contacts that are required to detect the impact and stiff points during the simulation. Setting this value to the highest level can optimise the various factors mentioned.

3.5.3   Influence of Friction and Displacement

Dynamic and static friction have been employed in this TPG methodology which makes it unique in comparison with other classes of typical toolpath generation. The friction constant along with other parameters, such as vibration and thermal drift, have a significant impact on the operation of real-time ultraprecision machining. In this study, the friction has been modelled as typical Coulomb friction, which represents the dynamic resistive force between the tool and freeform surface. According to Table 3.1, in this study, the dynamic and static

friction coefficients have been assigned as the contact friction based on dry steel material. However, from advantage point of view, the most appropriate material friction details can be specified for the contact set in ADAMS to employ the Coulomb friction method to solve the total friction force at each time step points. Also, this method could be extremely beneficial in future for studying the cutting force during the machining process and in-line measurement for ultraprecision manufacturing of freeform optical surfaces. Figure 3.15 shows the impact of the friction force with respect to displacement at the Z-Axis. Apparently, the friction force increases when the tool is in contact with the surface, where the gradient or the slope of the surface is very high.
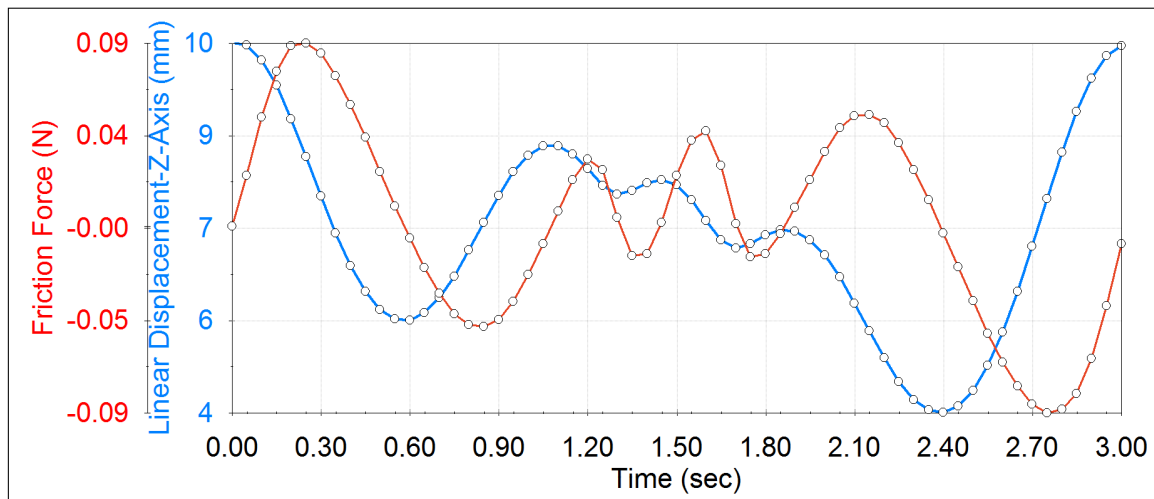
Fig. 3.15 TPG characteristic influence of Z-axis displacement vs friction force

As aforementioned, the freeform non-rotational surface is represented as a non-linear system and can be recognised as being a stiff one. The blue curves represent the displacement in the Z-direction, and the red curve is the magnitude friction force. It can be seen that the highest stiff value is triggered at the location in the surface where the curvature of the surface suddenly changes from concave to convex, and the friction forces are vary at this positions. Further, the validation of the system proves that the form error displacement of the tool generated in the Z-direction is relative to a friction force and hence, those points after post-processing in the CAM system will have less error in the final toolpath required for the machining. The approach

can be very helpful in finding the errors in direct drive motors during the machining operation and prepared for appropriate tuning.

3.6   Experimental Trials and CAM Validation

In this research work, a set of experimental trials has been prepared for the ultraprecision machining of the freeform surfaces applying proposed multi-body dynamics TPG methodology. Figure 3.16 shows the ultraprecision diamond turning for this method. Test part and geometry design of the workpiece and it's associated details can be found in Appendix A.3. Tool geometry and it's detail also indexed in Appendix A.1. Machining G-code and NC-file shown in Appendix A.2.

Fig. 3.16 Photograph of the diamond turning machine for the experimental trial and validation of CAM post-processing

For the experimental preparation, the generated displacement points in the XZ plane have been extracted from ADAMS numerical simulation, and the NC file has been created for CAM post-processing. The experiments were carried out for final validation of the ADAMS toolpath generation. Also, a comparison was made between traditional ultraprecision machining toolpath generation and ADAMS, with NanoCAM software being employed for validation. The experiments were run using Moor Nanotech 250UPL. Table 3.1 shows the setup data for toolpath generation based on the ADAMS methodology.

For accurate result, the spindle speed and frame per second increased to 60 RPM and 3600 frame respectively. The angular distance in C-axis increments was calculated as 0.1 degree which can be defined by dividing a circular cycle of 360 degree over the frame per second, 360/3600=0.1degree. Figure 3.16 illustrates the machining process for the experiments, with the STS machining technology being used. Two different workpieces with the same geometry shape have been used, one to test the effect of the surface resolution with the NanoCAM methodology and the second, to test the novel multi-dynamic toolpath generation, which in this study known as ADAMS technique. An aluminium alloy material was selected for machining. The same diamond tool geometry with a 0.6 mm tool nose radius was used for both experiments. The machining parameters for the NanoCAM NC code were set as 20 RPM with constant angular point distance of 0.1degree, 0.01 mm stepover feed in the X direction.

3.6.1   Geometry Form Error Comparison

The comparative results from the experiments show that the ADAMS toolpath computed precise points almost similar to or above those generated with NanoCAM software. Figure 3.17(a) compares the form error between the two methods, as described in the previous section and it can be observed that a maximum division (error) of 5 nm was experienced from the positioning points in one cycle per step time.
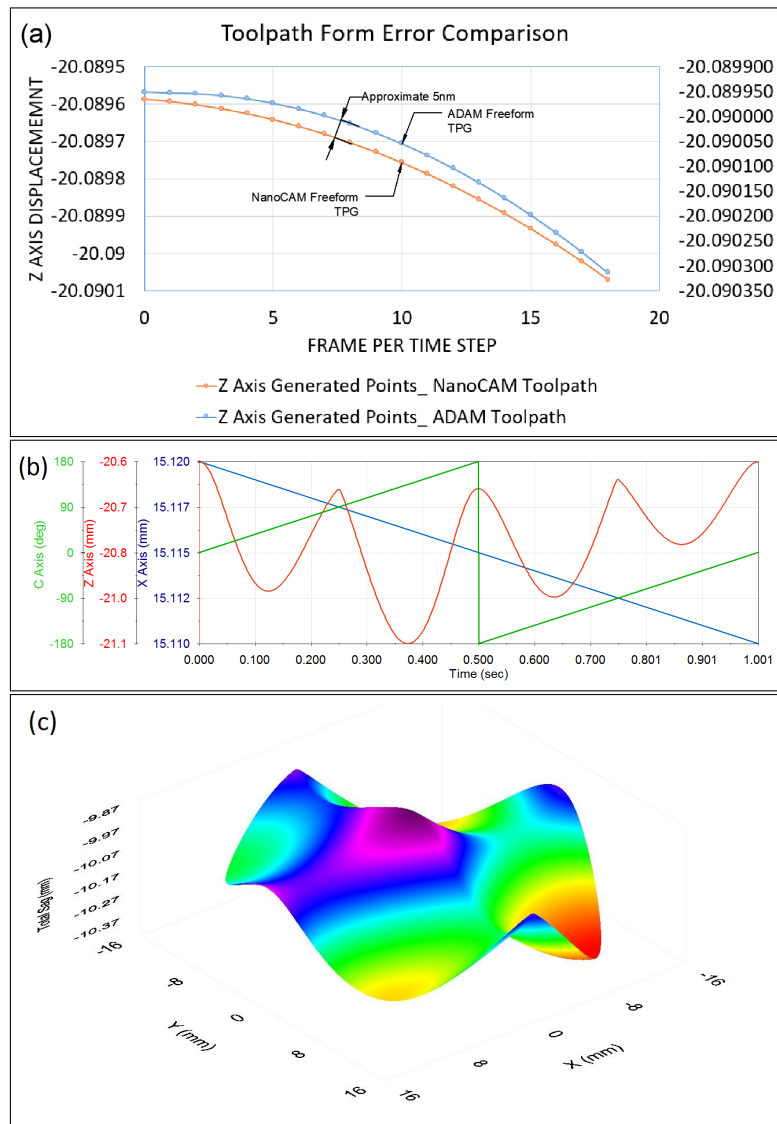
Fig. 3.17 Toolpath final generalised curve: (a) comparative geometrical form error diagram ADAMS vs NanoCAM; (b) generated displacement points in the C-axis, Z-axis and X-axis; (c) ADAMS toolpath sag evaluations

Figure 3.17(b) illustrates the final computed points based on the ADAMS methodology for the X, Z and C axes. The integration points generated by Jacobian evaluation provide validation of the precise and smoothness of the toolpath curve. Figure 3.17(c) shows a range of 0-0.5 mm of sag height in the freeform surface. It is apparent that the highest accuracy is accomplished with such a large amount of surface sag with the ADAMS toolpath experimental process.

3.6.2 Surface Roughness Measurement

A Zygo 3D surface profiler was employed for the final measurement validation. The surfaces roughness in both the machined components of ADAMS and NanoCAM have been measured, and a comparison accordingly made. Figure 3.18 shows the measured surface roughness of the freeform surfaces. Comparing the two results, it can be seen that the surface machined by the ADAMS toolpath has lower surface roughness due to the very precise contact points evaluated by the Jacobian predictor and the GSTIFF/WSTIFF integrator. Based on the results shown in Table 3.2, it is evident that the maximum values of the PV, Rms and Ra in the ADAMS tool path generation are less than when undertaken by the NanoCAM process.
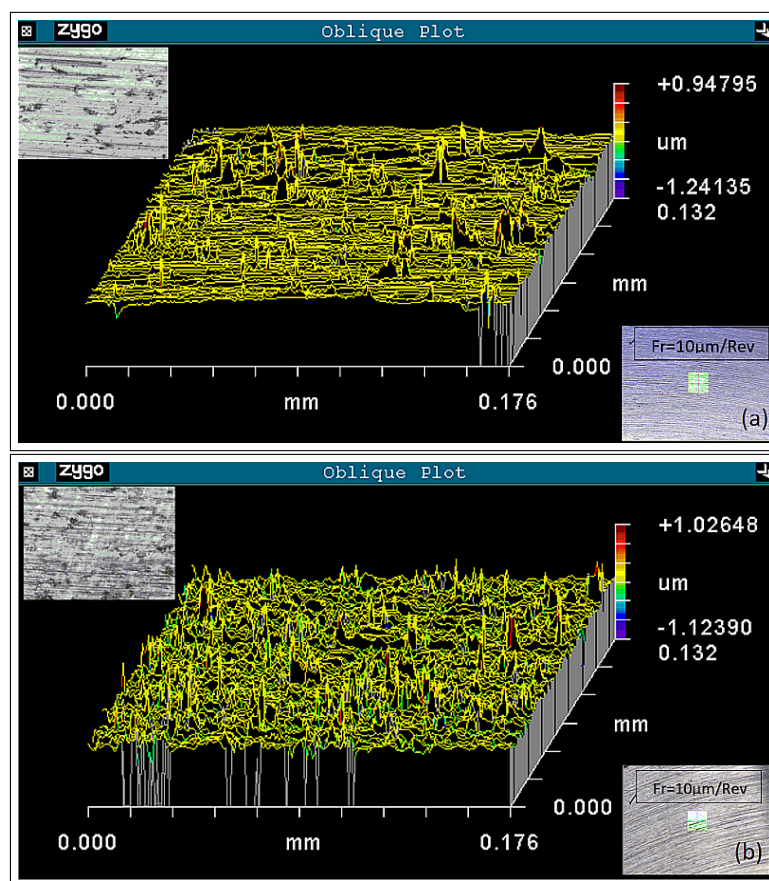
Fig. 3.18 Measurement results of the surface finishing profile: (a) using ADAMS TPG; (b) using NanoCAM TPG

Table 3.2 Surface finish profile comparative data

Analysis Data	ADAMS	NanoCAM
PV (μm)	0.303	0.774
Rms (μm)	0.030	0.068
Ra (nm)	19.926	45.923

3.7   Concluding Remarks

In this chapter, an innovative toolpath generation approach for ultraprecision machining has been proposed based on the Automatic Dynamics Analysis of precision engineering systems. The approach can be effectively implemented for ultraprecision machining of freeform optic surfaces using diamond turning. The approach also can be integrated with the conventional TPG methods for dynamic and kinematic investigation purpose in freeform surfaces. In this approach, the toolpath for very complex surfaces can be generated using the Newton-Raphson method to solve the kinematics and dynamics equations of the multi-axis motions. The proposed method additionally can overcome the issues currently existing in ultraprecision machining using the conventional CAM system, such as form error and compensation malfunctioning. The effect of friction and contact force have been studied, and very accurate toolpath curves can thus be generated. The impact of the points integration methodology and Jacobian re-evaluation have been investigated, with it being concluded that the time step size plays a critical role in generating the toolpath with high accuracy and resolution. Different types and factors for the time step have also investigated, showing that decreasing the step size will increase the generated points and thus, increase the accuracy of the integrator. Finally, GSTIFF/WSTIFF solver for solving the nonlinear equations of motion has been studied.

Chapter 4

Innovative Design and Development of the Smart Chuck

4.1   Introduction

Compliant flexure mechanism, has been widely used in precision engineering. A flexible mechanism, such as flexure joint, coupling, pivot, connector living and the compliant joint, can present a significant substitution to conventional mechanical joints and relive some of their problematic conditions. Flexure mechanisms practically employ instinct compliance of the material elasticity instead of restraining. The existence of conditions such as wear, backlash and friction can be eliminated with flexure joints. Most beneficially, due to successive monolithic construction, compliant mechanism can offer a sub-micron accuracy in high precision Micro-Nano applications. Compliant mechanism can also significantly integrate the components in assembly and reduce the noise and lubrication demands with high precision motion and repeatability. Extensive researches and developments in compliant flexure mechanism were carried out during the last two decades or so. Two variety of notch-type joint and leaf spring can be considered as a result of these researches. In high-precision engineering, the notch type joint assembly are widely utilised where the small displacement is the key parameter. The

generic flexural translational joint can be prepared by leaf springs where widely used in in the application such as medical applications, MEMS devices, PRBM compliant mechanism, high precision instrumentation, small displacement and positioning stages. In Micro-Nano engineering, the compliant mechanism has a wide range of association to precision engineering whereby they communicate and are synchronised simultaneously. For instance in ultraprecision machining, the variety range of compliant flexure types have a direct effects in the final outcome on the kinematic and dynamic performance of the application.

4.1.1 Clamping and Precision Characteristics in UPM

Clamping mechanism such as chuck widely utilised in the precision engineering with tooling machines such as micro-milling and diamond turning machine. In ultraprecision machining systems such as single point diamond turning machines (DTMs), the exact alignment of the workpiece with the rotary axis is the crucial. Doubtlessly, the misalignment between the centre of the workpiece and rotary axis affects the desirable finished surface resolution of the workpiece.

Concentrically unequal off-centre movement makes the misalignment (runout) which can occur the errors and results the cutting tool wears, therefore the alignment must be precise at the beginning and during the cutting process. Preparation of the workpiece for diamond turning using conventional mounting and work holding can be done by either a vacuum chuck or magnetic clamping system requires an extensive skill to decrease the eccentricity.

Also, the machining with the vacuum chuck in which is free from stress in the workpiece can cause misalignment during the cutting process. Besides, regarding mass production using diamond turning machine, the efficiency of the working progress is significantly low, and the consistent repeatability of the work is outstanding can cost energy and time respectively.

Regarding the radial runout issue in the ultraprecision machining, there are loads of researches, and new devices have been designed to overcome the problems. Some of the attempts

to address the issues were focused on designing certain of cost-effective devices that dependent on both workpiece and tool holder.

4.1.2 The Clamping Mechanism for UPM

Several inventions have been taken place in the purpose of aligning ability by using the centring and jaw mechanism. These developments are contained many components and very cost-effective in manufacturing. Some of these inventions are as followed:

- Workpiece positioning for especially turning machine using the self-centring method [76].

- Self-gradually locking chuck for drilling use [77].

- Circular optical component centering utilizing a Non-self-centering chuck accommodated to clamp the element at two grip strengths [78].

- A device to centre the chuck on securing part in the rotating spindle [78].

Dimensions and the size of the previously mentioned patents are non-adjustable.

Other attempts have been applied to ultraprecision machining in the optic field using collet type clamping. These devices invented by: Dent [79], De Bastiani [77], Bergrandy and Bergrandy [80] and Kiontke [81].

These inventions related to workpiece adjustment, centring and holding the lens using collet with slots with one end flexure.

Recently accomplished inventions in the market using a much precise mechanism such as Zero-point clamping. In such devices, the misalignment (runout) have been significantly decreased in most cases. For instance, as described by Sandmier [82], a clamping device which consists of a chuck that has a mechanism of sliding elements to support the workpiece in a very precise manner. Muttchen [83] invented a device with a set of rolling elements (balls) that

can clamp the device in the cage and can maintain equally force to align the external device that attached to the workpiece. The similar principle has been applied to a device as described by Obrist [84] which has additional coupling elements that attached to clamped items and locally fixed with a tension element (flexure). The method can precisely position the workpiece with less amount of misalignments. The invention described by Winkelmann [85], applied a methodology to the ultraprecision machining and produced aperture for tool holding and work holding to precisely locate and position the workpiece with exact alignment to the spindle rotary axis.

Despite the facts that all these devices can provide very accurate positioning, but in ultra-precision machining, there is such high time consuming for tooling and workpiece setting up. Also, the manufacturing of these devices are costly, and the tolerances and frictions between the sub-assemblies can significantly affect the accuracy and clamping performance of the device. Therefore, the requirements persist in designing and developing the mechanism more robustly where the consideration should be focused on avoiding the sub-assemblies with more frictionless elements to eliminate the misalignments between the workpiece and spindle rotation axis in ultraprecision machining. Nest section will brings some solution to overcome those issues by inventing a new workpiece holder in ultraprecision machining to obtain more precise positioning.

4.2   Smart Chuck Conceptual Design

The present invention in this research work can be associated with smart clamping technique for freeform surfaced workpiece, integrated with self-centring features for purpose of precise alignments and positioning in ultraprecision machining with diamond turning machine. The invention is also purposed to eliminate the runout and adjust the radial misalignment between the spindle rotary axis, the smart chuck and the workpiece.

4.2.1 Invention and Concept Design

It is a necessity in the invention to design and develop a work holder aperture being capable to centre the workpiece within the rotary spindle and making the alignment constant during the machining. Since existing chucks in current ultraprecision included with several sub-assembly parts with chain tolerances, achieving the sub micron accuracy in positioning becomes very difficult or impossible. Hence, designing a system that can eliminate those uncontrolled tolerances is vital. The invention is purposed to integrate all those parts with their associated tolerances in the assembly into one robust component, thus can prevent the unnecessary frictions and tolerances in the assembly. Also, the invention is subject to ease the user-defined machining setup for mass productions particularly in contact lens production in ultraprecision machining. The invention is also integrated with vacuum chuck based in diamond turning machine and using the vacuum forces as an actuating driver for jaws displacements. it is worth to mention that the vacuum force evaluation need be to examined, for the purpose of pulling in the smart chuck's jaws. in the following sections this aspect will be discussed.

The features in the invention are multifunctional, and designed base on compliance mechanism methods.

The methodology in this invention is composed of three steps: Self-centring the circular workpiece and aligning with the rotary axis, holding the workpiece in place by the jaws that have a hinge flexure joint; Applying the self-lock holding position to the workpiece during the machining process using centrifugal force, so the workpiece always secured in position in either CW and CCW rotational directions.

The advantages of the invention with comparison to existing designs can be specified as follows:

- Exact align ability between the workpiece and spindle axis at both low and high speed

- Sub-micron accuracy in spindle positioning registry

- Significantly combined

- Light and efficient integrated assembly

- Less noise and lubrication

- User-defined setup and efficiency

- Highly functional and capable for mass production

- Self-locking and secured work holding

- Workpiece self-centering

| (a) | (b) | (c) |
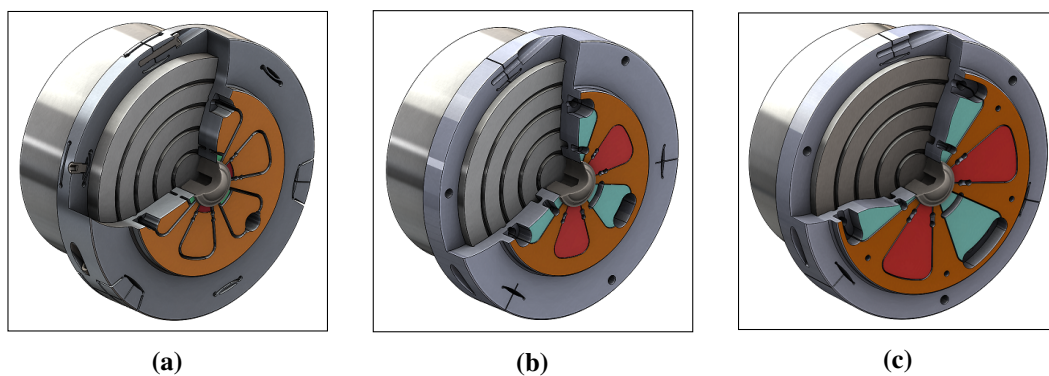
Fig. 4.1 Smart chuck concept design: (a) concept A; (b) concept B; (c) concept C

As illustrated in Figure 4.1, three concept models have been designed using Solidworks 2016. The concepts are identical in terms of the main principal of self-locking and self-centering features. However, different flexure form and shapes were designed for mounting the smart chuck to the DTM vacuum chuck design. Concept A has an extra axial clamping flexure to secure the holding of the smart chuck when it is required to run at a higher speed. This concept tends to have the disadvantage of manufacturing complexity. Concept B has a less flexural clamping mechanism and less effective area of the clamping surface. Since this concept tends to ease the prototyping and manufacturing process, the lack of stiffness can be occurred due to

Table 4.1 Smart chuck concept design scoring and ranking

Design Concept Scoring	Weight (%)	Design Concepts					
		A		B		C	
Selection Criteria	Weight (%)	Rating	Weighted Total	Rating	Weighted Total	Rating	Weighted Total
Vieability/ Capability/ Stability	20	10	200	5	100	15	300
Ease of Manufacturing/ Machining	20	5	100	20	400	20	400
Ease of Assembly/ Disassembly	15	15	225	10	150	15	225
Cost Effectiveness	25	5	125	25	625	25	625
Clamping Stiffness	20	20	400	5	100	20	400
Total score			1050		1375		1950
Rank			1		2		3
Continue?			No		Combine		Yes

the absence of sufficient effective surface area of clamping. Concept C is adapted to have an efficient manufacturing process and robust stiffness for the purpose of the clamping.

Table 4.1 shows a scoring technique used to specify the best concept of this design. There are five selection criteria that have a unique weighting percentage, hence for each concept criteria, the weighting will define a score rating. the total sum of these criteria will be 100%. the multiplication of the rating to the weighting score will then define the ranking of the concept in which will be chosen to finalise the design. The selection criteria outline the importance of the design and were selected in the area of viability, capability, stability, ease of manufacturing and machining, ease of assembly and dismounting, cost-effectiveness and clamping stiffness and accuracy. As can be seen from the data, concept two has counted lower score in clamping stiffness and viability and capability whilst the maximum score goes to concept three at these

criteria. Concept three scored the highest weight in manufacturing, clamping stiffness and cost-effectiveness in which can be selected for the final design.

4.3   Detail Design and Specifications

As stated in previous section, accurate positioning in ultraprecision machining is one of the challenges that need to be addressed for a successful surface finishing. As part of this research, a novel method for controlling the accurate positioning was carried out. Since the compliant mechanism is widely employed in mechanical engineering mechanism, the advantageous can be applied to maintain accurate positioning in ultraprecision machining.

In this invention, according to the gap identified in literature review, a new design and contribution to knowledge have carried out to overcome the positioning challenges in freeform surfaced workpieces and their clamping technique in ultraprecision machining system. Several flexure hinges were designed in a clamping mechanism in the smart chuck. The following section will describe the final design of the smart chuck and the explanation of the design methodology and specification will be followed to evaluate the design principal.

4.3.1   Invention Description and Exploration

For simplification purposes, the smart chuck geometry was assigned with the tag numbers in the drawing, so they cab be identified very efficiently. As illustrated in Figure 4.2, the Air Bearing Spindle **100** and the vacuum chuck **500** attached and fixed in the diamond turning machine and the smart chuck **200** concentrically located in the vacuum chuck **500** and will be held in-location by three socket head cap Screw **400**. The contact lens insert **300** (workpiece) will be located in the smart chuck **200** for machining purpose. Appendix B.1 and B.2 present the technical drawings for the invention include the details of the flexure design.
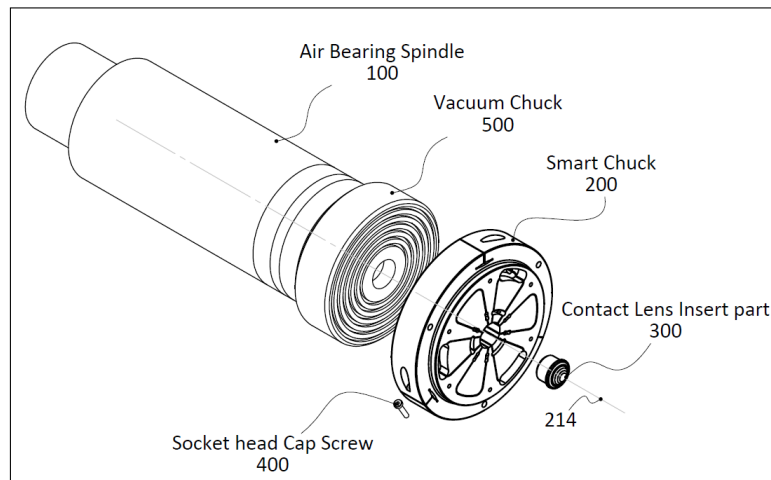
Fig. 4.2 3D view of the assembly of

Referring to particularly Figure 4.3, the smart chuck **200** of the invention using flexure mechanism as illustrated. Four type of flexure designed and developed in the invention. Two type of jaws; clamping and Self-locking, has been designed in this invention. All jaws have a through all slotted feature **212** and connect through the flexures mechanism to the main body **200**.

Self-centering and Clamping

Self-centring of the workpiece in this design also means alignment with the chuck centre while the alignment with the spindle centre might suffer from eccentricity. According to the nature of the design, the aperture can be setup in DTM's vacuum chuck in two sequence as followed:

1. First sequence is where the smart chuck will be adjusted with the spindle axis at its attached vacuum chuck. Flexure type FL1 **203** has the capability to adjust the entire smart chuck with sub-micron displacement, converting the horizontal movement generated by the screw cap **400** to vertical micro positioning. At this sequence, the smart chuck **200** will be aligned with spindle center line (axis). However, using the FL1 flexure at this stage will eliminate any possible runout that might exist in the spindle. Nevertheless, the smart chuck is always can be aligned with spindle radial runout. Axially alignment of the
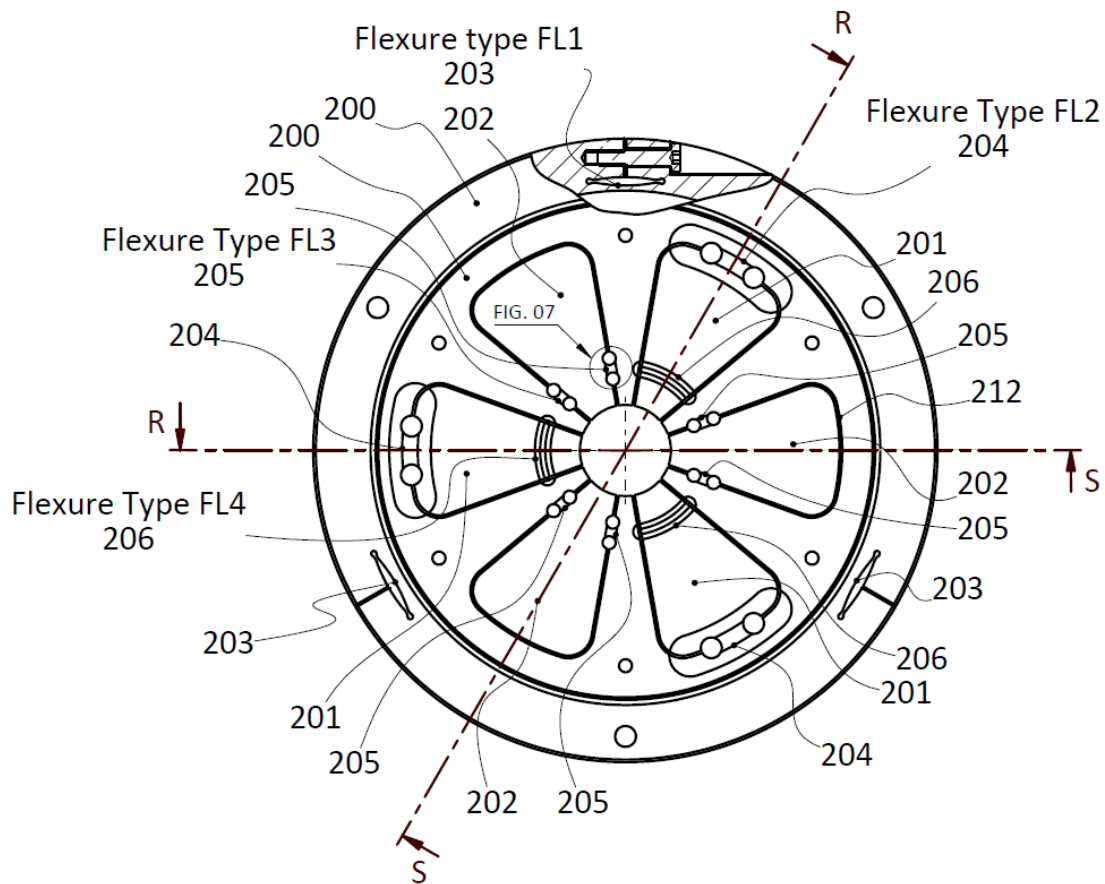
Fig. 4.3 Smart chuck, the main principle of the invention

smart chuck with the spindle will be applied once a time at the beginning of machining process. at this stage it is assumed that air bearing spindle has very low motion error. Cylindrical face **213** as illustrated in Figure 4.4 will be used for dialling the smart chuck.

2. The second sequence is loading the workpiece **300** in the place and activating the vacuum chuck to clamp the workpiece which is a contact lens mould insert part. In a broader definition, according to Figure 4.2 and 4.3, the vacuum force expected to axially actuate the clamping jaws **201**. Flexure Type FL2 **204** works as an cylindrical hinge flexure which can provide pivoting moments while the jaws at this position are only free to move towards the center of spindle and restricted to move on other directions.
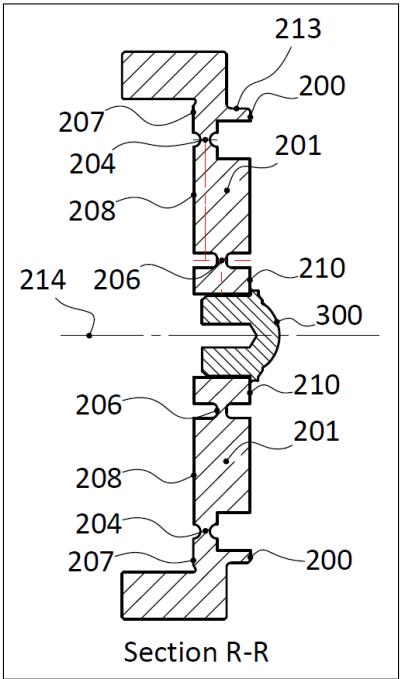
Fig. 4.4 Clamping jaws using flexure mechanism
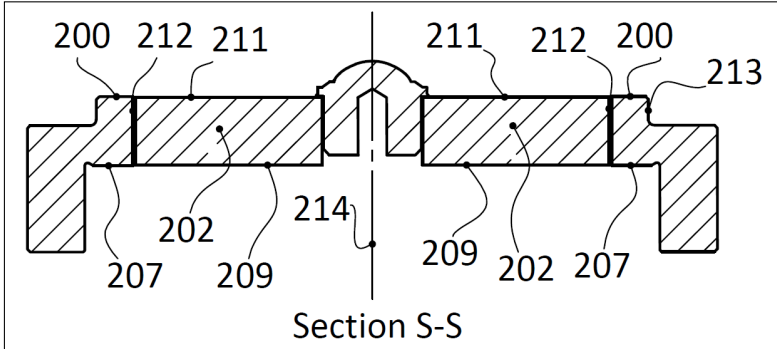
Fig. 4.5 Cross-section of the smart chuck

The flat surface of the main body of the smart chuck **207** coincidently mated with the flat surface of the vacuum chuck **500** and back face of the jaws **208** has a gap to prepare the displacement of the jaws **201** from the hinge **204**. This mechanism enabling the three designed self-centering jaws **201** touch the workpieces in three points whilst they pivoting from the Flexure **204**. At this stage, the jaws will locate the workpiece in the center of the smart chuck whilst the smart chuck being already aligned with the spindle axis **214**. Figures 4.6 and 4.7 illustrate the details of the workpiece clamping in a broader range.

The clamping mechanism consists of three stages as followed:

- The Rest position is the function where the lens or the insert part workpiece **500** will be loaded in the place. There is a surface gap between the front face of the jaws 201 and main body **200** to prevent the friction in the workpiece outer surface. However, the workpiece is always having contact with the main body **200** and not tended to move in Z-Direction when the jaws **201** are actuated.

- At Stage 01, when the jaws **201** actuated, the clearance L1 between the workpiece and the jaws **201** will be filled. The value of the $\theta 1$ and R (magnitude of the slope) are always constant and from these two parameters the value of the maximum displacement a2 in Z-Direction, and $\theta 2$ can be calculated. At this stage, the workpiece **300** is aligned with the spindle axis centre **214**.

- At Stage 02, the inner face of the jaws 201 will be fully contacted with the workpiece by functioning the fillet corned flexure type FL4 **206**. Preferably At this stage, the workpiece **300** is fully aligned with the spindle axis **214** and clamped in the place. The value of $\theta 2$ is now changed to Zero and $\theta 3$ will be evaluated based on the flexure structural elasticity at the flexure type FL4 **206**.
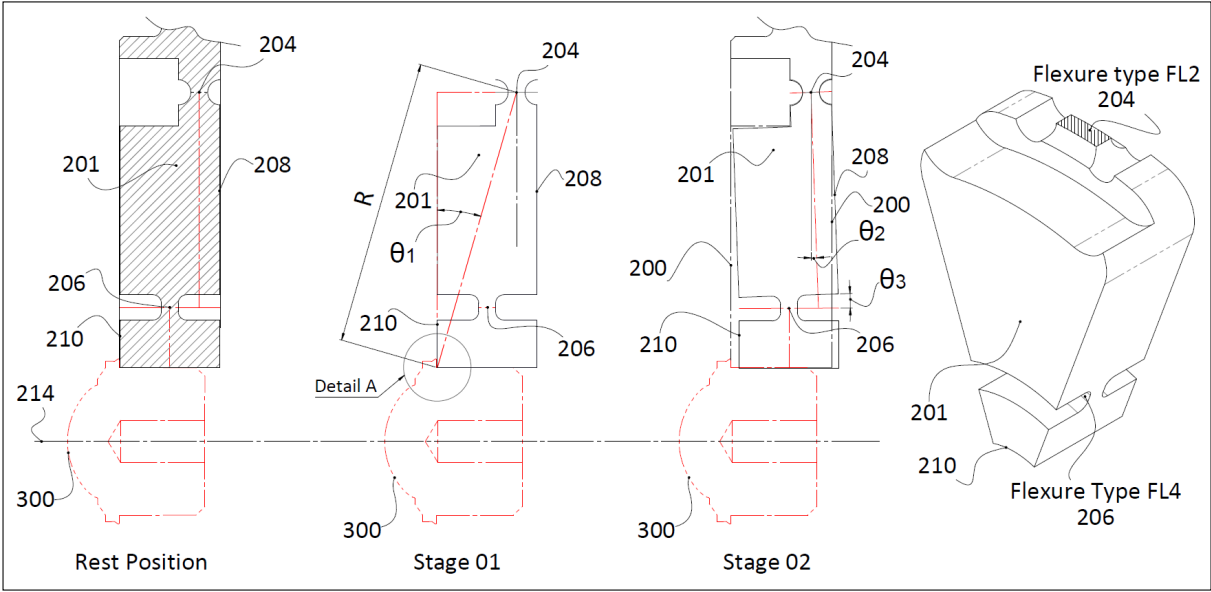
Fig. 4.6 Cross section of the clamping jaws and their functionality
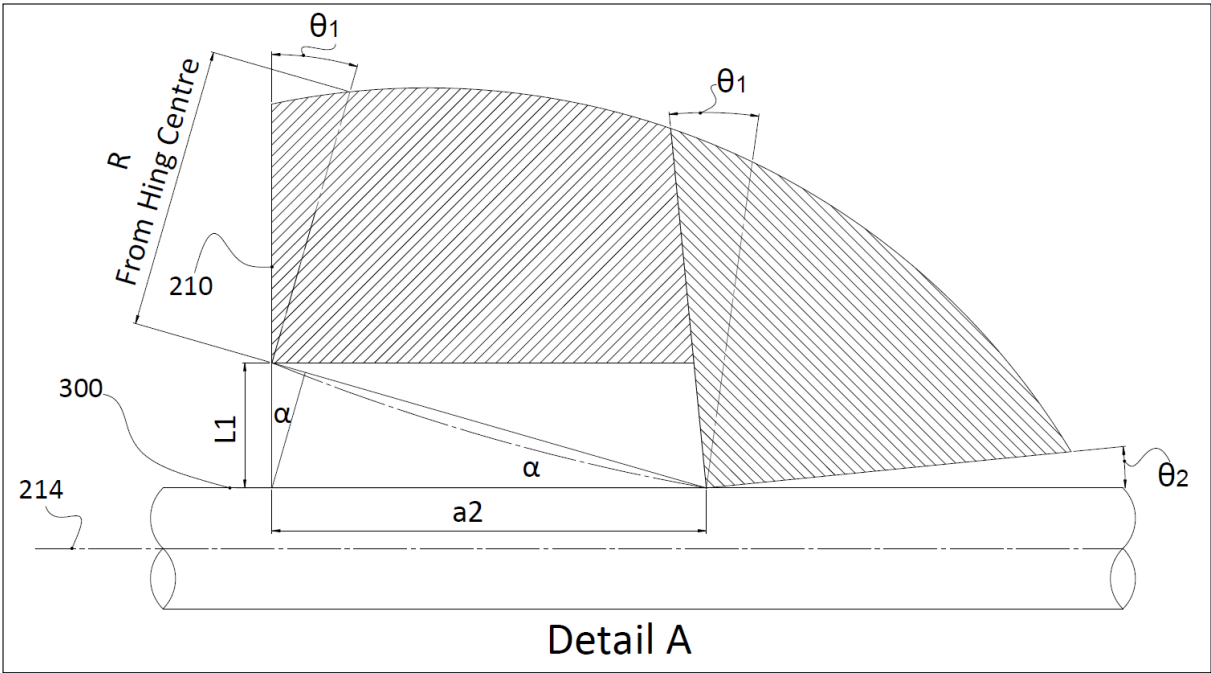
Fig. 4.7 Scaled detail of the stage 01

Self-locking and High-speed Securing

Figures 4.2, 4.5, 4.8 and 4.9 of this invention illustrate the self-locking functionality whilst the workpiece under the machining process. Three identical jaws **202** having the duty to lock the workpiece **205** preventing from any dismounting or misalignment during the machining process. Figure 4.8 illustrate the Flexure Type FL3 and its cross sections
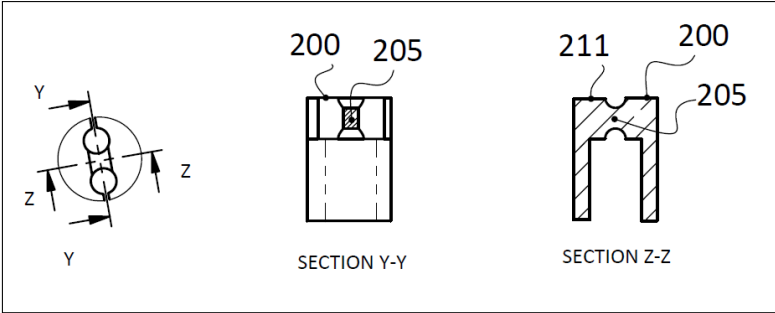
Fig. 4.8 Flexure Type FL3 and its cross sections
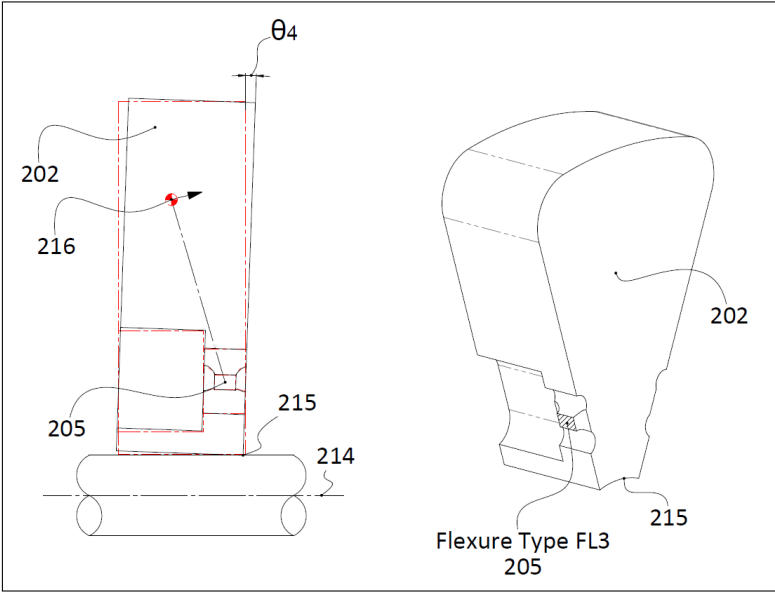
Fig. 4.9 Centrifugal mechanism for the self-lockings

The functionality of the jaws **202** is dependant to spindle speed by meaning that increasing the spindle speed expanding the clamping force respectively. Flexure type FL3 **205** was designed to fulfil the duty of self-locking particularly in jaws **202**. The invention of this feature

designed based on centrifugal force **216** phenomenon. The flexure **205** located off-line from the centre of mass **216** of the jaw **202**. Hence, it will produce a centrifugal moment and force from the pivoting point **205** of the flexure whilst the spindle in rotational mode. The centrifugal force will also creates a torsion force in flexure and subject to twist the flexure structure at this location and provide an angular displacement $\theta 4$ in the jaw. Thus, enable to displace the adjacent edge **215** of the jaws toward the workpiece. However, the contact between the jaws **202** and workpiece **300** are point to point connection **215** instead of being surface to surface.

4.3.2 Theoretical Analysis on Flexures Design

As aforementioned, there are four types of flexures, designed in the chuck to maintain the clamping and accurate positioning purposes in UPM. As part of the design, the flexures hinges intended to be three-dimensional and multiple-axis, include the longitudinal and transverse axis. This section is dedicated to determine the flexural compliant configurations and their characterisations. Generally, a flexural hinge is the components of a combined spring that can react to and transfer both translation and rotational displacements by means that each specific flexure hinges being characterised by a comprehensive set of compliances that determine its quasi-static loading mechanical response.

The vast majority of current researches concentrates on applications that employ corner-filleted circular flexure hinges in which their performances can be analysed through commercial finite element (FE) engineering software. In this study, the finite-element methodology was used to analyse and validate the results on the flexure design and viability and capability of the geometry design. In this section, for each individual flexure type, two-dimensional theoretical principal will be discussed, and will be followed by three-dimensional multiple-axis FEM modelling and discussion to finalised the design of the flexure on the smart chuck. It is necessary to point out that the purpose of this study and their contribution was structured to use current compliant mechanism based on recent research and studies for mechanical

engineering design of this chuck. Moreover, according to literature review, most of theoretical formulation and investigations in compliant mechanisms are carried out and standardised based on simplified flexural geometry shape. Due to the level of complexity of the design in this invention, the comprehensive mathematical formulation for verification of flexure design can not be fully managed by means that the FEA result for 2D and 3D geometry will be used for final verification of the study. Nevertheless, the general formulation of the two-dimensional flexure will be explained at each flexure type to underline the geometrical concept of the design.

Flexure Type FL2 and FL4

As for flexure design considerations, a generic mathematical theory was employed to initially obtain the capability of the flexures based on their geometrical shapes and design parameters. As illustrated in Figure 4.10, the self-centring jaw including two flexures, one circular and one fillet corner shape. Both flexures were modelled as to multiple-axis 3-dimensional flexure in the 3D model. However, the cross-section plane also shows the 2D surface of the jaw for investigating the effect of a generic 2D-axis formulation. As aforementioned in previous sub-section, due to complexity of the design with multi-functional property, only the flexure shape and geometry design parameters were discussed in this section. However, statical diagrams and graphical analysis for the flexure design were carried out to describe and investigate their relationship when integrated with those standard flexure shapes and design parameters. The definition of the flexure parameters was made based on current design and studies in compliant mechanism researches in the market. For more clarification, in this invention, most of the flexure geometry parameters were defined based on the resource available on [86]. The statical schematic view shows the beam elements at each compliant points from the fixed-end to the free-end degree of freedom (DOF). Flexure hinge type FL2 can be assumed as 2D single-axis circular flexure, while the Hinge type FL4 is considered as a 2D single-axis fillet-corner flexure.

A single-axis flexure hinge in a two-dimensional application generally has a constant width, while the flexures in this particular type designed to have different width for various purposes such as clamping and micro-positioning. Various configuration on the flexure geometry can subsequently be examined and distinct compliance equations, standardised for an explicit form such as parabolic, hyperbolic, inverse parabolic, elliptical, corner-filleted and circular for two-dimensional application hinges.
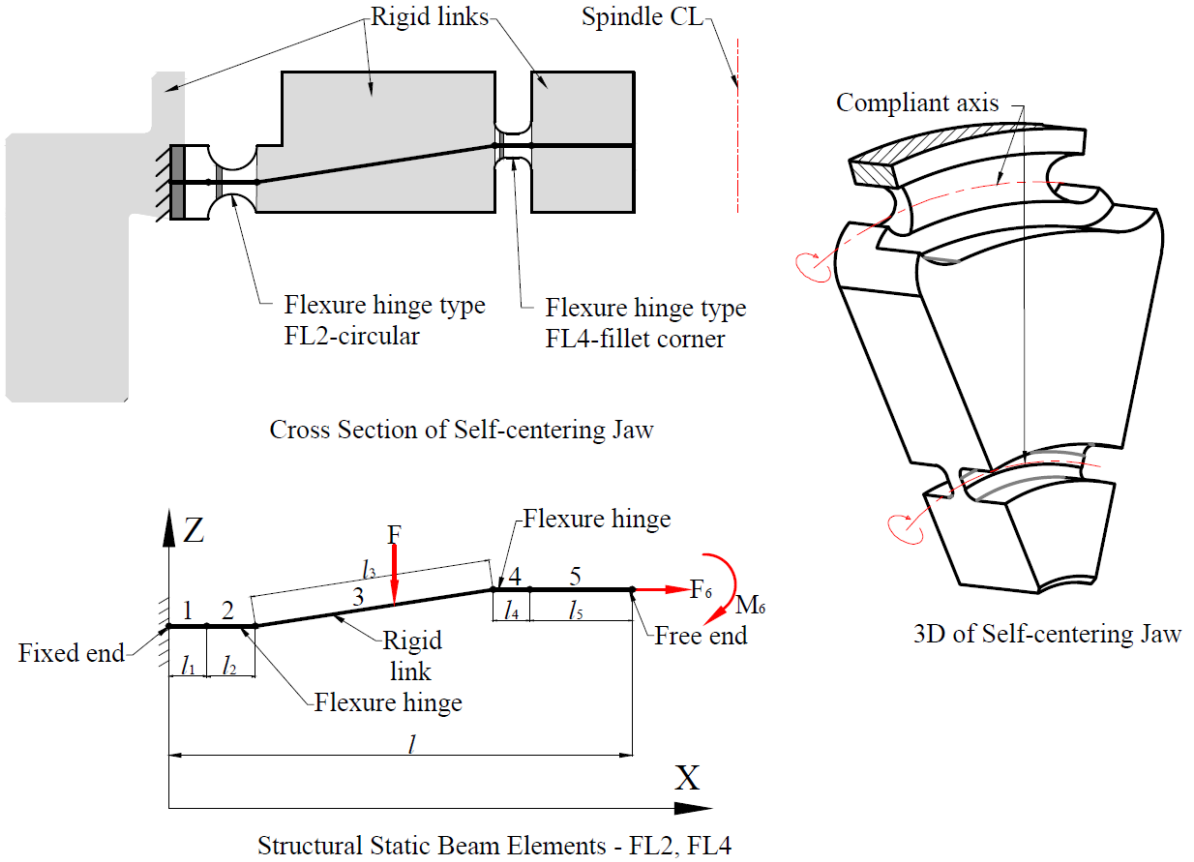
Fig. 4.10 Flexure design, schematic view of flexure type FL2 and FL4

As illustrated in Figure 4.11, type FL2 and FL 4, the flexure hinges have longitudinal and transverse symmetry axes and consequently, the configurations for two-dimensional single-axis flexure application can be defined using the generic mathematical methodology. Nevertheless, it is essential to point out that 2D mathematical and graphical analysis and formulation used in this particular flexures described only in the hinge shape, but not in the entire structure of the

jaw. Since the width or the compliant sensitive axis of the flexure has a various asymmetric shape, then the final result using the FEA will conclude the values of features motion.

According to the explanation made by Lobontiu [87], the generic formulation of the flexure hinges performance can be categorised to several criteria such as the capacity of rotation, the precision of rotation, sensitivity to parasitic loading and effect of stress level under fatigue conditions. Although there are comprehensive formulations discussed that could define those criteria for flexures with constant width for two-dimensional flexure hinge. However, the design of flexure type FL2 and FL4, in this case, have a different width, thus applying the generic mathematical methodology is going to be very complicated. Hence at this stage, the use of 2D FEA modelling methodology will be much sustainable and feasible to evaluate the result of the design for these particular flexures.

The geometrical detail of the flexure FL2 and FL4 can be found in Table 4.2. The indication of the detail shows the design was made by having the similar radius r and against the thickness of flexure t in flexure type FL4. Flexure type FL4 has the similar principle but different radius r which decreased while the total l was increased to propose the same magnitude for the thickness t.
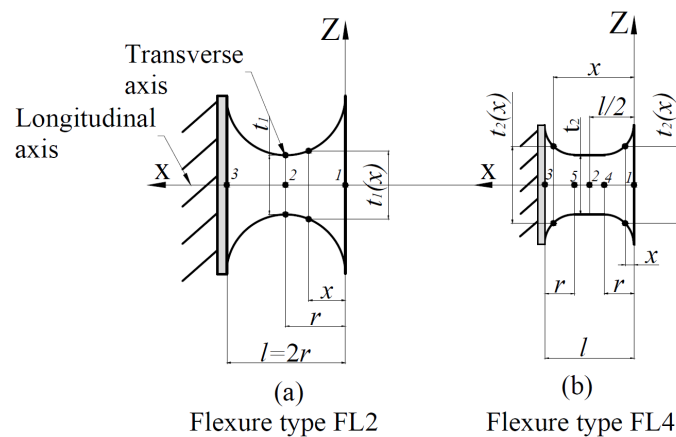
Fig. 4.11 Flexure design: (a) Flexure type 2; (b) Flexure type 4

For symmetric circular flexure hinge geometry as FL2, the variable thickness, $t_1(x)$, can be expressed as:

Table 4.2 Geometrical details of flexures type FL2 and FL4

Flexure type	r [mm]	l [mm]	t [mm]
Circular, FL2	2	4	2
Fillet corner, FL4	1	3	2

$$t(x) = t + 2[r - \sqrt{x(2r - x)}] \qquad (4.1)$$

Flexure Type FL3

Flexure type FL3 was designed as a generic circular hinge which has one end fixed to the body and a free end connected to the self-locking jaw. The flexure hinge has two longitudinal and transverse axis. The sensitive and/or the compliant axis subject to a torsional moment which caused by centrifugal force acted in the jaw when running at a specified rotational velocity.

Table 4.3 Geometrical details of flexure type FL3

Flexure type	r [mm]	l [mm]	t [mm]	w [mm]
Circular, FL3	1	2	2	2

As indicated in Figure 4.12, the flexure hinge is linking the jaw that subjects to provide an elastic displacement with a contact force between the workpiece and the adjacent front edge at the jaw. The flexure designed to generate maximum magnitude displacement of 10μm under 2,000 rpm of spindle speed. Moreover, it is essential to point out that increasing the rotation speed will increase the centrifugal force. Hence the complaint at this particular flexure becomes very sensitive, by meaning that, the higher rotational speed can achieve more clamping force at the contact region but less stiffness at the flexure itself. However, the design can be made to operate under such a higher rotational speed. Structural static beams diagram shows that the value of the total l has a direct impact on the performance and accuracy of the jaw. Same as another flexure type, constant flexure radius and thickness were design in this particular flexure
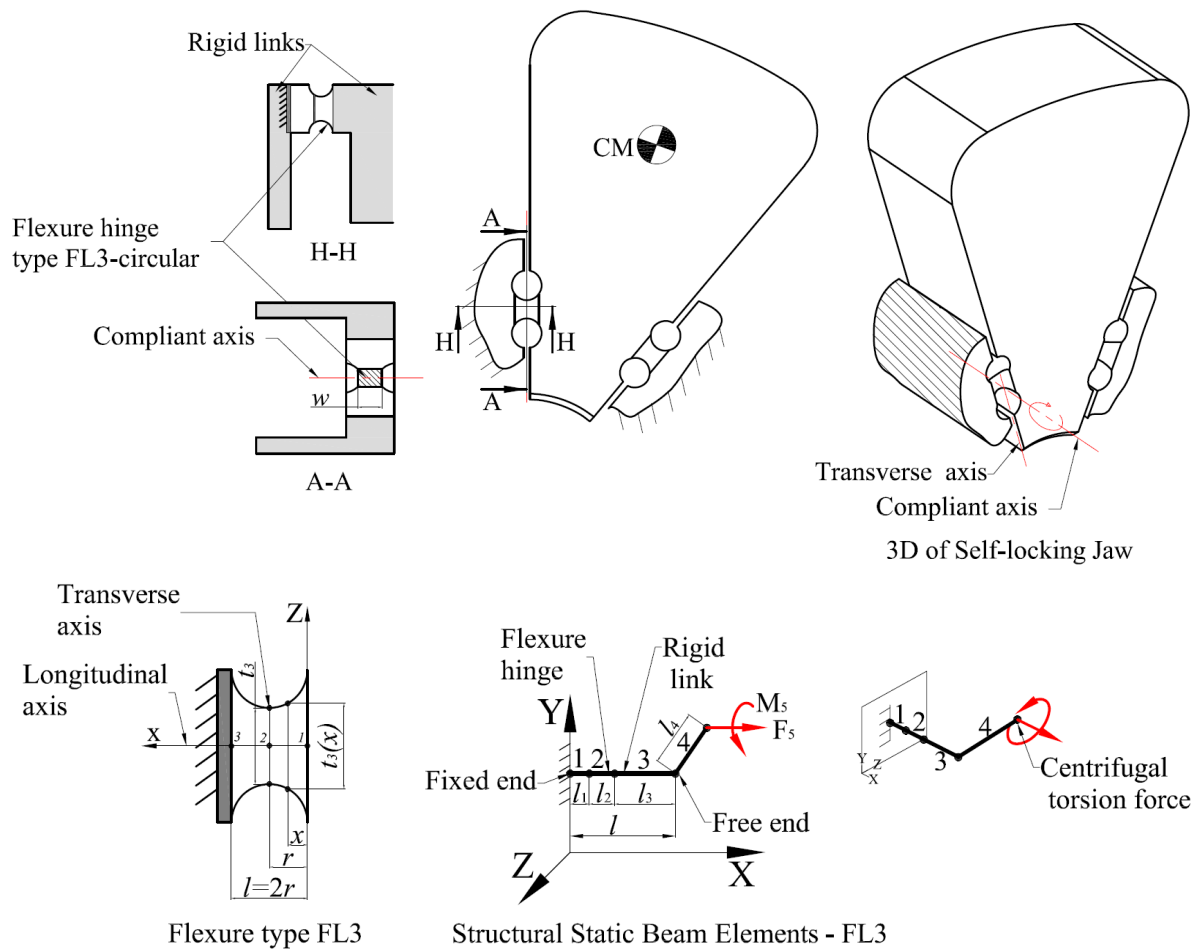
Fig. 4.12 Flexure design, schematic view of flexure type FL3

for ease of manufacturing capability. Table 4.3 indicates the geometrical details of the flexure type FL3.

Flexure Type FL1

Flexure type FL1 was designed as a generic custom hinge with 3-dimensional multiple axes. Since one of the objective of the smart chuck design was to maintain a very high and accurate positioning displacement, it's mounting status to the vacuum chuck significantly critical. The concentricity between the inner diameter of the smart chuck mating the outer face of the vacuum chuck is playing an important role in sustaining a secure mounting as well as being stiff enough to take all the loads during the ultraprecision machining process. Flexure FL1 was designed
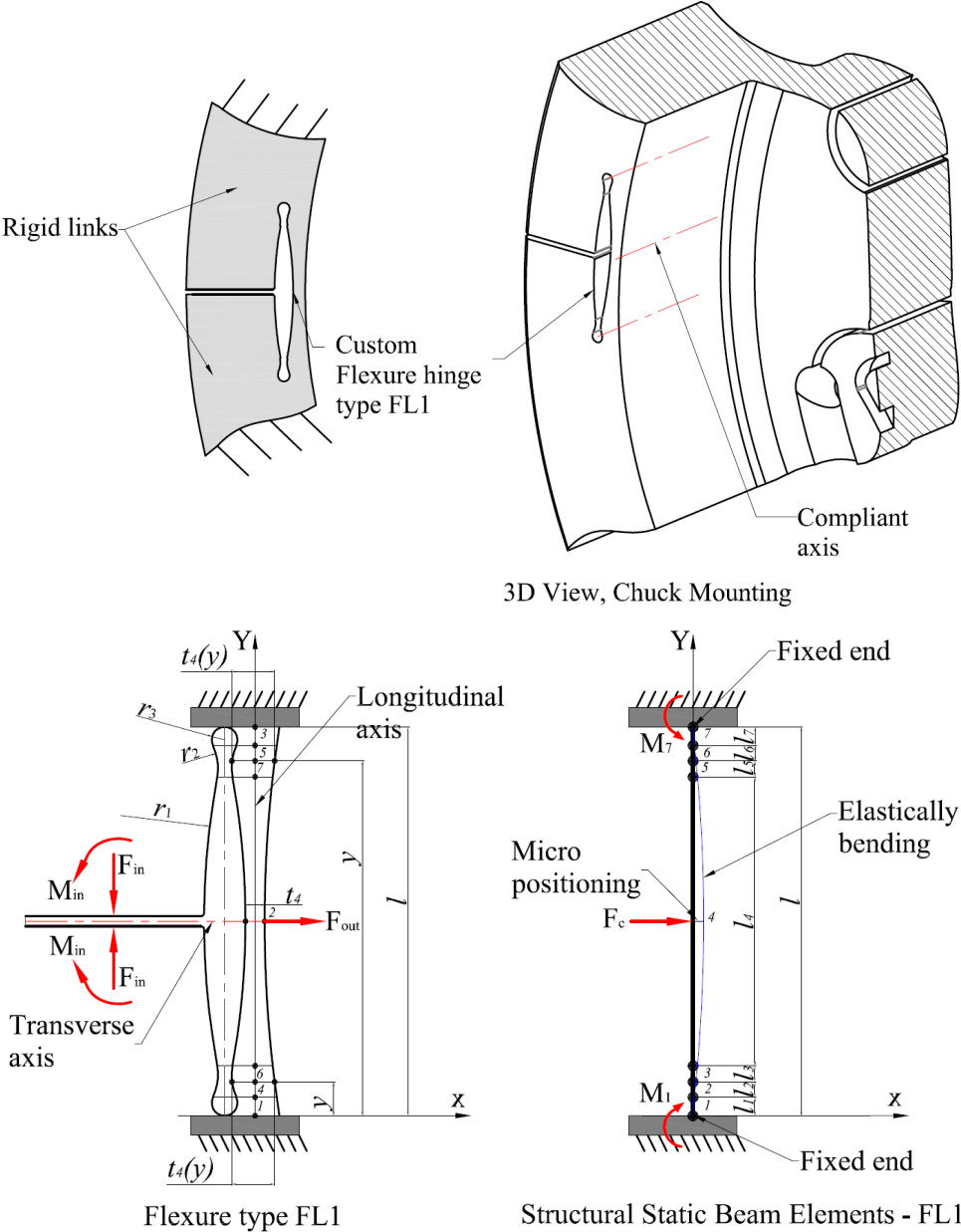
Fig. 4.13 Flexure design, schematic view of flexure type FL1

as a combined circular and parabolic hinge to fulfil the purpose as early mentioned. As seen

from Figure 4.13 which shows the geometrical detail design, the flexure hinge is capable of

converting the lateral displacement to diagonal. As explained in the design specification, the

mounting force at this stage will be applied by a bolt and a threaded screw bespoke designed

in the chuck. However, it is essential to highlight that the bolt and screws are not capable

to provide a micro-positioning for required accuracy even with fine pitch screws. Thus, a combination of the large displacement input with a custom flexure can maintain a very smooth micro-positioning displacement. As indicated in detail, the flexure consists of symmetrical circular shapes along its longitudinal and transverse axes. The Flexure thickness t_4 is critical in this flexure as it has been located in the compliant axis. As can be seen, identical F_{in} and M_{in}, by means that, input force and input moment respectively can direct towards the transverse axis and the differentiation of the compliant stiffness in the parabolic shapes can maintain the output force, F_{out} and translational displacement. As a structural static beam, the flexure can be categorised as an identical fix-fix endpoint that subjects to an identical elastic bending as a spring component over the applied force.

Table 4.4 Geometrical details of flexure type FL1

Flexure type	$r1$ [mm]	$r2$ [mm]	$r3$ [mm]	l [mm]	$t4$ [mm]
Custom, FL1	30.7	2	0.5	15	1

As specified in Table 4.4, the l_1, l_2 and l_3 will define the compliant micro-positioning of the the thickness t_4 in diagonal direction towards the center of the chuck.

4.4   Numerical Analysis

Since the initial geometry design of the flexure hinges were specified, FEA methodology was employed as a secondary procedure to evaluate and validate the design. At this stage, the structural analysis was made based on a 2D FEA model in which can verify the 2D design explained in the previous section for each flexure hinges geometry. Essentially, the 3D FEA is required and will be studied in a broader phase to substantiate accurate and conclusive results. In this section, both 2D and 3D FEA models will be explained, and a comparison between the results will be made. As for FEA 2D simulation, two scenarios were modelled. First scenario studies the model with the assumption of the clamping under **loaded condition** were

the workpiece included on the simulation for analysing the stiffness of the flexures. The second scenario will consider the flexure to work under **unloaded condition** where the mart chuck will function without the workpiece. As per unloaded scenario, it is expected that the flexures should function in much conservative behaviour while posing unconstrained DOF in X and Y direction. The 2D FEA simulation will be done in flexure type FL2 and FL4 only to overview the initial behaviour of the design. For FL3 and FL1, only the 3D FEA simulation is required whilst the compliant axis are located in their Z-directions.

4.5 Two Dimensional Analysis

4.5.1 Evaluation of DTM Vacuum Force

At this stage of design, it is vital to evaluate the capability of the vacuum chuck force, ensuring the capability of the pulling mechanism for the jaws. Applied force to the jaws must be equal to the maximum force capacity of the vacuum chuck in diamond turning machine. According to the vacuum specification, the maximum vacuum pressure of 100 kPa = 0.1MPa can be achieved for non stressed clamping of a workpiece in vacuum chuck. Maximum value of the vacuum pressure can be indicated from the gauge located in DTM as illustrated in Figure 4.14.

Fig. 4.14 DTM vacuum pressure indicator (gauge)

This maximum load also can be determined as for the applied force required for FEM analysis purpose.

4.5.2 FEA Modelling Setup for Vacuum Force Evaluation

As for 2D simulation preparation, a 2D surface was drawn using Solidworks software, and the model was imported into Ansys for static structural analysis as illustrated in Figure 4.15.
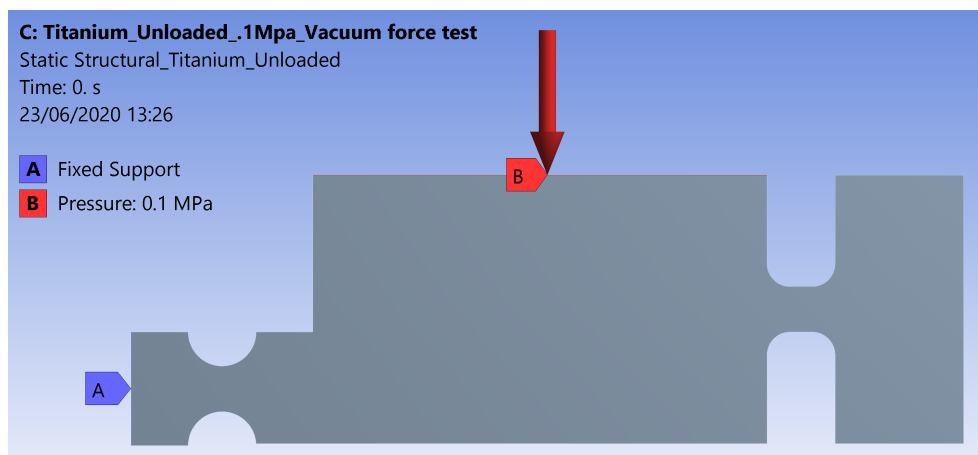
Fig. 4.15 2D FEA modelling setup for vacuum force evaluation

Titanium alloy material with the property details shown in Table 4.5 is assigned for the bodies and after the geometrical meshing generation, and the boundary conditions were modelled.

Table 4.5 Titanium alloy material properties

Titanium Alloy Material Properties	
Density ρ (kg ^-3)	4620
Coefficient of thermal expansion α (K^-1)	9.40E-06
Poission's Ratioo	0.36
Young's modulus E (Pa)	9.60E+10
Shear Modulus(Pa)	3.53E+10
Bulk Modulus (Pa)	1.14E+11
Tensile Yield Strength(Pa)	9.30E+08
Compressive Yield Strength(Pa)	9.30E+08
Tensile Ultimate Strength(Pa)	1.07E+09

A fixed end support was prepared at one end position at FL2, and 0.1 MPa pressure in which represent the vacuum force that approximately equivalent to 1 Bar pressure at the vacuum chuck was applied to the top face in the rigid link between the hinges. For evaluation of the vacuum force and its effect in the pulling mechanism on the smart chuck, the displacement and deformation result from simulation need to be interpreted. A directional deformation or displacement in the structural body is required. Local coordination was set up at the top right

corner where the first contacting point to the workpiece is expected to occur when the load is applied.

4.5.3   FEA Result For Vacuum Force Evaluation

Since the first simulation run was completed, a directional deformation results in both X and Y directions at the local coordination point were setup. Interpreting the result as illustrated in Figure 4.16(a) and 4.16(b) evidencing maximum displacement of 11 μm in X direction and approximate value of 39 μm in direction at the nose point in the self-centring jaw. By comparing the two result, as shown in Figure 4.16(c), a displacement ratio of 3.5 μm in the Y direction and 0.28 μm in the X direction can be calculated. By meaning that, if the vacuum chuck capable of producing 0.1 MPa pressure, the jaws can fill 11 μm of clearance at the workpiece clamping location. This early stage of the result can be acceptable with relation to the positioning persistence of the chuck and confirming that the design of the flexures is functional at this particular self-centring jaws. Despite the directional displacement result was successfully met the requirement, the clamping force need to be examined to evaluate the capability and liability of the design. Since the maximum pressure of the vacuum chuck indicates 0.1 MPa, the character of pressure loss should be considered very carefully. It can be concluded that the self-centring functionality on the smart chuck might not be achieved if the vacuum pressure suffers a loss in the energy. Hence, the jaws can not maintain proper clamping force while the applying force is very low.
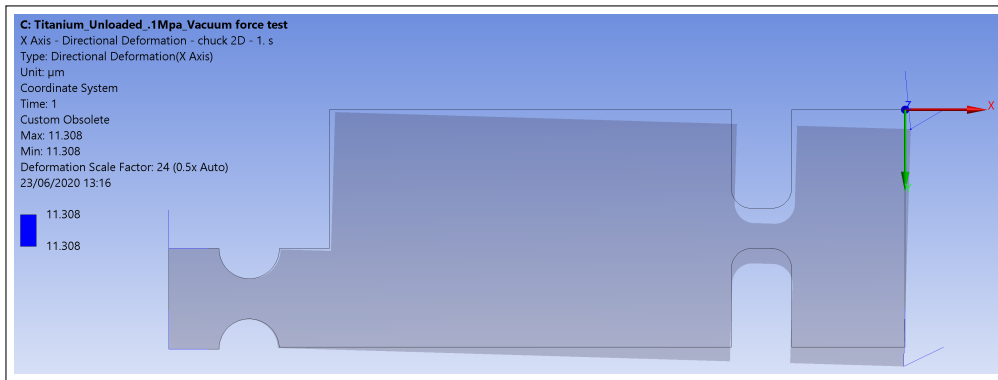
(a)
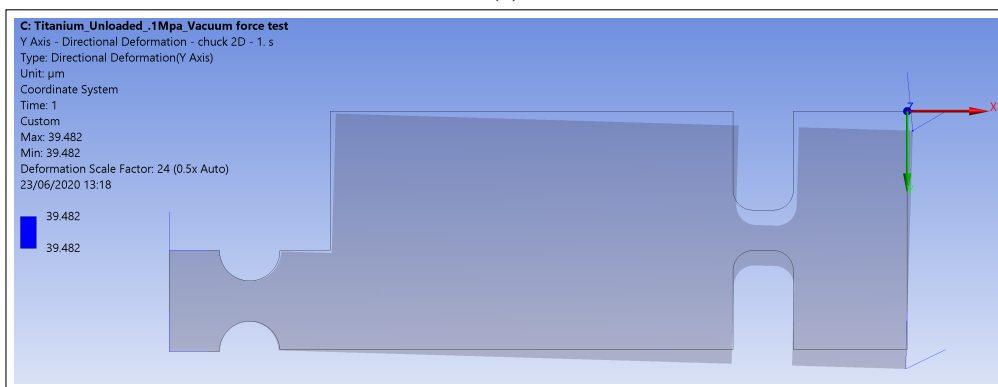
(b)
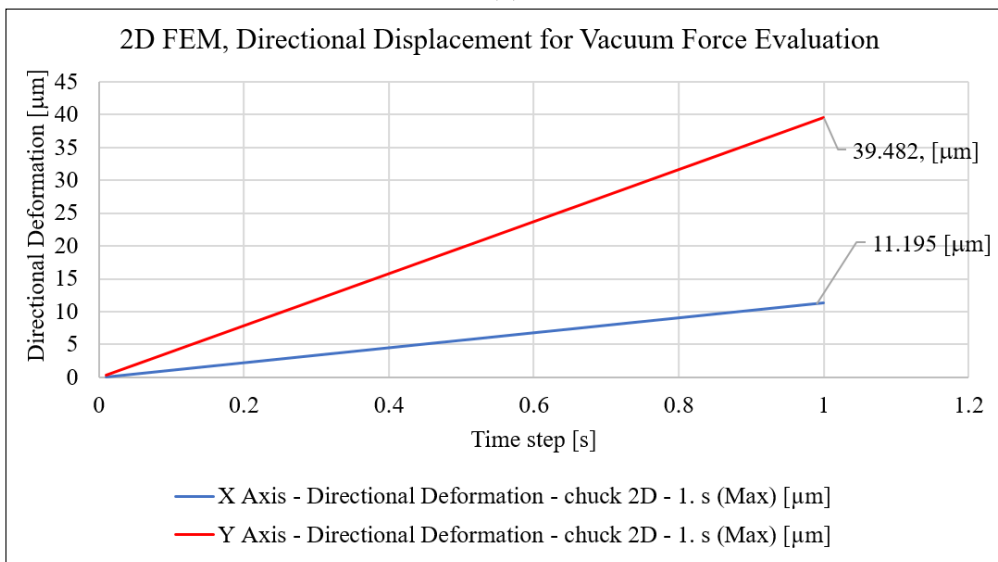
(c)

Fig. 4.16 DTM Vacuum force evaluation: (a) directional deformation in X-direction; (b) directional deformation in Y-direction; (c) X and Y displacement comparison diagram

In summing-up, employing the vacuum pressure as an actuator for the smart chuck is not achievable and can raising the concerns that could not maintain enough force and pressure for workpiece clamping purposes, despite the fact that the smart chuck structural design is viable. Nevertheless, alternative actuation systems such as mechanical or pressurised air or hydraulic are required to fulfil the purpose of the clamping force between the jaws and workpiece. Due to the limitation of the facility and equipment, the concept of using the pressurised air or hydraulic mechanism was not possible. Hence, a mechanical solution can solve the problem as an alternative way to analyse the clamping pressure for the design.

Next Section and subsection will demonstrate the simulation result for a mechanical solution by increasing the applied force from 0.1 to 1 MPa, assuming the pressure increased ten times than vacuum pressure. This amount of pressure enabling to analyse most of the characteristics of the design, including the clamping pressure.

4.6   FEM Result and Discussion (Mechanical Solution)

As discussed in the previous section, a new finite element modelling was carried out.
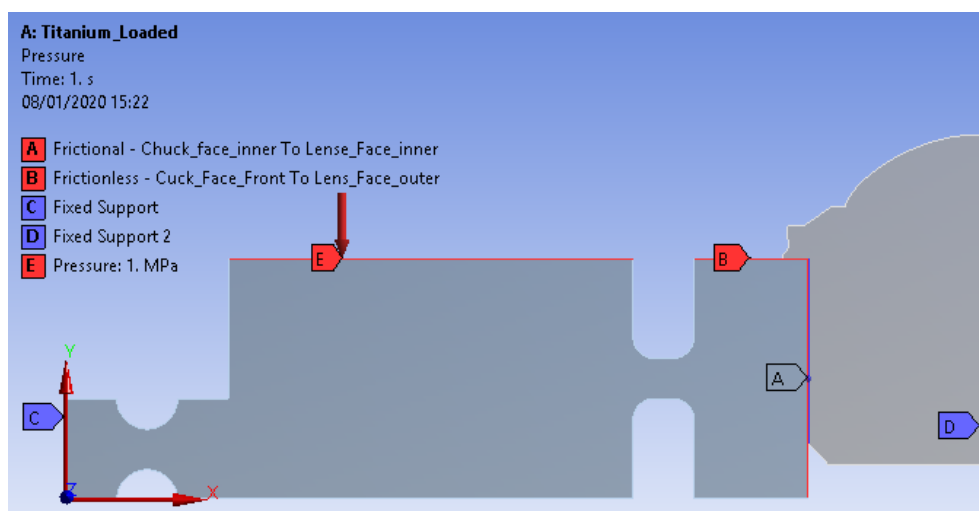
Fig. 4.17 Flexure hinges 2D FEA modelling setup

In this model, in particular, the pressure increased to 1 MPa, and a new set up was created for a condition where the workpiece also included in the model. As shown in Figure 4.17, the geometry of a Convex contact lens mould insert was included in the FEM. The material for this part was assigned as Aluminium alloy RSA-905. According to [88], the material property of the material listed in Table 4.6.

According to [89, 90], friction coefficient range of (0.3 - 0.7) can be determined based on statical dry sliding condition between two material of Titanium Alloy and Aluminium Alloy. In this Simulation value of 0.3 was determined for the contact boundary condition. Friction coefficient in this model tend to play a minor role as the small sliding feature designed to be allowed for self-centring.

Also, It is important to note that the ideal method for the coefficient of friction determination is a trial test. However, for simulation, in this case, the above-mentioned friction coefficient was determined using previous work data sheet. Nevertheless, according to the literature review, there is a lack of trial test data for dry, static frictional boundary condition between Titanium Alloy and Aluminium Alloy. Hence the assumption made that the value of 0.3 coefficient of friction is ideal for the simulation purpose in this case study.

Table 4.6 RSA 905, aluminium alloy material properties

Aluminum Alloy (RSA 905) Material Properties	
Density ρ (gr/cm $^\wedge$-3)	2,95
Thermal Expansion α (10^-6/K)	19,0
Stiffness (Gpa)	90
Hardness (HB)	180
Elongation e (%)	5
Yield Strength(MPa)	475
Tensile Ultimate Strength(MPa)	600

Upon simulation process completion, the result was interpreted based on several characters to define the evaluation of the flexure design and development. The analysis was also carried out in wider detail on both loaded and unloaded condition in this new setup to broadly investigate

the effects of the higher apply load in the flexures and their performance. The results were analysed in the 2D FEA model with mechanical solution, investigating total deformation, equivalent maximum stress, maximum principal stress, maximum principal strain, normal stress on both workpiece and whole bodies, directional displacement in the X-direction and directional displacement in the Y-direction.

4.6.1   Equivalent Stress

Equivalent stress results shows the maximum and minimum value, and can be seen in Figure 4.18. Analysing the result, indicates the maximum value of 520.4 MPa for the unloaded condition model and 155.29 MPa for the loaded condition model.

In either conditions, the maximum value calculated in Flexure type FL2 is as expected. Since the geometry in X-direction at the end of the jaw has a DOF, the maximum value of equivalent stress in the unloaded condition assumed to be in the highest level. Nevertheless, this maximum value is still within the elastic limit of or yield strength of the titanium material which is 930 MPa. Thus the geometry is functioning within the elastic or flexural region, and can be evaluate that the flexure FL2 is competent of taking the specific load at this location.

The flexure type FL4 has shown the minimum value of stress in unloaded condition as is assumed and explained in the geometrical design specification. Investigating the maximum stress in FL4 at loaded condition shows the stress of approximate 86 MPa. Therefore, it can be confirmed that this type of flexure at this location also has the capability to function properly when the jaws are in the clamped position.

Furthermore, comparing the value of equivalent stress between the loaded and unloaded condition model, the final decision can be made that both flexure hinge type FL2 and FL4 can be fully functional as their maximum value of the stress are not exceeded the maximum tensile strength value.
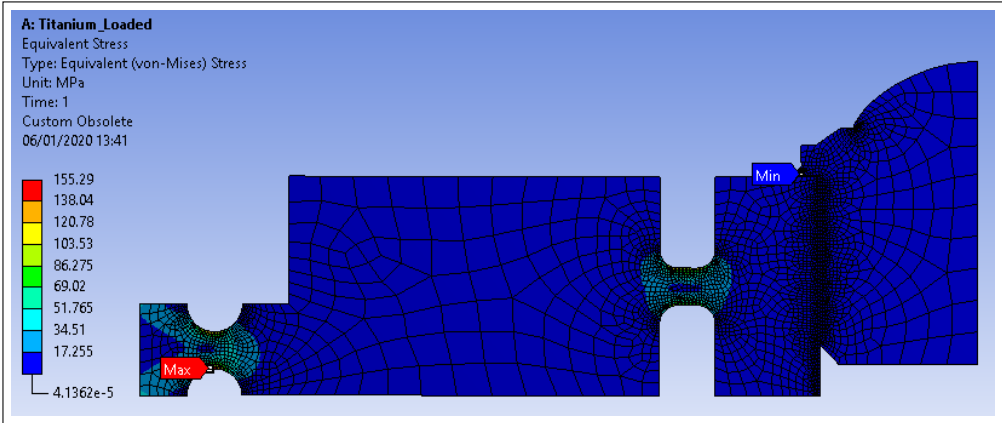
(a)
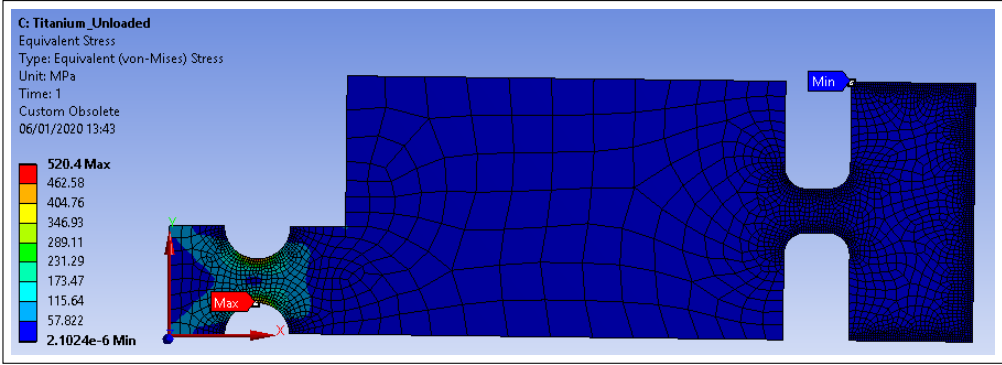
(b)
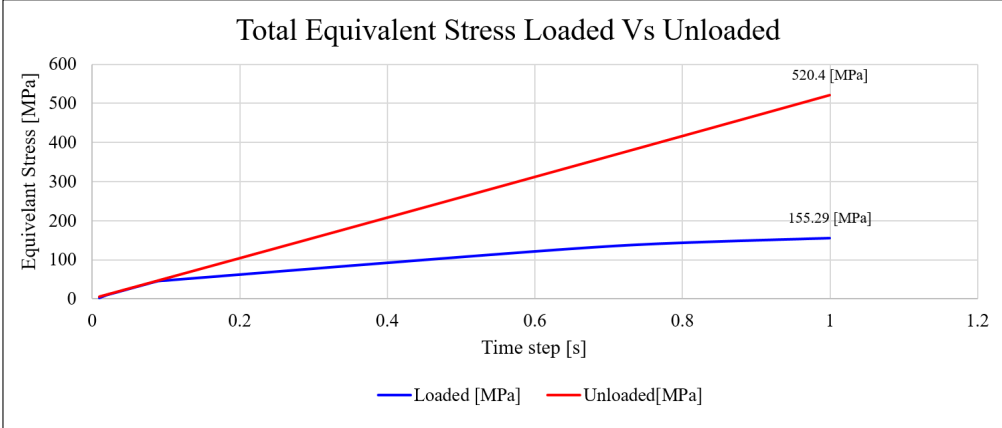
(c)

Fig. 4.18 Equivalent stress, loaded Vs unloaded: (a) loaded; (b) unloaded; (c) equivalent stress diagram

4.6.2 Total Deformation

Total deformation evaluated result shown in Figure 4.19 which indicates the maximum and minimum value. Interpreting the result, describing the maximum value of 0.4 mm for the model with the unloaded condition and 0.08 mm for the loaded condition model. According to the result in both loaded and unloaded conditions, the maximum displacement value was calculated in the unloaded model at the free-end location of the jaw in X-direction. The maximum value of total deformation in the unloaded condition expected to be higher than loaded condition. Nevertheless, the estimation can be done to characterise the maximum safe displacement of the structure under the specific load without experiencing any structural failure. The maximum value of 0.08 mm was indicated in flexure type FL4 in loaded condition. According to the total displacement result from FEA 2D model, the 10 micron gap between the workpiece and the self-centring jaw was filled. this can prove the proposed theory explained in the design specification indicated in Figure 4.6 at stage two. from the result, it can also establish the validity of the self-centring idea for workpiece using the flexure hinges and compliant mechanism. Hence, upon applying the load, the jaw can make a torsional force at the pivot point in the flexure hinges FL2 and locates the workpiece in radial direction towards the centre line of the spindle and finally provides a constant clamping force whilst contacted with the workpiece. Besides, comparing the value of total deformation between the 2D loaded and unloaded condition models, the final decision can be made that both flexure hinges type FL2 and FL4 can be fully functional and capable for self-centring purposes.

4.6.3 Directional Displacement in X and Y directions

Since total deformation in both loaded and unloaded conditions were evaluated, the local displacement at the contacting point between the workpiece and the clamping edge also need to be examined to evaluate the precise positioning as proposed in design specification.
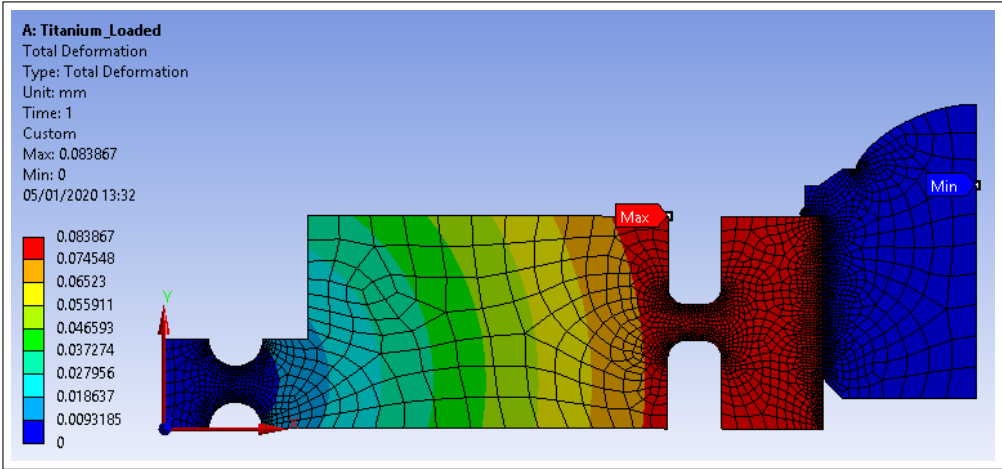
(a)
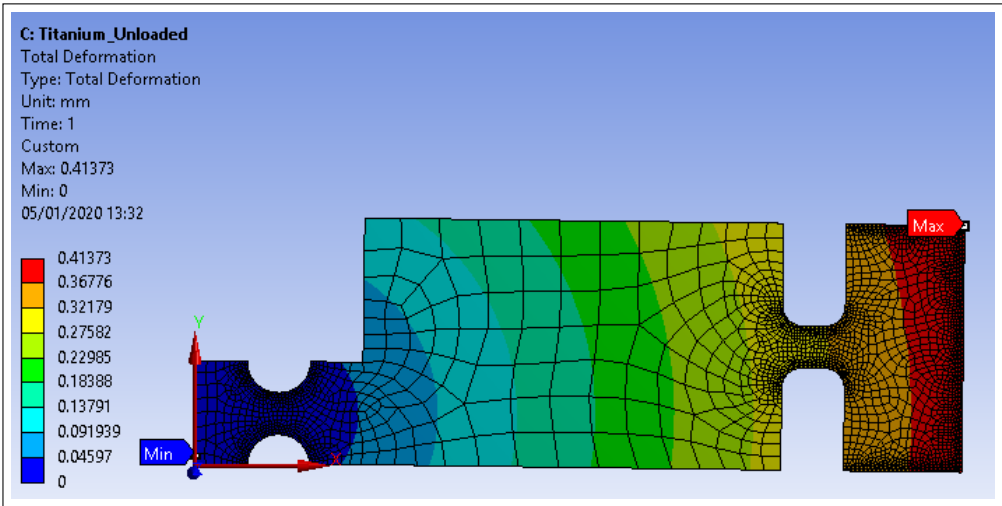
(b)
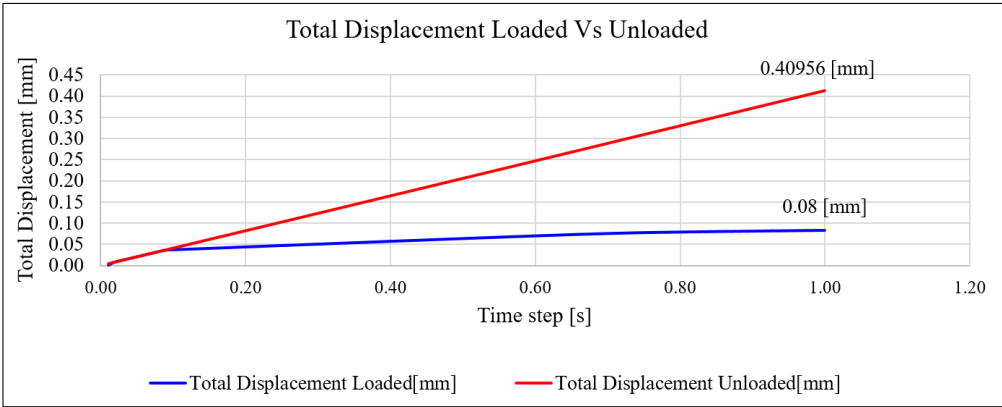
(c)

Fig. 4.19 Total deformation, loaded Vs unloaded: (a) loaded; (b) unloaded; (c) total deformation diagram

The directional displacement result in X and Y direction can specify the accuracy of the positioning as on of the objectives that require to be fulfilled from this research work. Figure 4.20 illustrates the directional displacement at X-direction for both loaded and unloaded condition models. Referring to the geometrical design, 10 micron tolerance between the Workpiece and clamping edge was modelled. The frictional contact gap was defined at this area in the FEA model whilst after filling the gap, the edge of the jaw and the workpiece become in contact. Since the applied load still is active, the clamping pressure will be occurred while these two faces are in contact. Analysing the displacement for unloaded condition model, the maximum x-directional displacement of 0.1 mm was achieved. As for loaded conditional model, the maximum displacement in X-direction was calculated 10 micron in which proves the total displacement required to fill that gap as aforementioned earlier.

Comparing the two results as illustrated in Figure 4.20(c), it shows that the clamping jaw in loaded condition displaces about 10 micron and pushes the workpiece edge towards the center line, whilst initial contacting point in X direction was occur.

It can be confirmed that the jaw and the flexure hinges are successfully made the compliant displacement required to position the workpiece in the centre of the spindle without any structural failure. The result in the unloaded condition model also can prove that the structural geometry at self-centring jaw can achieve maximum 0.1 mm gap displacement clearance between the clamping edge and workpiece. Since the accuracy in X-direction for self-centring was evaluated, the displacement in Y direction needs to be examined for positioning accuracy purposes.
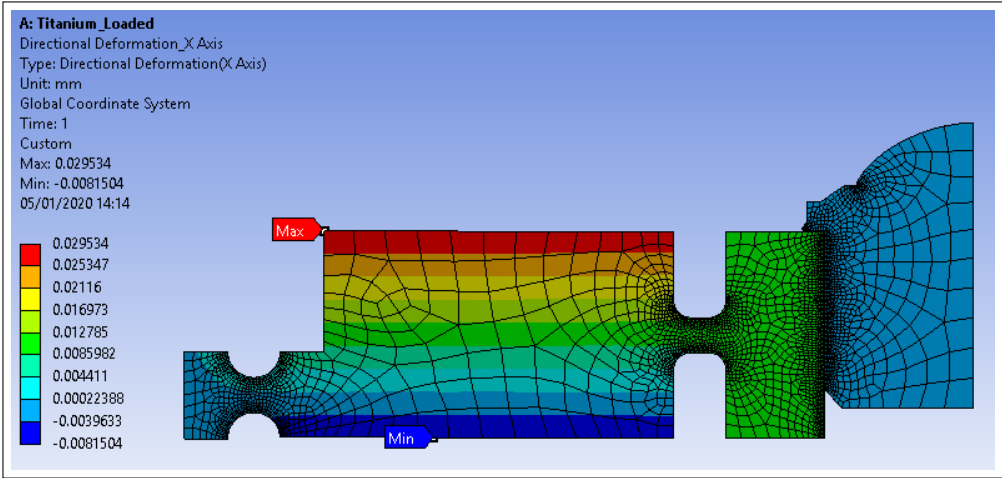
(a)
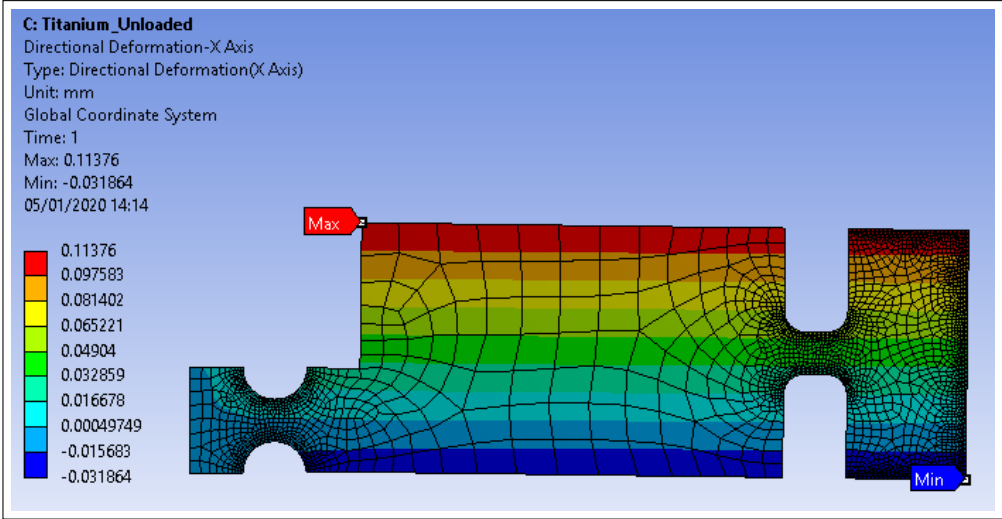
(b)
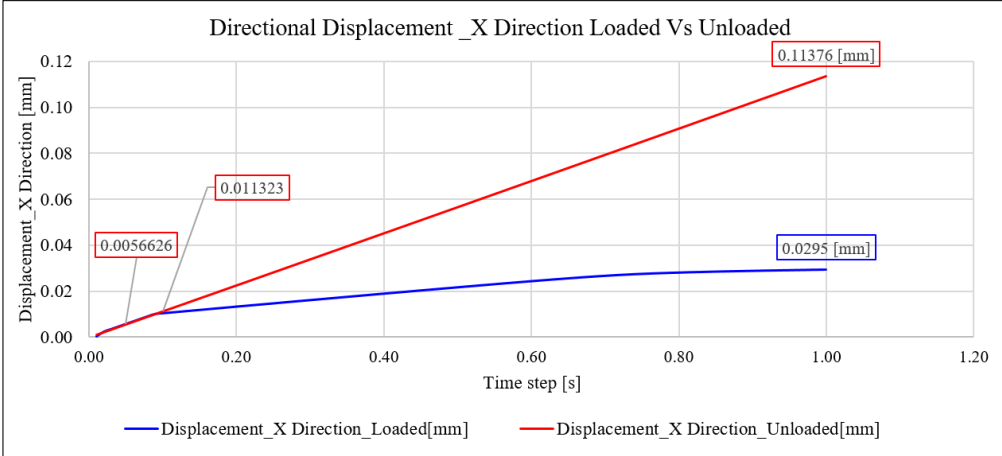
(c)

Fig. 4.20 Directional displacement, X-direction, loaded Vs unloaded: (a) loaded; (b) unloaded; (c) X-directional deformation diagram
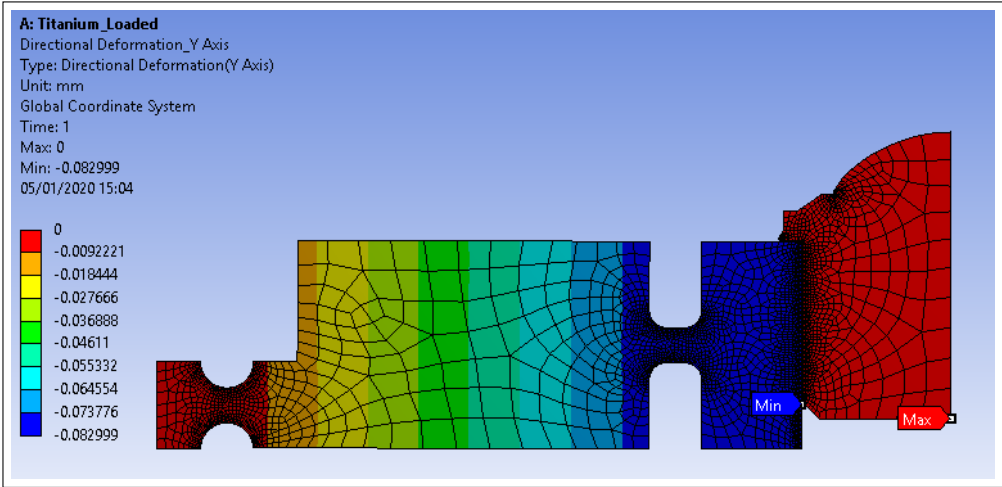
(a)
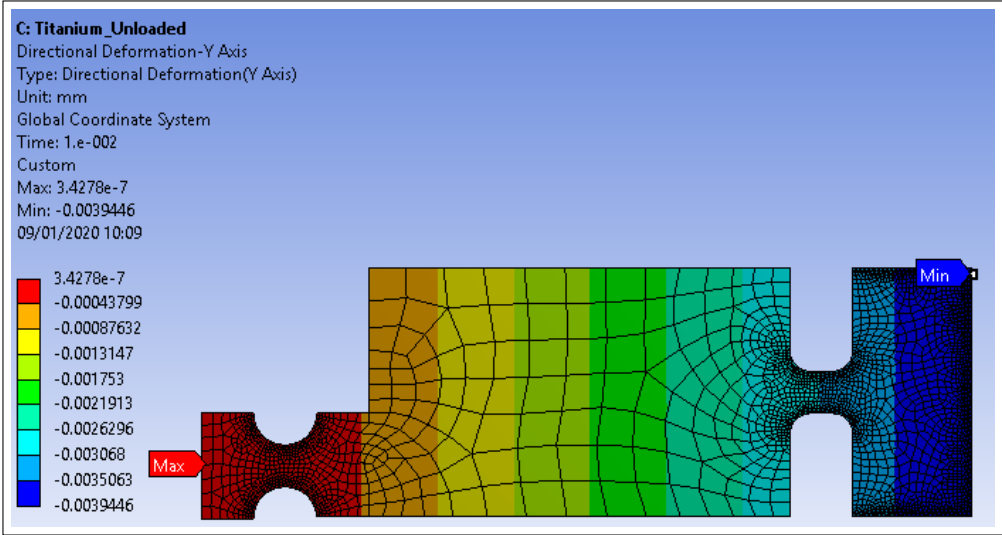
(b)
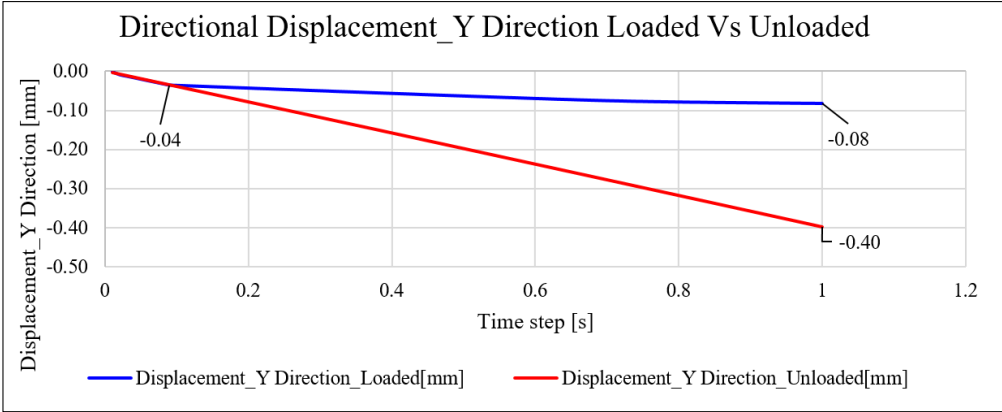
(c)

Fig. 4.21 Directional displacement, Y-direction, loaded Vs unloaded: (a) loaded; (b) unloaded; (c) Y-directional deformation diagram

As per designe specification, the chuck was invented for the purpose of a workpiece holding with zero displacements in Y-direction. Thus, a fixed support boundary condition was applied for the workpiece, while The displacement at this particular part assumed to have no displacement. Interpreting the result shown in Figure 4.21, the displacement of the workpiece indicates zero displacements in the Y direction for the loaded condition. However, the maximum directional displacement of 0.08 mm can be observed in the result which can be realised as a slipping phenomenon at the contact region between the jaw and workpiece. It is thought that this might be considered as a disadvantage. It is also meriting to emphasise that the 2D FEA simulation with half symmetric workpiece model might cause this issue. In this particular issue, a 3D FEA simulation required to investigate about this particular issue which will be explained in the following sections. Nevertheless, utilising the flexure hinge features for clamping and precise positioning still poses high value of advantageous in this invention.

4.6.4   Contact Pressure

As a result, contact pressure analysis can define the final clamping pressure between the jaw and workpiece. As illustrated in Figure 4.6, for design evaluation of flexures FL2 and FL4, the functionality of the clamping force in both stage01 and stage 02 need to be studied.

Figure 4.22 shows the contact pressure result and diagram in the loaded condition model. Interpreting the result observes that the contacts between the jaw and workpiece can be divided into three zones. According to the result shown in Figure 4.22b, the first zone is that, when the inner edge of the jaw from the resting position reaches the outer face of the workpiece by moving through a 10 micron gap.

At these steps, the contact pressure is counted zero value while there is no physical surface contact yet. The second step is the initial contact zone, when the inner front point of the jaw touches the workpiece's outer face, as it progress into the stage01. At this zone as visually can be seen, the pressure has the variety value of 0-25 MPa where flexure type FL2 assumed
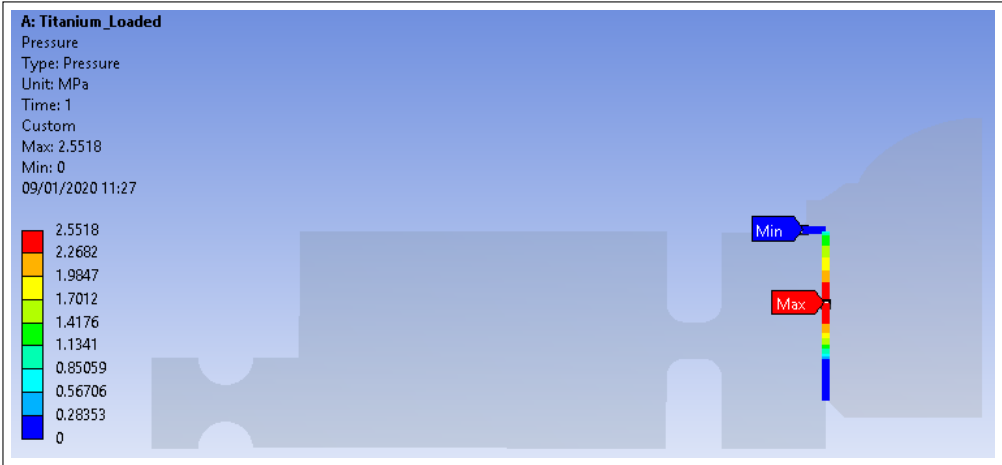
(a)
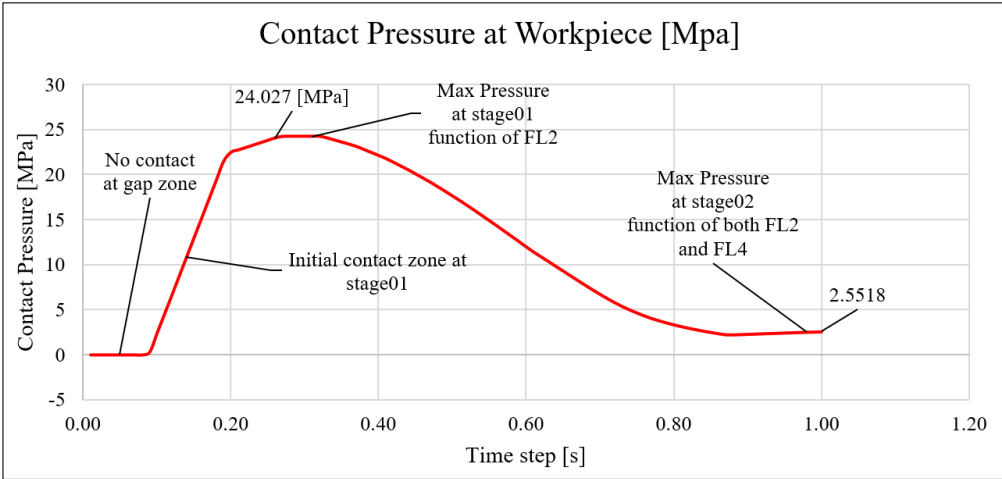
(b)

Fig. 4.22 Contact Pressure and clamping force: (a) loaded contact pressure; (b) contact pressure diagram

to make the self-centring function. From the graph, It can be observed that the status of the surface contact enters into a new zone where the pressure dropped significantly until it reaches the steady-state at 2.5 MPa. At this zone, as per specified in stage02 of the design, the flexure type FL4 assumed to provide the clamping force and stays constant until the input applied force is released. Therefore, the clamping pressure of the system with a 2D simulation model can be defined as maximum pressure of 2.5 MPa at the contact surface between jaw and workpiece. Since the result evaluated acceptable value in conact pressure with 2D simulation, a 3D FEA

simulation is required to specify precise contact forces for final evaluation and validation which will be explained in the following sections.

4.6.5 Safety Factors and Maximum Tensile Stress

Investigating the safety factor (SF) of the design as shown in Figure 4.23, illustrates the minimum and maximum value for both loaded and unloaded condition models.

Analysing the SF based on material yield strength, under the applied load of 1 MPa, calculated minimum value of 1.78 for unloaded condition and 5.98 for the loaded condition. Both factors exceed the minimum value required for the safety of one. The SF in the unloaded condition designed to be stronger as approximately twice as the applied load. The loaded condition model also has much promising SF, whilst is stronger as five times as applied force. This result base can prove that when the chuck is active during the machining process, the strength of material based on the geometry design, is capable of taking all the loads, including cutting force and rotational moments. Both minimum SF is indicated around the area of Flexure Type FL2 as expected. Despite the SF for 2D FEA of the design at flexures calculated an acceptable values, the 3D FEA simulation is required to clarify more safe and accurate factor for the design. In the next section, the safety factor will be examined.

4.6.6 Stress-Strain Diagram

Finally, the accuracy based in geometry design, under the specific load, can be determined by defining the stress-strain graph as illustrated in Figure 4.24. The elastic deformation described as strain ε versus the stress σ , under applied load for both loaded and unloaded condition models. The graph shows the ratio of the maximum principal stress versus maximum principal strain. As a result, it can prove that the principal material strain has a proportional and linear behaviour activity to the elastic module according to hook law. All the deformations effected in the elastic region and the stress are within the elastic limit strength of material zone according
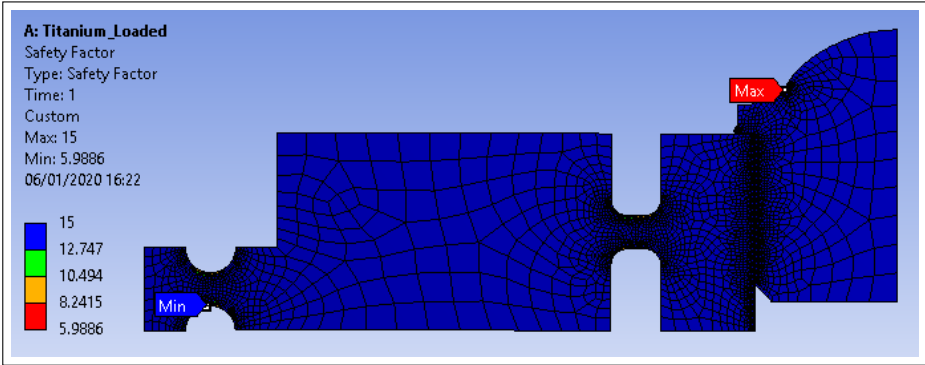
(a)
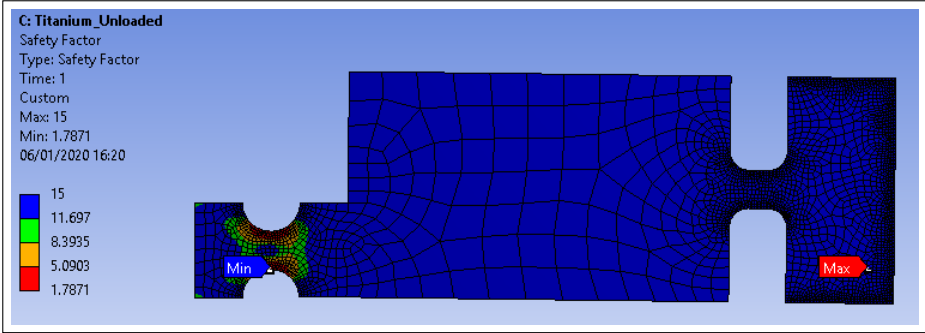
(b)
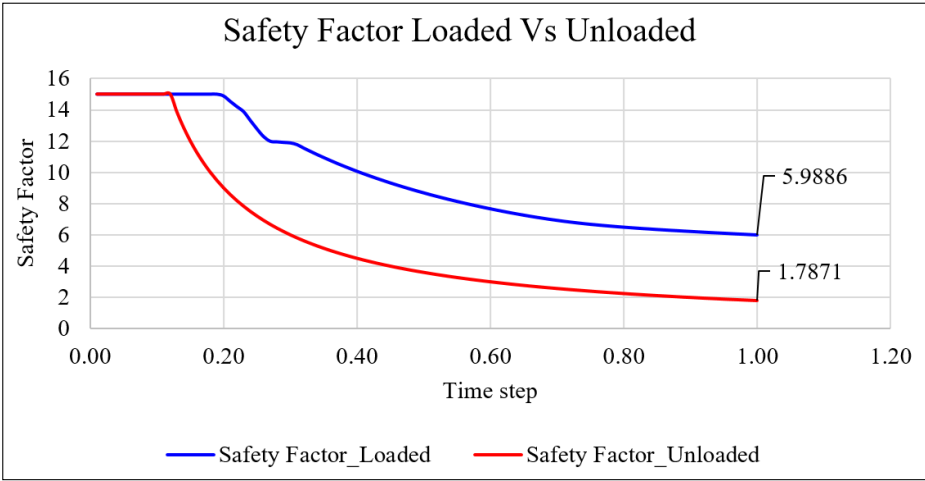
(c)

Fig. 4.23 Safety factors: (a) loaded safety factor; (b) unloaded safety factors; (c) safety factor loaded vs unloaded diagram

to the Hook laws. The maximum value of elastic stress and elastic strain of 137.43 MPa and 0.0014 mm respectively were calculated for loaded condition model and, the value of 520 MPa and 0.005 mm respectively were calculated for the unloaded condition model.

Table 4.7 2D FEA results data

	Total Deformation [mm]	Equivalent Stress [MPa]	Maximum Principal Stress [MPa]	Maximum Principal Strain [mm]	Directional Deformation X axis [mm]	Directional Deformation Y axis [mm]	Normal Stress Workpiece [MPa]	Normal Stress Workpiece &Flexure [MPa]	Min Safety Factor
Loaded	0.08	155.29	137.43	0.0014	0.02	-0.08	2.26	136.3	5.98
Unloaded	0.41	520	520.09	0.005	0.1	-0.03	-	519	1.7
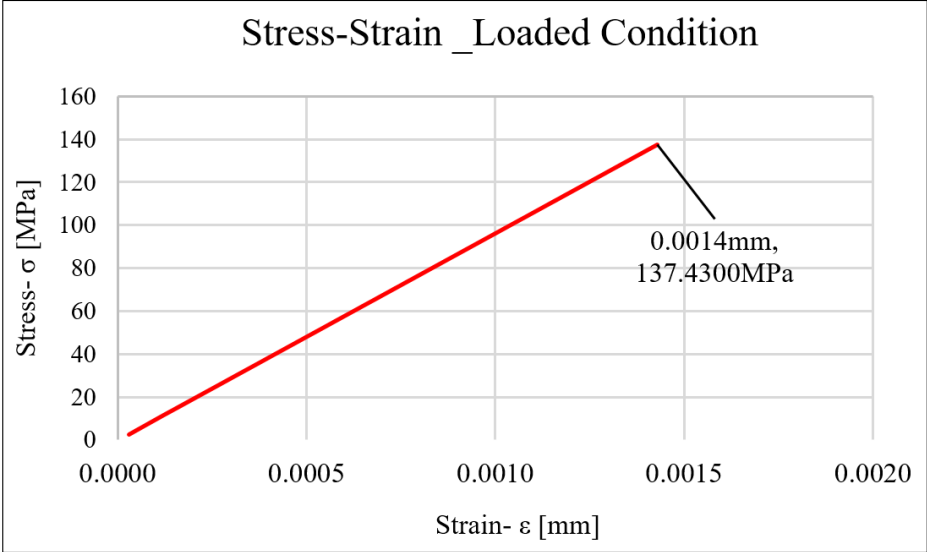
(a)
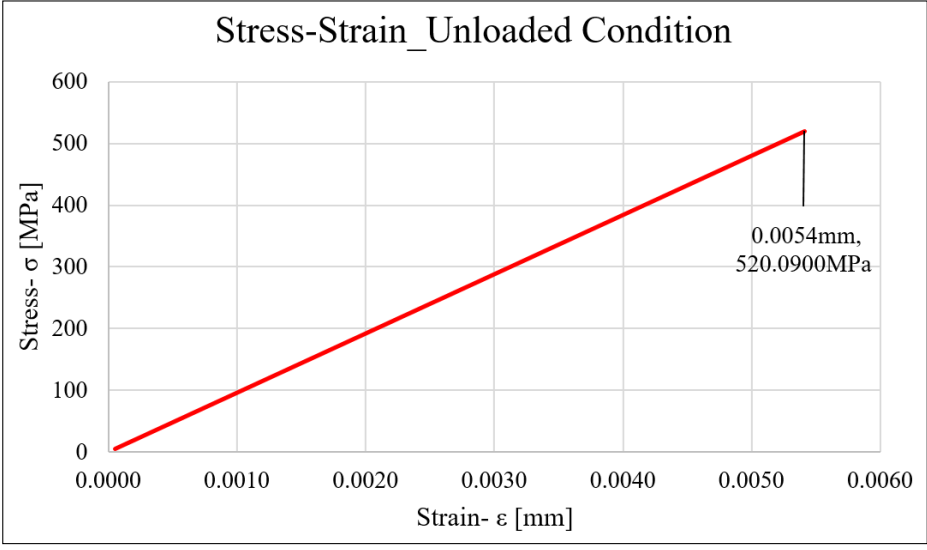
(b)

Fig. 4.24 Stress-strain diagram: (a) loaded condition; (b) unloaded condition

Thus, the conclusion can be made, that the accuracy of the geometry design of the jaw based on elastic deformation, for the loaded condition model is one micron, and five microns for the unloaded condition model, specifically under the designed applied load of 1 MPa. the simulation results data taken from 2D FEA analysis of the flexure type FL2 and FL4 can be seen in Table 4.7. In the next following section, the effect of load in the design of flexure with 3D FEA simulation will be analysed.

4.7   Three Dimensional Analysis

4.7.1   3D FEM for Flexure Type FL2 and FL4

Since the 2D simulation investigated the initial overview of the geometry design, a 3D FEA analysis is essential to finalise the verification of the entire design of the smart chuck. At this stage, a 3D FEA simulation was employed to evaluate and verify the flexure design. Also, in this section, the verification of the design for flexure type FL3 and FL1 is explained. Similarly, as 2D simulation, two scenarios of loaded and unloaded conditions were utilised. As per design specification, the chuck mainly designed to hold the circular shapes. Contact lenses mould insert was used as workpiece for loaded condition simulation model as. Moreover, a similar setup as the 2D environment and boundary condition such as applied load, Fixing supports and Material were assigned for this particular 3D simulation.

The 3D CAD model and geometry of the chuck was imported into Ansys version 19.1. After applying proper meshing sizes setting up the boundry condition, the FEA simulation was run, and the solutions for the particular criteria of results were evaluated. Figure 4.25 illustrates the 3D FEA modelling setup of the smart chuck. The frictional contact(A) region with 0.3 friction coefficient between the jaw inner face and lens outer face with overall $5\mu m$ (2.5 μm each side)tolerance were applied. Fixed support (C) applied at back face of the body of the

whilst it is attached to the vacuum chuck and the magnitude load pressure component of 1 MPa applied to the jaws in -Z direction.

Fig. 4.25 Flexure FL2, FL4 3D FEM setup

4.7.2   3D FEA Results

Similarly, as 2D Simulation, the interpretation of the result was carried out based on several characteristics such as deformation, equivalent maximum stress, maximum principal stress, maximum principal strain. The safety factor and stress-strain chart also were provided to define the accuracy of the clamping system with regards to positioning and stiffness.

- **Equivalent Stress**

Analysing the result shows the maximum value of 892.21 MPa for the model with the unloaded condition and 90.02 MPa for the loaded condition. Comparing the results with 2D simulation, it shows that von-misses increased in unloaded condition and decreased in the loaded condition. As illustrated in Appendix B.5(b), the equivalent stress values at FL2 in the unloaded condition model indicates the maximum value calculated. However, this value still is within the yield strength of the material and can be considered as fully functional feature. In the loaded condition, the equivalent stress shown even much favourably value as it has decreased in comparison to the 2D simulation. Appendix B.3(b) shows the equivalent stress chart for loaded

condition that proves the proportionality of the stress within elastic limit according to Hook Laws.

- **Total Displacement**

As shown in appendix B.5(a) and appendix B.6(a), total deformation result assessed displays the maximum magnitude value of 0.85 mm for unloaded condition and 0.02 for the loaded condition. According to the result, the maximum value of displacement in the unloaded condition shows a significant increase of 80% and a significant decrease of over 100% with compare to 2D simulation. This changes can describe the stiffness and flexibility of the flexures at this area of the geometry design. the total value of displacement are mostly occurred in applied load direction which is Z-direction. Also, since the disadvantage of sliding phenomenon in 2D simulation was detected, the 3D sliding shows less displacement value in the Z-direction. Thus, the conclusion can be made that the flexure FL2 and FL4 are capable of functioning on both loaded and unloaded condition with regards to self-centring, stiffness and precise positioning the same as 2D simulation.

- **Directional Displacement**

For directional displacement assessment in this model, the overall geometrical clearance of 2.5 μm between the circular outer surface of the jaw and the outer surface need to be filled to maintain the self-centring and clamping purposes. As illustrated in Figures 4.26 and 4.27. The maximum directional displacement of 0.2 mm in X-direction was calculated for unloaded condition model by means that the jaw can hold the workpieces with the clearance between a range of (0-0.2 mm) without affecting the stiffness in the flexure hinges. This result is quite promising and can prove the variability and flexibility of the clamping system for the freeform surfaces in this design.
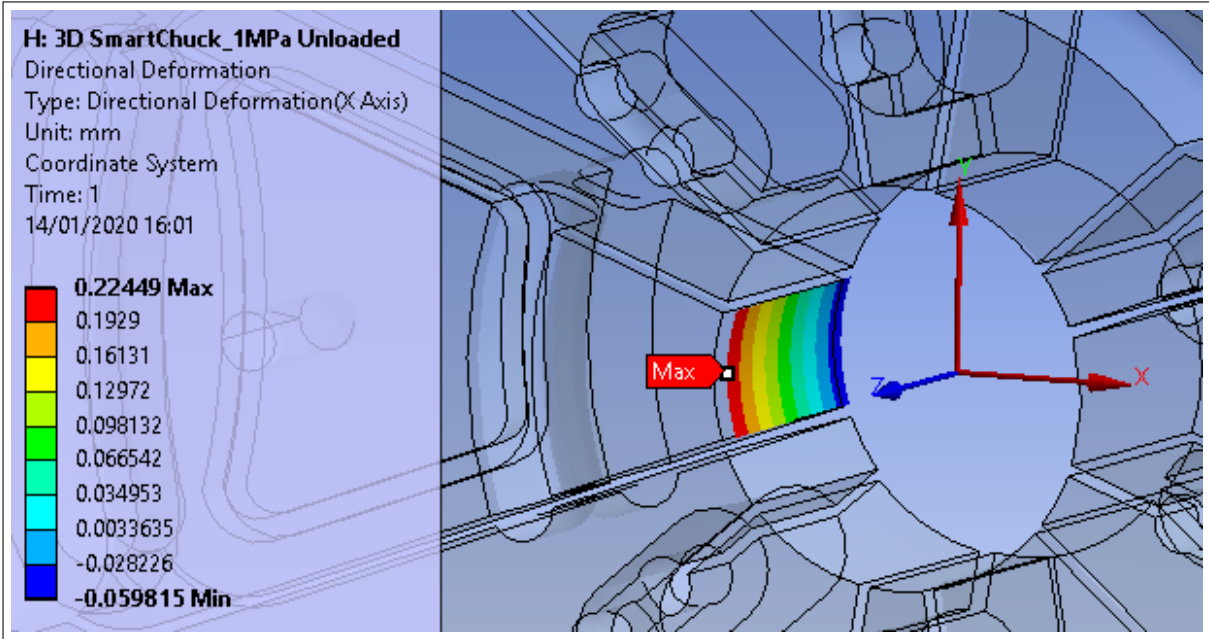
Fig. 4.26 Flexure FL2, FL4 3D FEM directional displacement
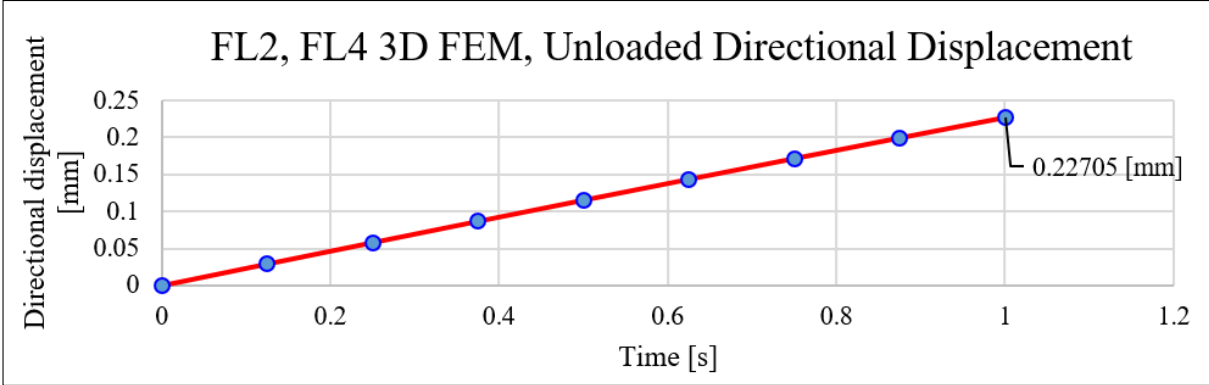
Fig. 4.27 Flexure FL2, FL4 3D FEM directional displacement diagram

- **Contact Pressure**

The contact pressure between the jaw and the workpiece in 3D FEM shows non-linearity, similarly as 2D simulation. Nevertheless, according to the result, the contact pressure at the contacting point has specific stability in compare to 2D simulation. The pressure also can be divided in three zones, as the initial, secondary and permanent region. Figures 4.28 and 4.29 indicate the statues of the contacting surface and the pressure values over the simulation

interval time. From the result it can be found that, the maximum contact pressure value of 31 MPa calculated in the jaw at the back face surface and average range between 3 to 10 MPa at the middle of the jaw's contacting point. The clamping force is sufficient for a permanent and secured workpiece clamping while not losing stiffness during the ultraprecision machining process.
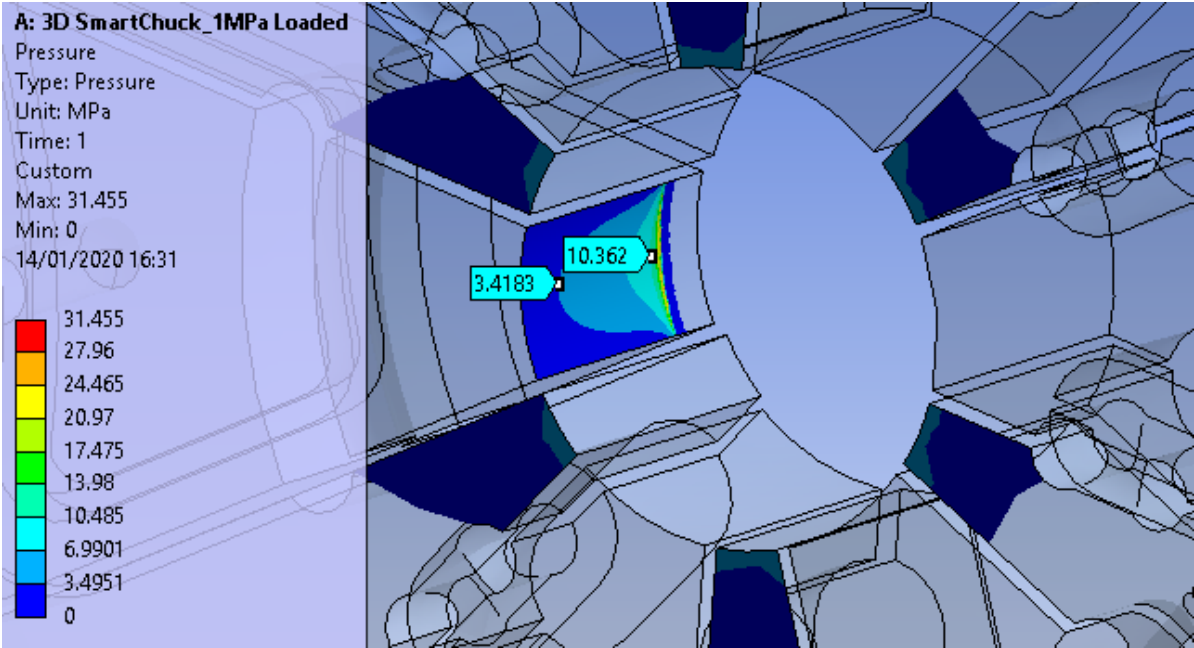
Fig. 4.28 Flexure FL2, FL4 3D FEM contact pressure
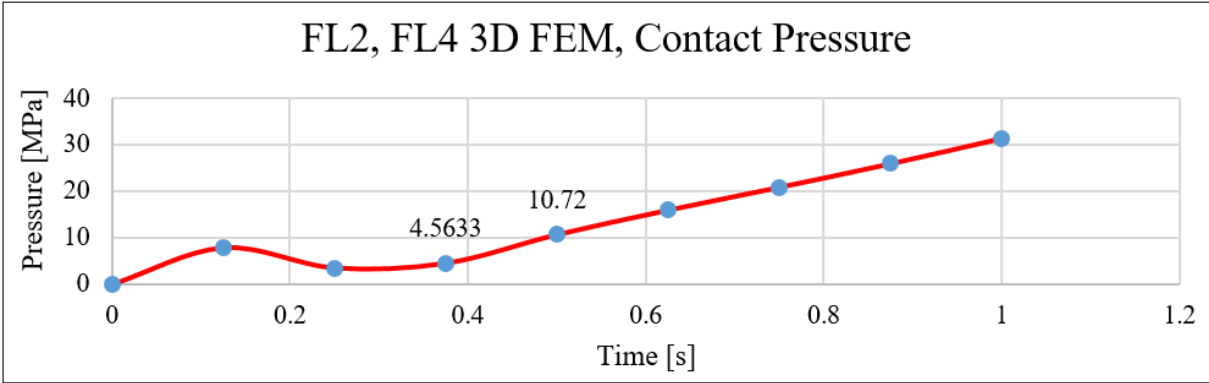
Fig. 4.29 Flexure FL2, FL4 3D FEM contact pressure diagram

- **Stress-Strain Diagram**

The stress-strain chart, as illustrated in Figure 4.30, shows the accuracy of the chuck for the loaded condition. Maximum principal stress indicates the value of 57.32 MPa and principal elastic strain value of 0.0005 mm. Maximum principal stress in the unloaded condition calculated 906.1 and principal strain of 0.0091. The decision can be made that the unloaded condition has critical status as the maximum value is nearly approaching the material maximum elastic limit and yield strength. Nevertheless, in the unloaded condition, for safe functioning, the total displacement of the jaw needs to be limited by half to maintain the safe stress and strain accuracy. The Principal stress and strain and its chart for the unloaded condition have been illustrated in appendix B.5. Interpreting the accuracy of the loaded condition as illustrated in Figure 4.30, shows very stable status as the principal strain of the structure calculated sub-micron value. Finally, it can prove that FL2 and FL4 in the self-centring jaw are fully functional within the elastic limit region of the material.
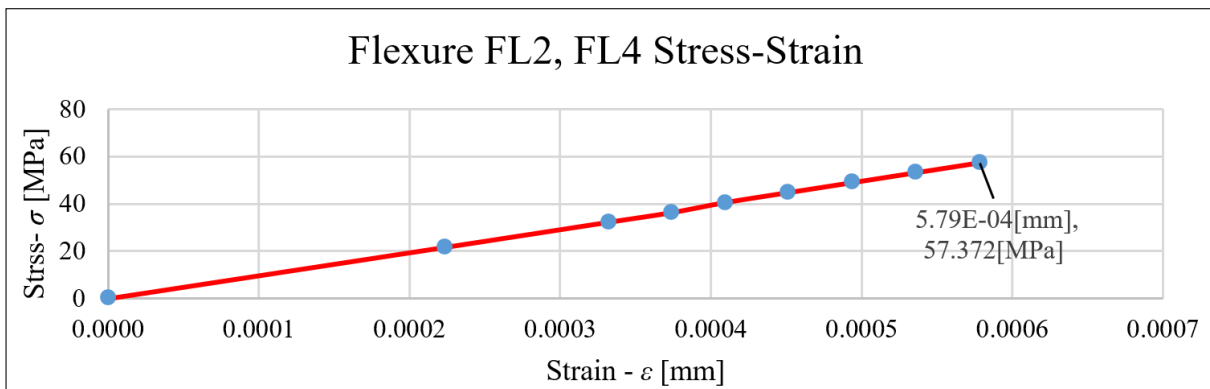
Fig. 4.30 Flexure FL2, FL4 3D FEM stress-strain diagram

- **Safety Factor**

Investigating the safety factor (SF) of the design for flexure type FL2 and FL4 with a 3D FEM method, as shown in Figurer 4.31, describes the minimum value for both loaded and unloaded condition. Based on the strength of material yield stress under the specific load of 1 MPa, the minimum safety factor value of 1.04 was calculated for unloaded condition and 10.33 for the loaded condition. Comparing the results as shown in Table 4.8 with the 2D simulation,

the minimum SF for unloaded condition shows a decreased value and increased in the loaded condition. As explained in the previous item, the principal elastic strain has a critical value in which has a risk to make the jaw dysfunctional under the unloaded condition. As can be seen, the minimum SF value for the unconditional condition is still within the material elastic limit, however it may subject to fail if additional unexpected loads were applied to the structure. The SF in loaded condition shows the ideal value while the structure responded as fully capable of functioning to take the loads within the material stiffness and elastic limit. Figure 4.32 shows the SF chart for the loaded condition with 3D finite element modelling methodology.

(a)   (b)
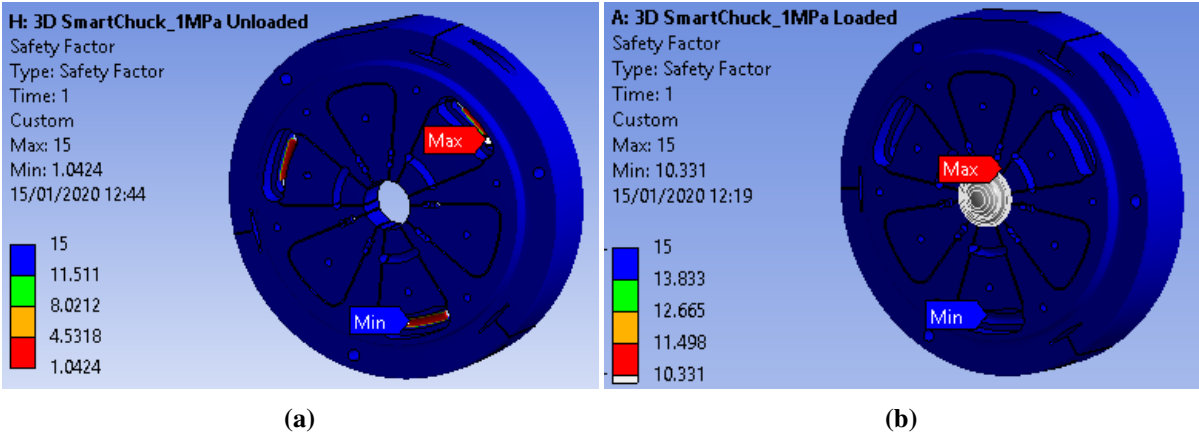
Fig. 4.31 Safety factors 3D FEM FL2,FL4: (a) safety factor unloaded; (b) safety factor loaded
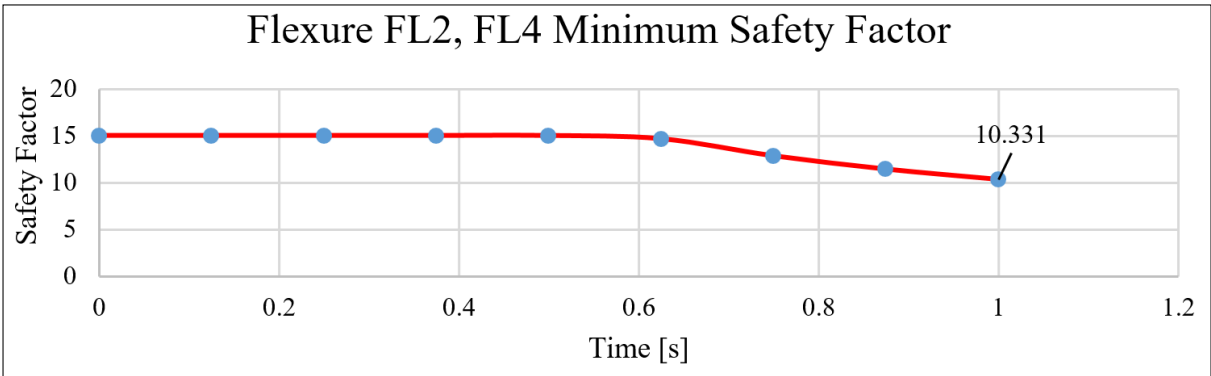
Fig. 4.32 Flexure FL2, FL4 3D FEM loaded condition safety factor

Table 4.8 Flexure FL2, Fl4- 2D vs 3D FEM results data

		Total Deformation [mm]	Equivalent Stress [MPa]	Max Principal Stress [MPa]	Max Principal Strain [mm]	Min Safety Factor	Titanium Yield Strength [MPa]
2D FEM	Loaded	0.08	155.29	137.43	0.0014	5.98	
	Unloaded	0.41	520	520.09	0.005	1.7	930
3D FEM	Loaded	0.02	90.02	57.32	0.0005	10.33	
	Unloaded	0.85	822.91	906.1	0.0091	1.04	

4.7.3 3D FEM for Flexure Type FL1

For design verification of the flexure type FL1, a 3D finite element analysis using Ansys19.1 was employed. According to the theoretical description as illustrated in Figure 4.13, two input prescribed displacement of 30μm was determined for modelling setup, as shown in Figure 4.33. This prescribed displacement presents the two reaction forces which considered to function as a coupling feature that can maintain equal force toward each other. Fixed support was applied at the touching point between the back face of the smart chuck and the vacuum chuck. As demonstrated in the theory of this flexure, the clamping force and directional displacement is the key characteristic. For simplification and simulation efficiency, the 3D FEM was set up as an individual part without assembly, therefore the spindle and the vacuum chuck excluded from the simulation to study maximum large deformation and stress in output as explained in the theoretical section. Since the simulation process was done, the key solutions in several measures such as directional deformation, maximum principal stress, equivalent maximum stress, total deformation and safety factor were studied. Also, the stress-strain chart to determine the final accuracy of the flexure was created. Reading the results as shown in appendix B.9, the maximum equivalent stress of 274 MPa, maximum total deformation of 30μm, maximum principal stress of 300 MPa and maximum Principal elastic strain of 0.0029 mm were calculated. As a result, these values all are acceptable and are within the elastic limits of the material properties. However, considering the micro-positioning at the output, from the result, it can be

seen that there is an uncertainty in structural deformation. The deformation at the clamping point is not homogenous while the back face of the coupling calculated larger displacement than the front face of the flexure. Having looked at the result, it has been found that front face of the coupling has less DOF than the back face, therefore, the displacement across the flexure compliant axis is expected to be varied. This phenomenon can be challenging and might cause the ovality in such can only have a point tp point clamping instead of permanent surface to surface contacting between the inner diameter of the smart chuck and outer diameter of the vacuum chuck.
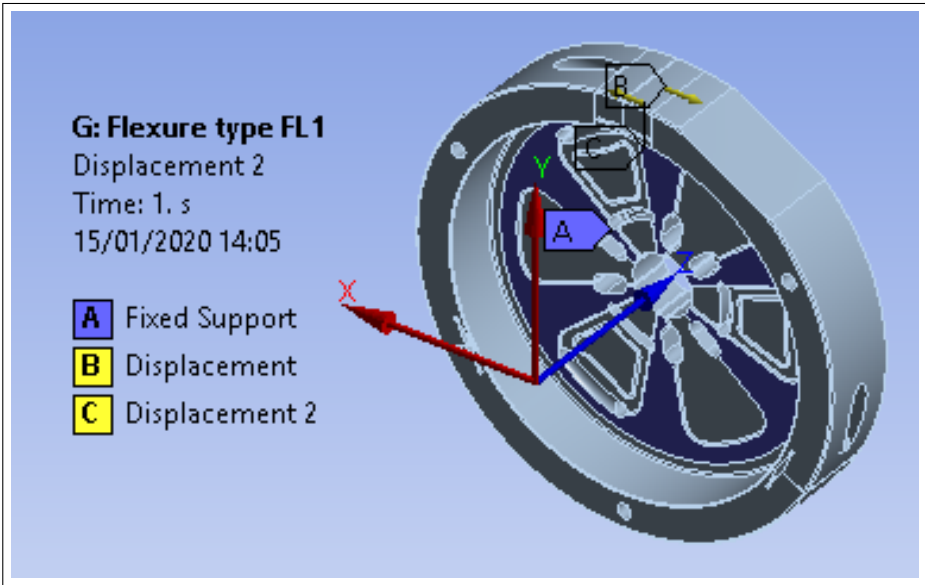
Fig. 4.33 Flexure FL1, 3D FEM setup
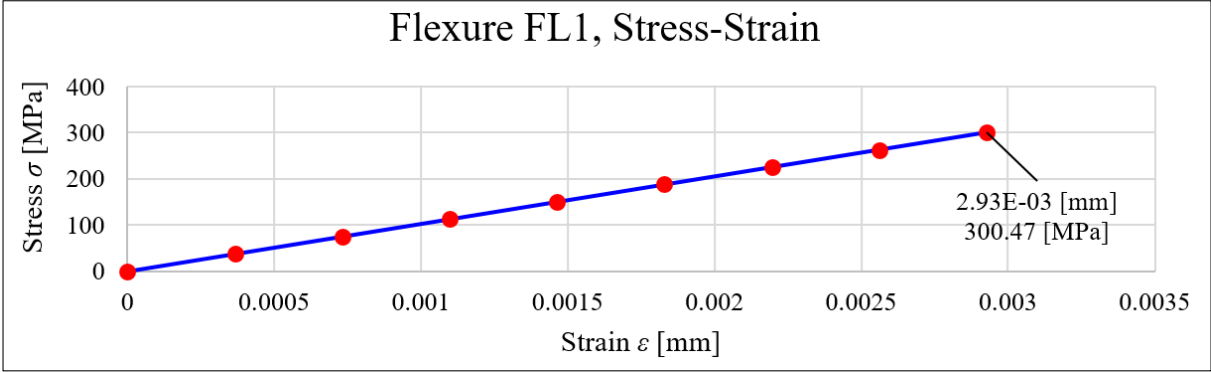
Fig. 4.34 Flexure FL1, 3D FEM Stress-Strain diagram
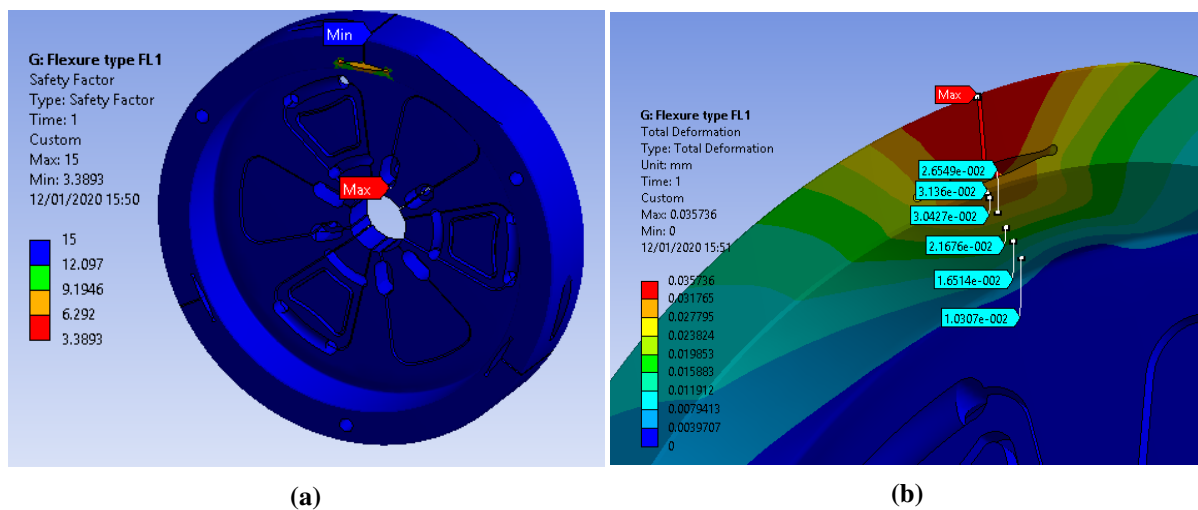
Fig. 4.35 FL1 3D FEM safety factor and directional displacement: (a) safety factor; (b) Directional Displacement

In order to study the deformation of the flexure output surface at the contacting point between the vacuum and smart chuck, a directional displacement prob was produced. According to result as illustrated in Figure 4.35(b) and Figure 4.36, the directional displacement in Y-direction towards the centreline of the spindle calculated a range of elastic deformation vale of 0-30 micron. The average value at the midpoint between the front and back face of the coupling calculated the value of 15 microns in which can confirm the approximate acceptable value for displacement of the flexure output at this particular flexure. Hence, the accuracy of the positioning at this particular flexure can be varied, according to the result.

Figure 4.34 shows the stress-strain chart of flexure type FL1 in which states the accuracy of 3 microns principal elastic strain over 300MPa principal maximum stress at this type of flexure. The Minimum SF value of 3.3 was calculated for FL1 as shown in Figure 4.35(a) and Figure 4.37. It can be observed that the distribution of the curve is nonlinear, however, the minimum value is still within the elastic limit of the material property.
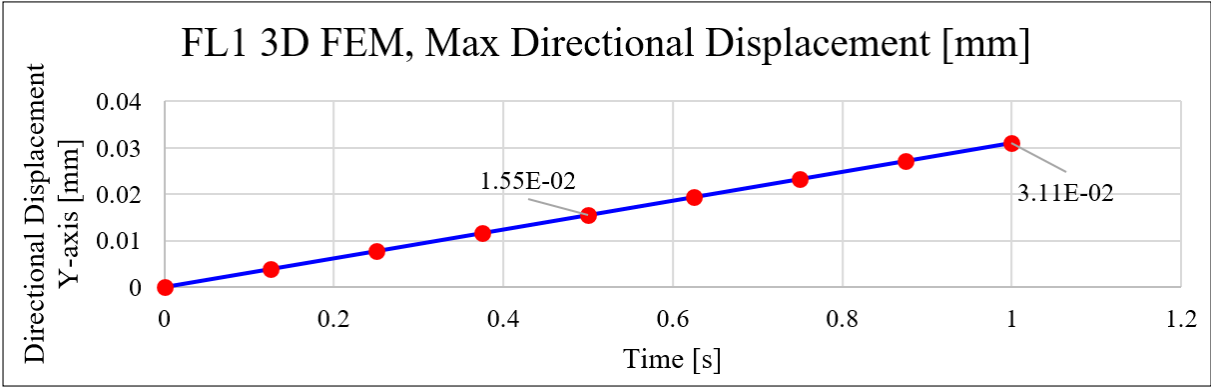
Fig. 4.36 Flexure FL1, 3D FEM directional displacement diagram
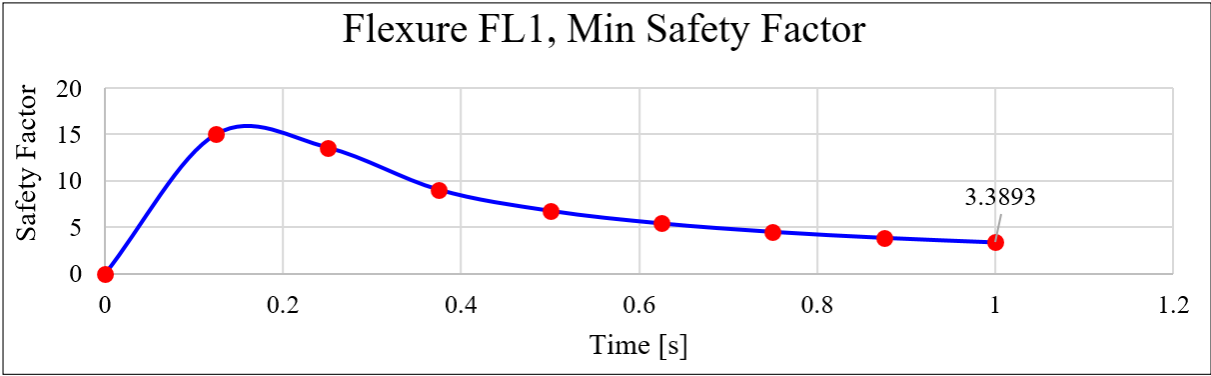
Fig. 4.37 Flexure FL1, 3D FEM safety factor

4.7.4   3D FEM FL3

The structural analysis for flexure type FL3 was carried out using 3D finite element methodology in Ansys19.1. According to the theory of the flexure type FL3 design, the flexure functions based on torsional load created by centrifugal force in a rotational position. For the FEM model setting up, as illustrated in Figure 4.38, fixed support applied to the back face of the smart chuck's body which has a touching surface to the vacuum chuck in the diamond turning spindle.

A rotational speed of 210 rad/s which equal to 2,000 rpm was applied to the inner diameter of the smart chuck. It is worth to point out that for more trustworthy results, the self-centring jaws excluded from the simulation by applying for the fixed support.

Whilst the simulation was done, the results were studied in several key characteristics such as maximum principal stress, total deformation, equivalent maximum stress, equivalent elastic strain and principal elastic strain. The SF and stress-strain charts also interpreted for determination of the self-locking accuracy . Analysing the results as illustrated in appendix B.10, proves that the self-locking jaws are subjects to a rotational displacement from their flexure link to the body as expected and explained in the theory section and as illustrated in Figure 4.12 .
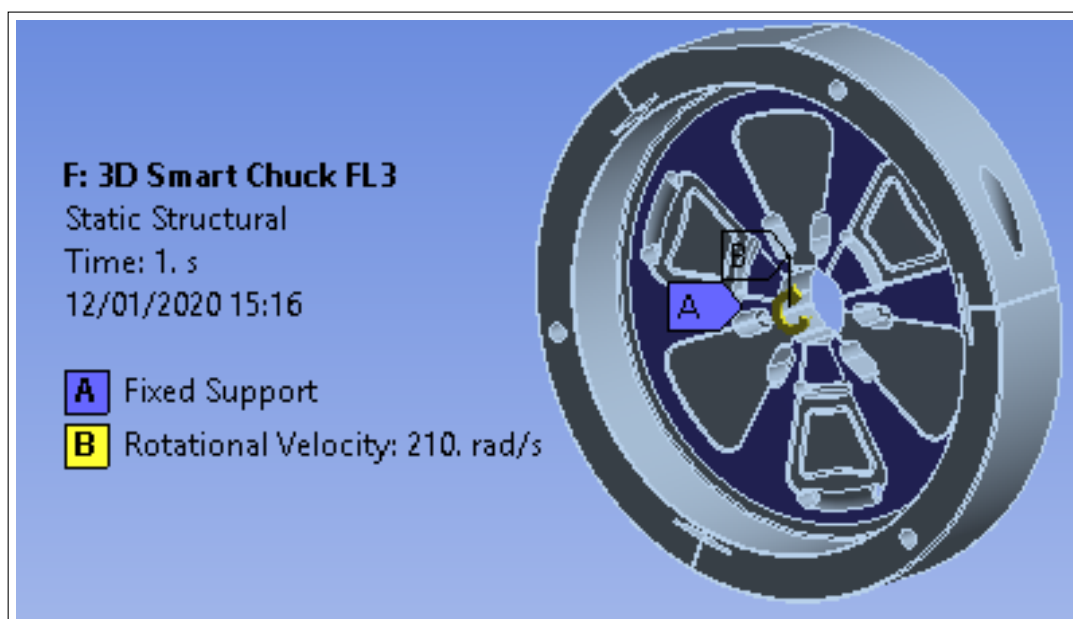
Fig. 4.38 Flexure FL3, 3D FEM setup

This can also confirm the Idea of employing the torsional loads in the flexure for purpose of micro-positioning in ultraprecision machining. With a closer sense of inspection, it can be seen that the maximum stress and strain are effected in the area where the flexure is linked to the body of the smart chuck, and the maximum displacement has occurred above the center of mass position in the self-locking jaw which, caused by centrifugal forces. From the result, the maximum equivalent stress of 112.58 MPa, maximum total deformation of 5.16e-02 mm, maximum principal stress of 92.319 MPa and maximum Principal elastic strain of 1.09e-03 mm were calculated.

(a)   (b)
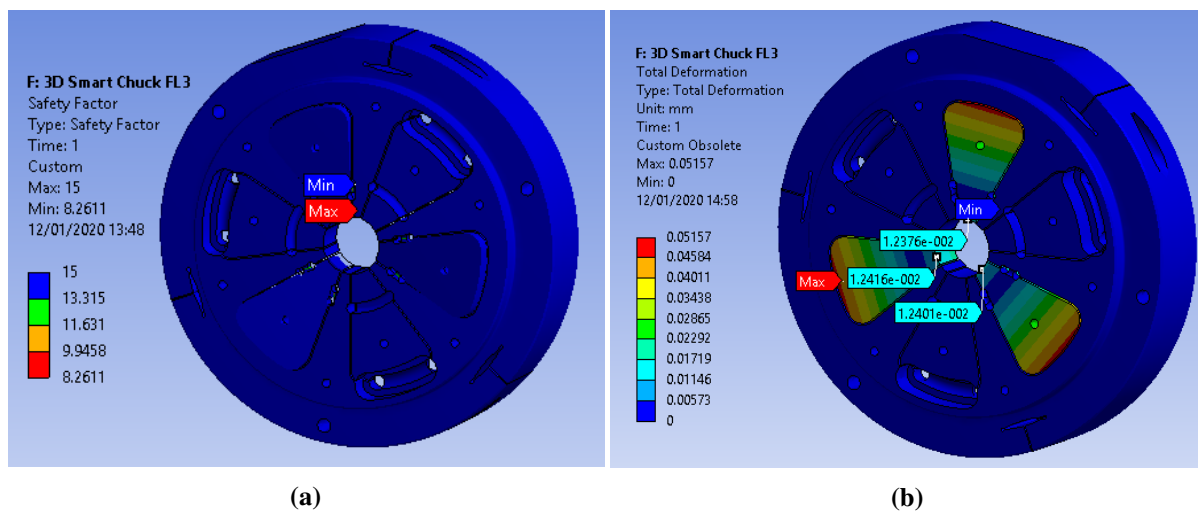
Fig. 4.39 FL3 3D FEM safety factor and directional displacement: (a) safety factor; (b) directional displacement

The calculated values for those measures, are satisfactory and within the elastic limit and yield strength of material properties. additionally, to verify the purpose of self-locking, the directional elastic deformation analysis at the contacting point between the workpiece and the locking jaws can specify the maximum displacement toward the lateral direction of the spindle centre. According to the result shown in Figure 4.39(b), the maximum directional displacement calculated the value of 12 μm in which can be increased by acceding the rotational speed of the spindle. Since the clamping jaws held the workpiece in the position, the locking jaws also can secure the holding in the position on both CCW and CW rotation directions. At this stage, it is very important to assure the flexure structural capability when the UPM process requires to run at various speed. The current result as for SF analysis illustrated in Figures 4.39(a) and 4.41, indicates the minimum value of 8.2 in which can confirm that the current structural design of current Flexure type FL3 is stiffened enough to take various loads where it needs to be applied during the ultraprecision machining.

Figure 4.40 shows the stress-strain chart of flexure type FL3 in which affirms the accuracy of 1.09e-03 principal elastic strain over 92.319 MPa principal maximum stress. The result of this particular flexure proves a very successful performance that can contribute the knowledge and

innovation across the ultraprecision machining workpiece clamping and maintaining precise positioning.
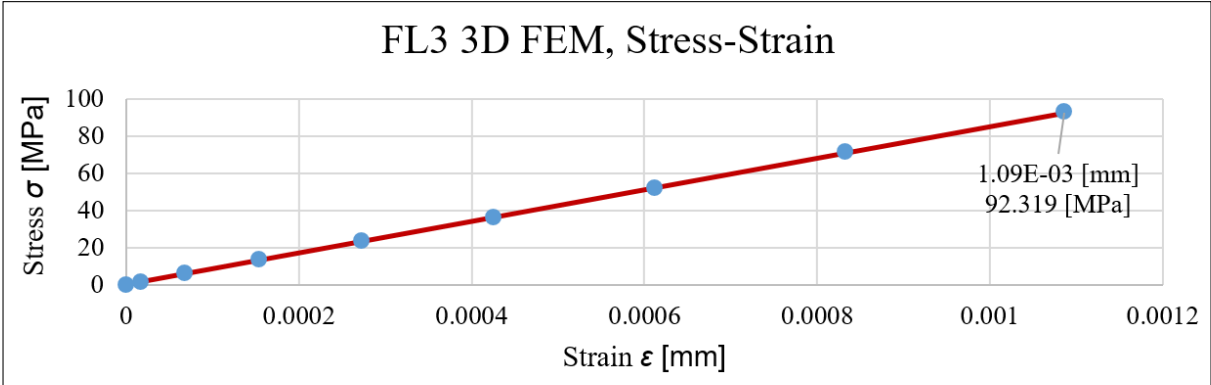
Fig. 4.40 Flexure FL3 3D FEM stress-strain diagram
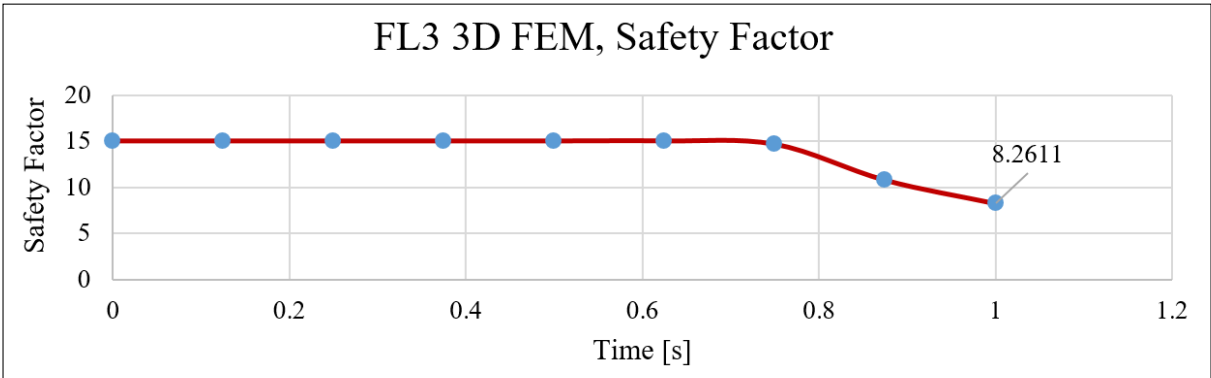
Fig. 4.41 Flexure FL3, 3D FEM safety factor

4.8 Implementation and Manufacturing Characteristics

4.8.1 Chuck Manufacturing

Whilst the design of the chuck was completed the technical drawings and manufacturing process planning produced. The technical drawings and details of the chuck design include all tolerances and manufacturing details have been attached in appendix B.1 and B.2. According to the design of the chuck, the manufacturing process such as wire EDM machining, milling and lath process were required. Since the design is rated as a precision complex part, the

implementation of the design becomes very challenging. Thus a capable manufacturer was selected for the final implementation process. Also, a rapid prototyping methodology was used before final manufacturing take place. Figure 4.42(a) shows the 3D printed part using ABS material. The manufacturing project plan was produced and the tendering procedure was set appropriately. After the manufacturing process completed, the dimensional checking process was carried out to examine the geometrical quality of the part. Figure 4.42(b) and 4.42(c) illustrate the final implemented part of the smart chuck.

| (a) | (b) | (c) |
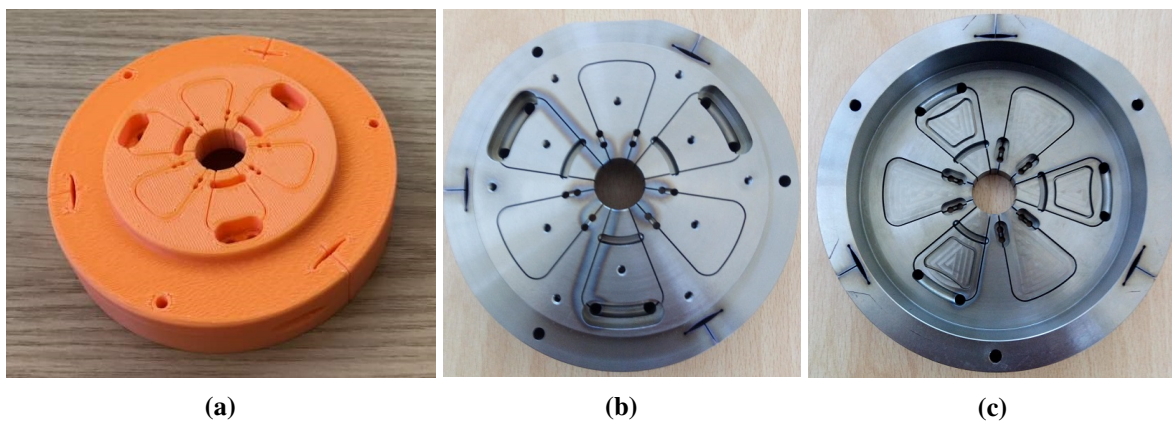
Fig. 4.42 Photograph of rapid prototype and manufacturing of smart chuck: (a) 3D printed part; (b) final manufactured part, front view; (c) final manufactured part, back view

4.8.2 Implementation Challenges

After the chuck installed into vacuum chuck located in the spindle nose at diamond turning machine, the pulling mechanism was examined by activating the vacuum chuck. At the first stage, the pulling for the 3D printed part with a vacuum activated under unloaded condition examined and the result was successful as the jaws responded to pull-in by vacuum force. Figure 4.43(a) illustrates the installation of the 3D printed chuck. At the second stage, the final design smart chuck installation in the chuck was examined. There found some difficulty in fitting the smart chuck into vacuum chuck. After inspection, some ovality found around the flexure type FL1 inside the inner diameter of the smart chuck in which prevented the chuck fit properly into the vacuum chuck. The wire EDM manufacturing process was used for the

implementation of the flexures. However, it has been found that the heat transfer and expansion plus the anodising process in the surface finishing caused this problem. After the redoing and manufacturing correction of these problems, the chuck again prepared for the installation. Successfully, the chuck was fitted properly into the vacuum chuck utilised in Moor Nanotech upl250 Diamond turning machine and passed for next stage of pulling mechanism examination. While the workpiece was loaded in the smart chuck, the vacuum chuck was activated. As a result, the vacuum was not fully capable to pull the jaws and maintain the clamping pressure for the workpiece. According to numerical results described in subsection 4.5.3, with vacuum force solution definition, there was a concern that this solution might be dis-functional as the vacuum force may be insufficient for jaw's pulling and self-centring purposes. However, the practical trial at this staged validated the simulation result, that the vacuum chuck can not maintain sufficient force for pulling mechanism in the smart chuck. Hence, the design with mechanical solution became vital while the FEM results evaluated successful solution for the design.

As for mechanical solution, according to the FEM results, the applied load was well-enough and capable of pulling mechanism of the self-centring jaws in the smart chuck. Nevertheless, for implementation purposes and trial experiment validation, the smart chuck was required to be redesigned. In addition, the implementation in real-time process the applied load in simulation model need to be examined, ensuring the capability of the pulling purposes. As per detailed in technical drawings, the maximum pulling displacement of 0.5 mm was designed in the geometry, which accounts only 60% of the allowable deformation was calculated in numerical analysis with the unloaded condition positioning. Also, an o-ring slut was designed to trap the air in the back face of the pulling jaws in the self-centring mechanism.
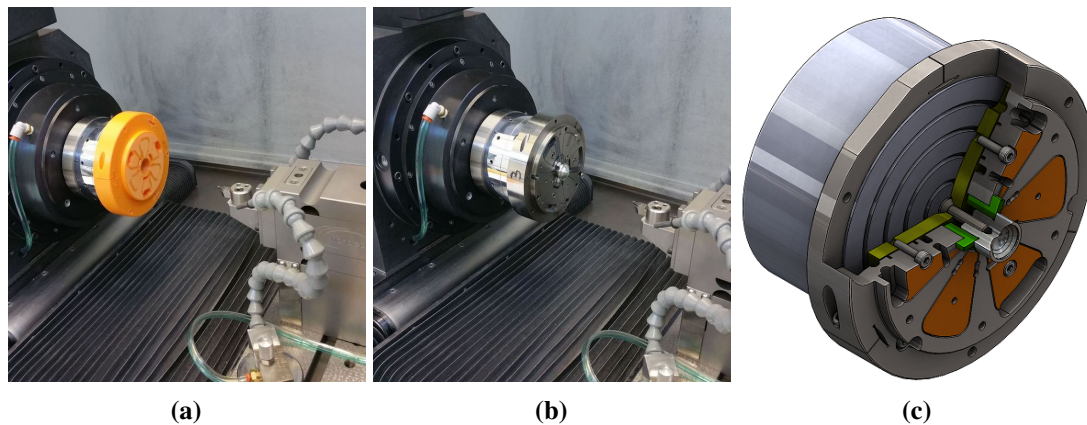
Fig. 4.43 Photograph of chuck installation: (a) 3D printed part installation; (b) final manufactured smart chuck assembly; (c) redesigned 3D model

Despite the vacuum's pulling incapability, the idea of the manually mechanical pulling mechanism was raised to examine the capability of the jaw for the purpose of the pulling mechanism. At this stage, some additional parts were designed and manufactured and installed into the smart chuck. A backplate fixed at the back face of the chuck and a collet with three pulling arms that sits on the front face of the jaws. The workpiece sits into the collet with maximum clearance rage of 1-5 microns. An oversized hole and bolt also located at the back of chuck can hold the workpiece on the front for tightening purposes. Whilst the workpiece is tighten, it pushes the collet inside and the collet arm push the jaws inside accordingly and apply the self-centring and clamping force into the workpiece. Based in this modification process, it is found that the main purpose of the design for clamping and self-centring worked perfectly although when the vacuum was deactivated. However, for future work and development, a different actuating mechanism such as pressured air or hydraulic, can be applied to fully automatised the pulling mechanism. After the installation of the modified chuck into the spindle successfully completed, the experiment was passed to the next stage for final implementation and cutting process. Figure 4.43(b) and 4.43(c) shows the final installation of the chuck and 3D model design, respectively.

4.9   Concluding Remarks

Compliant flexure mechanism is a methodology that can induce a wide range of benefit to precision engineering field including ultraprecision machining. In Micro-Nano Manufacturing, the compliant mechanism has a broad spectrum of association to precision engineering whereas they communicate and are synchronised simultaneously. Particularly in ultraprecision machining, the verity range of compliant flexure type has a direct effect in the final outcome on the kinematic and dynamic performance of the application. For an instant, the clamping mechanism in ultraprecision machining is one of the characteristics that can be problematic where the exact alignment of the workpiece with the rotary axis becomes an issue with a direct impact and affects to the optimal surface resolution and finishing accuracy. In this chapter, a novel clamping mechanism using the compliant mechanism was presented. A novel smart chuck was invented and implemented. In the design, two major characteristic issues with respect to clamping and precise positioning in UPM were considered and acceptable solving contribution to knowledge was delivered. Both self-centring and self-locking new mechanism using the circular and fillet corner flexure hinges was designed in the smart chuck. For validation of the design, Finite element method was employed and result for three types of flexures were interpreted. The implementation process for the manufacturing of the chuck was carried out and effective problem solving was provided during the implementation process. Finally, the functionality of the chuck with regards to precise clamping and positioning were examined.

Whilst the smart chuck design has been completed, the effective experiment required to evaluate the accuracy of the design. In the following chapter, the evaluation of the design will be discussed and a case study with industrial collaboration will have experimented.

Chapter 5

Validations through Precision and Accuracy Analysis

5.1 Introduction

Ultra-precision machining (UPM) is well-known as an enabling technology for manufacturing high-resolution optical components and devices. In comparison with conventional machining, dynamic performance and efficiency of ultra-precision machining often have a limitation due to the stability required for the high precision process. Over the last decade or so, however, the ultra-precision machining technology has been experiencing significant developments and advances in machine design and efficiency improvement against the increasing requirement for industrial scale ultra-precision production [91–94].

Contact lens manufacturing is ultra-precision mass production using injection molding with ultra-precision machined insert moulds. Considering medical regulations and standards, high precision and contamination-free of the moulds are essentially crucial to the quality assurance of the lenses and thus human health and safety. Therefore, form accuracy and acceptable surface finishing are characteristic and challenging in contact lenses manufacturing [95–97]. The optimum surface finish of contact lens moulds through ultra-precision machining is closely

associated with the machining dynamics and the process precision. Precision positioning of the mould in the machining is another critical parameter to successfully maintain an acceptable optical surface in contact lens moulds manufacturing [98–101]. Even though UPM can offer direct machining of contact lens moulds with very fine tolerances and nanometric level surface finish, few research was carried out on the dynamic loop effect in the machining process linking the workpiece, chuck, spindle, machine bed, slideway, tool holder and cutting tool. Therefore, scientific research is needed to investigate the effect of dynamic loop engaging the cutting tool tip and the mould surface and consequently the machining accuracy and surface finish of the mould.

In this paper, an innovative approach is presented to investigate the geometric accuracy and surface precision of the contact lens moulds through ultra-precision machining. The machining dynamics and efficiency for ultra-precision production of contact lens moulds are further investigated by using a smart chuck and the associated dynamic machining loop concepts. The paper also presents the statistic analysis on the data for the geometrical run-out effect of the lens moulds, before and after ultra-precision machining, and the associated in-depth discussion.

5.2 Clamping and Machining Dynamic Accuracy

Although cutting force in ultraprecision machining is small in absolute value of 1 N level, but it does have impact on the surface finishing because of the cutting dynamics and tool wear. This is further supported by the investigation of geometrical positioning analysis and dynamics on the machining system and processes [102]. The cutting force even in a small range applied on the workpiece can be transmitted to the clamping system of the workpiece and consequently influence the final accuracy of the finished components. Clamping system for ultraprecision machining needs to be stiffly designed and built for specific applications. For instance, in ultraprecision machining of contact lens mould inserts, the positioning and clamping accuracy of the mould inserts is required at the highest level.
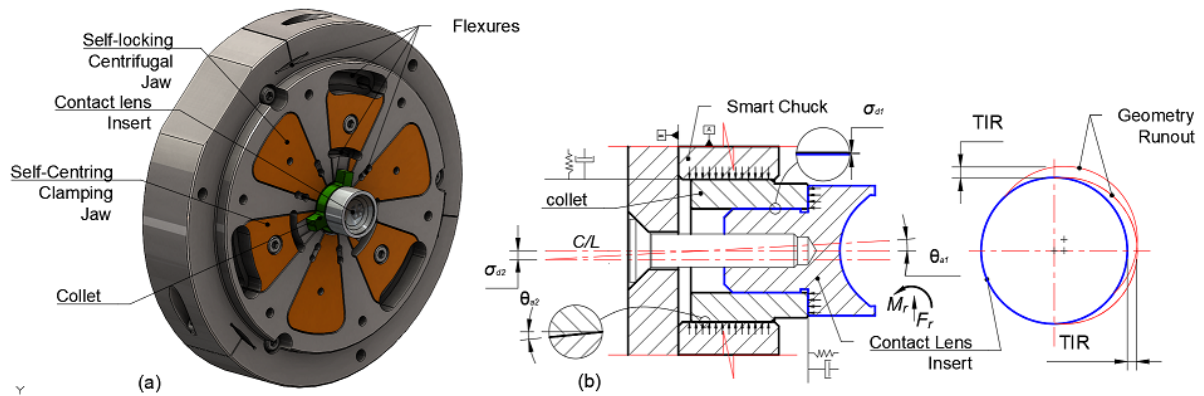
Fig. 5.1 Positioning accuracy: (a) smart chuck overview; (b) schematic of runout principle

The designed and developed smart chuck as explained in Chapter4 using flexure and compliant mechanism for holding the mould inserts in ultraprecision machining shown in Figure 5.1(a). It can also be used extensively as a universal clamping chuck for high precision components. The chuck include of a few types of flexure, which enable the self-locking mechanism and the unique design for ultraprecision positioning and maintaining optimum stiffness of the clamping system for long stable and efficient machining cycles. The chuck is designed smartly to work under a multi-functional strategy to overcome the current challenges existed in contact lens mould inserts ultraprecision machining. From this capability perspective, accuracy analyses is endeavored to investigate the impact of the stiffness against any positioning displacement during the machining process. The purpose of the concentricity of the mould insert with the spindle axis is considered as C/L, which is one of the most characteristic challenges to be investigated as it has a direct effect on the final surface finishing of the component. The premier investigation is focused on the effect of the geometrical runout before and after the machining process. Figure 5.1(b) shows a schematic preview of the clamping mechanism of the chuck in the process. The mould insert is directly clamped with the clamping chuck. However, for more accurate measurement of the runout, a new collet was designed. It is presumed that the tolerance σ_{d1} between the collet and the insert should remain constant.

Defining the stiffness of the machining system during and after the process, the total indicated reading (TIR) value is used to determine the positioning accuracy of the process.

In ultraprecision machining of the contact lens mould inserts, through the rough, semi-finishing and finishing processes, the TIR measurement value is varied before and after the machining processes due to the effect of depth of cut (DOC). Hence the creation of lateral force Fr and torsional moments M_r by the effect of DOC can make translational and angular positioning misalignments σ_{d2} and θ_{a1} respectively. At the chuck itself, the angular displacement θ_{a2} can have an impact. Although these factors have a significant influence on the clamping system, in-depth investigation is needed to study the effects of those factors on the accuracy of the clamping and the entire machining system.

5.3 Ultraprecision Machining Process Sequences for the Mould Inserts

For a successful fulfilment of the accuracy analysis, the machining cycle time was divided into several stages.
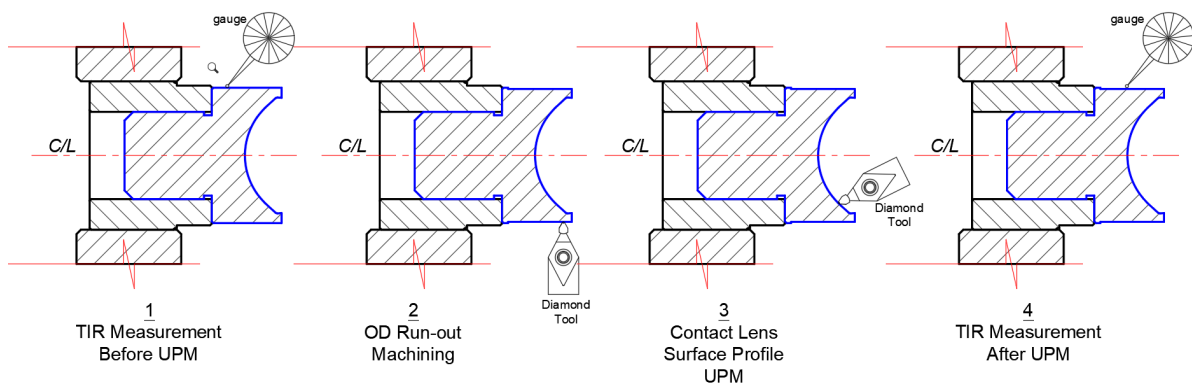
Fig. 5.2 TIR measurement sequence in ultraprecision machining

As illustrated in Figure 5.2, four stages are employed for data acquisition from the machining system. After full adjustment and constraining of the chuck on the spindle at first stage, the

contact lens mould inserts, concave or convex, need to be mounted within the chuck, and the TIR of the outer diameter (OD) is measured using built-in indication gauge. At the second stage, the current runout is machined. Hence, the machined surface can be used as a reference datum to identify any TIR after machining if it is occurred. The third stage is the profile ultraprecision machining of the insert components, which consists of roughing, semi-finishing and final finishing. During those processes, a varied range of DOC is applied. Therefore, if the machining system corresponds to a stiff and accurate factor, the TIR measured from the previous step should re- main unchanged. At the final stage, the TIR is measured again to identify any possible misalignment or displacement caused by previous machining processes. At this stage, the measured TIR should not have a significant change as it will determine the final accuracy and precision evaluation of the system.

5.4 UPM Experimental and Manufacturing Trials

Experimental work and further investigation are needed to validate the approach for accuracy and precision analysis. The experimental trials were carried out in collaboration with a contact lens mould inserts manufacturer for data collection in particular. In the experimental trials, a diamond turning machine (Nanotech 250UPL) was employed and a number of mould inserts including concave and convex ones were machined. Figure 5.3(a) illustrates the machining trial setup and Figure 5.3(b) shows some of the finished mould inserts. For each insert component, several sets of data were gathered for the accuracy analysis purpose.

Table 5.1 lists the diamond tool parameters applied in experimental trials against the ultraprecision machining of concave and convex mould inserts respectively. According to the data, RSA-905 was used for both concave and convex insert components. NanoCAM software is used for generating the NC toolpath files and coding based on the mould insert geometrical segments. The diamond tool was chosen based on the minimum radius of the segment of 0.2 mm at the lens profile. Diamond tool data illustrated in appendix C.5and C.6.
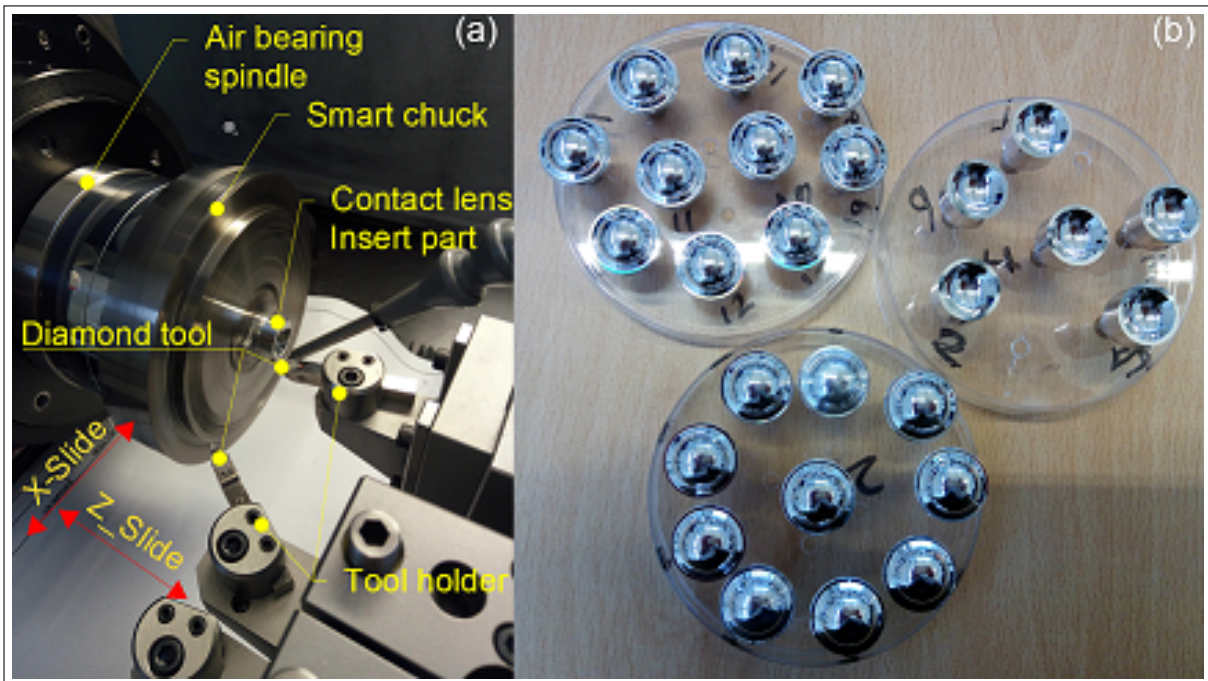
Fig. 5.3 Photograph of contact lenses insert part ultraprecision machining: (a) Moor Nanotechnology DTM; (b) finished product of the concave/convex contact lenses insert moulds

Table 5.1 Contact lens mould inserts: geometry parameters and the corresponding diamond tool data

		Segments			
	Material	Number	Radius [mm] Min - Max	Curvature [mm] Min - Max	Sag Min - Max
Concave (Die)	RSA-905	5	(0.30) (10.32)	(0.10) (3.33)	(0.2) (1.19)
Convex (Punch)	RSA-905	9	(0.20) (-9.92)	(-0.1008) (5)	(-0.017) (-1.32)
	Diamond Tool Parameters				
	Radius [mm]	Rack angle	Include angle angle [mm]	Clearance angle [deg]	
Diamond Tool (controlled Waviness)	0.19	0	55	45	

Table 5.2 lists the critical machining process parameters used in experimental trials. For achieving the desired surface finish, various sets of parameters were examined for both concave and convex inserts during the roughing, semi-finishing and finishing processes.

Table 5.2 Machining process parameters for concave/convex contact lenses mould inserts

	Roughing Conc - Conv	**Semi-finished** Conc - Conv	**Finish** Conc - Conv	**Cycle time [min]** Conc - Conv
Spindle Speed [rpm]	500 - 500	500 - 500	2000 - 2000	10 - 12
Feed rate [mm/min]	20 - 20	10 - 20	3 - 3	10 - 12
Surface Increment [mm]	0.005 - 0.005	0.005 - 0.005	0.002 - 0.002	10 - 12
Total Loop (Passes)	6 - 4	2 - 2	2 - 2	10 - 12
Depth of Cut [mm]	0.02 - 0.02	0.01 - 0.01	0.005 - 0.005	10 - 12

5.4.1 Metrology Measurements

TIR Measurement

The measurement of TIR was done using a built-in Gauge software called NanoMETER available withing Moor Nanotechnology UPL250 diamond turning machine. This software allows the user to measure the roundness of the workpiece by using contact prob with a high-precision on-screen gauge. The Moor Nanotechnology machine includes two types of high-precision high-resolution contact displacement-measuring system channel, one for Air-Bearing LVDT and the other for an electric level indicator. The LVDT gauge is the finest contact-measurement tool that can measure the sub-micron resolution. The software is also supported by an application program interface for data analysis named as StripChart. However, in this study, the method of contact prob with electrical level indicator was used for roundness measurement due to only available facility in the current diamond turning machine. Some challenges were to be dealt with to pursue the sub-micron resolution while the electrical level indicator was employed. According to the machining sequences illustrated in Figure 5.2, the gauge needs to be fully in contact with the outer circular surface of the workpiece, and by rotating one cycle, the TIR need to be captured by the NanoMETER software. It has been found that, through one rotational cycle, the indicator used to show very sensitive and unstable data while the StripChart ran. While the calibration of the gauge was trustful, it has been recognised that the prob is becoming very sensitive whilst moving on the surface and showing some errors

as overshoot in the curve in cases where the TIR value meant to be very low. For problem-solving, the decision made to measure a random partial contact probing, be means, the three parts on the circular surface were measured, and at each measuring step, the StripChart data were recorded. The average output data from the StripChart was calculated to maintain the final measurement data for the TIR at each workpiece item. However, using LVDT measurement method can be a further validation for data accuracy.

Surface Measurement:

Surface measurements also carried out using a Zygo 3D profiler instrument. Whilst the optimum freeform surfaces measurements in precision/ultraprecision machining categorised as one of the challenging tasks, thus a simplification and optimisation method for obtaining a trustable and accurate surface data is required. Since the geometry of the mould inserts contact lenses include both aspherical and flat segments, the resolution of the surface can be assumed consistent through all the segments. Hence, measuring the flat surface segment can maintain much accurate surface resolution data for the trial. Therefore, a consistent parameters for measurement setting up was applied for each mould insert item in the instrument. Figure 5.4(a) and 5.4(b) illustrate the minimum surface measurement results value for concave mould inserts and convex mould inserts respectively. As can be seen from the oblique 3D plot, a consistent range of 0-0.35 mm in Length and 0-2.63 mm in Width and the various value of the Height. The 2D surface profile shows the graph of the length (distance) vs the height in which the statistic of this study was made based in the values extracted from the profiler instrument. Full surface measurements data can be found in appendix C.1 for concave and appendix C.2, C.3 and C.4 for convex mould insert components.
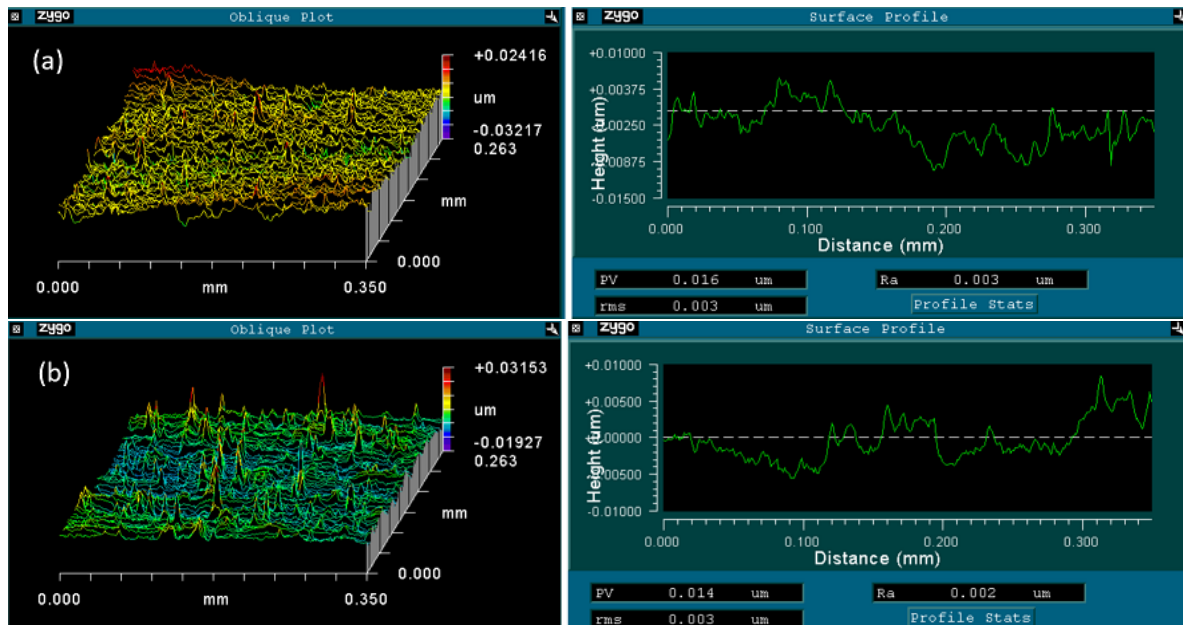
Fig. 5.4 Illustration of surface measurement : (a) Minimum surface data on concave mould insert item; (b) Minimum surface data on convex mould insert item

5.5   Results, Analysis and Discussion

Statistical data analysis was carried out to examine the accuracy and precision of the machining system. Following the experiment method described in the section above, contact lens inserts manufactured were measured with data and recorded.

Table 5.3 Experimental data for the contact lenses mould inserts before and after the machining

	Min [μm]	Max [μm]	Mean [μm]	Std.Dev [μm]
TIR after UPM	0.001	0.0534	0.02023	0.016
TIR before UPM	8	46	25.55	11.0267
PV (Surface)	0.014	0.043	0.02346	0.0064
Ra (Surface)	0.002	0.004	0.0028	0.0005

Table 5.3 illustrates the recorded data for TIR measurement before and after the inserts machining. The surface finishing data, such as peak-to-valley (PV) and surface roughness average (Ra) were also measured and recorded accordingly. Standard deviation of 11.0267 μm and 0.016 μm before and after the machining respectively.

5.5.1 Standard Deviation and Variance

The data observed from the TIR measurements analysed to specify the dispersion or the variation. Standard deviation (SD) has a width range, particularly recognised from the Mean of the data and tended to be close to mean. In this study, the statistical analysis for the SD was carried out. The statistical data, as listed in Table 5.3 shows the Mean of 20n and the SD of 16n. For detailed analysing, a fitting curve needs to be provided to justify the width range of the standard deviation. Figure 5.5 illustrates the cubic interpolation fitting curve to identify the TIR accuracy within the SD range of the data observed from the machining system for each mould insert component. As can be seen from the data the lower range from the Mean identifies 4 nanometres and the upper range of 36 nanometres. The source data show the identification of the items is within the standard deviation zone. Reviewing the SD from the chart reveals the range of 0.01- 0.036 μm, which represent width range of SD for entire machining experiments of the mould inserts.
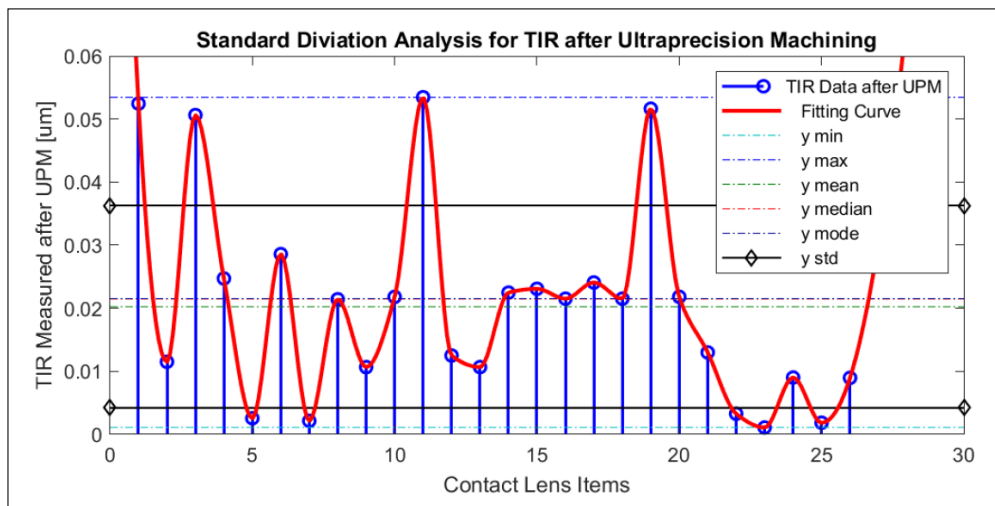
Fig. 5.5 TIR measurement standard deviation data

5.5.2   Residual and Error Analysis

An empirical polynomial rationale model with the aid of Matlab Curve Fitting tool was employed to define a ratio of the error and residual of the machining system. The theoretic model can be defined as:

$$y = \frac{\sum_{i=1}^{n+1} p_i x^{n+1-i}}{x^m + \sum_{i=1}^{m} q_i x^{m-1}} \tag{5.1}$$

where n is degree of the numerator polynomial in the range of $0 \leq n \leq 5$, and m is the degree of the denominator polynomial with the range of $1 \leq m \leq 5$. The coefficient associated with x^m is always one. Thus, numerator and denominator remain unique when the degrees of polynomial are identical. Rationals can be described with respect to the degree of the numerator over the degree of denominator, for instance, a quadratic over the cubic rational equation can be define as:

$$y = \frac{p_1^{x^2} + p_2^x + p_3}{x^3 + q_1^{x^2} + q_2^x + q_3} \tag{5.2}$$

Table 5.4 Response data of rational statistical data

Fit Type	(SSE) Sum of squared error	(R-Square) Root mean square	(DFE) Degrees of freedom	(Adj R-sq) Degree-of-freedom adjusted coefficient of determination	(RMSE) root mean square error	(Coeff) with 95% confident bounds
Rational	0.005 μm	0.132 μm	24 μm	0.096 μm	0.0153 μm	2

The best fit for the model was defined with numerator degree of zero and denominator degree of one. Figure 5.6 illustrates the the rational model with predicted curve fitting obtained from the TIR data observed and measured after ultraprecision machining. A 95% confidence

(a)

(b)
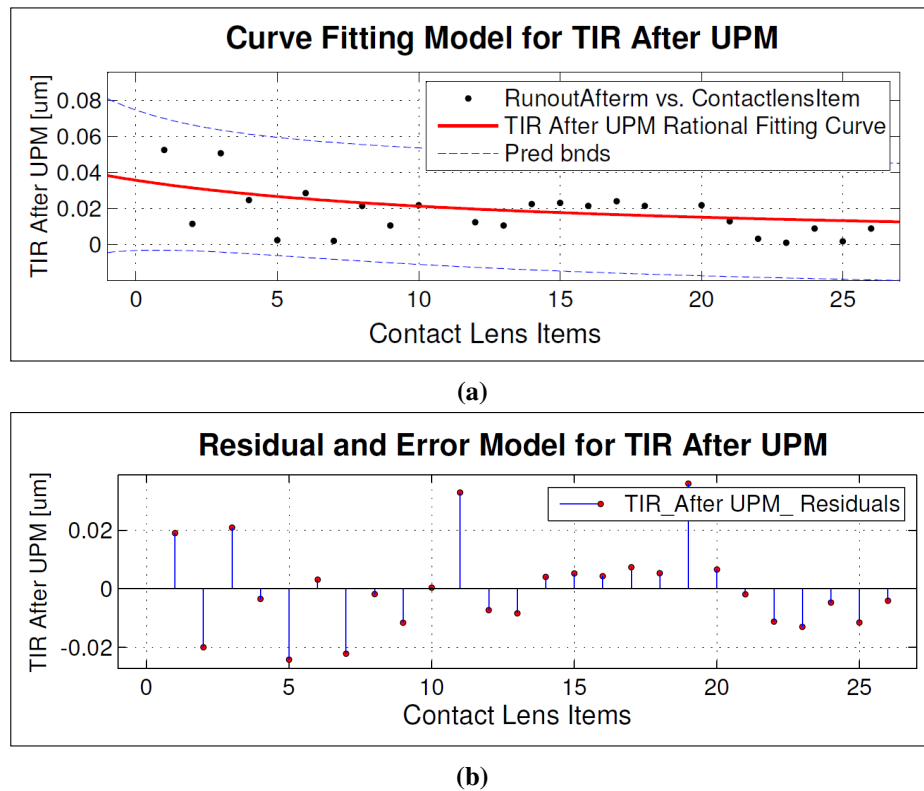
Fig. 5.6 Residual and error of the system: (a) curve fitting model for TIR data after UPM; (b) residual and error model for TIR after UPM

bounds for the prediction was defined in order to obtain maximum accuracy for the prediction curve. It can be found that the rational curve fitted for data is within 95% of predicted boundary of the observed data. Figure 5.6 also illustrates the residual and error ration of the system. Table 5.4 shows the goodness of the fit and response data of the model where the sum of squared error (SSE), root mean square error (RMSE), coefficient of determination (R- square), degrees of freedom (DFE) and adjustment of degree of freedom of the model were calculated. According to Equation 5.1, two Coefficients with 95% confidence bounds were calculated with $p_1 = 0.53$ and $q_1 = 14.88$ respectively. The SSE of 5 nm was achieved for the machining system, which specifies the maximum error of the model or in other definition, the accuracy of the TIR data observed from experimental trials after ultraprecision machining of the mould inserts parts.

5.5.3 Normal Distribution and Statistical Model Comparison

To validate the statistical modelling of the experiments, the distribution analysis of the data with regards to the TIR measured after ultraprecision machining is required.
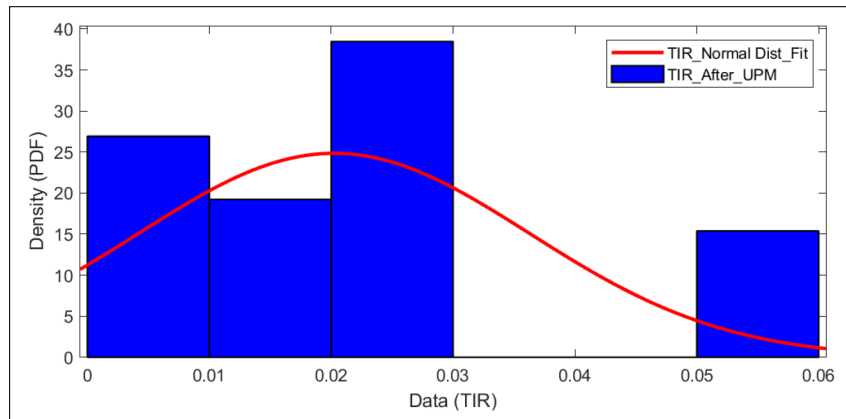
(a)
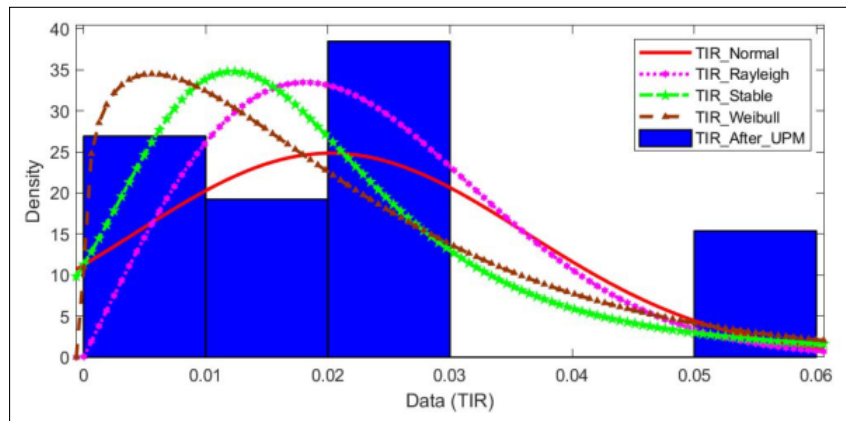
(b)

Fig. 5.7 Statistical model of the probability distribution model: (a) normal distribution model; (b) comparison of different probability distribution model

The normal distribution is known as Gaussian distribution, which can be defined as a two-parameter family of curves. The Central Limit theorem is the common justification for using the normal distribution for modelling, which specifies that the sum of independent observed (measured) samples from any individual distribution with finite variance and mean converges to the normal distribution as the size of samples moving toward the infinity. In generic terms, a Normal Distribution object be composed of parameters, a model description, and sample data

for a normal probability distribution. The distribution employs two parameters to define the probability curve such as Mean (μ) and Standard deviation (σ). Moreover, maximum likelihood estimates (MLEs) which parameters that estimates the maximum likelihood function for Mean and Standard deviation for the normal distribution. According to Matlab documentation, the MLEs of Mean (μ) and Standard deviation (σ) for normal distribution respectively can be determine as:

$$\bar{x} = \sum_{i=1}^{n} \frac{x_i}{n} \tag{5.3}$$

and

$$s_{MLE}^2 = \frac{1}{n} \sum_{i=1}^{n} (x_i - \bar{x})^2 \tag{5.4}$$

where $\bar{x}$ is the mean of samples $x_1.x_2,....x_n$. s_{MLE}^2 is a biased estimator of the parameters σ^2, by meaning that its value is unequal to the parameter. In this study, the normal distribution was carried out based on the probability density function (PDF) whereas the MLEs are the parameter estimates that will define the maximum likelihood functions for the fixed value of x. The pdf can be define as:

$$y = f(x|\mu, \sigma) = \frac{1}{\sigma\sqrt{2\pi}} e^{\frac{-(x-\mu)^2}{2\sigma^2}} \tag{5.5}$$

According to statistical data using the probability density function (PDF) of a normal distribution, the Mean value of 0.02 μm with probability density of 25 was defined as the

maximum probability distribution value for the peak of the system. The maximum likelihood of 71.02 also was calculated for the TIR data measured from the experiments. Interpreting the result can evident that %71 of the TIR observed data have a normal distribution value range 16 to 20 nano accuracy. Figure 5.7(a) illustrate the normal distribution with PDF probability function of the machining data observed for the TIR after ultraprecision. Several distribution models including Rayleigh, Stable and Weibull were applied to analyse and compare. Figure 5.7(b) illustrate the comparison of different distribution models for the system.

5.5.4 Accuracy and Repeatability Analysis

The positioning accuracy and clamping repeatability analysis of the system were carried out from the experimental data measured for TIR. A Polar modelling function based on the standard deviation was used. The data distributed on polar coordination and the SD was sat on both x and y axes to analyse the goodness of the system accuracy and precision. Figure 5.8 illustrates the results in circular shape for the accuracy and precision analysis TIR measurement data after ultraprecision machining of the mould inserts components. From this analysis model, it can be found that around 18 mould insert out of total 26 components with TIR observed after UPM successfully meet the positioning prediction within the standard deviation. Hence, it can be characterized that the system is around 76% higher accurate and precise. The remaining 24% of the system is allocated for the insert workpieces as indicated with inaccurate positions.

from interpreting the analysis model, it can be found that three accuracy zone can be defined according to the data, as: a) 20nano, b) 40nano and c) 60nano. Highest accuracy range of the 20 nm zone includes the largest amount of the mould insert components with around 12 items. The middle range of the 40 nm zone include 10 items and respectively the 60 nm zone include 4 items. The accuracy percentage for first zone is 46% and second zone 84% and 100% for zone three respectively. The overall accuracy percentage of 76% can be calculated to finalise

the accuracy of the system. The best accuracy of the positioning and clamping repeatability obtained from TIR experimental measurements can be within the range of 20-40 nm.
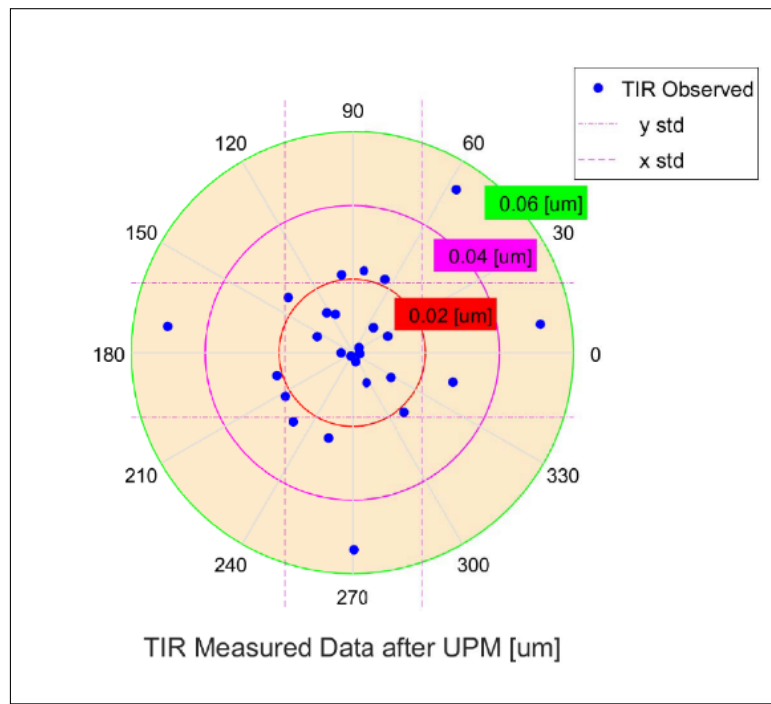
Fig. 5.8 Illustration of the accuracy and precision analysis data for the machining system

5.5.5   Clamping Stiffness vs Positioning

The stiffness of the clamping mechanism can be assumed by measuring the TIR at the end of UPM process cycles. At this stage the collet is directly clamped by the chuck jaws and its immediate current position should not be effected by applying the cutting force to the work pieces during the whole process of machining. The TIR measurement of the inner circular surface of the collet as shown in Figure 5.9 indicates almost zero, which can be proved the chuck being stiff and accurate enough to hold the collet in position.
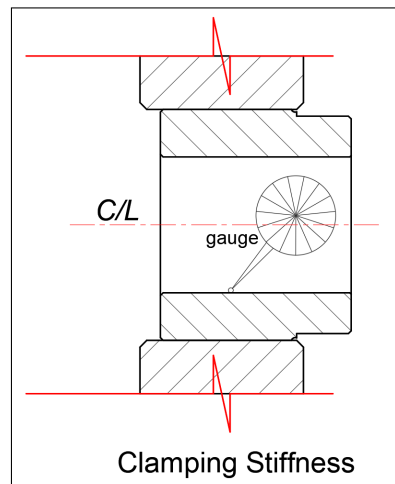
Fig. 5.9 Smart chuck clamping stiffness measurement methodology

5.6   Concluding Remarks

The research presented in this chapter sets out to determine the effect of the clamping accuracy and precision positioning of the smart chuck for ultraprecision machining of contact lens mould inserts in an industrial scale. The work also assesses the dynamic influence of geometrical runout and/or the roundness, on the workpiece, as so called total indication reading (TIR) for the positioning accuracy and clamping in the ultraprecision machining system. Ultraprecision machining of contacts lens mould inserts was chosen to evaluate and validate the concepts and approach presented, as they have the high accuracy and positioning requirement in a stringent highly productive ultraprecision production environment. It is found the accuracy of the machining system can be coined in two major dynamic effects, i.e. the effect of TIR and the effect of workpiece clamping stiffness. The analysis of TIR measurement shows that larger amount of runout can significantly move the workpiece from its desired positioning location and consequently have the effect on the accuracy and precision of the system. Furthermore, the clamping stiffness of the chuck itself has a direct effect on the accuracy of the system. The TIR measurement data after ultraprecision machining processes, show that the collet clamped by the chuck has no significant displacement. It can thus conclude the robustness of the chuck clamping and its dynamic stiffness. Regarding the accuracy of the system, the maximum

SD of 0.016 μm and 5 nm residual in geometrical runout were achieved after ultraprecision machining. The clamping accuracy and repeatability were obtained in three zones, 20nano, 40nano and 60nano for all mould insert components including concave and convex. Finally, the system obtains 76% of clamping accuracy and precision confidence with the best accuracy of the positioning of and clamping repeatability within the range of 20-40 nm. The surface finishing is very promising with the maximum 4 nm of Ra and 0.043 μm of PV as achieved through experimental machining trials.

Chapter 6

Multi-body Dynamic Analysis of Hydrostatic Bearing with the MMC Material

6.1 Introduction

Linear slideways integrated with either hydrostatic or aerostatic bearings have been widely used in ultraprecision machining systems combined with STS and FTS techniques. According to the literature review, machining the freeform surfaces using STS technique, faces some challenges in dynamics, related to linear slide motions performance and functionality. The motion accuracy often at the sub-micron level. Hence, the slideway design considered to be extremely reliable in machine design, and being capable to eliminate all external impacts such as thermal expansion, vibrations, and frictions. The load-carrying capacity can be generated by the externally supplied high-pressure liquid, typically oil, in a hydrostatic bearing [103, 104]. The oil is subject to create wide range of viscose damping. The bearing clearance between the stationary and movable carriage is in the range of 10 to 100 μm. Design, development and manufacturing of hydrostatic bearings components, due to their requirements for higher

level of precision engineering, are limited within the range of few manufacturer companies. In ultraprecision machine and component design such as diamond turning machine, the hydrostatic bearings are manufactured based on the customer requirement with no standard with regards to the oil pressure and oil resource. Thus, the design of a hydrostatic bearing is dependant to the maximum load capacity required for the particular application. Also, designing the supply pressure has a correlation between two factors, speed and load capacity. For instance, if the hydrostatic bearing need be designed based on higher load capacity factor, higher supply pressure needs to be considered to maintain the maximum loads, whereas if the concern goes for the speed factor and temperature, the lower pressure will be more suitable. Thus, the design of an UPM utilising the hydrostatic bearings, has a direct correlation with load capacity and high-pressure oil supplied [105].

The main advantages of hydrostatic bearings with incompressible liquid and high-pressure are: high damping, high static stiffness, proper pressure distribution in bearing surface imperfection and high load-carrying capacity [106]. The ratio of the error motion in a hydrostatic bearing is normally below 100 nm, even with imperfect bearing surface finishing [107]. Nevertheless, the hydrostatic bearings experiencing some limitation in their performance related to higher dynamic friction coefficient at higher linear speeds. The dynamic friction at lower speed in a linear hydrostatic bearing is low and often is neglectable. In general, utilising the hydrostatic bearings in UPM spindles where the angular velocity is high, reducing the power losses should be considered. STS technique usually uses the hydrostatic bearing to accomplish those desired motion accuracy due to its robust stiffness and damping in bearing load and acceptable linear accuracy in the back and forward motion steps during the machining process [108]. However, in terms of motion, there are some limitations with regard to the speed and acceleration for the hydrostatic bearing utilised in STS mode. For instance, if the velocity is too high, then the thermal and heat expansion in the slides at the contact surfaces will be raised rapidly due to the constant, repeatable frictions. However, based the oil film gap has also a correlation

with thermal and heat generation in linear hydrostatic bearings, effecting their linear motion accuracy. In this research work, an approach can be delivered to quantifying the linear motion accuracy through its straightness or linearity. Nevertheless, while the hydrostatic bearings utilised in UPM tend to have repeatability factor through their constant back and forth linear motion, the investigation of their motion accuracy becomes priority.

One of the objectives in this research work is to investigate the feasibility and dynamics for further improvements in the ultraprecision machining system using the light weight material such as metal matrix composite (MMC) material, optimising the motion robustness and dynamics in the hydrostatic bearing slideways for STS mode. The feasibility study is focused on the structural stability of the linear hydrostatic bearing's components when they designed with MMC material. In the next following sections, the effect of MMC material on the motion accuracy will be discussed.

6.2 Metal Matrix Composite Material

Two or more based engineering materials can be combined to create new type of material, aggregated with new constituents properties, ideally known as composite material. However, there are classifications of this new type of materials such as metal, polymer, and ceramic. Nowadays, in industrial engineering fields, MMC has utilised for prototyping for the space innovation, automotive industry, commercial airliners, and a variety of other applications like component manufacturing and sustainable design systems [109]. While the majority of the based matrix composites are aluminium, due to the operational characteristics such as wear-resistant, dampening properties and mechanical strength, the significant number of applications requires the matrix properties of super-alloys such as titanium and magnesium. This type of new material has its own structural benefits, however, processing can be challenging, whilst integrated with other material that included low wettability of reinforcement particles phase within the molten based metal [110] . This phenomenon consequentially does not allow for

synthesis by conventional processing. General advantages for metal matrix composite are as follows [111]:

- Corrosion and wear resistant

- Increase in mechanical strength and stiffness

- Decrease in fatigue

The disadvantages for MMC materials are:

- Costly

- Chemicals and /or solvents exposure

- Time-consuming in the manufacturing process

- Specialised equipment needed for fabrication and processing

It is imperative to state that the material properties of the MMC under the dispersed phase can be enhanced by enforcement of the particle, which can increase the yield strength, tensile strength and creep resistant but also thermal stability. Like all currently existing composite materials, aluminium-matrix composites are not a single material but instead developed with other materials whose mechanical properties such as strength, stiffness, density, thermal and electrical properties can be customised. Despite the MMCs variations, however, aluminium composites still endeavour the decisive advantage of low cost over most other MMCs currently available in the market or near-completed development. In addition to the cost advantages, MMC offers superior thermal conductivity, non-flammability, high-temperature operation, high shear strength, excellent abrasion resistance, as well as minimal surface degradation due to its potential exposure to corrosives, solvents and the ability of being geometrically formed through traditional manufacturing process methods [112, 109].

Aluminium MMCs can be manufactured by powder metallurgy, deposition physical vapour deposition, stir casting, hot isostatic pressing, EDM, in situ development of reinforcements, squeeze casting, and short or long fibre pressing techniques [113]. For instance, today's super-alloy composites reinforced and strengthened with tungsten alloy fibres are being produced for elements in jet turbine engines that work with temperatures of 1,000 °C and above. Decreasing the size of the reinforcement particle-phase from micro to nano level is such that the interaction of the particles with their displacement becomes something of consequence, strengthening the interaction of the particles and resulting in a remarkable increase in the material mechanical properties such as the development of wear behaviour [113]. This phenomenon can open the debate of utilising the MMC material for hydrostatic bearings components such as sliding parts, considering the contact between the guide rail and the workbench slider. Moreover, from component fabrication point of view, there will be a challenges, such as low wettability of the ceramic particles with the molten base metal matrix which do not allow for traditional casting processes but preferably modified fabrication processing methods. For example, in Powder Metallurgy, small powder aggregates are prone to form molecular to macro clusters, therefore, dropping their capability to be homogeneously scattered evenly throughout the matrix structure. The manufacturing of MMC materials can be categorised into two main groups, ex-situ and in-situ. Ex-situ is a synthesis route which composed of adding molecular reinforcement to the molten liquid or powdered metal while the in-situ processes belong to other methods that require the generation of ceramic molecular/nano compounds by reaction during processing. Most commonly powdered metallurgy techniques have been shown that they're highly successful in being accepted for stable MMC parts [114]. It would be necessary to compare both materials MMC and monolithic material. Matrix composite with strengthened particle for reinforcement is being considered as an alternative material to monolithic metal. Compared to monolithic metals [115], MMCs materials offer higher strength-to-density and stiffness-to-density ratios, better fatigue resistance, better-elevated temperature properties, lower creep rate, lower coeffi-

cients of thermal expansion and better wear resistance. For contributing in this research work, a numerical analysis required to study the behaviour of the dynamic effects of linear slideways when their material replaced with MMC. The next section will explain the numerical analysis method to qualify the study with regards to sustainable design and development of the system in ultraprecision machining.

6.3   Design of Linear Slides Utilising MMC Material

6.3.1   Design Specifications

For linear slideway hydrostatic bearing design, a multiple factors need to be considered. For this research work, as part of the design process, the initial data and information was collected. Logical step can be taken to construct the design specifications, focusing on the operational and functional capability of the slidway components, using MMC material. From the fundamental logics, the research will be involved in designing the hydrostatic bearings with magnetic preload and single guide components. The design also will be defined based on an existing UPM hydrostatic bearing and their material on the slide component and investigate the new study while replacing those existing components with MMC material. Geometrical data is gathered by approximation measurement of the slides component, designed in existing conventional UPM system, to obtain accurate results for final validation. The design specifications will be focused base on operational forces, environment characteristic of the mechanical components with the aid of multi-physics and multi-body dynamics simulation. For validation of the design, comparative method will be evaluated to investigate the effectiveness of MMC material utilisation in the linear hydrostatic bearing slideway . This contribution will provide a unique understanding of the dynamic behaviour of the system when different materials were employed for the components. Various type of simulations, including Structural analysis, Modal and Harmonic analysis, need to be employed in order to specify the natural frequency and the

response in the system. latter, the stiffness and damping of the system will be calculated for vibration and multi-body dynamic (MBD) analysis. Figure 6.1 illustrates the design specification structure required to compare the dynamic behaviour of two different material.

Hence, in this study, the methodology sequences can be specified as follow:

- 3D modelling and design of an existing linear hydrostatic bearing slideways.

- Importing the design into a simulation environment.

- Development of simulations using multiple operational multi-physics such as structural dynamic stress loading, modal analysis to specify the natural frequency, harmonics analysis on the frequency response, and dampening/stiffness analysis.

- Preparing multi-body dynamic models to investigate the characteristics of the slideway.

- Comparative analysis with between two different materials, existing and MMC.

6.3.2   Design and FEA Simulation

In the following section, the linear hydrostatic bearing slideway and its design capability will be investigated by using Finite Element Analysis methodology. FEA analysis is essentially used to analyse and determine the system's damping and stiffness required for later MBD analysis. Through MBD analysis, the vibration study will be the key point to determine the performance differences in the STS system when the hydrostatic component being replaced by MMC. Both prestressed and unloading scenario is to be examined using two different materials such as the existing alloy steel as a reference and MMC (AL2O24) material with particle volume of SiC 30%. According to [9], table 6.1 lists the material properties for MMC (Al2024) with average particle size of 3 μm which was assigned to the hydrostatic bearing components in this research work.
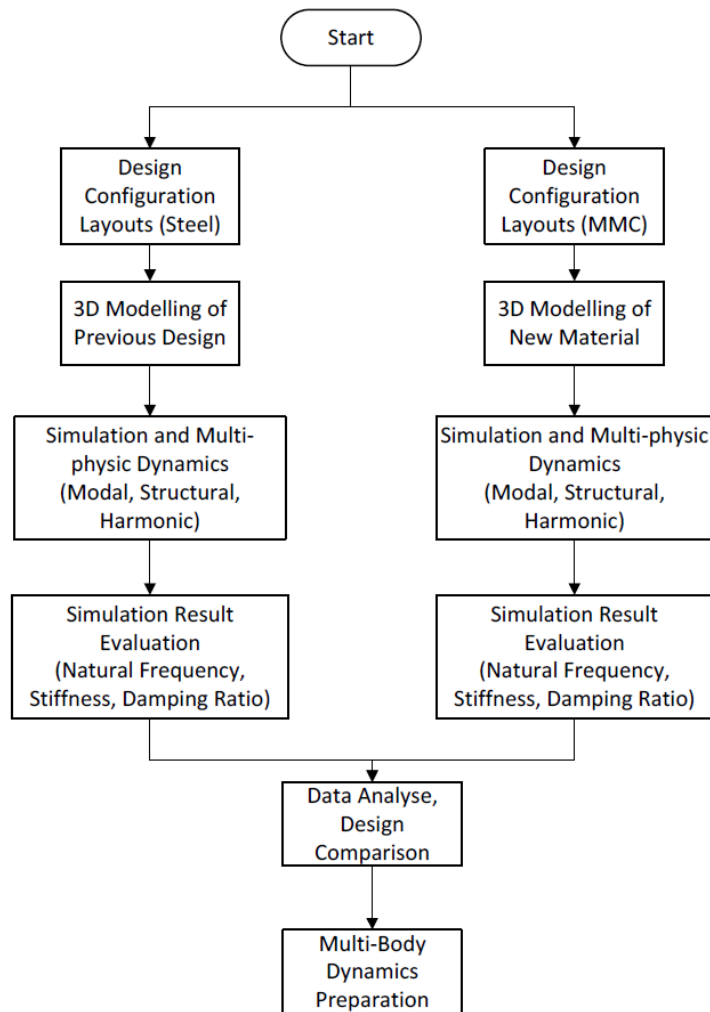
Fig. 6.1 Design specifications of the slideway and its design protocol

Table 6.1 Material properties of the AL-MMC (Al 2024)

Al-MMC (average particle size: 3 μm, 30% SiC)	
Density ρ (g/cm^3)	2.9
Young's modulus E (GPa)	115
Hardness (HV 0.1)	276
Thermal conductivity κ (W/(mK))	145
Specific heat capacity c (J/(kgK))	828
Thermal diffusivity a (m^2/s)	$6.04 \cdot 10{-}5$
Coefficient of thermal expansion α (1/K)	$15.6 \cdot 10{-}6$
Residual (compressive) stress prior to turning (MPa)	−4

As for structural analysis, the geometrical model of Z-axis will be imported for FEM analysis, including the toolpost and cutting too. The model includes two component groups. The fixed component being assigned with steel material and the slider carrier assigned with the MMC material. As illustrated in Figure 6.2, there is an element of mechanical contact within the components, varying from the static to the vibration study.
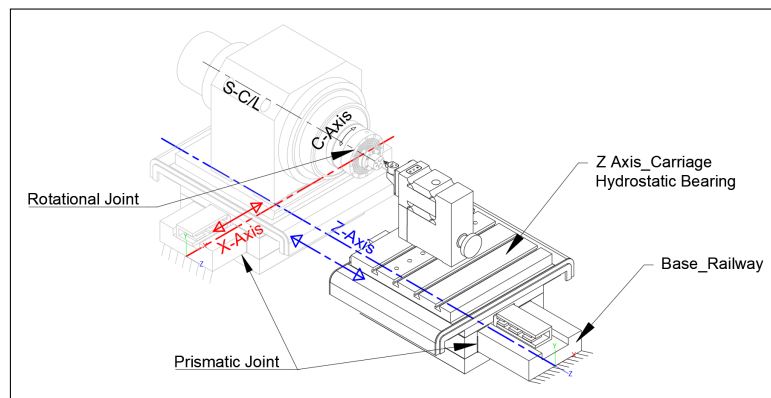
Fig. 6.2 Schematic estimated geometry CAD model of Moor Nanotechnology Upl250, Z-axis

Therefore the contact between the Z-axis carriage and base needs to be considered maintaining the specific mechanical property for this particular material interface zone. Those properties consist of frictionless surface factor for its static coulomb friction value. According to non-standard hydrostatic bearing specification, the range of 10-30 microns, depends on maximum loads required. Narrow damping film of 20 microns were designed between the slider carriage and the base, which considered as a railway in this type of hydrostatic bearing design. the assumption can be made that narrowing gap has a damping film not only allows for absolute frictionless behaviour but it also works as a smooth spring with pre-specified stiffness.

Moreover, the operational maximum carrying load capacity also applied to study the dynamic effects on the structural properties when the slide subjects to maximum linear speed under the loaded condition. The load capacity in this study was determined at 6,500 N with a maximum linear speed of 0.15 m/s. These values was determined based on the range of the industrial linear hydrostatic bearing slideway design specification. For vibration study, the

consideration should be focused on certain critical properties such as, the total mass of the carriage along with their components young's modulus, Poisson ratio and material stiffness. All of these properties have an impact in final result in the vibration study. In general manner, considering the total mass of the components for technical analytical behaviour, if increased, then the natural frequency of the system expected to be reduced. Thus, the harmonic analysis of the system in terms of vibration behaviour with lighter material, should prove the performance of the system without compromising the system operational stability. However, the structural analysis with harmonic actuation can highly define the pick value of the stiffness and damping of the system which can assist to evaluate the final frequency response and bandwidth of the system when integrated with controlling system to improve the robustness of linear dynamic motion in UPM using STS technique. The next sub-section will explain the FEA setup for this study.

6.3.3   FEA Setup

The simulation is mainly focused on the modal and harmonic response analysis. The preliminary study on the modal analysis is to obtain the maximum natural frequency of the system. Secondary analysis will study the harmonic simulation utilising the maximum natural frequency in both material MMC and Steel to determine the initial stress and displacement in the linear hydrostatic bearing structure which will be necessary to explore the frequency response and stiffness/damping of the entire system. However, for purposes of comparative data analysis, an existing design of the hydrostatic bearing is required. The datasheet of a commercial hydrostatic linear bearing was collected from TAC Rockford Ltd [116], which can be used as a reference to determine the applying capacity load for the harmonic simulation. According to the datasheet, the maximum capacity load of 6,500 N needed for slidway carriage component with 40 mm width [116].

6.3.4   Modal and Harmonic Analysis

The vibration analysis include two loading classifications, unloaded and preloaded structures. Unloaded structure classified as modal, presents the vibrational behaviour without external loaded while the preloaded structure accounts with external force, acceleration, or displacement factors, being used in the form as an external source. Hence the preloaded classification contributes more relevant derived knowledge regarding the operational capability of the structure. Therefore, if a mechanical based structure is subject to take an external load, facing significant tensile or compressive stresses, resulting general behaviour in the structure such as, changing the structure's stiffness and consequently its 'n-th' mode shapes of vibration. To study those process, the modal or eigenmode analysis needs to be applied on a the structure. Therefore, primarily, modal analysis results become crucial for the preparation of pre-stressed vibrational analysis. Operationally, this type of modal analysis estimates the developing stress due to external loads which can have an impact on the stiffness of the structure. The actual modal analysis computes its vibrations modes by estimating the change in stiffness. Considerably, between the two types of stresses, tensile stress increases the natural frequencies while compressive stress decreases natural frequencies. In addition, compressive stresses generate negative vector stress stiffness in which decreases the resultant stiffness as well as the natural frequencies. Since tensile stresses develop a positive vector stress stiffness that appends to the elastic stiffness of the material, therefore, the resultant stiffness can be increased, which should be speculated by the higher natural frequency with compare to the unloaded or modal outline. Given the general idea of vibrational analysis, the factors such as geometry, structural mass and distribution, structural constraints, material and structural stiffness and application of tensile or compressive loads need to be considered for natural frequencies and mode shapes in the structure. Acknowledging those factors contributing that, this type of structural analysis renders certain penetration resonance such as the natural vibrating frequency and its natural amplification through the structure. While the structure vibrates at a particular frequency, the

structural frame might catastrophically fail, thus the studying the knowledge of the occurrence is highly recommended for the development of any structure that subjects to the external force acting on it. Additionally, the deformation or displacement of a vibrating structure critically provides the insight with the peak natural 'harmonic' frequency vibration point in the structure with an applied external force.

Modal Analysis

In this study, Ansys 2019 version R19.1 was employed for modal analysis. For the initial simulation setup CAD geometry of Z-axis from a conventional UPM was imported. As for the first model, standard structural material was assigned while second model the MMC SiC 30% material was added in the engineering data library, and assigned for modal analysis. Table 6.2 listing the FEA setup data and material properties for both structural and MMC models.

(a)   (b)
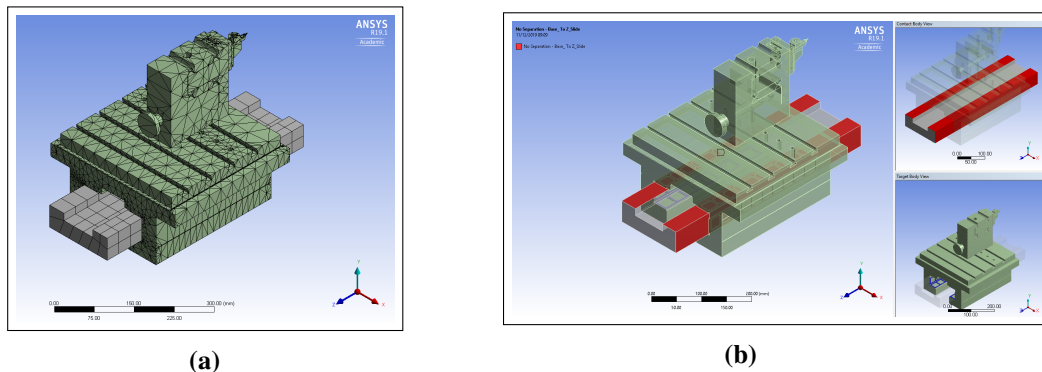
Fig. 6.3 Modal analysis Z-axis: (a) Meshing; (b) Contact regions;

As illustrated in Figure 6.3, the meshing and the contact setting were applied in the model. As mentioned earlier, a non-separating frictionless contact was defined between the base or the rail and the carriage to present the constraint oil film narrowing gap. Table 6.2 also shows the FEM setup parameters for both structural steel and MMC models. The material properties for MMC was assigned as per specified in Table 6.1.

Table 6.2 FEA environment setup data and material properties

		Structural Steel	**MMC-SiC30%**
Definition	Stiffness behavior	Flexible	Flexible
	Reference temperature	Environment	Environment
Material	Assignment	Structural Steel	MMC30
	Nonlinear effects	Yes	Yes
	Thermal strain effect	Yes	Yes
Properties	Volume	1.0529e+007 mm^3	1.0529e+007 mm^3
	Mass	82.652 kg	30.534 kg
	Centroid X	2.3589e-003 mm	2.358e-003 mm
	Centroid Y	83.992 mm	83.992 mm
	Centroid Z	269.39 mm	269.39 mm
	Moment of Inertia lp1	9.937e+005 kg.mm^2	3.6712e+005 kg.mm^2
	Moment of Inertia lp2	1.1731e+006 kg.mm^2	4.3337e+005 kg.mm^2
	Moment of Inertia lp3	9.3386e+005 kg.mm^2	3.4499e+005 kg.mm^2

Modal Analysis Results

Result interpretation from modal analysis for both MMC and structural material were carried out, and the initial outcome data recorded. The modal simulation was done based in 10 different shape modes. For each mode, the maximum modal displacement was plotted. The differentiation of the natural frequencies shown in Table 6.3 for both materials. The maximum resonates natural frequency pick of 4,030.5 Hz was achieved for structural steel while the MMC material has recorded the pick of 5,160.9 Hz resonates.

At this stage of the simulation, a comparison analysis can be done based on the current geometry of the model. Having interpreted the values of the frequency changes, showing that, MMC material resulted higher frequency than the structural material. In order to underline better knowledge of this earlier stage of the result, a comparison chart as illustrated in Figure 6.4 was carried out. The graph can evidence the principle of the vibration, and clearly implies that the lower amount of the mass and density can increase the resonates and natural frequency in the structure of linear hydrostatic bearing. This result can be beneficial, considering the,
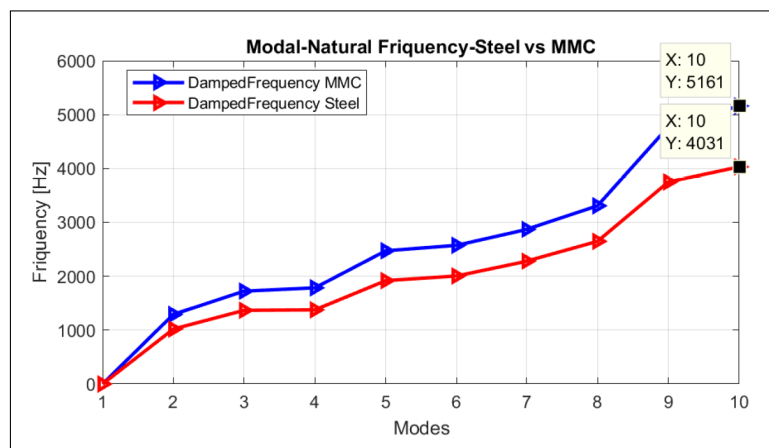
Fig. 6.4 Natural Frequency, modal analysis, MMC vs steel
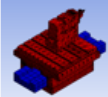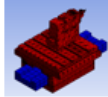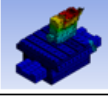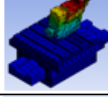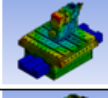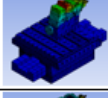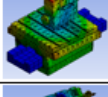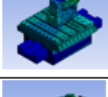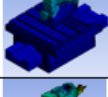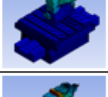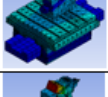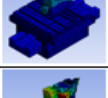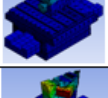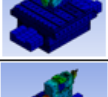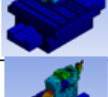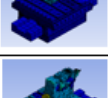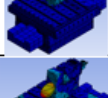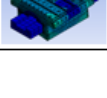
higher resonate in the MMC material can significantly increase the performance of the motion while using STS mode. The stiffness and feasibility of the material while in machining process need to be studied . In the next sub-section those resonant will be used to study the harmonic effect in the system to determine the frequency response of the system with regards to the damping and stiffness factors.

Since previous simulation investigated the modal analysis and natural frequency of the system, the displacement or the mode shape of the simulation were imaginary and recorded substantial value, which means that the structure of the hydrostatic bearing is significantly un-damped. However, by applying the load to the system, the resonant of the model will be decreased and will result in more damping toward the steady-state damping ratio. In the next subsection, the harmonic frequency will be applied, and the response of the system will be studied, and the capacity load will be employed in the structure to determine the final resonant of the system with regards to static structural results such as stress, strain and displacement.

Harmonic Frequency Response

Following section describes the facts that harmonic analysis can be applied to find the stiffness and damping response of the system. The sinusoidal actuation will be applied to the model in order to determine steady-state responses of the linear structure at Z-axis and the structural

Table 6.3 Natural frequency data, modal analysis

Mode	Damped Frequency_Steel [Hz]		Damped Frequency_MMC[Hz]	
1	0		0	
2	1020.4		1292.4	
3	1367.9		1723.6	
4	1376.8		1785.3	
5	1918.7		2472.6	
6	2005.2		2574	
7	2280.7		2871.2	
8	2647.8		3307	
9	3750.1		4774.4	
10	4030.5		5160.9	

responses at several frequencies will be calculated. The values of the responses will obtain the graph in which can quantify the maximum amount of displacement, stress and strain of the structure versus the time. Hence, interpreting the frequencies responses can provide the structural stiffness and damping of the where the functioning need to investigated under the loaded condition. In this simulation, the capacity load of 6,500 N applied to the top face of the Z-axis, and the bottom face of the base was defined as a fixed constraint. Comparative models

were made for two different material of MMC, and structural steel and differentiation graphs were made.

The frequency ranges for harmonic simulation were assigned from the modal analysis. The range of 0-4,030 Hz for steel and 0-5,160 Hz for MMC respectively was setup to maintain the solution from the simulation. It is assumed that those frequencies value that already calculated for the natural frequency will exert with the harmonic phenomenon to implies the final response for the system.

Harmonic Response Result

As a result, from the harmonic simulation with preloaded external force, an analytical comparison between two different material can be obtained. The frequency responses result from the model, including the Normal Stress response, Elasticity Strain response, Deformation and Phase angle amplitudes for both Steel and MMC has shown in Table 6.4 and Table 6.5 respectively.

The result from these outcome data, indicate the peak amplitude of the system versus the frequency. For the steel material, the value of (3627, 4.41e-01) for normal stress response, (3627, 2.04e-6) for the elastic strain, (4030, 6.15e-4) for deformation and 180-degree phase angle in the component of Y direction were calculated. Since this is a comparison model, the normal stress response of (4644, 0.37643), the elastic strain of (4644, 3.0001e-6) and maximum deformation of (5160, 9.20e-4) were calculated for the solution of harmonic response with alternative MMC material.

Rendering the data between the two material evidence that the amplitude of the response to the frequencies within specific criteria in the system is significantly different and evident that the resonant the system also significantly reduced with responses to the externally applied forces in the structure. Statically, this can prove that the applied forces to different material have a considerable various performance impact on the system. Comparative graph were created to

maintain a broader understanding of those differences between the two materials. Figure 6.5 illustrates the three different criteria of the result for MMC and Steel material and compare the frequency responses differences between those criteria.

Table 6.4 Frequency response results, structural steel

Frequency [Hz]	Frequency Response_Normal_Stress (Amplitude) [MPa]	Frequency Response_Elastic Strain (Amplitude) [mm]	Frequency Response_Elastic Strain (Phase Angle) [°]	Frequency Response_Deformation (Amplitude) [mm]	Frequency Response_Deformation (Phase Angle) [°]
403	7.52E-02	3.51E-07		6.20E-05	
806	7.72E-02	3.60E-07		6.36E-05	
1209	8.09E-02	3.76E-07		6.40E-05	
1612	8.67E-02	4.06E-07		7.90E-05	
2015	9.69E-02	4.56E-07	180	9.04E-05	180
2418	9.99E-02	4.57E-07		7.85E-05	
2821	0.12738	5.90E-07		1.16E-04	
3224	0.17621	8.16E-07		1.75E-04	
3627	0.4414	2.04E-06		5.52E-04	
4030	0.31068	2.60E-07		6.15E-04	

Table 6.5 Frequency response results, MMC

Frequency [Hz]	Frequency Response_Stress (Amplitude) [MPa]	Frequency Response_Strain (Amplitude) [mm]	Frequency Response_Strain (Phase Angle) [°]	Frequency Response_Deformation (Amplitude) [mm]	Frequency Response_Deformation (Phase Angle) [°]
516	0.069768	5.622E-07		8.87E-05	
1032	0.071514	5.7602E-07		9.08E-05	
1548	0.074718	6.0004E-07		9.03E-05	
2064	0.079702	6.445E-07		1.11E-04	
2580	0.087828	7.1341E-07	180	1.30E-04	180
3096	0.09298	7.3714E-07		1.17E-04	
3612	0.11441	9.1386E-07		1.62E-04	
4128	0.1537	1.2272E-06		2.40E-04	
4644	0.37643	3.0001E-06		7.84E-04	
5160	0.29006	1.2866E-06		9.20E-04	

Comparing the stress, strain and deformation frequency show that the response of the MMC material from 3,000 Hz upward significantly increased while the amplitudes of the y-axis remain the same as the steel. Moreover, the result can conclude that using the MMC
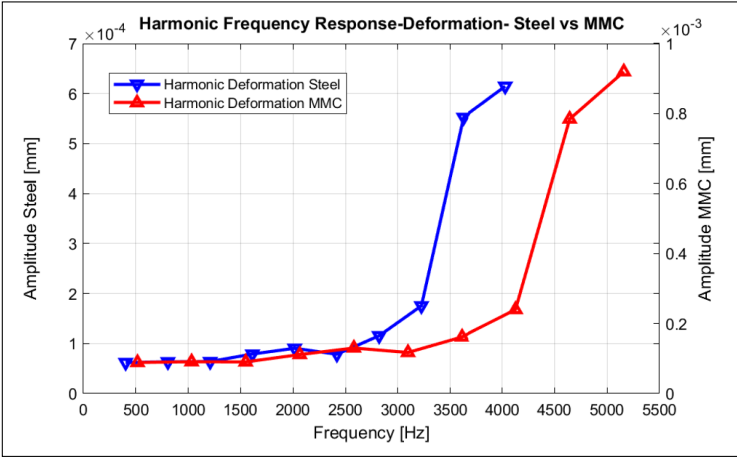
(a)
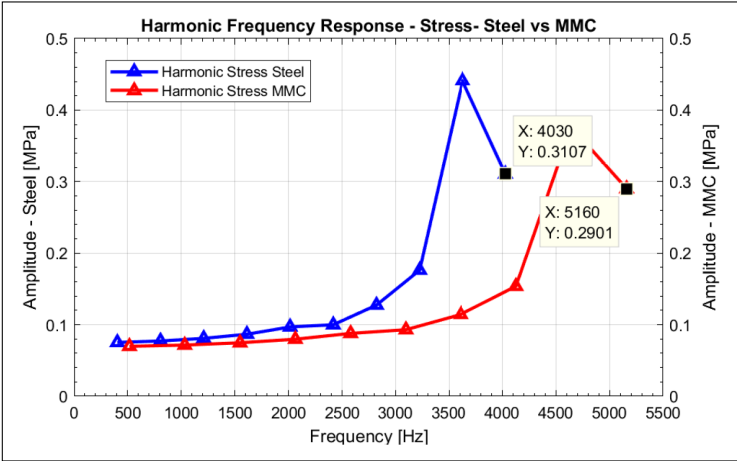
(b)
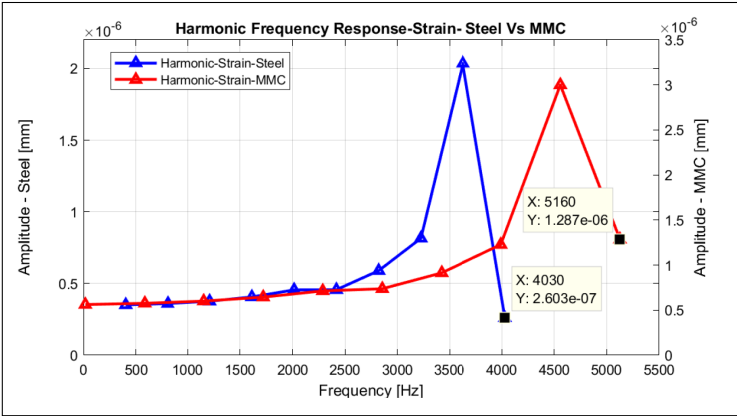
(c)

Fig. 6.5 Harmonic analysis: (a) frequency response deformation; (b) frequency response stress; (c) frequency response strain
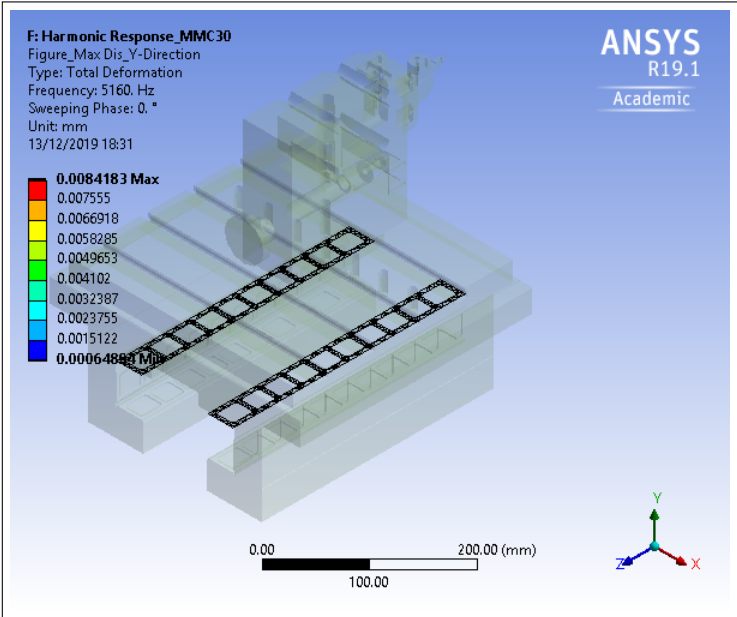
(a)
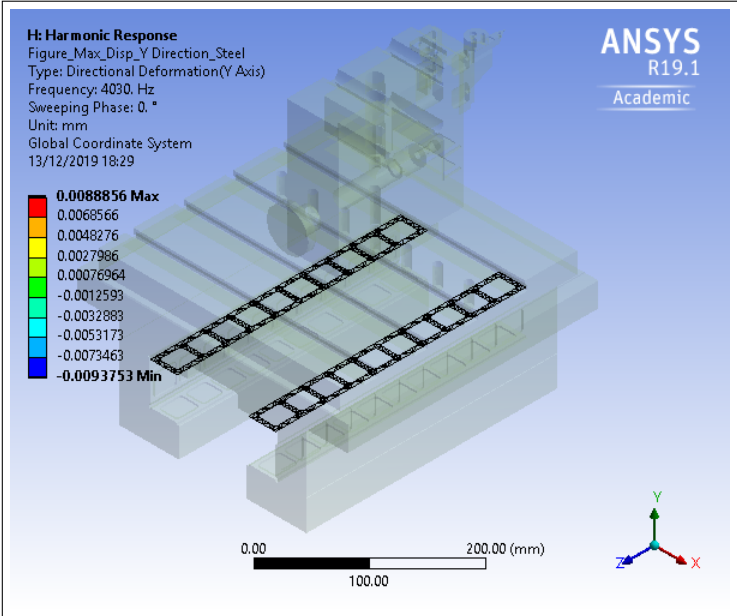
(b)

Fig. 6.6 Harmonic analysis: (a) total displacement, MMC; (b) total displacement steel

material can respond quicker with the same stiffness and damping as steel. Despite the fact that 'frequency response' waveform across MMC materials are faster, the vibrational behaviour of the slideway system does not change. This result can be apprehended as a development achievement to replace the existing alloy material with MMC in hydrostatic bearing design

for slideways. The maximum displacement result for both MMC and steel at the contacting region, between the base and the carriage in Z-axis, illustrated in Figure 6.6. Comparing the two values show that the maximum displacement of 6 μm for steel and 7 μm for MMC. The maximum displacement specified in the datasheet from the current manufacturer of hydrostatic bearing [116], is comparable with the simulation result. It can prove that replacing the MMC material in the hydrostatic bearing can be viable.

Since, statically, with the aid of harmonic simulation, the structure of the MMC material was investigated, a dynamic simulation also is essential to study the stiffness and damping of the system. For this purpose, a multi-body dynamic can be employed to simulate and analyse the entire Z-axis components with a comparison analytical solution between two different material. Following section will investigate the dynamic effects of the system, utilising two different materials to evaluate the feasibility and viability of the MMC material replacement at UPM hydrostatic bearing.

6.4   Multi-body Dynamics Analysis

6.4.1   Mathematical Theory

In actuator based system, the responses can be classified into groups such as free response, un-tuned active damping, forced vibration and adaptively tuned active damping. Moreover, in analytical terms, those responses will implement the waveform of the system in which can be standardised as actuators types and characters. However, given the competence of tuning in the control system, the over-tuning issue can be characteristic, thus, in real-time functioning, the performance response is associated with naturally dampen phenomenon instead of being a fully-tuned system. Hence, employing this type of free response to the system as an actuator can improve the effectiveness and robustness, by investigating to replace different light-wight material such as MMC and Steel for Multi-body Dynamics simulation.

Mathematically, the model can be simplified as a second-order differential by obtaining the transfer function and Laplace assuming the zero initial condition for the transforming of the differential equations. Therefore, the prediction of the transient response of the system from the pole location can be acheived. A second-order system can be modelled as a canonical transfer function as:

$$G(s) = \frac{Y(s)}{U(s)} = \frac{K\omega_n^2}{s^2 + 2\xi\omega_n s + \omega_n} \tag{6.1}$$

where ξ indicates the damping ratio, ω_n is undamped natural frequency, K is DC gain in which is the constant of the system. Simplifying the system by considering the Z-axis as a spring-cart mechanism under unloaded condition can determine the output of the system to obtain the stiffness response when the MMC material assigned in the carrier. Figure 6.7 shows the free body diagram of the system with the constants key parameters are as follows:

- k is the spring constant

- M is the Mass of the Z-axis carriage

- B is the coefficient of viscous friction acting between the base and Z-axis carrier

- f(t) is applied force to the Z-axis

- x(t) is the displacement of the carriage from its equilibrium position

- $\dot{x}(t) = \frac{dx(t)}{dt}$ is the speed of Z-axis

- $\ddot{x}(t) = \frac{d^2x(t)}{dt^2}$ is the Z-axis acceleration

From the free body diagram the acting forces can be calculated as:

$$M\ddot{x}(t) + B\dot{x}(t) + kx(t) = f(t) \tag{6.2}$$

The Laplace transforming equation can then be found by the transfer function of the output X(s) to the input F(s) with zero initial condition: then,
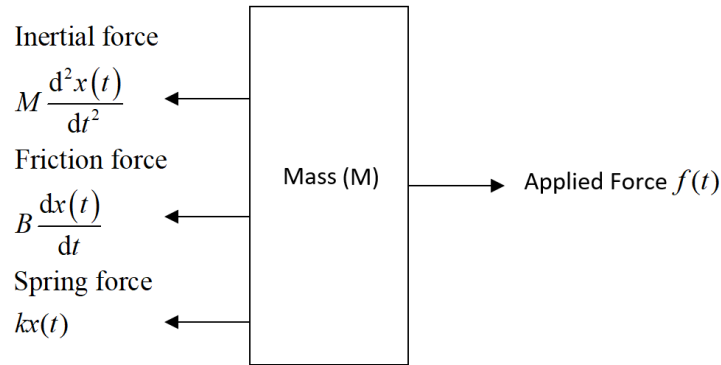
Fig. 6.7 Free body diagram of the the forces acting on the slideway carriage

$$(Ms^2 + Bs + k)X(s) = F(s) \tag{6.3}$$

$$\frac{X(s)}{F(s)} = \frac{\frac{1}{M}}{s^2 + \frac{B}{M}s + \frac{k}{M}} = \frac{k\omega_n^2}{s^2 + 2\xi\omega_n s + \omega_n^2} \tag{6.4}$$

From Equation 6.4, it is easy to understand that the spring constant k and the mass of the system M have direct influence on the undamped natural frequency ω_n:

$$\omega_n = \sqrt{\frac{k}{M}} \tag{6.5}$$

The viscous friction or damping coefficient B, as well as the other constants, are influencing the damping ratio ξ:

$$\xi = \frac{B}{2\sqrt{kM}} \tag{6.6}$$

As a motivation example, according to the time responses analysis explained above, maintaining the theory for Z-axis, the time responses zero initial conditions (state) can be assumed for its dynamics system analysis. Since the transfer function of zero initial state was determined then the time response will function as zero state response. in this case, the assumption can be made by applying some internal energy stored in the initial condition making the system react as a zero-input response instead. For the mathematical modelling, Z-Axis carriage considered as

spring cart supposedly can be displaced to a specific location from its equilibrium and brought to the rest by applying an external force to it. As a result, the force will suddenly be removed at time t=0 and vibrate until it rests due to potential energy stored in the spring. Equations 6.7 to 6.12 show the calculations of the simplified model from differential equation to applying the Laplace transformations with initial condition included system for linear displacement factor.

$$M(s^2X(s) - sx(0) - \frac{dx(0)}{dt} + B(sX(s) - x(0)) + kX(s) = 0 \tag{6.7}$$

$$M(s^2X(s) - 2.0s - 0) + B(sX(s) - 2.0) + kX(s) = 0 \tag{6.8}$$

$$M(s^2 + Bs + k)X(s) - (2Ms + 2B) = 0 \tag{6.9}$$

For simplification, the assumption was made below.

B=0.1, M=2 and K=1, then the expression for X(s) can be found as:

$$X(s) = \frac{2Ms + 2B}{Ms^2 + Bs + k} = \frac{2s + 2\frac{B}{M}}{s^2 + \frac{B}{M}s + \frac{k}{M}} = \frac{2s + 0.1}{s^2 + 0.05s + 0.5} \tag{6.10}$$

Using the transform pair, the displacement of the Z-axis can be described as:

$$\frac{s + k}{(s + a)^2 + \omega^2} \rightarrow \frac{\sqrt{(k - a)^2 + \omega^2}}{\omega} e^{-at} \sin(\omega t + \phi) \tag{6.11}$$

where:

$$\phi = \arctan \frac{\omega}{(k - a)} \tag{6.12}$$

6.4.2   Simscape Model Setup

For multi-body dynamic (MBD) analysis, 3D CAD model of the slideways on both X an Z axes used to investigated the dynamic effects of the ultraprecision diamond turning machine. Also,

to examine the dynamic motion behaviour of the linear hydrostatic bearings component such as carrier slid when different material assigned to it. the entire moving part which is the carrier, is specified as one individual rigid body to be actuated with mechanical spring as aforementioned in previous section. The programmable mass of Z-axis is as follow:

- 80Kg (Alloy Steel)

- 27Kg (30%SiC, MMC)

and X-axis:

- 180Kg (Alloy Steel)

- 60Kg (30%SiC, MMC)

For the carrier, the base has a fixed mass, including prismatic joint block system, simscape system block of world reference, solver, and transform configuration. Also, the rigid body itself has co-dependent system properties such as geometrical properties and inertia, meaning both the carrier and base will have the same set of properties as shown in the carrier and base solid properties dialogue box below, only the core inertial properties will defer. Nevertheless, the solver and transformation configuration will be identical as to allow for a single environmental sandbox setup. As illustrated in Figure 6.8, the MBD models divided into two parts with different density and mass for both material on MMC and alloy steel. The Blue Diamond turning machine presents the material of alloy steel for bothe x and z-axis while the red diamond turning machine present as for the MMC material.
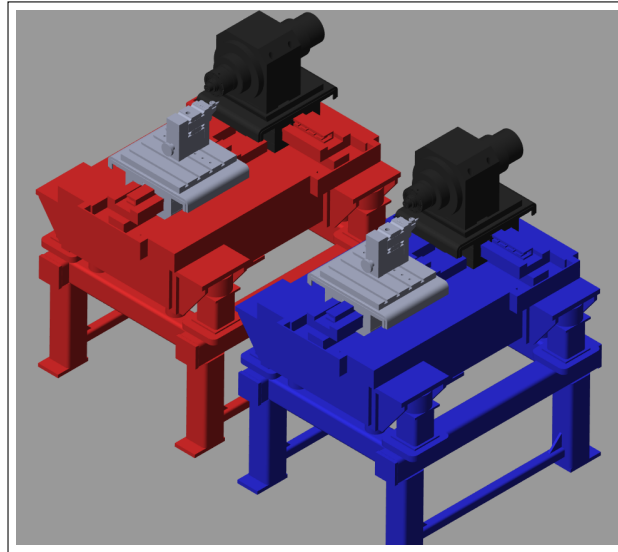
Fig. 6.8 MBD Simscape model setup

After the modelling and configuration set up have been done in Simscape software, the prismatic joint was applied to the Z-axis and X-axis in this MBD simulation model. The prismatic joint allows the lateral displacement along a particular axis of motion. It estimates the initial displacement at 5mm. The velocity will be automatically calculated based on the damping and stiffness of the mechanical input of the joint. Also, the core internal mechanics and self-actuation of the joint relationship between the two materials (Alloy Steel and MMC), are programmed through the prismatic joint, defined as a spring stiffness and damping of 1,000 N/m and 650 N/ms respectively. In addition, selected prismatic joint affords the capacity for kinematic sensing of position, velocity, and acceleration automatically calculated or provided from the control signal of the slideway control system. The determination of spring stiffness of the prismatic joint was assumed methodologically as the system spring stiffness (constant) of the coupled slideway body under an exerted force competing for maximum load-carrying capacity. Modelling of the spring in the prismatic joint at this stage was an assumption based as it gives sufficient input data to predict and approximate differentiation for the output responds for comparison analysis of these two materials. Nevertheless, mechanical force as explained in theory, determining the amount of applied force needed to accelerate the slideway's structure

mass, as well as pre-determined final velocity in regards to its mass/inertial properties. With regards to sliding friction coefficient, ideally assumed as a free-friction system, which means that truly only a small amount of applied force is needed to achieve the programmable motion pre-set values.

6.4.3   MBD Actuator

After the mechanical joints and initial condition were defined between the fixed and movable component in the linear hydrostatic bearing slide, the actuator is required to attain the motion in the motor. Experimentally, the actuator creates acceleration and a force as output which then delivered to the moving element of the coupled body-carrier. It is assumed that the initial behaviour of the actuator will result higher output value for the MMC material compared the alloy steel carrier. The actuator system damping ratio expected to be higher than the MMC material even though they're still numerically below 1. It is suggested that the materials used in this case with their mass and density are enough to command a relevant change in the output. And due to use of the lighter mass of the alternatives such as MMC material, the actuators, as a result, have a higher range of linear motion regardless of the oscillatory behaviour of the second-order actuator system.

In this case study a sweep actuator model utilised to achieve the multi-phasic of the motion study of the linear motor. As seen in Figure 6.9 and 6.10, a sweep signal with a range 1-50 Hz with gaining of 110 to amplify the magnitude of 5,500 Hz was generated. The generated signal then applied to the prismatic joint on both x and Z-axis. The same parameters of the actuators and prismatic joints applied to both deferred materials of alloy steel and MMC. Table 6.6 lists the configuration parameters applied to generate the actuator signals. The actuator generates a signal with a range of frequency between 1-50 Hz, initially starting from phase zero for a period of sweep time of two seconds.

Table 6.6 MBD actuator parameters

Actuator Parameters							
Frequency sweep	Sweep mode	Initial Frequency [Hz]	Target Frequency [Hz]	Target time[s]	Sweep time[s]	Initial phase[rad]	Sample time
Logarithmi	Unidirectiona	1	50	1	1	0	1/8000

The sweep mode is calculated as logarithmic unidirectional mode. Appendices D.3 and D.4 illustrate the multi-body dynamics models using Simscape for this case study and simulation for using MMC and alloy steel materials respectively.
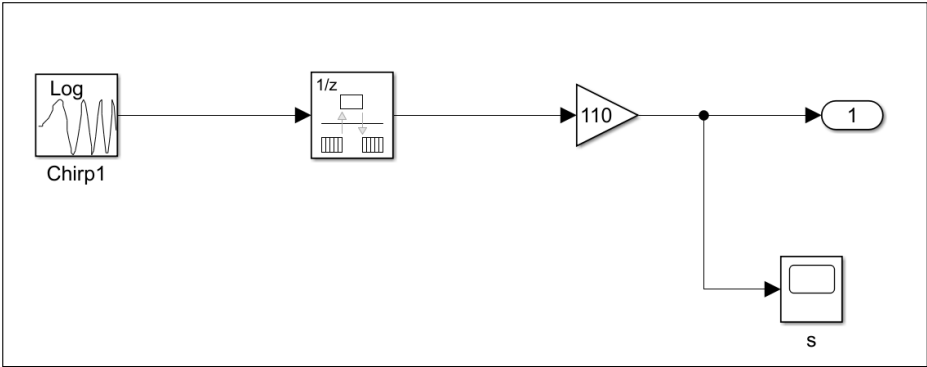
Fig. 6.9 MBD Simscape actuator
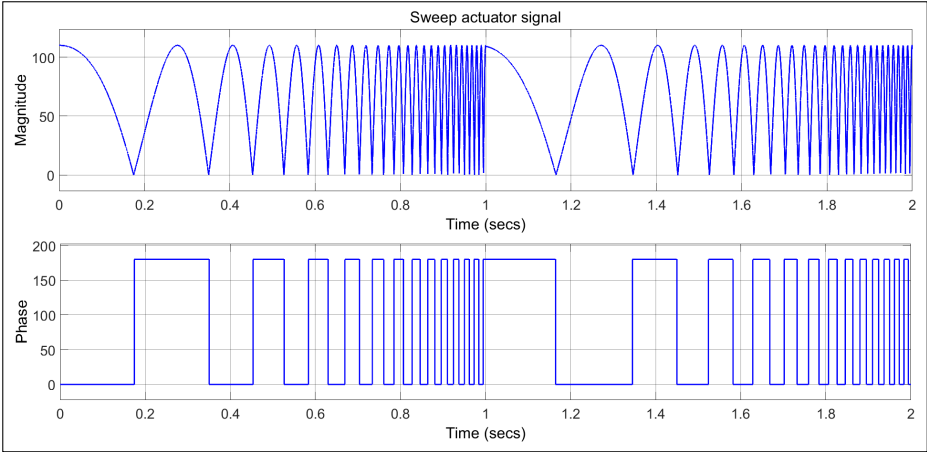
Fig. 6.10 Actuator signal

6.4.4   MBD Discussion and Results

From the result, position, velocity and acceleration at truly MBD scale were extracted. Initially, the approximate displacement, acceleration and velocity at the specific actuation frequency and vibration of the z-axis and x-axis were configured for the prismatic joints. Thus, the output will be calculated with an approximate value to obtain final comparison data for both MMC and alloy steel material. After the simulation completed, the out data for both X and Z-axis with alternative MMC material were charted, and the comparison graph was produced as shown in Appendix D.1 and D.2. Table 6.7 also shows the list of output data for approximate values of acceleration, velocity and position. Interpreting the result for acceleration proves that, the maximum value occurs in the benchmark scenario for MMC material is higher than alloy steel. Analysing this data can prove that, the lighter material such as MMC with higher frequency can respond quicker with compare to high-density material such as alloy steel. This phenomenon also confirmed the theory, as earlier explained in previous section, in structural frequency respond analysis. Overviewing the result data of the accelerations shown in Table 6.7, states the maximum value of 1.46 m/s^2 in z-axis for alloy steel and 2.8 m/s^2 for MMC material. The results show that more than 50% increase in acceleration when MMC material was employed. This differing in value is much considered in the x-axis where the mass is normally higher than z-axis. The value calculated in X-axis with MMC material is approximately equivalent to the Z-axis with alloy steel material. Conceivably, the replacement of the lighter material such as MMC, as stated in the literature review, can elaborate and brings much efficient and capable design and viable machining with regards to hydrostatic bearing in ultraprecision machining and precision engineering fields.

Table 6.7 MBD signal statistic comparison, MMC vs alloy steel

			Signal Statistic					
			Max	**Min**	**Peak**	**Mean**	**Meadian**	**RMS**
Alloy	Z-axis	Acceleration [m/s^2]	1.46	-1.48	2.9	1.30E-03	7.39E-03	9.40E-01
		Velocity [m/s]	8.97E-02	-7.95E-02	1.69E-01	2.20E-03	7.60E-04	3.96E-02
		Position [m]	1.40E-02	-6.73E-03	2.11E-02	4.29E-03	4.30E-03	6.10E-03
	X-axis	Acceleration [m/s^2]	6.47E-01	-6.55E-01	1.3	2.30E-03	4.90E-03	4.33E-01
		Velocity [m/s]	5.50E-02	-5.00E-02	1.05E-01	1.80E-03	1.47E-03	2.18E-02
		Position [m]	9.80E-03	-2.23E-03	1.20E-02	4.25E-03	3.56E-03	5.44E-03
MMC	Z-axis	Acceleration [m/s^2]	2.87	-2.75	5.62	2.00E-03	8.03E-03	1.74E+00
		Velocity [m/s]	1.34E-01	-1.30E-01	2.64E-01	2.18E-03	9.20E-04	5.90E-02
		Position [m]	1.70E-02	-9.33E-03	2.60E-02	4.30E-03	4.40E-03	6.70E-03
	X-axis	Acceleration [m/s^2]	1.29	-1.3	2.6	1.40E-03	6.90E-03	8.44E-01
		Velocity [m/s]	8.44E-02	-7.70E-04	1.59E-01	2.20E-03	7.70E-04	3.65E-02
		Position [m]	1.38E-02	-6.17E-03	1.90E-02	4.28E-03	4.34E-03	6.02E-03

Analysing the velocity output data in Z-axis also affirms a significant development utilising the MMC material with compare to alloy steel. The maximum velocity of 8.97e-02 m/s for alloy steel and 1.34e-01 m/s for MMC calculated, which shows an acceptable increase in the velocity value where the MMC material was used. Analysing the positioning output data can validate the robustness of displacement when the MMC material was used. From the output result data indicated in Table 6.7 and Appendix D.1, the linear motor's movement response along its axis, it has been found that the MMC material is more instantaneous than the alloy steel. As can be seen in appendix D.1(c), the maximum linear displace in z-axis evaluated value of approximately 1.7e-02 m (17 mm) for MMC material and 1.4e-02 m (14mm) for alloy steel within 0.2 s. repeatedly, interpreting this value dispenses more the idea of using the MMC material in the hydrostatic linear motor in precision engineering particularly where the STS technique need to be used for freeform surface machining. This advantage can bridge the gap in ultraprecision machining of freeform surface using STS mode, enabling bandwidth frequency with a longer stroke.

6.5 Concluding Remarks

Linear slideways both hydrostatic and aerostatic bearings are widely used in ultraprecision machines for machining freeform surfaces. The kinematic and dynamic effects have direct impact on the performance of the machining system. Hence the proper design of the linear slideways is playing a major role in precision engineering and dealing with such characteristics and challenges. One of these characteristic challenges is the load-carrying and lack of sufficient bandwidth in slow tool servo technique. In this chapter, a novel solution to that characteristics was presented. A new method of using metal matrix composite (MMC) was described. The literature of the MMC material also reviewed. In this research study also a new design based in existing linear slideways was carried out, and the analytical comparison was made. The FEA methodology was utilised to investigate the influence of structural design between alloy steel material and alternative material such as MMC material. A modal and harmonic analysis was made to find the natural frequency of the system and harmonic frequency responses. A result also was compared with existing commercial design. For validating the idea of using lighter material such as MMC material, a multibody body dynamic model was set up using Simscape software. Finally, the design and the result analytically compared some characteristic Kinematic effects such as acceleration, velocity and positioning. The result has shown permissible output in utilising the MMC material in the linear hydrostatic bearing.

Despite the effect of dampening and stiffness capacity and its correlation to motion properties in a kinematic system for a hydrostatic bearing with sweep vibrational feature occurrences has already been explained, the study of dynamic effect scenario with regard to the system configuration and responses where a freeform surfaced component utilised is essential. The following chapter will discuss the dynamics effect of an ultraprecision machining of freeform surfaced component will be investigated, and an analytical comparison will be made to find out the machining performance of the system and their influence in the output data.

Chapter 7

Hydrostatic Bearing and Dynamic Characteristics in UPM

7.1 Introduction

Ultraprecision machining of freeform surfaces through diamond turning is becoming one of the most reliable enabling processes, as it can deliver high accuracy and efficiency by integrating distinctive precision engineering techniques of fast tool servo (FTS) and slow tool servo (STS). Freeform surfaces are increasingly employed in precision engineering industries, including automotive, optics, electronics, aerospace and biomedical engineering industries [4, 94]. In its ultraprecision machining process, it normally starts by using a CAD/CAM tool to generate the toolpath trajectory. The toolpath generation can base on the real form of the freeform surface, and/or use tool compensation trajectory to deal with the surface form error and correction modification of the final toolpath [47, 54]. In ultraprecision machining components with NURBS (Non-uniform rational basis spline) surfaces, the diamond tool has to move as a function of the spindle rotation and translation of the machine slide. The method is different from using tool servos to generate the tool motion [38, 97].

Moreover, the mechanism of material removal is different in using FTS and STS modes machining. The achievement of good surface finishing is still challenging in ultraprecision machining through FTS and STS configurations [50, 6]. To fulfil the increasing requirements for high precision and productivity in ultraprecision machining of freeform surfaces, it is essentially important to scientifically understand the dynamics, material and mechanical stiffness, friction, tooling, and accuracy of the servo system, and their collective effects and underlying implementation perspectives in next generation ultraprecision machining systems.

The research presented in this chapter is focused on a multibody dynamics-oriented approach to ultraprecision machining of freeform surfaces and beyond, in the light of scientific understanding of the underlying protocol and algorithms of the approach and its implementation perspectives. The approach is centred on interfacial cutting dynamics at the tool and workpiece surface interactions, while the tool and workpiece are supported by a chain of multibody elements on the machine. The approach is evaluated and validated through industrial case studies on ultraprecision machining of freeform surfaces and components against industrial requirements. To some extent, it also provides an innovative exploration from engineering science fundamentals (mechanics and dynamics) to precision engineering, and next generation ultraprecision machining systems for higher precision and beyond (such as pico-precision).

7.2   Dynamics Effects and Slow Tool Servo Mode Ultraprecision Machining

Slow tool servo (STS) can be directly applied on any modern diamond turning machine. It can achieve a few millimeter displacements in non-rotational symmetric applications [117]. Unlike the FTS technique, STS does not require any additional axis for the tool motions, as the tool directly sits on the slide to produce the synchronized slide-spindle motions and thus freeform surfaces generation [34]. However, there is still a substantial mileage in improving

the dynamics of the synchronized motions. Furthermore, it is fundamentally essential for having scientific understanding of the dynamics chain supporting the interfacial interaction between the cutting tool tip and the surfaces generated, and therefore leading to development of next generation ultraprecision machining systems with higher precision and manufacturing productivity.

7.2.1   Dynamics Characterisation

Several key characteristic features need to be valid for undertaking STS mode machining on a diamond turning machine, which are mostly applied to friction- free linear and rotary axes. The control system with high speed data processing capacity plays a key role in very accurately actuating the motors and all the direct drive axes. The key factors affecting the precision positioning in the machining system should be taken fully account, including the encoder resolution, thermal stability, high-order trajectory generation, precision data acquisition method and the system stiffness in the control loop. In-process analysis of the positioning loop and the loop dynamics is critical in STS mode ultraprecision machining, since the freeform surface topology has a direct effect on the cutting tool velocity and acceleration. The implementation of high positioning loop bandwidth is therefore also an essential requirement in STS. The evaluation of the actuation acceleration and velocity at the machining system is dependent on the freeform surface curvatures and sagittal features so as to maintain the appropriate bandwidth. Analysis of the freeform surface geometry in relation to the tool tip and workpiece interfacial surface is thus required to specify the dynamics in the system, rendered by the mechanical structure, electrical actuation, in-process positioning feedback, and control algorithms, etc. collectively.
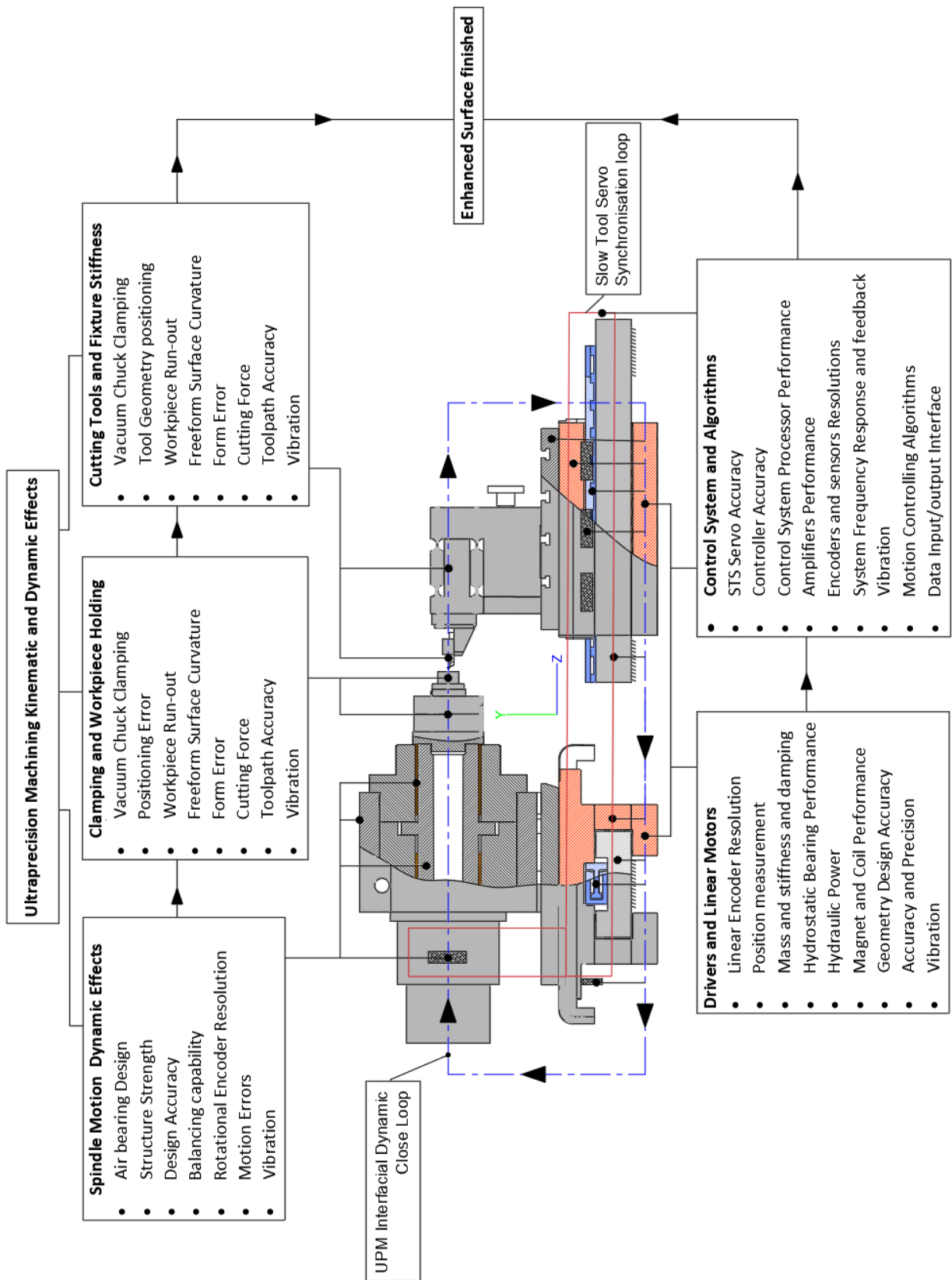
Fig. 7.1 Ultraprecision machining kinematic and dynamics characteristics

The tool trajectory method for conventional ultraprecision toolpath generation is unable to effectively harness the system dynamics affected by the freeform surface itself, such as the tool velocity and acceleration, tool friction and surface contact force. Figure 7.1 illustrates the most characteristic elements maintaining the dynamics characteristics in a typical ultraprecision machining system. Scientific understanding of the interfacial dynamics between the tool tip and workpiece surface and further the dynamics in the machining loop is fundamentally essential for developing future ultraprecision machining systems particularly in working towards higher precision and productivity.

7.2.2   Dynamic Cutting Force and Characteristics

Based on the specifications and design of the freeform surface, the tool path should be generated at the initial stage of the process. Machining process parameters based on both tool and surface geometry are selected to fulfil the targeted requirement while taking account of the dynamic cutting forces. Tool interference analysis needs to be carried out to check, identify and eliminate the overcutting between the tool and surface. The tool axis motion analysis is also required for the toolpath generation process, from which numerical modelling is further developed to predict the theoretical surface generation and its reliant features. Tool compensation analysis is needed to make sure that the real surface profile and topography are achieved after machining.

Whilst the current toolpath generation method can provide a cutting tool path for freeform surfaces in ultraprecision machining, the dynamics and kinematics effects on the tool and surface features are not included. Therefore, in freeform surfaces ultraprecision machining, further research is needed to investigate the intrinsic relationship between those dynamic effects and surface finish for achieving the higher precision and machining efficiency in particular.

7.2.3 Tool Geometry and Surface Characterisation

Tool geometries play a significant role in successful machining using STS methodology. The tool feature selection relates directly to the topology of the freeform surface, such as curvature and sagittal elements. A freeform surface consists of various curvature features that need to be considered very carefully in STS machining. Compatibility between the cutting tool nose radius and surfaces maximum and the minimum curvature is a key requirement to avoid any interference during the machining process. Furthermore, the form error can occur when the minimum surface curvature is less than that of the tool nose. The curvature of the surface can be defined as 1/R for both the tool nose and the freeform surface. Tool included angle and front clearance angle are dependent and should be less than the maximum surface curvature angle at the tangent point. Dynamically, in the larger sagittal curvature of the surface, the tool acceleration and velocity are higher for the STS machining technique. Thus, the dynamic and kinematic effects of the tool on the surface geometry should be considered.

7.3 Towards Higher Precision and the Associated Implementations

At existing modern ultraprecision machine tools and machining practices, the positioning and motion control of the machine actuation systems, such as the slideway and spindle, are heavily dependent on using linear and rotary encoders. However, the positioning control is quite 'passive' in terms of not directly monitoring and control of the tool and the workpiece positions in the dynamic machining process, which is under the assumption of the machining system being rigid and cutting dynamics stable. Such machine design configurations or existing issues are hindering the progress in ultraprecision machining towards higher precision, e.g. pico-precision , which is inevitably needing to be addressed while likely having to be in an innovative step-change manner [118, 119].

7.3.1 Ultraprecision Machining MBD for Freeform Surfaces

Three-axis ultraprecision machining can be synergized as a rigid body sliding wedge with a preloaded spring following a freeform trajectory. Motor loads and actuation are normally under preloaded magnetic forces, the contact point between the tooltip and the workpiece surface can therefore be identified as a spherical joint and their resultant forces are varied with respect to the curvature of the workpiece freeform surface. Figure 7.2(a) shows the multi-body diagram of the three-axis ultraprecision machining of freeform surfaces. Individual points of the toolpath are recognized as the input for the controller, through which the servo motors driving X and Z and C axes are synchronized and close the loop of the STS mechanism.
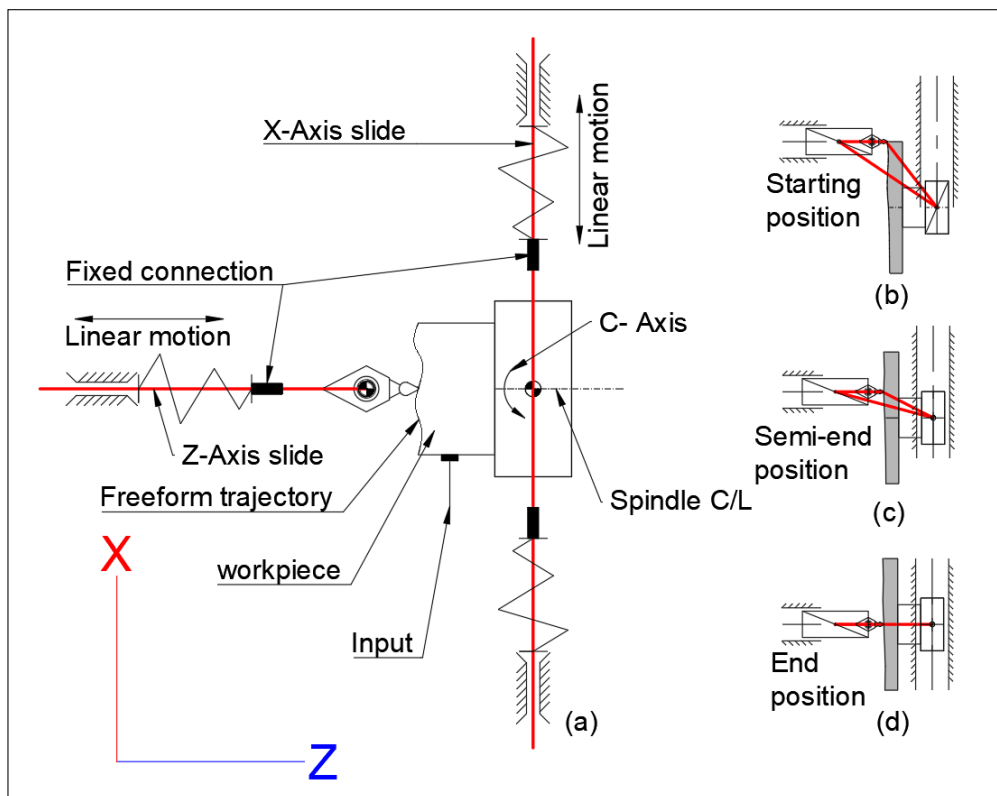

Fig. 7.2 UPM multi-body diagram vectors: (a) three axis UPM diagram; (b) starting position; (c) semi-end position; (d) end position

Figure 7.2(b), 7.2(c) and 7.2(d) respectively illustrate the multi-body linkage of the resultant vectors and simplification of the system mechanism diagram from the starting point to the

semi-end and end positions acting on the linear and rotary motors. From the dynamics point of view, as shown at the diagram, it is found that each point at the toolpath trajectory has a different resultant vector that forms the linear motions of the linear motors, which generates non-linear reaction forces at the moveable bodies in the system during the cutting process. The reaction forces have characteristic influence and the impact on the precision positioning of the tool. The coordinates and notation system used to specify the linear drive acting forces and their distribution is illustrated in Figure 7.3 particularly for the ultraprecision machining scenario as discussed. .

As seen from the figure, the system consists of three major force vector components in which the resultant force F_R always acting from the center of mass of the slides, COMz and COMx respectively and vice versa. Each moving slide (carriage) is identified as a rigid body carrying 6 degrees of freedom (DOF) at the center of mass, i.e. including three translational and three rotational components. The rotational components are the Pitch, Yaw and Roll at x, y, z directions in the Cartesian coordinate system. The contact point between the tooltip and the workpiece surface is also subject to varied interfacial force $F_C y$ along its x and y directions respectively. The resultant of this interfacial force is translated through the component force vector of F_z and F_x.

With respect to the force $F_C y$ it is envisaged that the freeform surfaced workpiece has varied reaction forces at the individual interfacial points in the machining process due to varied curvatures. The behaviour of the forces reacted at the center of the slide mass can be nonlinear. This phenomenon highlights the cutting forces at the contact point between the tooltip and workpiece surface always has a mutual influence and impact on the performance of the moving slides, which should not be neglected. Furthermore, the ability of measuring the forces at each individual point of the toolpath can enforce the capability of the control system by shifting from the semi-close loop to full close loop, i.e. the interfacial forces being used as a feedback to monitor and control the dynamics of the slide and the spindle in a much direct and robust
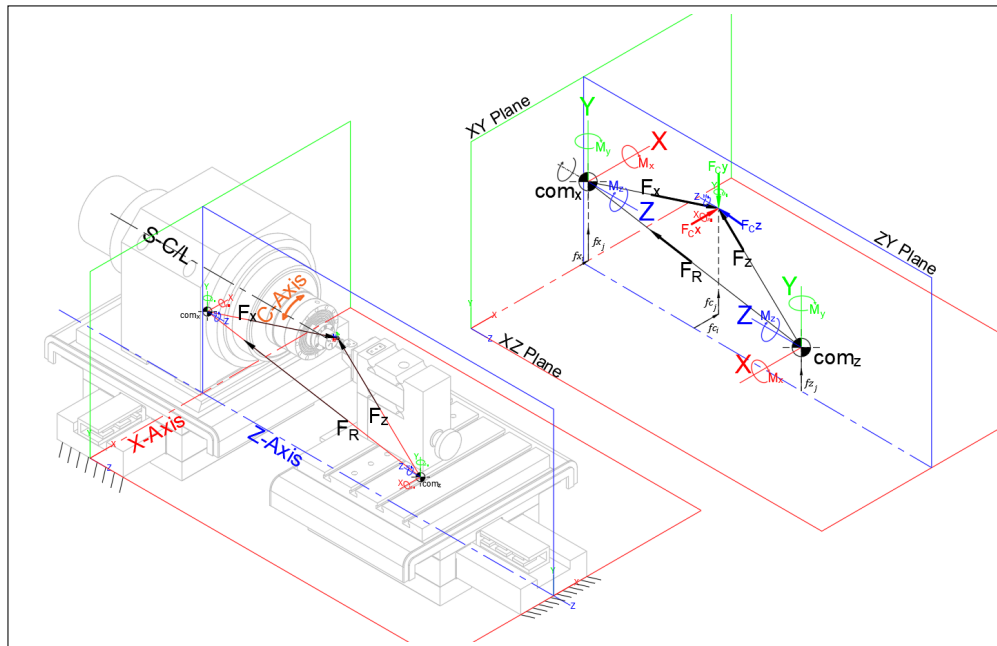
Fig. 7.3 Dynamic force free body 3D diagram for UPM

way. The next two subsections will describe and explore the mutual impact of the interfacial forces above on the hydrostatic linear sideways and the air-bearing spindle.

7.3.2 Freeform Curvature and Dynamic Cutting Force Effects

The resultant interfacial forces at the contact point between the tooltip and workpiece surface is varied due to the surface curvatures and geometrical topology. This phenomenon has significant impact on the workpiece surface finishing. As illustrated in Figure 7.4, in ultraprecision machining of a freeform surface, the chips formed in the process are subject to the three-zone material removal coherently with the changes of curvature geometries. Those zones are characterized as Flowing, Normal and Fracturing.

The chip occurred at Flowing zone is when the tool approaches onto the surfaces with a larger curvature angle. During the cutting process, when the tangential plane of the curvature is perpendicular to the tooltip, there is a normal force distribution on the cutting chip. As the
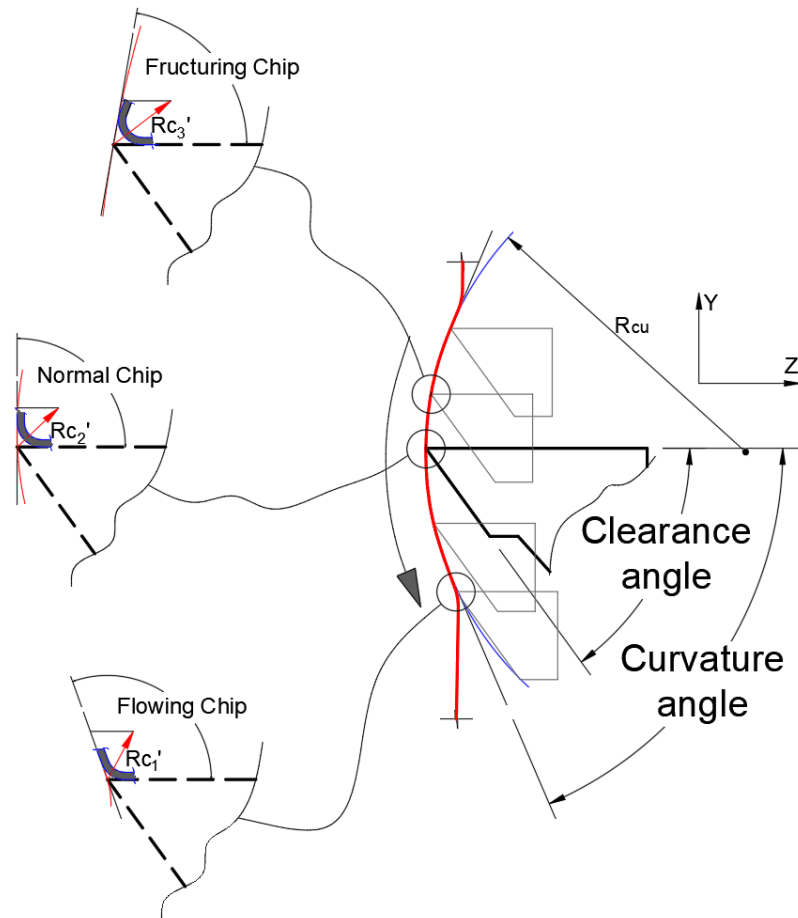
Fig. 7.4 Curvature effects and dynamics cutting force in freeform surfaces

cutting process continues and when the tool approaches to a tight curvature angle, there is the highest amount of the resultant forces generated and acting on the chip fracture.

This phenomenon can influence the dynamics of the machining system particularly through the force impact on the hydrostatic bearing supported slide and the rotational air-bearing spindle. Therefore, scientific understanding and prediction of the interfacial forces acting at the tooltip-workpiece surface are important for further increasing the dynamic capacity and performance of an ultraprecision machining system.

Figure 7.5 highlights the major dynamic effects and factors needing to be considered in dynamic monitoring and control of the tool and workpiece positioning.
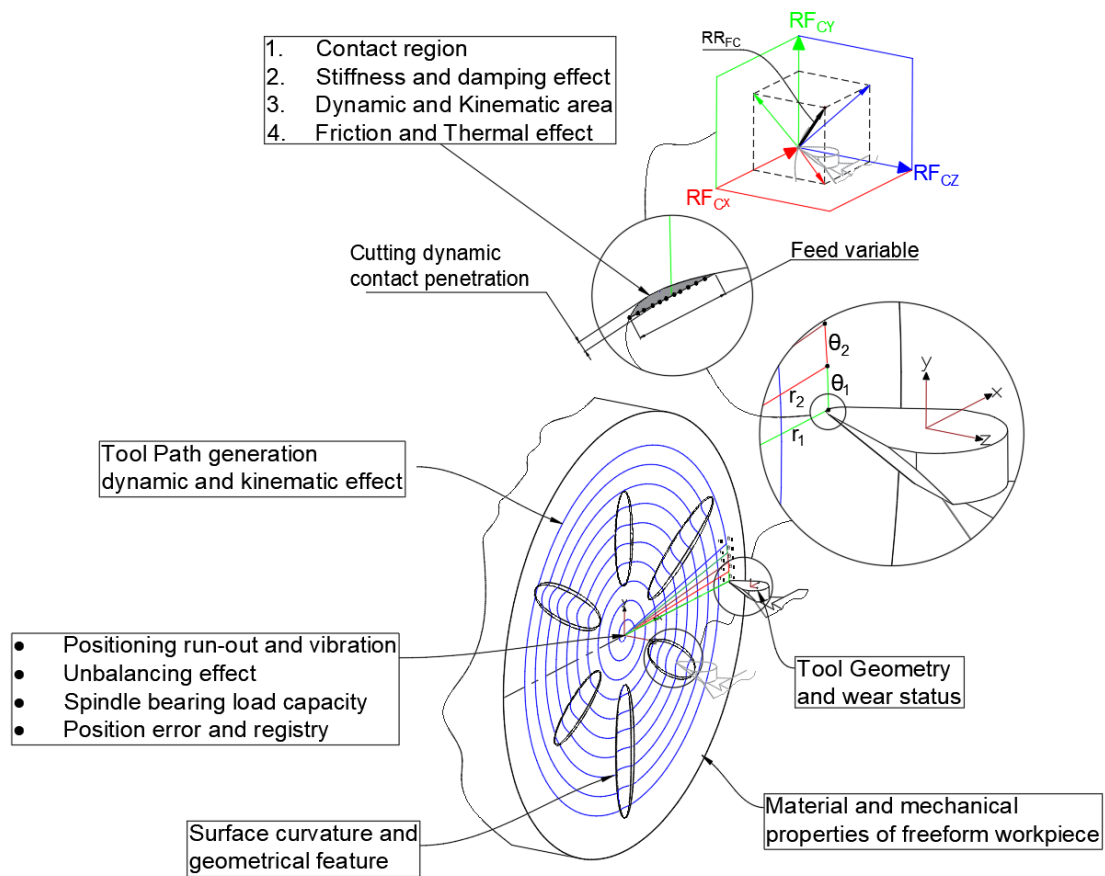
Fig. 7.5 Dynamic effect factors in positioning controls

Although the resolution of the currently employed encoders in ultraprecision machining systems is highly capable for kinematic positioning control of the slide and spindle elements, it is still far from the full close loop control taking account of the dynamic interfacial interactions of the tooltip and workpiece surface as the feedback input. Nevertheless, the full close loop control with the dynamics and interfacial interactions of the tooltip and workpiece surface is essential for the next generation ultraprecision machining system particularly working towards higher precision requirements.

7.3.3   Dynamic Effects at the Hydrostatic Bearing Supported Linear Slide-way

Hydrostatic bearing supported slideways are often applied in an ultraprecision machining system for maintaining high stiffness and loading capacity. As illustrated in Figure 7.6, the load capacity **Fv** includes all resultant forces from cutting forces, static loading and damping in the machining process transferred onto the constraint planner joints between the stationary and moveable parts. The pressure of the hydraulic flow through the orifices has a gradient and being varied by mass flow rate of the oil fluid. Despite the hydrostatic bearing supported slideways being applied at precision machines for a few decades, very few investigations were carried out on the influence of the system dynamics particularly linked to the hydrostatic bearing system, in the STS mode ultraprecision machining of freeform surfaces.

In hydrostatic bearing design specifications, the oil orifices or constraint slot entries to the hydrostatic bearing are at the dimensional range of 10-20 μm based on the load capacity and stiffness requirements, which is fundamentally subject to dynamics and kinematics linking to motion displacement, velocity and acceleration between the rail block and carriage at the constraint plane. The second order mass-spring-damping system theory is applied as the Newtonian fluid forms the pressure zone and force distribution around the constraint pockets horizontally in F_{hh} and vertically in F_{vh} respectively. Therefore, in machining freeform surfaces, the resultant vectors F_{Hc} and F_{Vc} can respectively determine nonlinear force curves at the constraint plane against the pressurized fluid flow through the constraint orifice or slot entries. Those forces have influences on dynamics and dynamic performance of hydrostatic bearings and the slideway.

7.3.4   Dynamic Effects and Encoders Resolution for Higher Precision

As discussed in the previous subsections, the positioning accuracy in ultraprecision machining is highly affected by machining dynamic and substantially needs to be considered with the
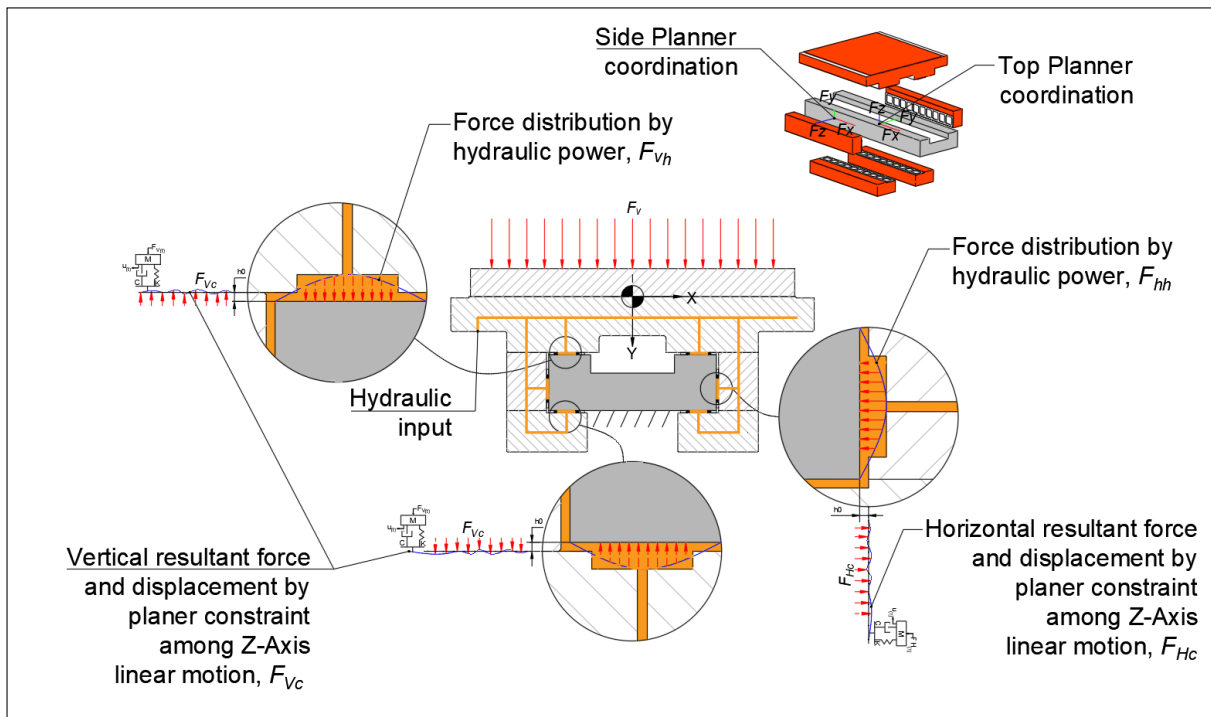
Fig. 7.6 Linear hydrostatic bearing dynamic effect

machining system dynamics simultaneously. The interfacial cutting force among all other dynamic parameters should be linked to the positioning control in STS mode machining of freeform surfaces, since it has the direct impact on obtaining higher finishing of the surfaces.

Figure 7.7 shows a graphical illustration of the intrinsic linkages and effects of the dynamic force compositions including interfacial cutting force, and the pressurized oil-film layer h0. During the cutting process, it is envisaged that two different respective zones, stable and unstable, are occurred in the film gap h_0.

The stable pressurized zone is at the area between the stationary and moveable part, where the hydrostatic oil is affected by its viscosity stiffness and damping coefficient. While at the unstable zone, the interfacial resultant forces caused by the workpiece's surface curvature are transferred through the moveable slider constraint forces into the stable pressurized zone. The force ratio and distribution are quite small; however, they are varied dependent on the linear displacement range $\Delta\mu_s$ of the slider. The existing encoders with high resolution are
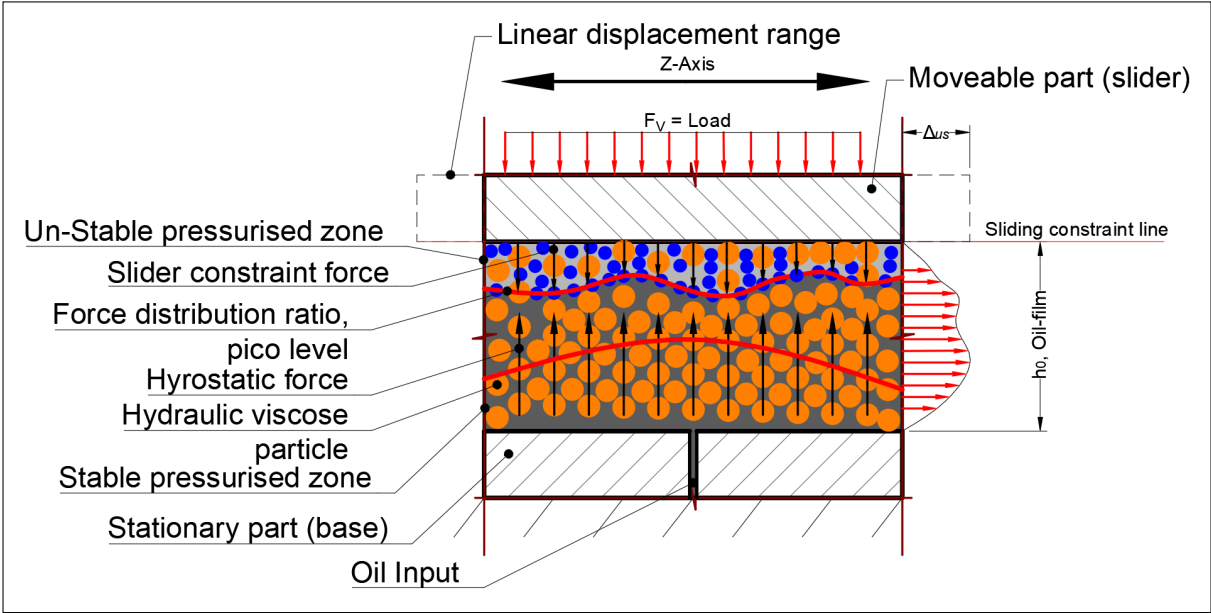
Fig. 7.7 Pico-precision effects and encoder resolution

still unable to capture the uncertainty of the dynamic displacement and the dynamic forces in the constraint line, as they are not designed and configured for fulfilling the full closed-loop control as discussed for the machining system.

7.4   Dynamics Simulation using ADAMS

Kinematic and dynamic effects in an open-loop slideway with linear motion were analysed, and the results were explained in Chapter 6. Nevertheless, the investigation of the dynamics and kinematic effects of the freeform closed-loop with freeform toolpath is essential.

(a)

(b)

Flat surface

Multi-curvature
surface

ADAMS
Toolpath

(c)
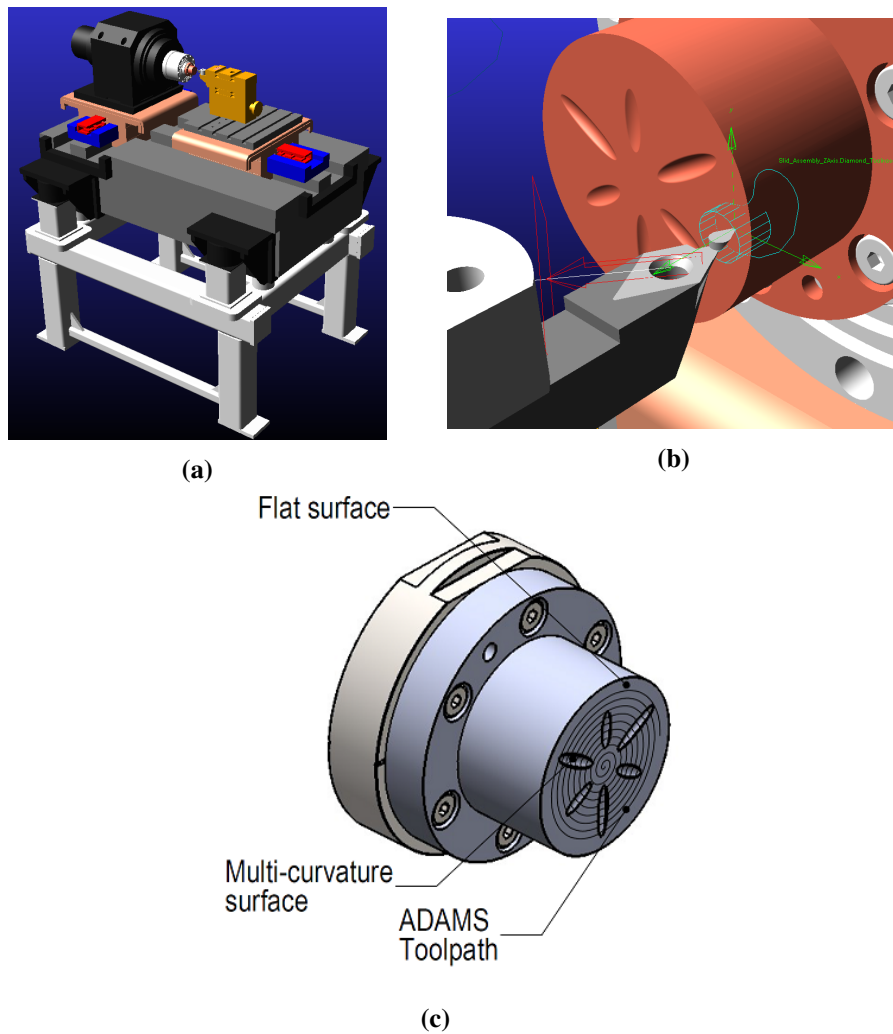
Fig. 7.8 ADAMS model for hydrostatic bearing slideway analysis: (a) imported CAD model of UPM; (b) multi-curvature workpiece; (c) workpiece with toolpath generated by ADAMS

To fulfil the solution for the knowledge gap identified in the literature review with regards to STS technology in ultraprecision machining, two types of simulation models was prepared utilising ADAMS software. As explained in previous sections in this chapter, machining the freeform surfaces is related to the surface topology and geometrical curvature of the workpiece. Hence, for the purpose of this study, an existing diamond turning machine in standard industrial level was modelled using the CAD software and imported into ADAMS for dynamic and kinematic analysis. The primary model was set up with a standard prismatic linear connection joint for the slideways in both X and Z axis. The secondary model was prepared based on

Table 7.1 Numerical motion study and analysis data

Analysis Data	Value	Units
Rotary motor speed	30	RPM
Feed rate (x-axis)	0.01	mm/s
initial force	1	N
Dynamic friction	0.25	-
Static friction	0.3	-
Elastic impact stiffness	100000	N/mm
Max Damping	50	$N/(mm/s)$
Penetration	0.0	mm
Integrator	Value	Units
Frames per second	360	-
3D Contact Resolution	High	-
Accuracy	0.0000001	-
Integrator Type	WSTIFF	-
Max Iteration	25	-
Initial Integrator Step Size	0.00001	-
Min Integrator Step Size	0.000001	-
Max Integrator Step Size	0.01	-
Jacobian Re-evaluation	Every Iteration	-

planar joint constraint which can be applied between the base and carriage planar surfaces to maintain the linear motion for hydrostatic bearing. The results of both models will be explained in the following section and the effect of their characteristic impacts will be investigated. Figure 7.8 shows the ADAMS model and the workpiece designed with multi-curvature for this study.

7.4.1   Numerical Analysis

Numerical analysis has been carried out for both models as abovementioned, to investigate the dynamic effect of the STS machining process. While the 3D CAD model was imported into ADAMS, a toolpath generation process was formed using the recently developed multi-body dynamic methodology as described in Chapter 3 [120].

Table 7.1 shows the ADAM/solvers parameters data for TPG and numerical setup in this study. Figures 7.9(a) and 7.9(b) illustrate the final 3D toolpath curve, which has been generated in a vector type of X, Y and Z direction in the Cartesian plane. A different approach has been

conducted to investigate the dynamic impact in a freeform surface with more considerable sag. Figure 7.9(c) shows a freeform surface that includes several different groves with higher curvature value. As shown in Figure 7.9(d), the curvature analysis shows the maximum curvature value in the groves. After running the simulation, a precise toolpath was generated based on the tool and surface geometry, as illustrated in Figure 7.9(b). From an advantage perspective, the dynamical effects within the toolpath generation, such as contact force, velocity, acceleration, moment force and displacements can be calculated with the multi-body dynamic method.

(a)

(b)

(c)

(d)
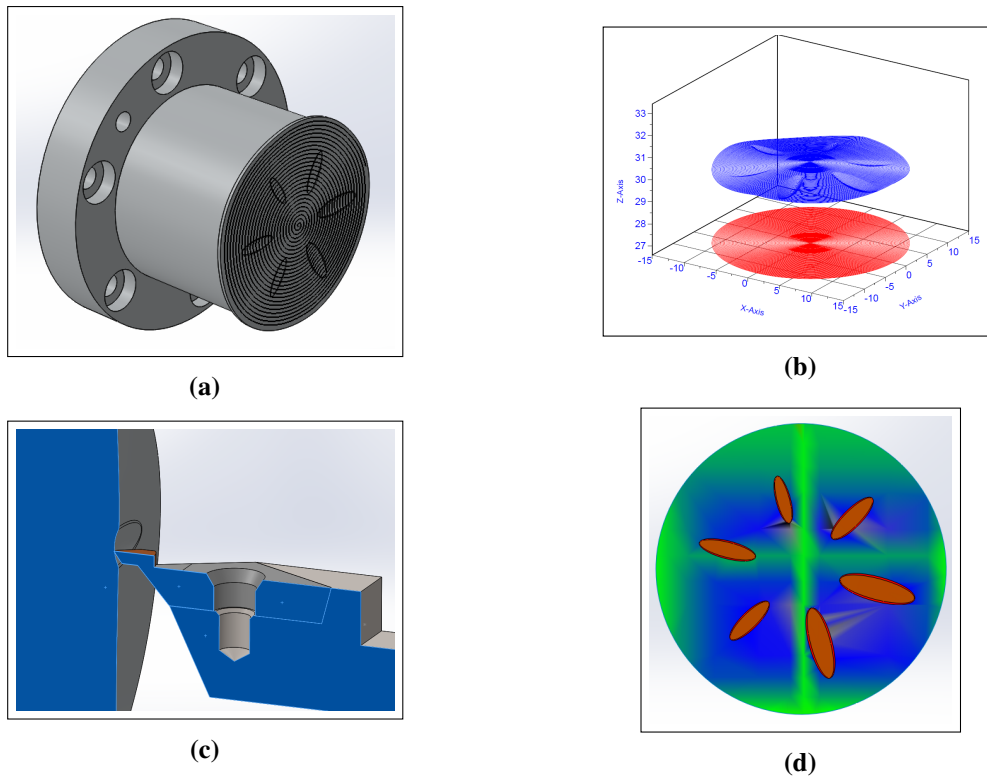
Fig. 7.9 Freeform surface with large curvature: (a) freeform workpiece; (b) toolpath generated by the ADAMS/solver; (c) freeform workpiece with groves; (d) surface curvature analysis

7.4.2   Dynamic Effect of Prismatic Linear Joint

As for primary dynamic simulation with standard constraint joint set up for the slideways, a comparison method was used to investigate the effect of dynamics and kinematics of the system.

As illustrated in Figure 7.10, a prismatic joint was set up between the base and the Z-axis, similarly as well as X-axis. A rotational joint also was set up for the spindle between the fixed hosing and rotational shaft. After the simulation was completed, the result was set to extract the data of the interest. For the kinematic analysis, the data extracted base in acceleration, velocity and position quantitative characteristic. It is important to mention the controlling system in this simulation was excluded whilst the effect of the dynamic will be studied only base in freeform toolpath in the workpiece geometry. Since the controlling system in ultraprecision machining is a semi-closed loop, the dynamic effects of the system will be relying on the kinematic controlling while the equation of motion will be achieved only base on positioning in the controller. in wider explanation, the dynamic effects such as forces in the linear motor and the tooltip, the controller have no control. Thus the principle of the study would be in a method that can predict and calculate both kinematic and dynamic characteristics in the system to make the controlling system function as fully closed-loop.

Fig. 7.10 ADAMS model with prismatic linear joint

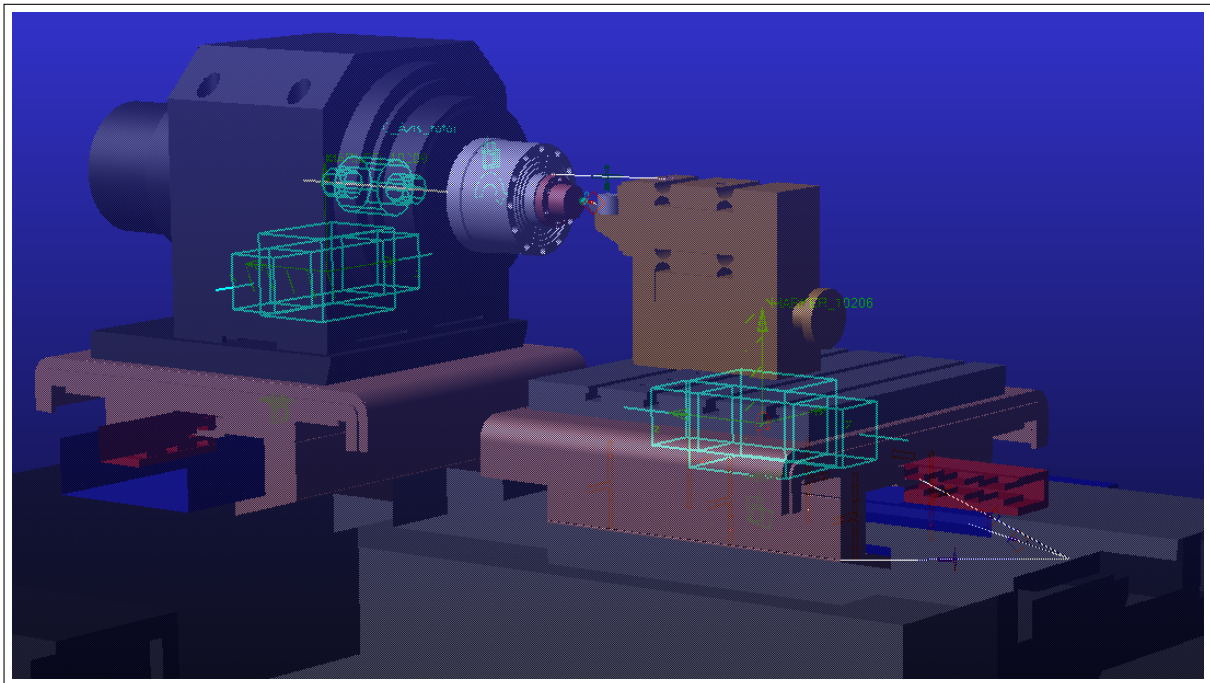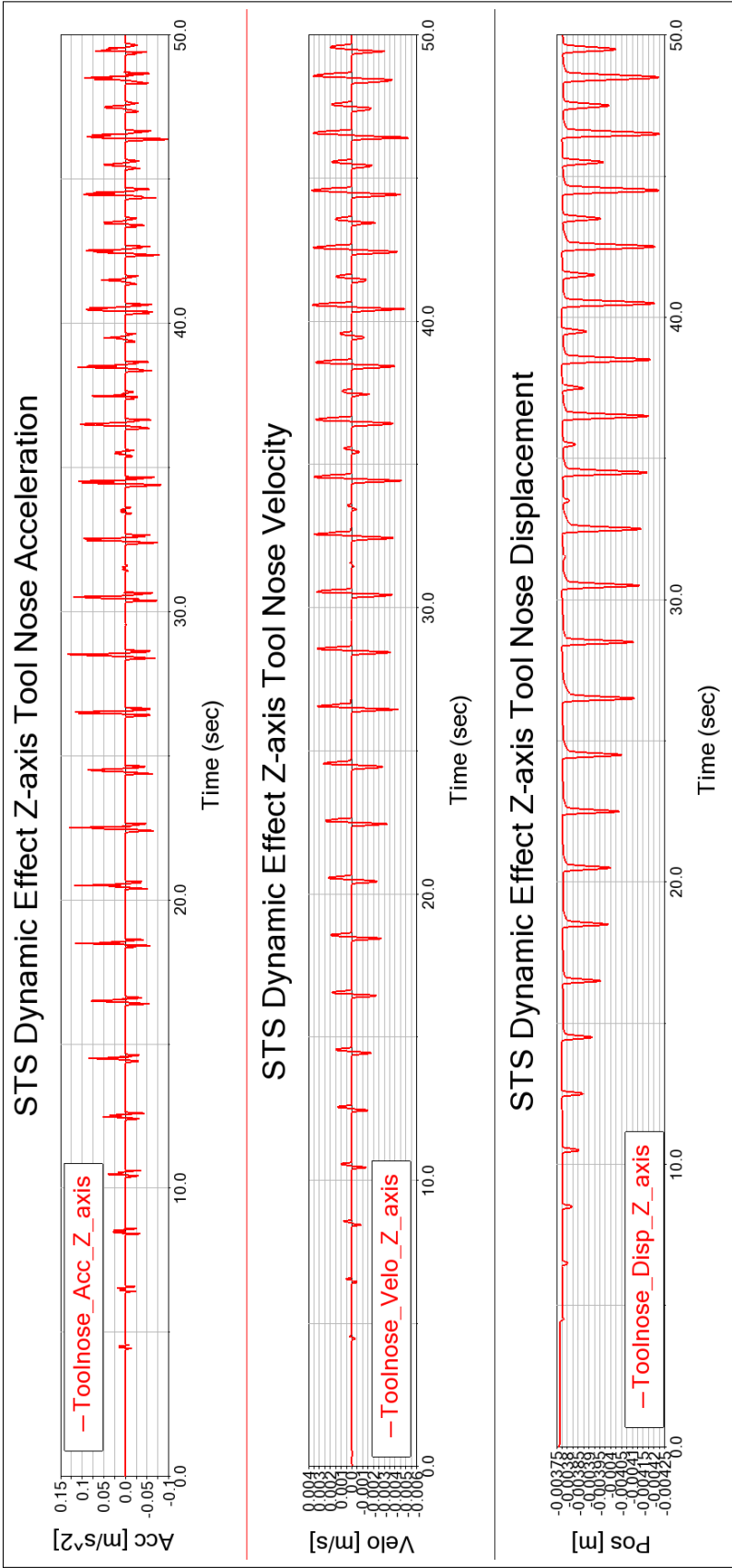**Fig. 7.11** Kinematic calculated tool nose acceleration, velocity and position during the toolpath generation process using the multi-body dynamics methodology

In order to model this environment in the system, the tool nose was constrained in the freeform toolpath. Hence, when the spindle rotates in such rotational speed, it supposes to have a different response with regards to the reaction force in the freeform toolpath constraint. However, accurate measurement for reaction forces can be made in the tooltip and the linear hydrostatic bearing as well.

While these forces were extracted from the result, then they can be used to communicate with the controlling system in closed-loop. After the completion of the simulation, as a result, the kinematic data were analysed. Accordingly, Figure 7.11 illustrates the graph of the calculated acceleration, velocity and position in the tool nose when Alloy steel material assigned to z-axis slideway. As can be seen, the maximum value of the acceleration and velocity have been calculated in the freeform surface in which are within the accepted value in the UPM. Interpreting the result can prove that the value of the output is varied when the curvature of the surface is changed during the machining process. Maximum peak value calculated in the maximum curvature in the geometry.

Dynamically the forces also were analysed. Three types of forces were investigated including, a) the tool nose contact force, b) the prismatic joint force and c) the toolpath mate reaction forces in which thought to be the interfacial forces of the tooltip occurred in the freeform surfaces. The comparison analysis was made between MMC and Alloy steel materials to find out the dynamic impact of the system. The graph stated in Figure 7.12, illustrates the dynamic forces calculated in Y-direction of the prismatic joint comparing both MMC and Alloy material. Y-direction, as explained in the previous section, is the effective vector that the cutting force assumed to be applied in. Thus, analysing the dynamic impact in this direction is critical. Translating the result can prove that the peak value calculated for MMC is lower than alloy steel in the prismatic joint employed in the z-axis slideway by means that the influence of the mass has a direct effect in the performance of the motions.
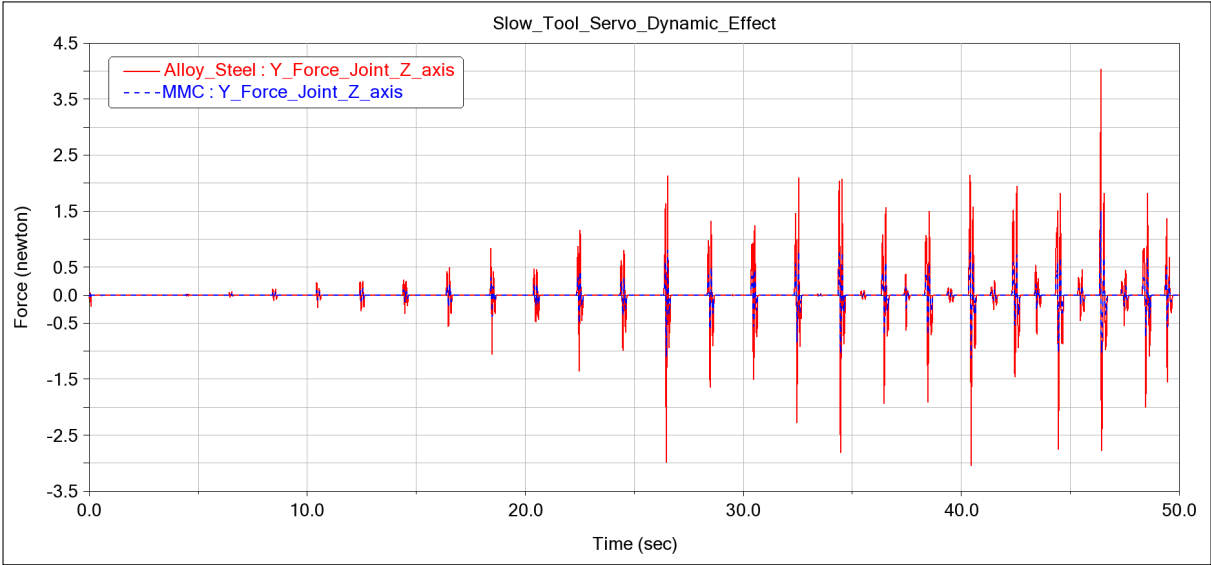
Fig. 7.12 Dynamic force comparison in both MMC and alloy steel, prismatic joint Y-direction reaction force
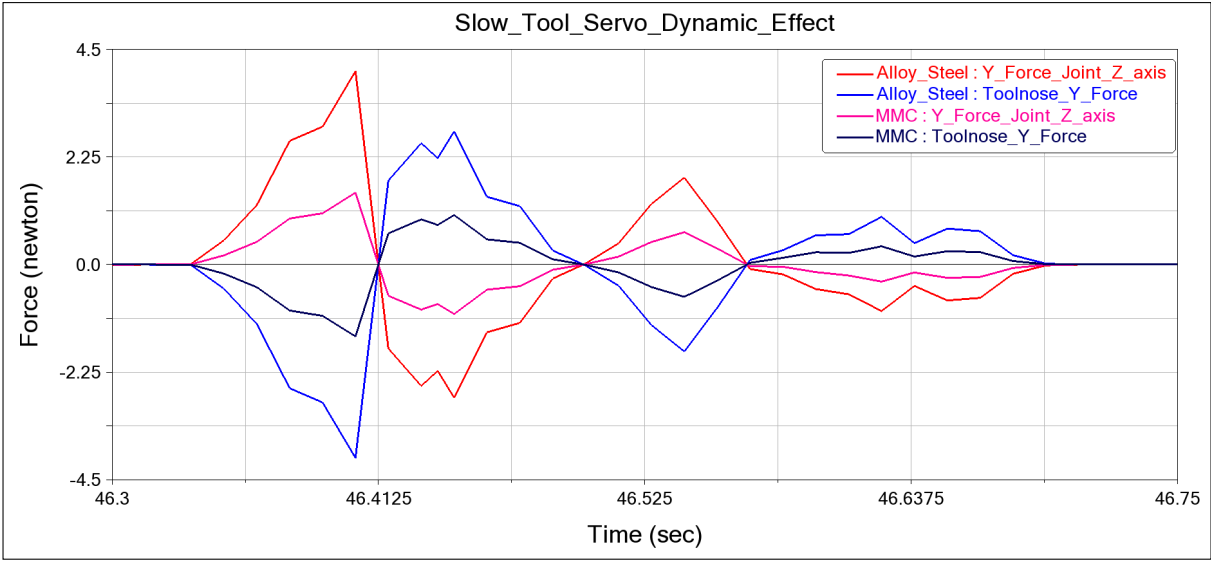
Fig. 7.13 Calculated dynamic force in both MMC and alloy steel, tool nose Y-direction reaction force vs prismatic joint Y-direction reaction force

As expected, the sum of the forces around the tooltip has their influence directly in the linear slideway. Since the prismatic joint reaction forces were defined in the manner of a permanent sliding phenomenon in which has their dynamic static frictional coefficient, the value for the hydrostatic bearing was defined about 0.03 in this simulation model. It is also thought that the

tool nose should have various value of the Y-direction value as it has been influenced by contact forces and friction. As illustrated in Figure 7.3, the force vector at the tool nose is opposite to its reaction at the joint position by means that the tool nose force reaction should have negative value in Y-direction. Figure 7.13 shows the prove assumption idea as explained.

The force reaction value calculated for MMC is lower than Alloy steel in which is within the interest of this study and the direction of the force in the tool nose is opposite to the reaction force in the prismatic joint.

However, in real scenario and nature of the hydrostatic bearing constraint are known to be set up as a planar joint where the fixed planar surfaces in the base body are parallel to the moveable known as carriage planar surfaces. Next follow up section will investigate the effect of the toolpath pressure and its reaction in the system. It will also be followed to examine the dynamic effects where the planar joint need to be applied instead of the prismatic joint.

7.4.3   Dynamic Effects in Toolpath and Interfacial Dynamic Force

For validation of the interfacial force affected in the toolpath, two different models were analysed. The assumption was made based in employing two different material density, steel and metal matrices composite (MMC). According to the qualitative result obtained from the simulation, the preliminary analysis proves that the exchange in the mass will result significant dynamic response in the system whilst the reaction forces in Cartesian coordination at the tooltip will increase the impact pressure in the toolpath.

Figure 7.14 illustrates the effect of the reaction force differentiation due to the change in surface curvature at the tooltip connected to toolpath. From the result, it can be seen that the forces in Z and X directions of the slides, RFcx and RFcz respectively, subjected to a larger amount of reaction forces. The result also clearly proves that using reduced mass MMC material, will result in decreasing the pressure at the cutting toolpath and finally reduce the

reaction forces at the tooltip during the cutting process in which can improve the dynamic performance of the system more robustly and feasibly.

7.4.4 Dynamic Effects in Slideway Planar Constraint

As discussed in Section 7.3, with reference to the philosophy of the dynamic effects in the linear hydrostatic bearing used in STS technique, the load capacity **Fv** include all the cutting forces, interfacial forces, toolpath pressure, dynamic stiffness/damping and contact forces can be distributed along the constrain plane on both top and side planer joints between the stationary base and moveable carriage at the hydrostatic linear sideways. The reaction force in these plane can be varied due to the multi-curvature of the freeform surface workpiece.

The connect joints coordination position is illustrated in Figure 7.15 which shows the reaction forces in the Cartesian plane calculated from each slide's centre of mass position at the top and side planar joints. A comparative reaction force analysis for different material at the planar connection joints can be found in Figure 7.16. Strong evidence can be found from the results, that the reaction forces at the planar joint are vary with association to the curvature of the freeform surface. Furthermore, the result obtained from the analysis shows promising proof that the MMC material produced less reaction force by means that the positioning error at the linear slides can be significantly decreased and finally improves the performance of the machining dynamics. Comparing the reaction forces between the steel and MMC material demonstrating that the maximum forces were reacted at Top Planer **Fx** direction vector as illustrated in Figure 7.16(d) and **Fy** at Side Planar joint on both Z and X slides. The most surprising aspect of the result can be observed from reaction force illustrated in Figure 7.16(a) at side planar joint in **Fx** vector whereby a very small value for reaction force captured in which can open a new era to the Idea of pico engineering science.
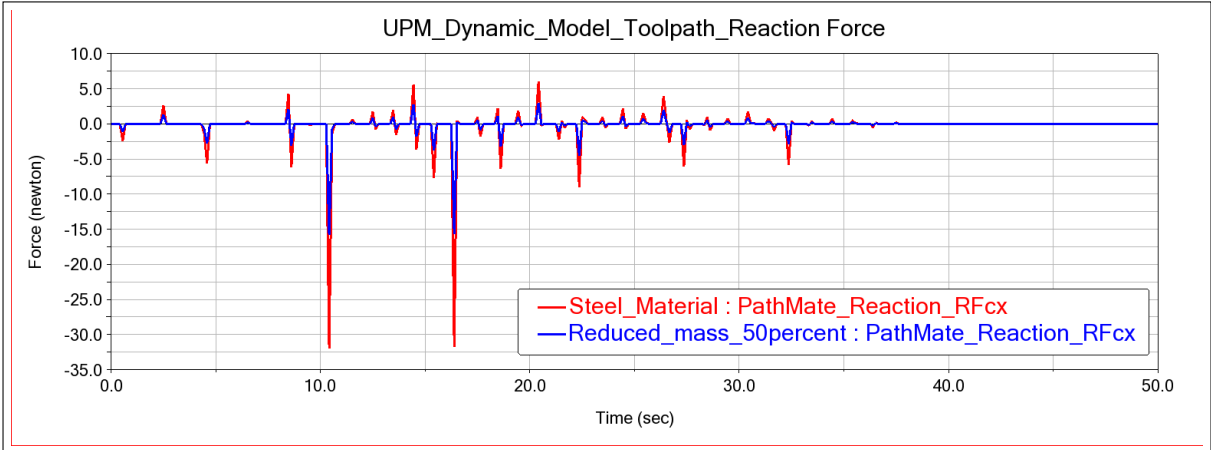
(a)
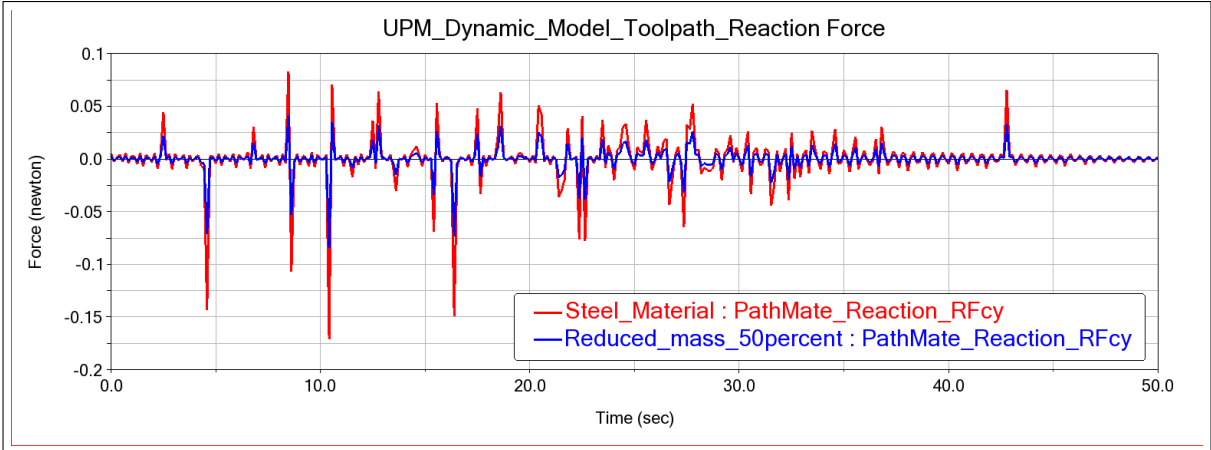
(b)
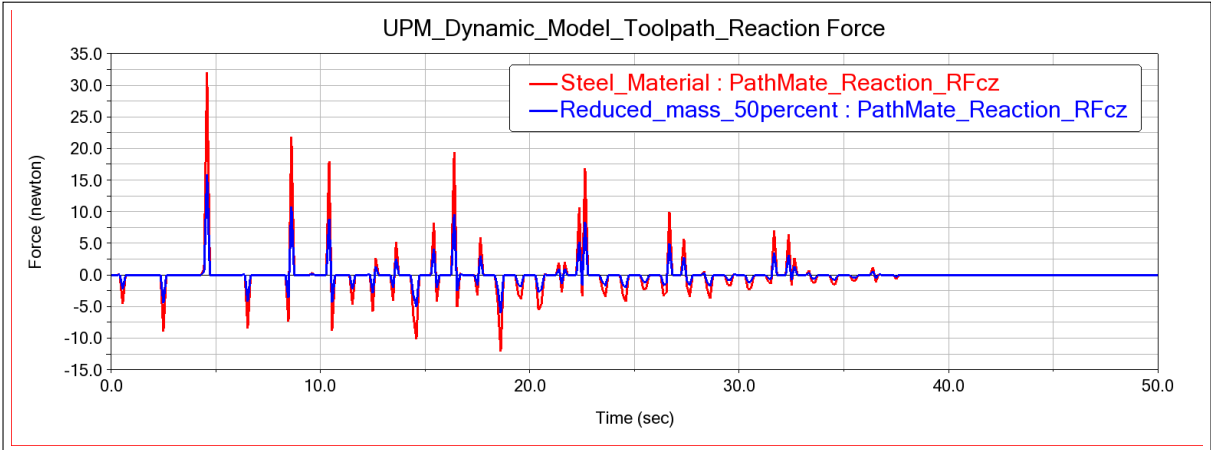
(c)

Fig. 7.14 UPM toolpath dynamics: (a) reaction force RFcx; (b) reaction force RFcy; (c) reaction force RFcz
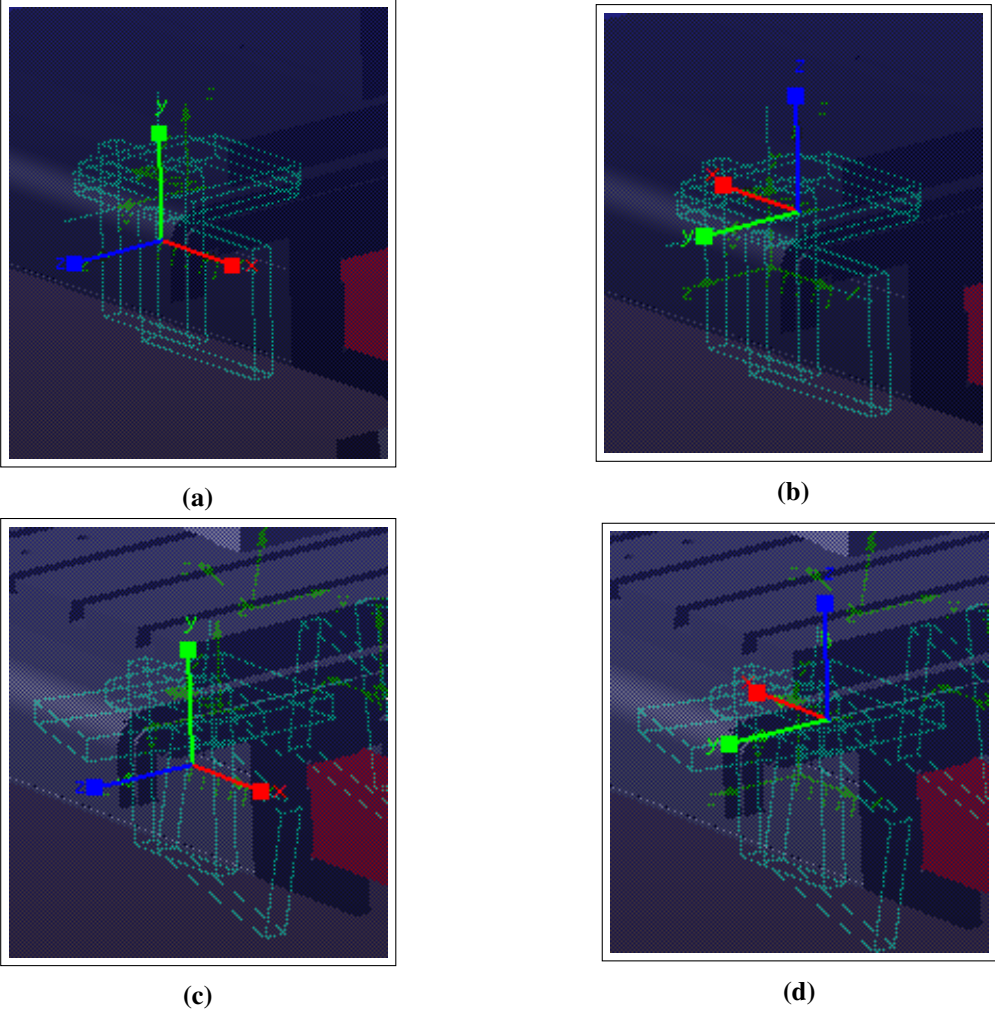
Fig. 7.15 ADAMS model slideway coordination: (a) X-axis side planar; (b) X-axis top planar; (c) Z-axis side planar; (d) Z-axis top planar

Fig. 7.16 Hydrostatic bearing reaction forces at linear planar joints

Based on the terminology of the hydrostatic linear bearing shown in Figure 7.6, the above-mentioned simulation parameters required to be analysed thus the current ADAMS model was integrated to validate the prediction of the impact of those parameters at the Planar joints in both linear X and Z axis respectively. The results obtained from the constraint planes applied to the hydrostatic linear slides were analysed.
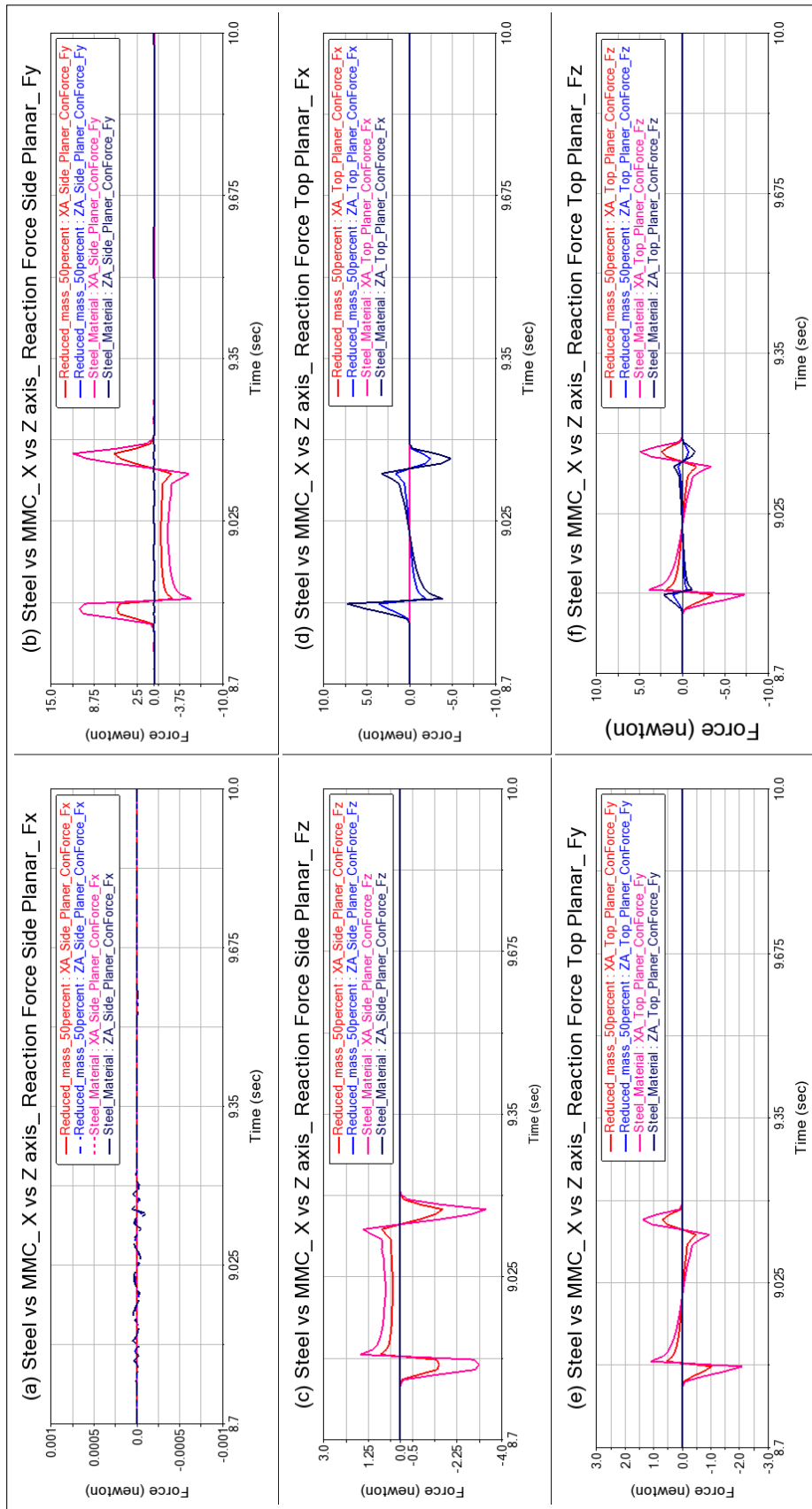
7.5   Concluding Remarks

In this chapter, an innovative toolpath generation approach for ultraprecision machining of freeform surfaces is proposed based on multi-body dynamics analysis. A multibody dynamics-oriented simulation method is presented aiming for achieving higher precision in the ultra-precision machining system. The approach and method are evaluated and validated by using ADAMS based simulations, and further supported by experimental testing. The interfacial cutting forces at the tooltip and workpiece surface and their effects are investigated through simulations on STS mode ultraprecision machining of freeform surfaces, the conception and results are valid for design and development of next generation UPM systems. Furthermore, A comparative analysis is carried on using two different materials, Steel and MMC, and the effects on dynamic performance of the slideways. It is found that the interfacial forces at the tooltip-workpiece surface is varied with the change of the freeform surface curvatures and the toolpath pressure being significantly reduced by using MMC material. In addition, the results at the slideway planar joints show strong evidence that the interfacial cutting forces have direct influence and impact on the performance of the linear slideways and thus the ultraprecision machining system. The interfacial cutting physics and dynamics are the promising basis with great potential for leading to higher precision positioning and motion control, which is essentially important in developing the next generation ultraprecision machining systems.

Chapter 8

Conclusions and Recommendations for Future Work

8.1 Major Conclusions and Contributions

In this PhD study, an endeavour of investigating smart tooling dynamics in ultraprecision machining of freeform surfaces was carried out. Novel tooling design and machining methodology were proposed and implemented with integrated collaboration at the industrial scale. Consequently, four major research objectives were achieved for dynamics analysis and its effects on ultraprecision machining of freeform surfaces, which can be concluded as follows:

1. **Design and development of a novel technology to generate toolpaths for ultraprecision machining of freeform surfaces including:**

   - An innovative method for generating a toolpath for ultraprecision machining using multi-body dynamics and ADAMS solvers;

   - The evaluation of the dynamic effects such as velocity, acceleration and cutting forces in the machining process;

   - Dynamic and kinematic simulations on the freeform surface finishing;

- Real-time dynamic and static contact effects on the interfacial area between the tooltip and freeform surfaces.

2. **Design and development of an innovative clamping system (smart chuck) for ultra-precision machining of freeform surfaces using flexure mechanism, covering:**

   - The innovative development of clamping system by employing the flexure mechanism;

   - A novel clampings technique of circular workpiece self-centring;

   - Innovation design and development of a self-locking mechanism for the workpiece while operating at high speed;

   - Integration and combination of the chuck's sub-assembly to one single component;

   - Ultraprecision positioning for freeform surfaces and the spindle registry;

   - Quantitative and qualitative analysis on the accuracy and precision of the spindle-clamping system.

3. **Machining dynamics investigation in ultraprecision machining using the slow tool servo (STS) technique for freeform surfaces, including:**

   - Multi-body dynamics simulation and analysis on the STS and extracting the reaction force in the linear motors during the machining of freeform surfaces;

   - Extracting the dynamic and static forces on the freeform surface using STS technique;

   - Development of an analytical approach and comparative investigation for dynamic machining effect on the toolpath generation;

   - Curvature and freeform surface topology analysis and its impact on the slow slide servo.

4. **A comparative analysis for replacement of alloy-steel with MMC material in hydrostatic bearing design for the ultraprecision machining system, focusing:**

   - Modal analysis and harmonic response analysis on these two alternative bearing system designs;

   - Development of the control system simulations using the PMAC controller and PVT.

The four conclusion headings above also highlight the contributions to knowledge from this PhD research.

8.2   Recommendations for Future Work

The following recommendations are proposed for future work in continuing this very promising research:

- ADAMS Toolpath generation at automation manner;

- Self Post-processing and user interface integration;

- Application Programming interface with the conventional CAE software;

- PLC scripts for run-out detection on the smart chuck and its in-process sensing capabilities.

List of Publications Arised from this Research

1. A. Khaghani and K. Cheng, "Investigation on multi-body dynamics-based approach to the toolpath generation for ultraprecision machining of freeform surfaces," Proc. Inst. Mech. Eng. Part B J. Eng. Manuf., p. 095440541986396, Jul. 2019.

2. A. Khaghani and K. Cheng, "CFD-based design and analysis of air-bearing-supported paint spray spindle," Nanotechnol. Precis. Eng., vol. 1, no. 4, pp. 226–235, Dec. 2018.

3. A. Khaghani and K. Cheng, "Investigation of machining dynamics in ultraprecision machining of freeform surfaces using the slow tool servo (STS)," in 13th Lamadamap Conference, Calibration, Coordinate measuring machine (CMM), Metrology, 2019.

4. A. Khaghani and K. Cheng, "Investigation on an innovative approach for clamping contact lens mould inserts in ultraprecision machining using an adaptive precision chuck and its application perspectives," Int. J. Adv. Manuf. Technol., 2020. (Submitted)

5. A. Khaghani and K. Cheng, "Investigation on the multibody dynamics-oriented approach to ultraprecision machining of freeform surfaces," Proc. Inst. Mech. Eng. Part B J. Eng. Manuf., 2020. (Submitted)

Patent and IP

1. A. Khaghani and K. Cheng, "Adaptive precision chuck," GB201914672D0, 10-Oct-2019.

Awards

1. HEIDENHAIN Best Oral Presentation Scholarship at the 13th Lamdamap Conference, AMRC Sheffield, 2019.

References

[1] W. Quanying, Q. Lin, Yujingchi, C. Hao, and W. Yuanyuan, "Design for progressive addition lenses - art. no. 67220C," *Advanced Optical Manufacturing Technologies, Pts 1 and 2*, vol. 6722, no. 1-2, p. C7220, 2007.

[2] Y. Feng, Zhijing and Wu, Hongzhong and Guo, Zhenyu and Zhao, Guangmu and Zhang, "Fabrication of a free-form lens with computer-controlled optical surfacing," *Advanced Optical Manufacturing and Testing Technology 2000*, vol. 4231, no. 2000, pp. 194–201, 2000.

[3] J. E. Meister, Darryl and Sheedy, "Introduction to ophthalmic optics," *SOLA Optical USA*, pp. 1–5, 2000.

[4] L. Zhou and K. Cheng, "Dynamic cutting process modelling and its impact on the generation of surface topography and texture in nano/micro cutting," *Proceedings of the Institution of Mechanical Engineers, Part B: Journal of Engineering Manufacture*, vol. 223, no. 3, pp. 247–266, 2009.

[5] D. H. Huo and K. Cheng, "A dynamics-driven approach to precision machines design for micro-manufacturing and its implementation perspectives," *4M 2006 - Second International Conference on Multi-Material Micro Manufacture*, vol. 222, pp. 29–34, 2006.

[6] F. Z. Fang, X. D. Zhang, A. Weckenmann, G. X. Zhang, and C. Evans, "Manufacturing and measurement of freeform optics," *CIRP Annals - Manufacturing Technology*, vol. 62, no. 2, pp. 823–846, 2013. [Online]. Available: http://dx.doi.org/10.1016/j.cirp.2013.05.003

[7] G. E. Davis, J. W. Roblee, and A. R. Hedges, "Comparison of freeform manufacturing techniques in the production of monolithic lens arrays," vol. 7426, p. 742605, 2009. [Online]. Available: http://proceedings.spiedigitallibrary.org/proceeding.aspx?doi=10.1117/12.824451

[8] H.-S. Kim, E.-J. Kim, and B.-S. Song, "Diamond turning of large off-axis aspheric mirrors using a fast tool servo with on-machine measurement," *Journal of Materials Processing Technology*, vol. 146, no. 3, pp. 349–355, 2004.

[9] J. C. Aurich, M. Zimmermann, S. Schindler, and P. Steinmann, "Effect of the cutting condition and the reinforcement phase on the thermal load of the workpiece when dry turning aluminum metal matrix composites," *International Journal of Advanced Manufacturing Technology*, vol. 82, no. 5-8, pp. 1317–1334, 2016.

[10] F. Z. Fang, X. D. Zhang, and X. T. Hu, "Cylindrical coordinate machining of optical freeform surfaces." *Opt.Express*, vol. 16, no. 10, pp. 7323–7329, 2008.

[11] X. Z. X. Zhou, H. Z. H. Zhang, and L. M. L. Ma, "The influence of process parameters on the surface topography in diamond turning of freeform optics," *Mechanic Automation and Control Engineering (MACE), 2010 International Conference on*, no. 50775099, pp. 4–7, 2010.

[12] D. P. Yu, S. W. Gan, Y. S. Wong, G. S. Hong, M. Rahman, and J. Yao, "Optimized tool path generation for fast tool servo diamond turning of micro-structured surfaces," *The International Journal of Advanced Manufacturing Technology*, vol. 63, no. 9-12, pp. 1137–1152, dec 2012.

[13] J. F. Rakuff, Stefan and Cuttino, "Design and testing of a long-range, precision fast tool servo system for diamond turning," *Precision Engineering*, vol. 33, no. 1, pp. 18–25, jan 2009. [Online]. Available: http://linkinghub.elsevier.com/retrieve/pii/S0141635908000354

[14] F. Yang, Y.-f. Dai, F. Wan, and G.-l. Wang, "A surface data generation method of optical micro-structure and analysis system for Fast Tool Servo fabricating," *Proceedings of SPIE*, vol. 7655, no. 1, pp. 76 552F–76 552F–6, 2010. [Online]. Available: http://link.aip.org/link/doi/10.1117/12.866829/html

[15] H. Ma, J. Tian, and D. Hu, "Development of a fast tool servo in noncircular turning and its control," *Mechanical Systems and Signal Processing*, vol. 41, no. 1-2, pp. 705–713, 2013. [Online]. Available: http://dx.doi.org/10.1016/j.ymssp.2013.08.011

[16] L. B. Kong, C. F. Cheung, and T. C. Kwok, "Theoretical and experimental analysis of the effect of error motions on surface generation in fast tool servo machining," *Precision Engineering*, vol. 38, no. 2, pp. 428–438, 2014.

[17] A. Meinel, M. Meinel, J. Stacy, T. Saito, and S. Patterson, "Wave-front correctors by diamond turning," *Applied Optics*, vol. 25, no. 23, p. 4228, 1986. [Online]. Available: http://www.ncbi.nlm.nih.gov/pubmed/19580042

[18] S. G. Rasmussen, JD and Tsao, T-C and Hanson, RD and Kapoor, "Dynamic variable depth of cut machining using piezoelectric actuators," *International Journal of Machine Tools and Manufacture*, vol. 34, no. 3, pp. 379–392, 1994.

[19] J. F. Cuttino, A. C. Miller, and D. E. Schinstock, "Performance optimization of a fast tool servo for single-point diamond turning machines," *IEEE/ASME Transactions on Mechatronics*, vol. 4, no. 2, pp. 169–179, 1999.

[20] R. C. Montesanti, "High bandwidth rotary fast tool servos and a hybrid rotary/linear electromagnetic actuator," no. September, p. 555, 2005.

[21] Y.-B. Kim, Ho-Sang and Lee, Kwang-Il and Lee, Kyoung-Min and Bang, "Fabrication of free-form surfaces using a long-stroke fast tool servo and corrective figuring with on-machine measurement," *International Journal of Machine Tools and Manufacture*, vol. 49, no. 12-13, pp. 991–997, oct 2009.

[22] B. Nathan P, "Live axis turning," Ph.D. dissertation, North Carolina State University, 2005. [Online]. Available: http://www.lib.ncsu.edu/resolver/1840.16/1595

[23] F. Yang and Y.-f. Dai, "Machining parameters selecting and optimization for fast tool servo considering the FTS dynamics," in *Advances in Optoelectronics and Micro-/nano-optics*. IEEE, dec 2010, pp. 1–5. [Online]. Available: http://ieeexplore.ieee.org/document/5713582/

[24] D. Trumper and X. D. Lu, "Fast Tool Servos: Advances in Precision, Acceleration, and Bandwidth," *Towards Synthesis of Micro-/Nano-systems*, pp. 11–19, 2007. [Online]. Available: http://www.springerlink.com.libproxy1.nus.edu.sg/content/h22q134x518790uq/fulltext.pdf

[25] S. S. Douglass, "A machining system for turning non-axisymmetric surfaces," Ph.D. Dissertation, The University of Tennessee, Knoxville, 1983.

[26] W. Greene and D. Shinstock, "Design of a linear voice coil actuator for fast tool servo applications," in *Proc. of ASPE 1997 annual meeting*, 1997.

[27] S. J. Ludwick, D. A. Chargin, J. A. Calzaretta, and D. L. Trumper, "Design of a rotary fast tool servo for ophthalmic lens fabrication," *Precision Engineering*, vol. 23, no. 4, pp. 253–259, 1999.

[28] M. F. Byl, "Design and control of a long stroke fast tool servo," Ph.D. dissertation, Massachusetts Institute of Technology, 2005.

[29] Q. Liu, X. Zhou, and L. Wang, "A new hybrid macro- and micro-range fast tool servo," *2010 International Conference on Mechanic Automation and Control Engineering, MACE2010*, pp. 3124–3127, 2010.

[30] S. Tian, Fujing and Yin, Ziqiang and Li, "Fast axis servo for the fast and precise machining of non-rotational symmetric optics," vol. 9281, p. 928103, 2014. [Online]. Available: http://proceedings.spiedigitallibrary.org/proceeding.aspx?doi=10.1117/12.2067863

[31] J. Shang, Y. Tian, Z. Li, F. Wang, and K. Cai, "A novel voice coil motor-driven compliant micropositioning stage based on flexure mechanism," *Review of Scientific Instruments*, vol. 86, no. 9, p. 095001, 2015.

[32] X. Wang, B. T. Yang, and Y. Zhu, "Modeling and analysis of a novel rectangular voice coil motor for the 6-DOF fine stage of lithographic equipment," *Optik*, vol. 127, no. 4, pp. 2246–2250, 2016. [Online]. Available: http://dx.doi.org/10.1016/j.ijleo.2015.11.107

[33] H. Feng, R. Xia, Y. Li, J. Chen, Y. Yuan, D. Zhu, S. Chen, and H. Chen, "Fabrication of freeform progressive addition lenses using a self-developed long stroke fast tool servo," *International Journal of Advanced Manufacturing Technology*, pp. 1–8, 2017.

[34] Y. E. Tohme and J. A. Lowe, "Machining of freeform optical surfaces by slow slide servo method," *Proceedings of the American Society for Precision Engineering*, pp. 26–31, 2003, aSPE.

[35] L. Li, "Fabrication of diffractive optics by use of slow tool servo diamond turning process," *Optical Engineering*, vol. 45, no. 11, p. 113401, 2006. [Online]. Available: http://opticalengineering.spiedigitallibrary.org/article.aspx?doi=10.1117/1.2387142

[36] a. Y. Yi and L. Li, "Design and fabrication of a microlens array by use of a slow tool servo." *Optics letters*, vol. 30, no. 13, pp. 1707–1709, 2005.

[37] L. Li and A. Y. Yi, "Development of a 3D artificial compound eye." *Optics express*, vol. 18, no. 17, pp. 18 125–18 137, 2010.

[38] L. B. Kong, C. F. Cheung, and W. B. Lee, "A theoretical and experimental investigation of orthogonal slow tool servo machining of wavy microstructured patterns on precision rollers," *Precision Engineering*, vol. 43, pp. 315–327, 2016. [Online]. Available: http://dx.doi.org/10.1016/j.precisioneng.2015.08.012

[39] C. Flucke, J. Osmer, B. Lünemann, O. Riemer, and E. Brinksmeier, "Scaling in machining of optics with reflective to diffractive function," in *Proceedings of the 9th international Euspen conference*, vol. 1, 2009, pp. 17–20.

[40] O. Olufayo and K. Abou-El-Hossein, "Preliminary investigation of surface finish of a contact lens polymer in ultra-high precision diamond turning," in *2013 6th Robotics and Mechatronics Conference (RobMech)*. IEEE, 2013, pp. 117–122.

[41] B. W. Hamilton, O. R. Tutunea-fatan, and S. Hussein, "Fabrication of right triangular prism retroreflectors," 2017.

[42] T. Moriya, K. Nakamoto, T. Ishida, and Y. Takeuchi, "Creation of V-shaped microgrooves with flat-ends by 6-axis control ultraprecision machining," *CIRP Annals - Manufacturing Technology*, vol. 59, no. 1, pp. 61–66, 2010. [Online]. Available: http://dx.doi.org/10.1016/j.cirp.2010.03.054

[43] S. Hussein, B. Hamilton, O. R. Tutunea-Fatan, and E. Bordatchev, "Novel Retroreflective Micro-Optical Structure for Automotive Lighting Applications," *SAE International Journal of Passenger Cars - Mechanical Systems*, vol. 9, no. 2, pp. 2016–01–1407, 2016. [Online]. Available: http://papers.sae.org/2016-01-1407/

[44] E. Brinksmeier, R. Gläbe, and L. Schönemann, "Diamond Micro Chiseling of large-scale retroreflective arrays," *Precision Engineering*, vol. 36, no. 4, pp. 650–657, 2012. [Online]. Available: http://dx.doi.org/10.1016/j.precisioneng.2012.06.001

[45] Q. Hu, H. Wu, J. Sun, D. Yan, Y. Gao, and J. Yang, "Large-area perovskite nanowire arrays fabricated by large-scale roll-to-roll micro-gravure printing and doctor blading." *Nanoscale*, vol. 8, no. 9, pp. 5350–7, 2016. [Online]. Available: http://www.scopus.com/inward/record.url?eid=2-s2.0-84959422252{&}partnerID=tZOtx3y1

[46] R. Wang, D. Guo, G. Xie, and G. Pan, "Atomic Step Formation on Sapphire Surface in Ultra-precision Manufacturing," *Scientific Reports*, vol. 6, p. 29964, 2016. [Online]. Available: http://www.nature.com/articles/srep29964

[47] D. W. K. Neo, A. Senthil Kumar, and M. Rahman, "CAx-technologies for hybrid fast tool/slow slide servo diamond turning of freeform surface," *Proceedings of the Institution of Mechanical Engineers, Part B: Journal of Engineering Manufacture*, vol. 230, no. 8, pp. 1465–1479, 2016.

[48] R. Steinkopf, Ralf and Dick, Lars and Kopf, Tino and Gebhardt, Andreas and Risse, Stefan and Eberhardt, "Data handling and representation of freeform surfaces," *SPIE, Optical Fabrication, Testing, and Metrology IV*, vol. 81690, pp. 81 690X–81 690X–9, 2011.

[49] P. Paolo, "Using application programming interface to integrate reverse engineering methodologies into solidworks," 2006.

[50] M. C. Liu, J. Q. Lin, and X. Q. Zhou, "Recent Advances in Ultraprecision Diamond Turning of Non-Rotationally Symmetric Optical Surfaces," *Applied Mechanics and Materials*, vol. 110-116, pp. 3600–3607, 2011.

[51] T. A. Dow, M. H. Miller, and P. J. Falter, "Application of a fast tool servo for diamond turning of nonrotationally symmetric surfaces," *Precision Engineering*, vol. 13, no. 4, pp. 243–250, 1991.

[52] S. J. Ludwick, "A Rotary Fast Tool Servo for Diamond Turning of Asymmetric Optics," p. 414, 1999.

[53] Z. Q. Yin, Y. F. Dai, S. Y. Li, C. L. Guan, and G. P. Tie, "Fabrication of off-axis aspheric surfaces using a slow tool servo," *International Journal of Machine Tools and Manufacture*, vol. 51, no. 5, pp. 404–410, 2011.

[54] H. Gong, Y. Wang, L. Song, and F. Z. Fang, "Spiral tool path generation for diamond turning optical freeform surfaces of quasi-revolution," *CAD Computer Aided Design*, vol. 59, pp. 15–22, 2015.

[55] X. Zhou Errata, C. Zuo, Q. Liu, and J. Lin, "Surface generation of freeform surfaces in diamond turning by applying double-frequency elliptical vibration cutting," *International Journal of Machine Tools and Manufacture*, vol. 104, pp. 45–57, may 2016.

[56] K. O. Wood, "Single block mounting system for surfacing and edging of a lens blank and method therefor," May 11 1993, uS Patent 5,210,695.

[57] C. Volken, U. Wyler, and O. Lack, "Block piece for holding an optical workpiece, in particular a spectacle lens, for machining thereof," Jun. 27 2006, uS Patent 7,066,797.

[58] M. Bono and R. Hibbard, "A flexure-based tool holder for sub-μm positioning of a single point cutting tool on a four-axis lathe," *Precision engineering*, vol. 31, no. 2, pp. 169–176, 2007.

[59] Gunter Schneider, "Preformed Block Piece With Three Points of Support," 2008. [Online]. Available: https://patents.google.com/patent/US20080132157A1/de

[60] Y. Felten and M. Le Gall, "Lens blocking and deblocking method and related device," May 26 2011, uS Patent App. 13/054,622.

[61] Frank Breme, "Block piece for holding an optical workpiece,," 2011. [Online]. Available: https://patents.google.com/patent/US8905388

[62] C. Wenzel, R. Winkelmann, R. Klar, P. Philippen, R. Garden, S. Pearlman, and G. Pearlman, "Advanced centering of mounted optics," vol. 9730, p. 973012, 2016. [Online]. Available: http://proceedings.spiedigitallibrary.org/proceeding.aspx?doi=10.1117/12.2213125

[63] P. Langehanenberg, J. Heinisch, C. Bub, and C. Wilde, "High-Precision Mounted Lens Production Directional adhesive bonding versus alignment turning," pp. 41–45, 2014.

[64] S. Sitzberger and R. Rascher, "An investigation on the efficiency of the manufacturing of components in precision optics," vol. 10009, p. 100090Y, 2016. [Online]. Available: http://proceedings.spiedigitallibrary.org/proceeding.aspx?doi=10.1117/12.2236137

[65] W. Sawangsri and K. Cheng, "An innovative approach to cutting force modelling in diamond turning and its correlation analysis with tool wear," *Proceedings of the Institution of Mechanical Engineers, Part B: Journal of Engineering Manufacture*, vol. 230, no. 3, pp. 405–415, 2016.

[66] R. F. Harik, H. Gong, and A. Bernard, "5-axis flank milling: A state-of-the-art review," *CAD Computer Aided Design*, vol. 45, no. 3, pp. 796–808, 2013.

[67] Q. Liu, X. Zhou, and P. Xu, "A new tool path for optical freeform surface fast tool servo diamond turning," *Proceedings of the Institution of Mechanical Engineers, Part B: Journal of Engineering Manufacture*, vol. 228, no. 12, pp. 1721–1726, 2014.

[68] T. C. Kwok, C. F. Cheung, L. B. Kong, S. To, and W. B. Lee, "Analysis of surface generation in ultra-precision machining with a fast tool servo," *Proceedings of the Institution of Mechanical Engineers, Part B: Journal of Engineering Manufacture*, vol. 224, no. 9, pp. 1351–1367, 2010.

[69] S. Ji, H. Yu, J. Zhao, X. Liu, and M. Hu, "Analysis and comparison of two different ultra-precision manufacturing methods for off-axis parabolic mirror with single point diamond turning," *Proceedings of the Institution of Mechanical Engineers, Part B: Journal of Engineering Manufacture*, vol. 230, no. 11, pp. 2026–2035, 2016.

[70] D. Huang, L. Zhang, S. Ji, and J. Zhao, "Tool path generation for ultra-precision polishing of freeform optical surfaces in an off-axis three-mirror imaging system," *Proceedings of the Institution of Mechanical Engineers, Part B: Journal of Engineering Manufacture*, vol. 231, no. 5, pp. 814–824, 2017.

[71] X. Chen, M. Kang, X. Wang, M. Hassan, and J. Yang, "Tool path optimal design for slow tool servo turning of complex optical surface," *Proceedings of the Institution of Mechanical Engineers, Part B: Journal of Engineering Manufacture*, vol. 231, no. 5, pp. 825–837, 2017.

[72] F. J. Fahy and W. G. Price, *IUTAM Symposium on Statistical Energy Analysis*, ser. Solid Mechanics and Its Applications, F. J. Fahy and W. G. Price, Eds. Dordrecht: Springer Netherlands, 1999, vol. 67. [Online]. Available: http://link.springer.com/10.1007/978-94-015-9173-7

[73] C. W. Gear, "The Automatic Integration of Ordinary Differential Equations," *Communications of the ACM*, vol. 14, no. 3, pp. 176–179, 1971.

[74] D. Negrut and A. Dyer, "Adams/solver primer," *Ann Arbor*, 2004.

[75] M. Pekal and J. Fraczek, "Comparison of Selected Formulations for Multibody System Dynamics with Redundant Constraints," *Archive of Mechanical Engineering*, vol. 63, no. 1, pp. 93–112, 2016.

[76] S. C. Meissner and R. C. Brost, "Method of alignably supporting a work piece for rotary movements," Nov. 30 2004, uS Patent 6,824,142.

[77] G. De Bastiani, G. Faccioli, R. Aldegheri, and L. R. Brivio, "Self-gradually locking chuck," May 9 1989, uS Patent 4,828,277.

[78] B. Ben-Menachem and M. Gilo, "Centering method for optical elements," Mar. 22 2012, uS Patent App. 13/304,959.

[79] M. J. Dent and I. L. Handricks, "Method of manufacturing a contact lens," Oct. 28 1986, uS Patent 4,619,082.

[80] K. Bergandy and W. Bergandy, "Collet system for use in lens production," Jan. 26 2006, uS Patent App. 10/896,231.

[81] S. Kiontke, "Collet," 2016. [Online]. Available: https://patents.google.com/patent/US9457411

[82] B. Sandmeier, "Clamping fixture including a chuck and a workpiece pallet releasably located thereon," Apr. 10 2012, uS Patent 8,152,151.

[83] J. Mettchen, "Clamping device for clamping a tie bolt supplying locking balls sideways," pp. 1–18, 2004, european Patent EP1442832A1.

[84] B. Obrist, "Clamping device and clamping assembly for clamping work pieces or tools in a well defined position," Jul. 18 2000, uS Patent 6,089,557.

[85] R. Winkelmann and R. Klar, "Method for ultra-precise shaping of surface of workpiece," 2012, dE102012022844 A1.

[86] N. Lobontiu, *Compliant Mechanisms: Design of Flexure Hinges*. CRC Press, 2002. [Online]. Available: https://books.google.co.uk/books?id=ivnKBQAAQBAJ

[87] N. Lobontiu and J. S. N. Paine, "Design of Circular Cross-Section Corner-Filleted Flexure Hinges for Three-Dimensional Compliant Mechanisms," *Journal of Mechanical Design*, vol. 124, no. 3, p. 479, 2002. [Online]. Available: http://mechanicaldesign.asmedigitalcollection.asme.org/article.aspx?articleid=1447055

[88] RSP Technology, "RSP Technology - Datasheets & news -." [Online]. Available: http://www.rsp-technology.com/datasheets-news.html

[89] Roymech, "Coefficients Of Friction - Roy Mech." [Online]. Available: https://roymech.org/Useful_Tables/Tribology/co_of_frict.html

[90] J. Davis, *Concise Metals Engineering Data Book*, ser. Ingenieria e ingenieria civil. A S M International, 1997. [Online]. Available: https://books.google.co.uk/books?id=A_SS2k2EsJ0C

[91] G. Chapman, "Ultra-precision Machining Systems ; an Enabling Technology for Perfect Surfaces," *Moor Nanotechnology System*, pp. 1–9, 1970. [Online]. Available: http://www.nanotechsys.com/technology/technical-papers/

[92] B. Denkena, D. Dahlmann, and N. Sassi, "Analysis of an ultra-precision positioning system and parametrization of its structural model for error compensation," *Procedia CIRP 62 (2017)*, vol. 62, pp. 335–339, 2017.

[93] L. T. Vu, C.-C. A. Chen, and C.-W. Yu, "Optical design of soft multifocal contact lens with uniform optical power in center-distance zone with optimized NURBS," *Optics Express*, vol. 26, no. 3, p. 3544, feb 2018. [Online]. Available: https://www.osapublishing.org/abstract.cfm?URI=oe-26-3-3544

[94] D. Huo, K. Cheng, and F. Wardle, "A holistic integrated dynamic design and modelling approach applied to the development of ultraprecision micro-milling machines," *International Journal of Machine Tools and Manufacture*, vol. 50, no. 4, pp. 335–343, 2010. [Online]. Available: http://dx.doi.org/10.1016/j.ijmachtools.2009.10.009

[95] N. Efron, *Contact Lens Practice E-Book*. Elsevier Health Sciences, 2016.

[96] O. Olufayo and K. Abou-El-Hossein, "Evolution of High Precision Manufacturing of Contact Lenses," *Materials Science Forum*, vol. 828-829, pp. 374–380, aug 2015. [Online]. Available: https://www.scientific.net/MSF.828-829.374

[97] O. Riemer, "Advances in ultra precision manufacturing," *Proc. Jpn. Soc. Precis. Eng*, 2011.

[98] J. Franse, "Manufacturing techniques for complex shapes with submicron accuracy," *Reports on Progress in Physics*, vol. 53, no. 8, pp. 1049–1094, 1990.

[99] D. Teissandier, Y. Ledoux, S. Arroyave-Tobon, V. Delos, and J. M. Linares, "Effect of form errors on the positioning precision of over-constrained systems," *CIRP Annals*, pp. 2–5, 2019. [Online]. Available: https://doi.org/10.1016/j.cirp.2019.04.068

[100] Y. T. Liu and B. J. Li, "A 3-axis precision positioning device using PZT actuators with low interference motions," *Precision Engineering*, vol. 46, pp. 118–128, 2016. [Online]. Available: http://dx.doi.org/10.1016/j.precisioneng.2016.04.006

[101] K. Cheng and P. Shore, "Special issue on design of ultraprecision and micro machine tools and their key enabling technologies," *International Journal of Machine Tools and Manufacture*, vol. 50, no. 4, p. 309, 2010.

[102] K. Cheng and D. Huo, "Micro-Cutting: Fundamentals and Applications," *The Wiley Microsystem and Nanotechnology Series*, pp. 1–348, 2013.

[103] S. Mekid, "High precision linear slide. Part I: design and construction," *International Journal of Machine Tools and Manufacture*, vol. 40, no. 7, pp. 1039–1050, 2000.

[104] S. Yang, P. Zhao, Y. Xu, L. Sun, P. Wu, X. Long, and Z. Jiang, "Hydrostatic worktable performance of an ultra-precision optical aspheric machine tool," *Procedia CIRP*, vol. 27, pp. 187–191, 2015. [Online]. Available: http://dx.doi.org/10.1016/j.procir.2015.04.064

[105] J. K. Martin, "Hydrostatic Journal Bearings," in *Encyclopedia of Tribology*, Q. J. Wang and Y.-W. Chung, Eds. Boston, MA: Springer US, 2013, pp. 1774–1780. [Online]. Available: https://doi.org/10.1007/978-0-387-92897-5{_}51

[106] H. Garg, H. Sharda, and V. Kumar, "On the design and development of hybrid journal bearings: a review," *Tribotest*, vol. 12, no. 1, pp. 1–19, 2006.

[107] F. Xue, W. Zhao, Y. Chen, and Z. Wang, "Research on error averaging effect of hydrostatic guideways," *Precision Engineering*, vol. 36, no. 1, pp. 84–90, 2012. [Online]. Available: http://dx.doi.org/10.1016/j.precisioneng.2011.07.007

[108] X. Luo, K. Cheng, D. Webb, and F. Wardle, "Design of ultraprecision machine tools with applications to manufacture of miniature and micro components," *Journal of Materials Processing Technology*, vol. 167, no. 2-3, pp. 515–528, 2005.

[109] B. Vijaya Ramnath, C. Elanchezhian, R. Annamalai, S. Aravind, T. Sri Ananda Atreya, V. Vignesh, and C. Subramanian, "Aluminium metal matrix composites-a review." *Reviews on Advanced Materials Science*, vol. 38, no. 1, 2014.

[110] T. Ozben, E. Kilickap, and O. Cak\ir, "Investigation of mechanical and machinability properties of SiC particle reinforced Al-MMC," *Journal of materials processing technology*, vol. 198, no. 1-3, pp. 220–225, 2008.

[111] S. Vellingiri, "The Future in Metal Matrix Composites for Automotive Industry: A Review," *International Research Journal of Automotive Technology*, vol. 1, no. 6, pp. 88–100, 2018.

[112] B. V. Ramnath, C. Elanchezhian, R. Annamalai, S. Aravind, T. S. A. Atreya, V. Vignesh, and C. Subramanian, "Aluminium metal matrix composites–a review," *Rev. Adv. Mater. Sci*, vol. 38, no. 5, pp. 55–60, 2014.

[113] J. T. Blucher, U. Narusawa, M. Katsumata, and A. Nemeth, "Continuous manufacturing of fiber-reinforced metal matrix composite wires—technology and product characteristics," *Composites Part A: Applied Science and Manufacturing*, vol. 32, no. 12, pp. 1759–1766, 2001.

[114] A. Kumar, M. M. Mahapatra, P. K. Jha, and Others, "Fabrication and characterizations of mechanical properties of Al-4.5% Cu/10TiC composite by in-situ method," *Journal of Minerals and Materials characterization and Engineering*, vol. 11, no. 11, pp. 1075–1080, 2012.

[115] K. Utsumi, Y. Shimada, Teruyukiikeda, and H. Takamizawa, "Monolithic multicomponents ceramic (MMC) substrate," *Ferroelectrics*, vol. 68, no. 1, pp. 157–179, 1986.

[116] Takrockford, "Hydrostatic Linear Motor Guide," p. 1, 2019, https://tacrockford.com/product/machine-components/milling-machine/hydrostatic-systems/hydrostatic-linear-motor-guide. (Accessed 2019-12-14).

[117] D. Lutrell, "Innovations in Ultra-Precision Machine Tools: Design and Applications," pp. 1–4, 2010.

[118] H. Ohmori, S. Umezu, Y. Kim, Y. Uehara, H. Kasuga, T. Kato, N. Itoh, S. Kurokawa, T. Kusumi, Y. Sugawara, and S. Kunimura, "A high quality surface finish grinding process to produce total reflection mirror for x-ray fluorescence analysis," *International Journal of Extreme Manufacturing*, vol. 2, no. 1, p. 015101, mar 2020. [Online]. Available: https://doi.org/10.1088%2F2631-7990%2Fab7a29

[119] W. Gao, H. Haitjema, F. Fang, R. Leach, C. Cheung, E. Savio, and J.-M. Linares, "On-machine and in-process surface metrology for precision manufacturing," *CIRP Annals*, vol. 68, no. 2, pp. 843–866, 2019.

[120] A. Khaghani and K. Cheng, "Investigation on multi-body dynamics based approach to the toolpath generation for ultraprecision machining of freeform surfaces," *Proceedings of the Institution of Mechanical Engineers, Part B: Journal of Engineering Manufacture*, p. 095440541986396, jul 2019. [Online]. Available: http://journals.sagepub.com/doi/10.1177/0954405419863961

Appendix A

Tool Path Generation Specifications

A.1   Tool Geometry
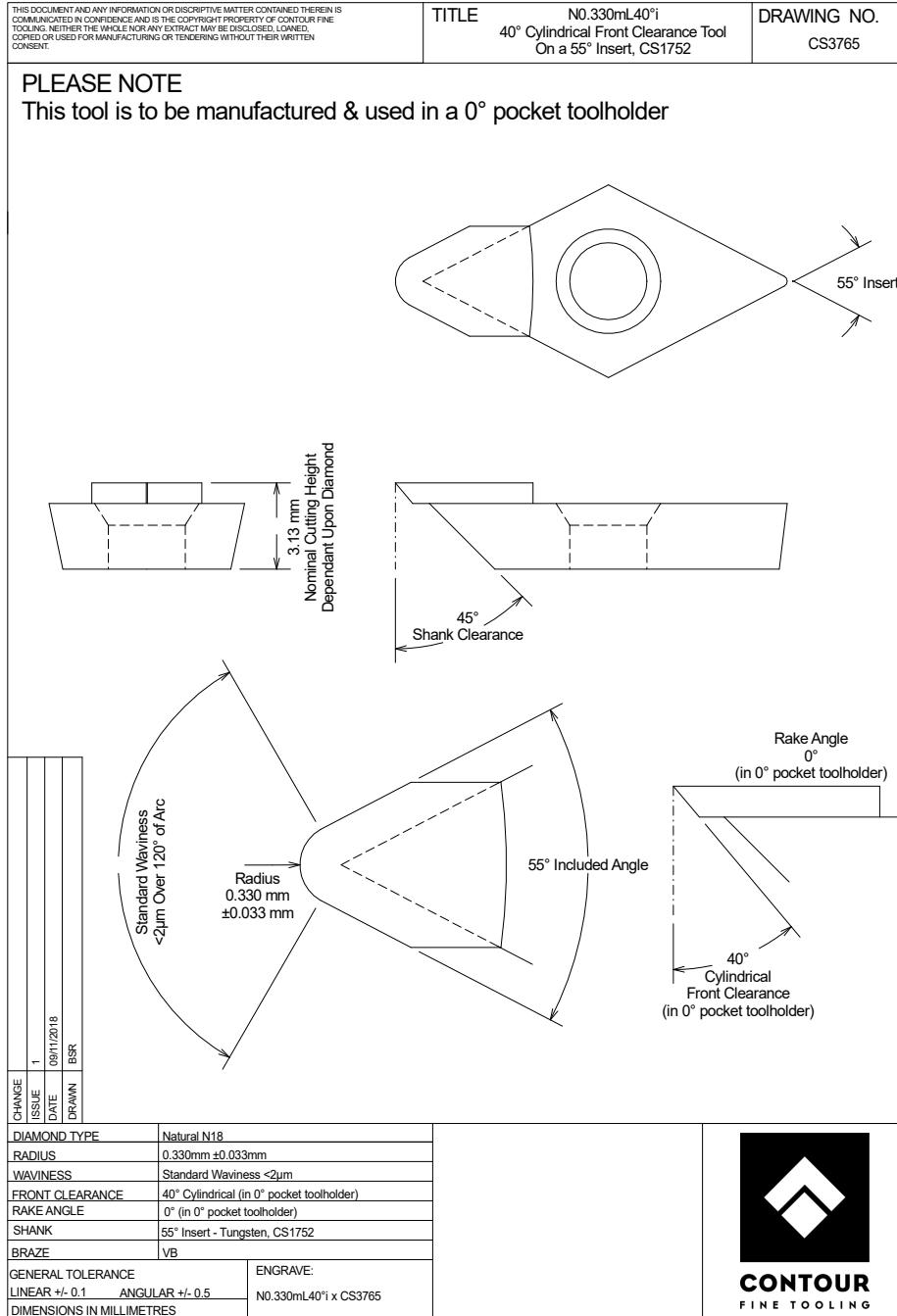
Fig. A.1 Contour diamond tool geometry for ADAMS toolpath generation experiment

A.2   G Codes Programming for ADAMS Experiments

(CREATED : Tuesday 04/09/2018)

(OPERATOR : Adam toolPath generation_04)

(Aperture Type : Circle)

(Tool : Diamond Tool [Tool ID - 2])

(Name : T0404)

(Tool Info :   )

(Diamond Type : Conical)

(Tool Radius : 0.33 mm)

(Included Angle : 55 deg)

(Rake Angle : 0 deg)

(Horizontal Orientation : 0 deg)

(Vertical Orientation : 0 deg)

(Primary Clearance : 10 deg)

(Spindle and Tool Direction : Clockwise - Edge_To_Center)

(X Start and X End : 15.5 mm, 0.0 mm)

(LeadIn and LeadOut Distance, Increment : 0.01 mm, 0.01 mm, 0.005 mm / rev)

(SSS Output Type : SteadyX)

(Radial Feed per Revolution : 0.01)

(Inverse-Time Feed, Block Time : 0.001)

(============== SECTION - COMMANDS =================)

#551 = 2   (TOTAL LOOPS)

#552 = 0.00500000   (DEPTH OF CUT)

#500 = 0   (PASS COUNTER)

#501 = 0.00   (USER INPUT - OVERALL LENGTH)

#503 = 0.00   (USER INPUT - ZORIGIN=FLAT)

```
#504 = 0.0            ( USER INPUT - TOOL NOSE RADIUS FOR MACHINE COMP )

#507 = 26             ( MIST NUMBER )

T0404                 ( ACTIVATE TOOL OFFSET  )

G01 G71 G90 G40 G18 G94 G54

G01 X17.00000000 F200 ( PARKING POSITION - X )

Z10.00000000          ( PARKING POSITION - Z )

#550 = #501 + [#551*#552] + #503 + #504  ( INDIVIDUAL STOCK REMOVAL )


WHILE[#500LT#551]DO 1

#550 = #550 - #552    ( CURRENT CUTTING OFFSET )

G52 Z[#550]           ( SET COORDINATE SYSTEM OFFSET )


M80                   ( C AXIS ORIENTATION )

G09 C0.0              ( USER INPUT )

G92 C0                ( SET COORD SYS )

( LEAD IN BLOCKS )

G01 C0.0 X15.5 F100

Z-20.0893

M[#507]                           ( MIST ON )

G01 G93 F0.010


C0  X15.5  Z-9.948351

C0.25  X15.499986  Z-9.948978

C0.5  X15.499972  Z-9.949116

C0.75  X15.499958  Z-9.949319

C1  X15.499944  Z-9.94959
```

```
C1.25   X15.49993   Z-9.949929

C1.5   X15.499916   Z-9.950315

C1.75   X15.499902   Z-9.950

......

......

......


C357   X0.000166   Z-9.870682

C357.25   X0.000152   Z-9.870681

C357.5   X0.000138   Z-9.870681

C357.75   X0.000125   Z-9.870681

C358   X0.000111   Z-9.870681

C358.25   X0.000097   Z-9.87068

C358.5   X0.000083   Z-9.87068

C358.75   X0.000069   Z-9.87068

C359   X0.000055   Z-9.87068

C359.25   X0.000041   Z-9.870679

C359.5   X0.000027   Z-9.870679

C359.75   X0.000013   Z-9.870679

C0   X0   Z-9.870679


G04 P1              ( DWELL )

( PARKING POSITION )

G94 G01 Z10 F200

X17.00000000

( =============== SECTION - FOOTER ================== )
```

```
M29

#500 = #500 + 1

END 1

G52                                              ( RESET G52 OFFSETS )

M30
```

A.3   Freeform Workpiece Geometry
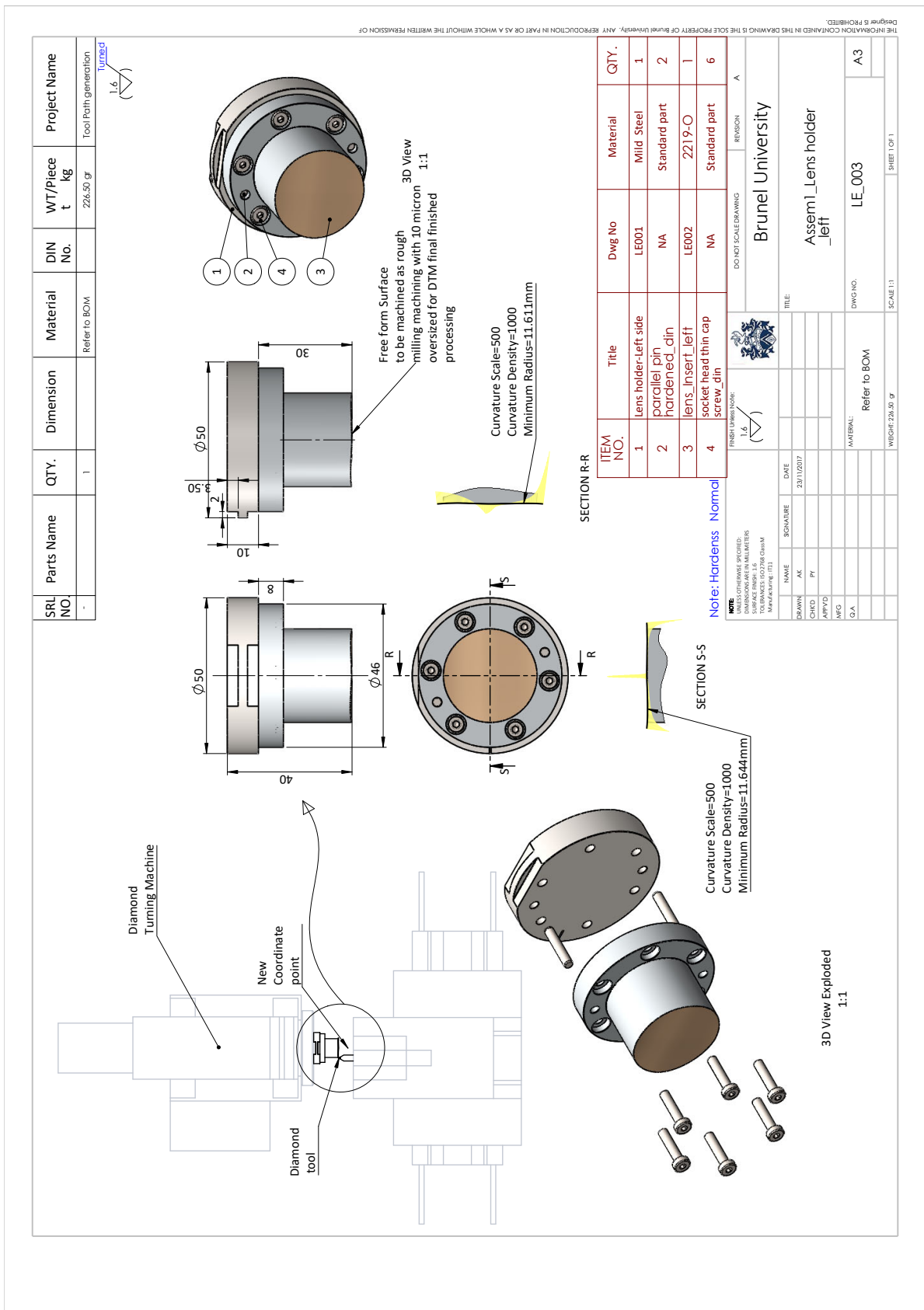
Fig. A.2 Freeform workpiece geometry-assembly
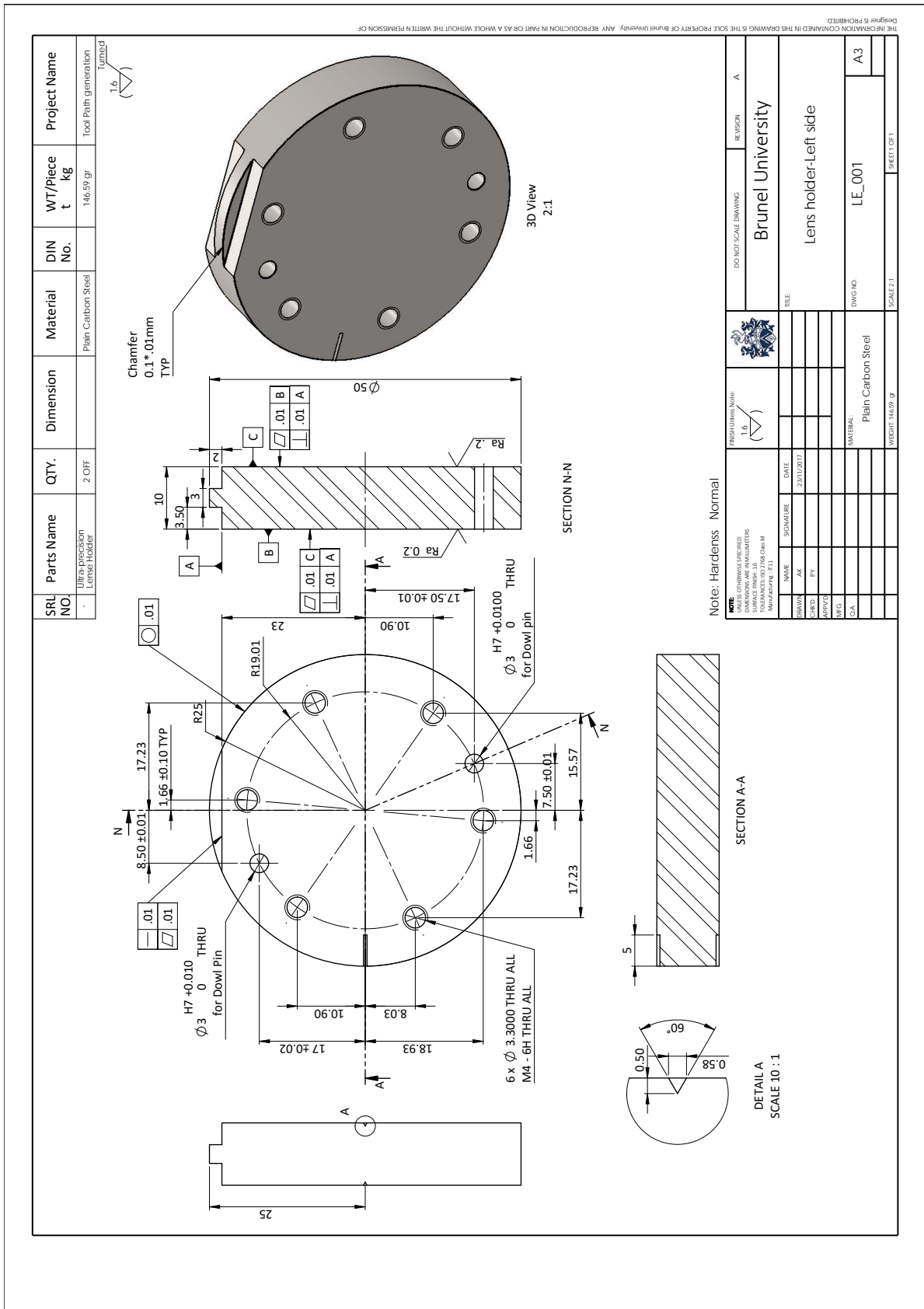
Fig. A.3 Freeform workpiece geometry-lens holder
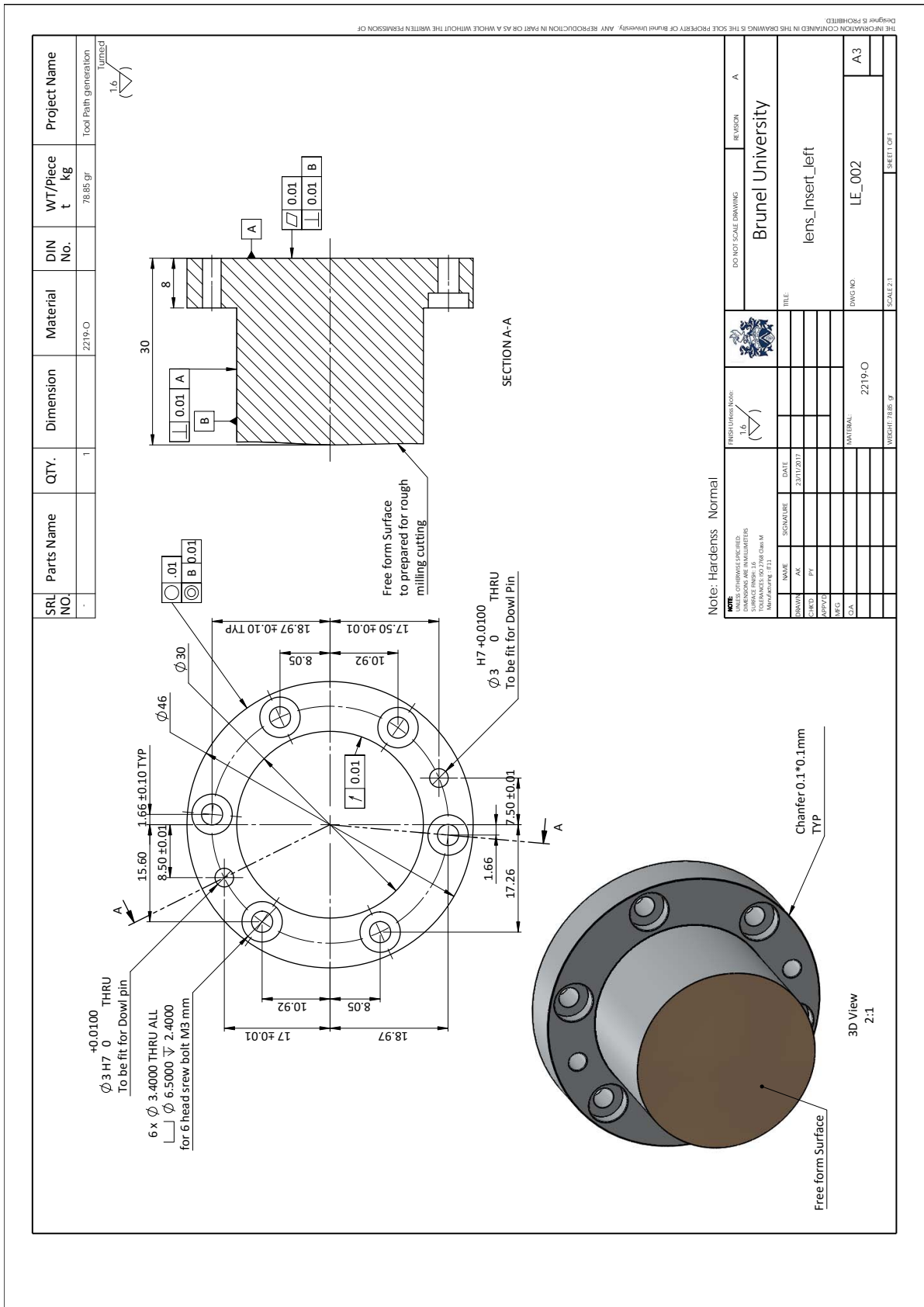
Fig. A.4 Freeform workpiece geometry-workpiece
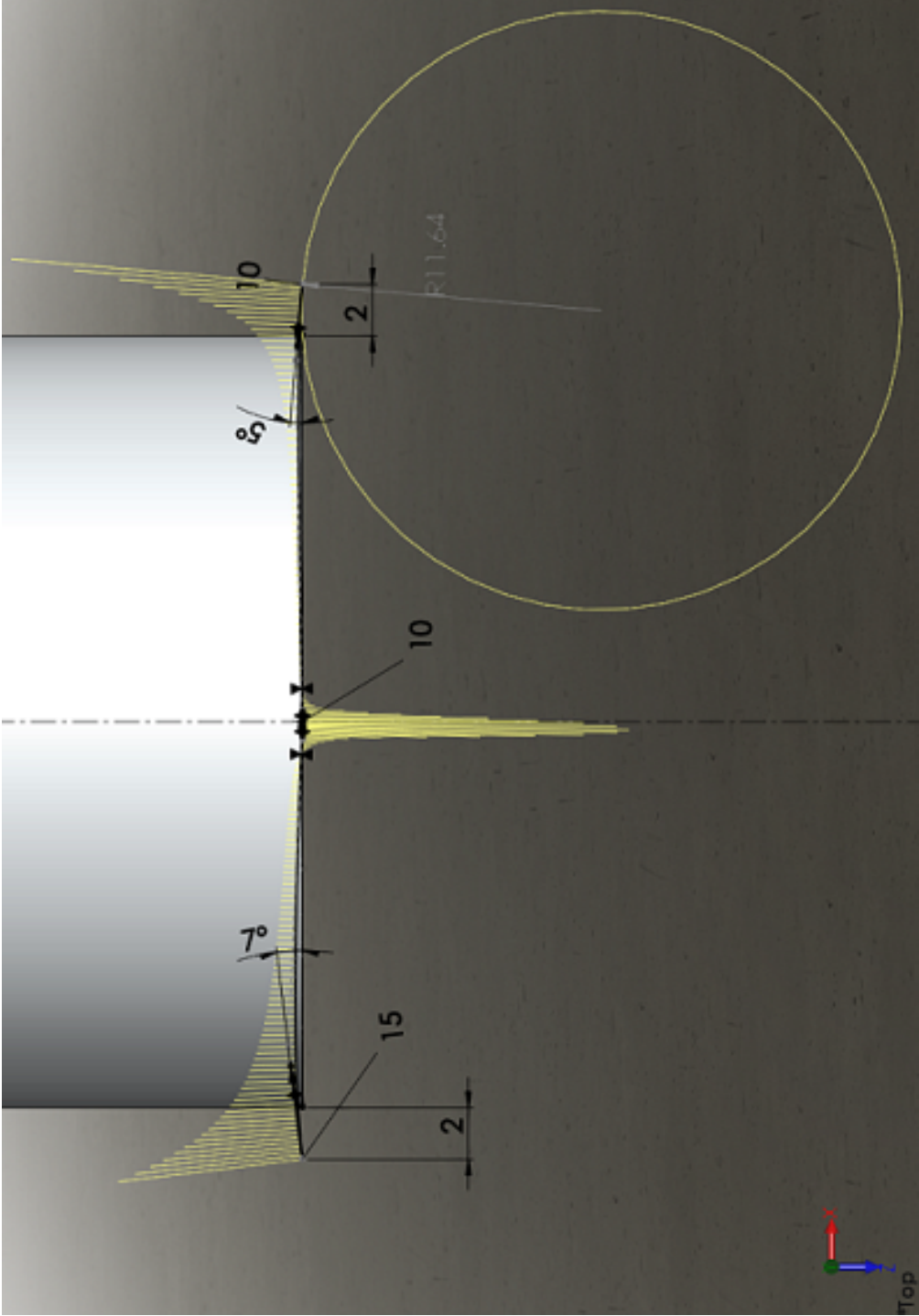
Fig. A.5 Test part surface geometry-top section
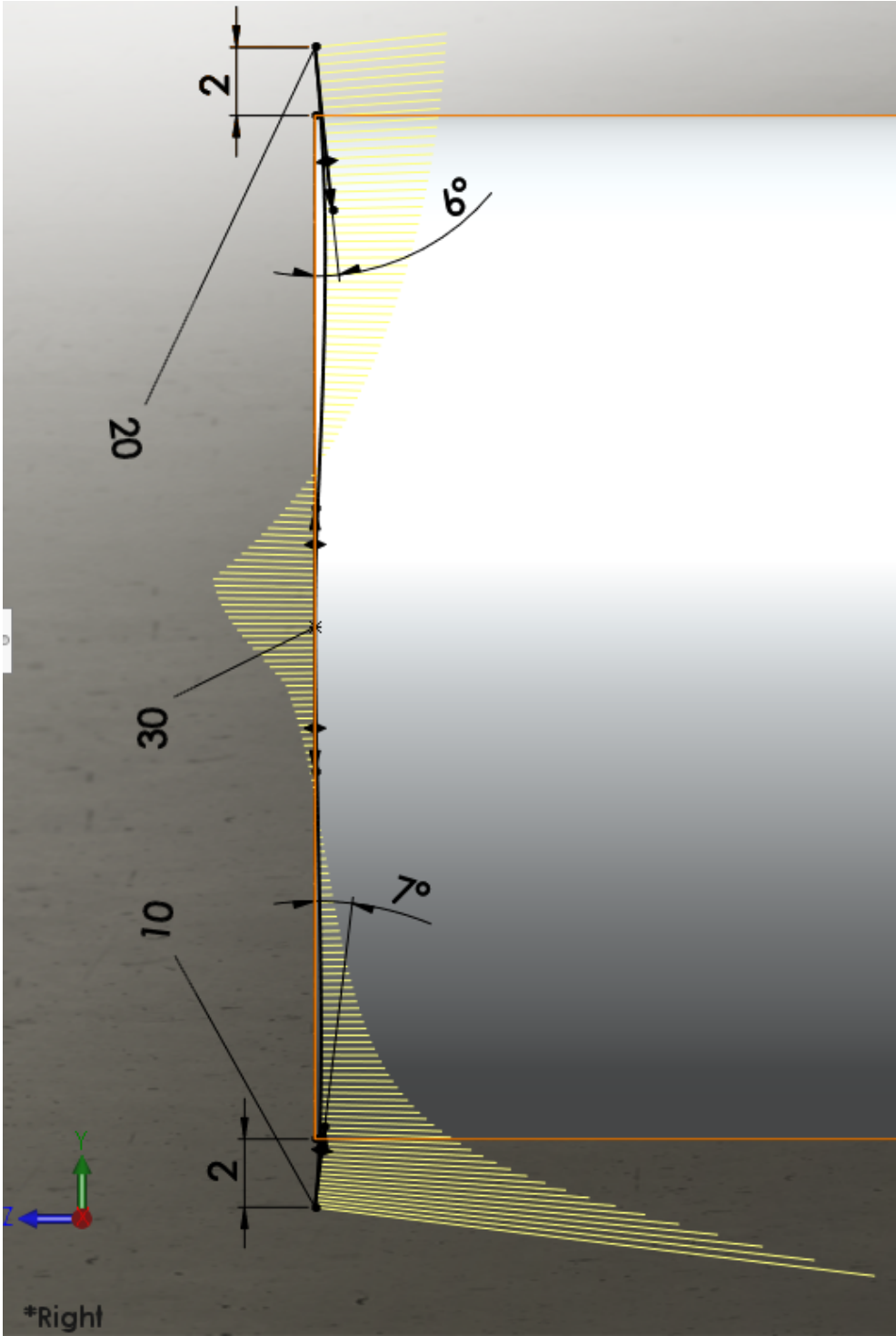
Fig. A.6 Test part surface geometry-right section

Appendix B

Smart Chuck Design

B.1   Technical Drawings

SC01, SC02
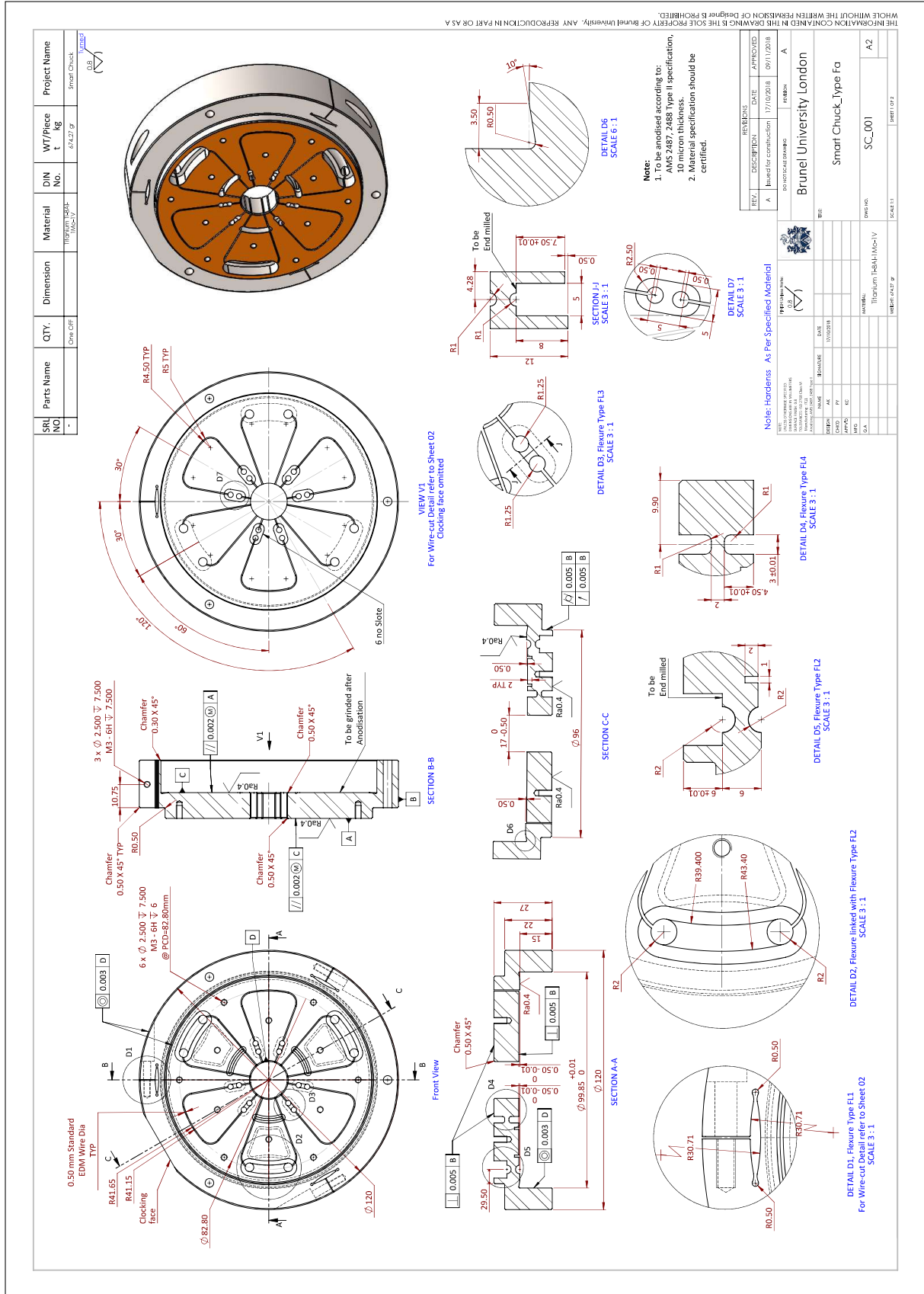
Fig. B.1 Smart chuck technical drawings, sheet 01
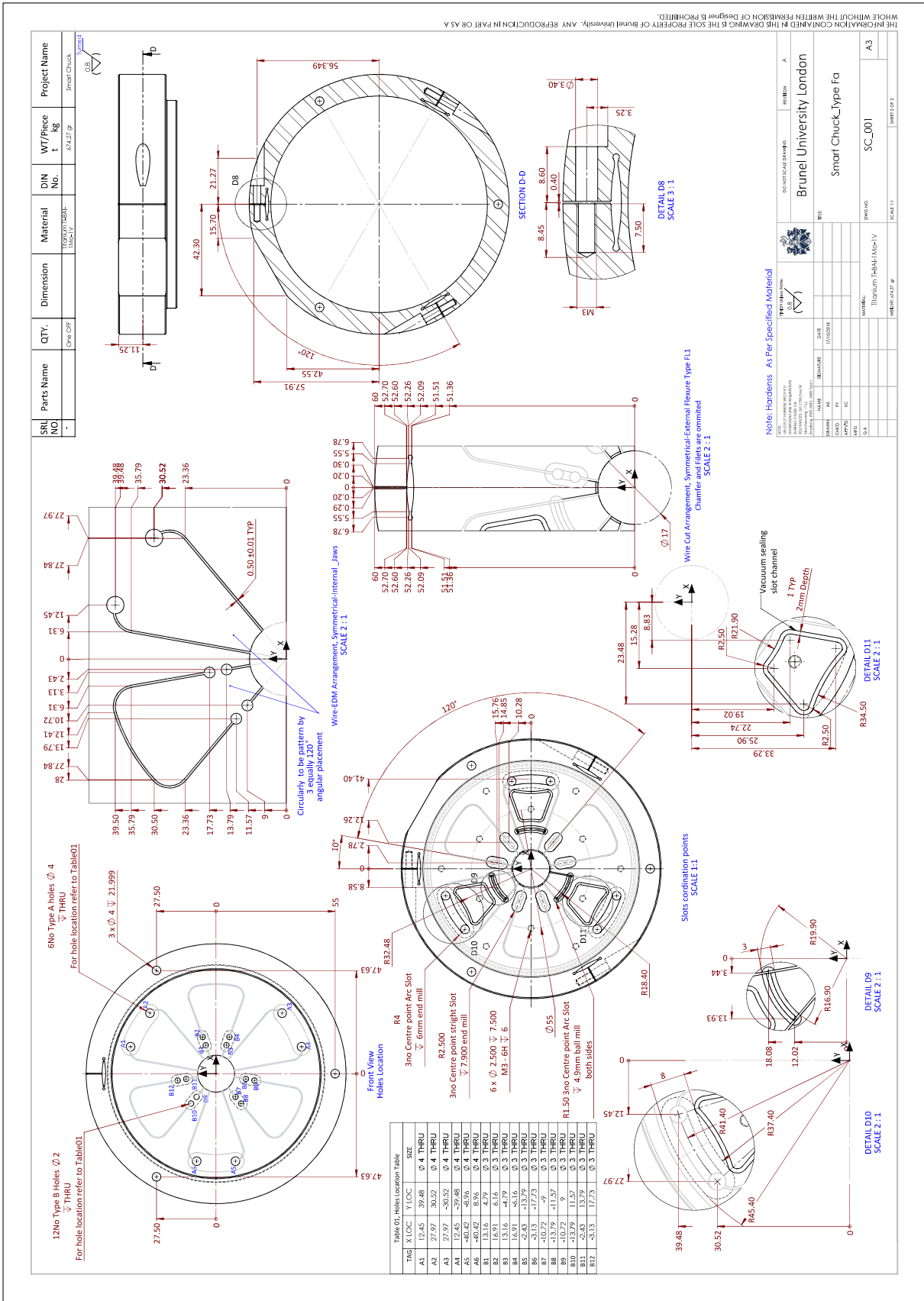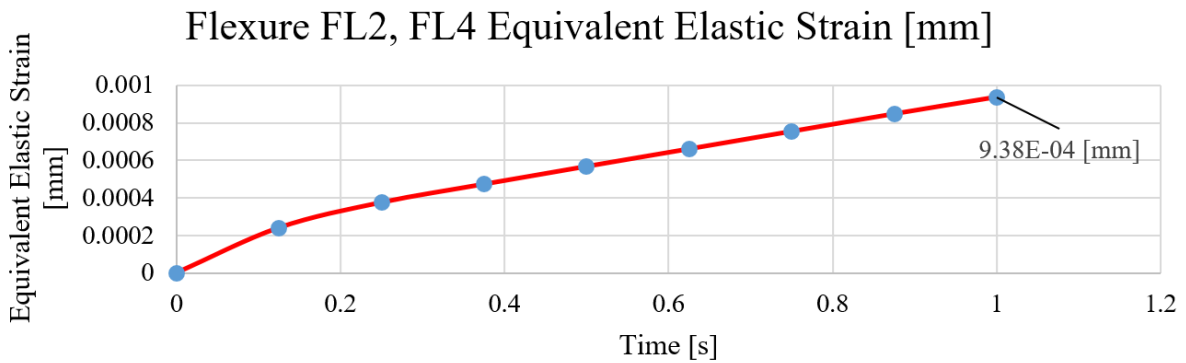
Fig. B.2 Smart chuck technical drawings, sheet 02

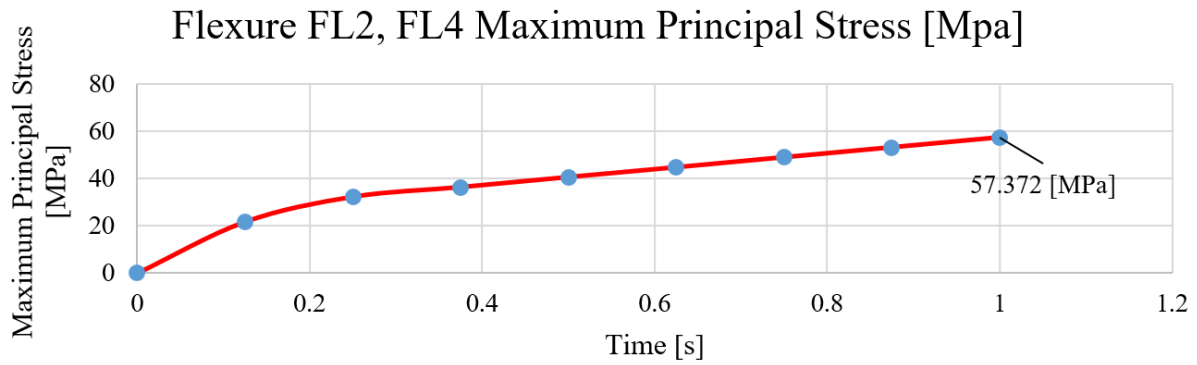# B.2 FL2, FL4 3D FEM Result Diagrams and Figures
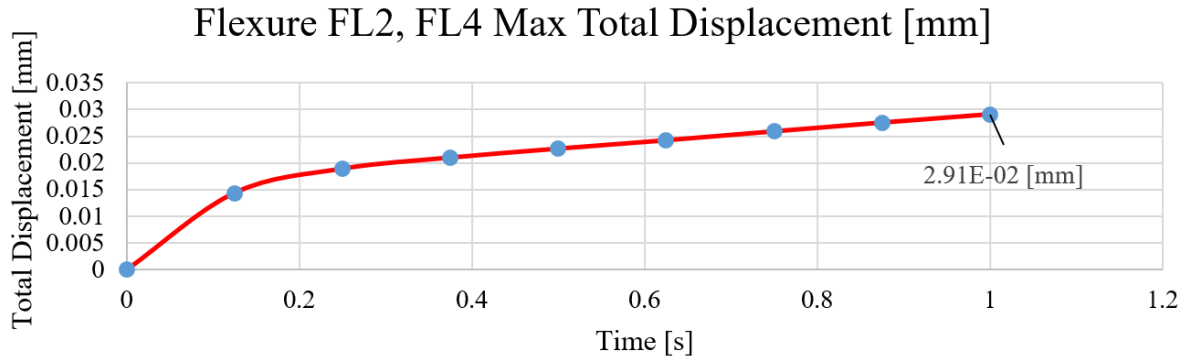
(a) Total displacement
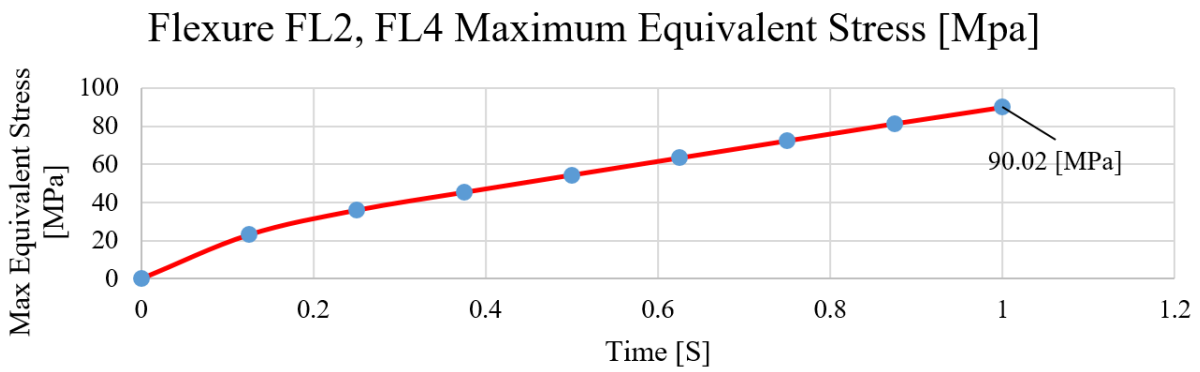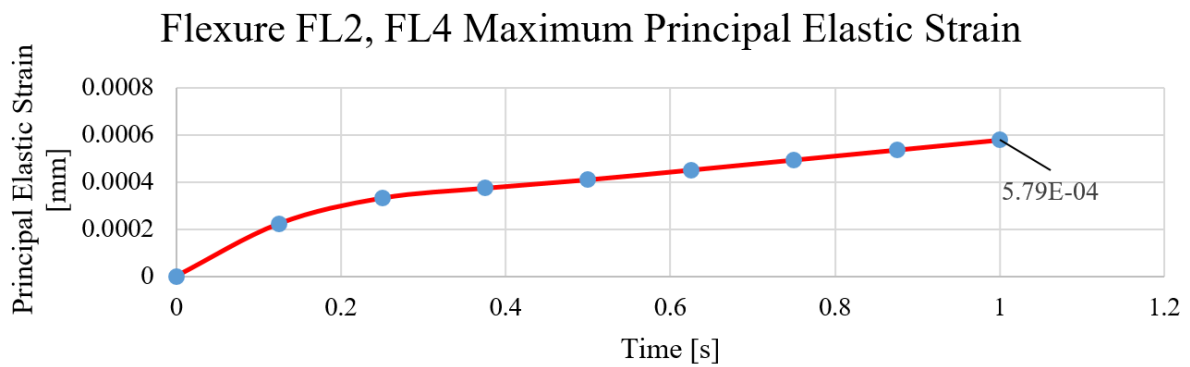

(b) Equivalent stress

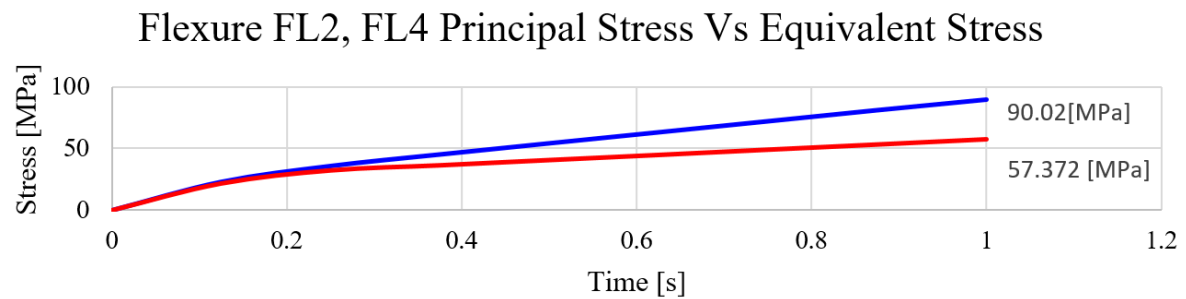
(c) Equivalent elastic strain

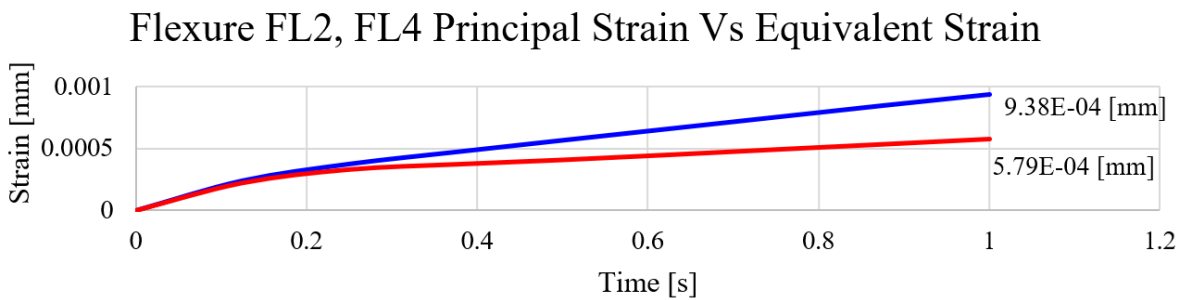**Fig. B.3** Flexure FL2,FL4 3D FEM analysis, loaded condition, results data Sheet 01

(a) Principal stress
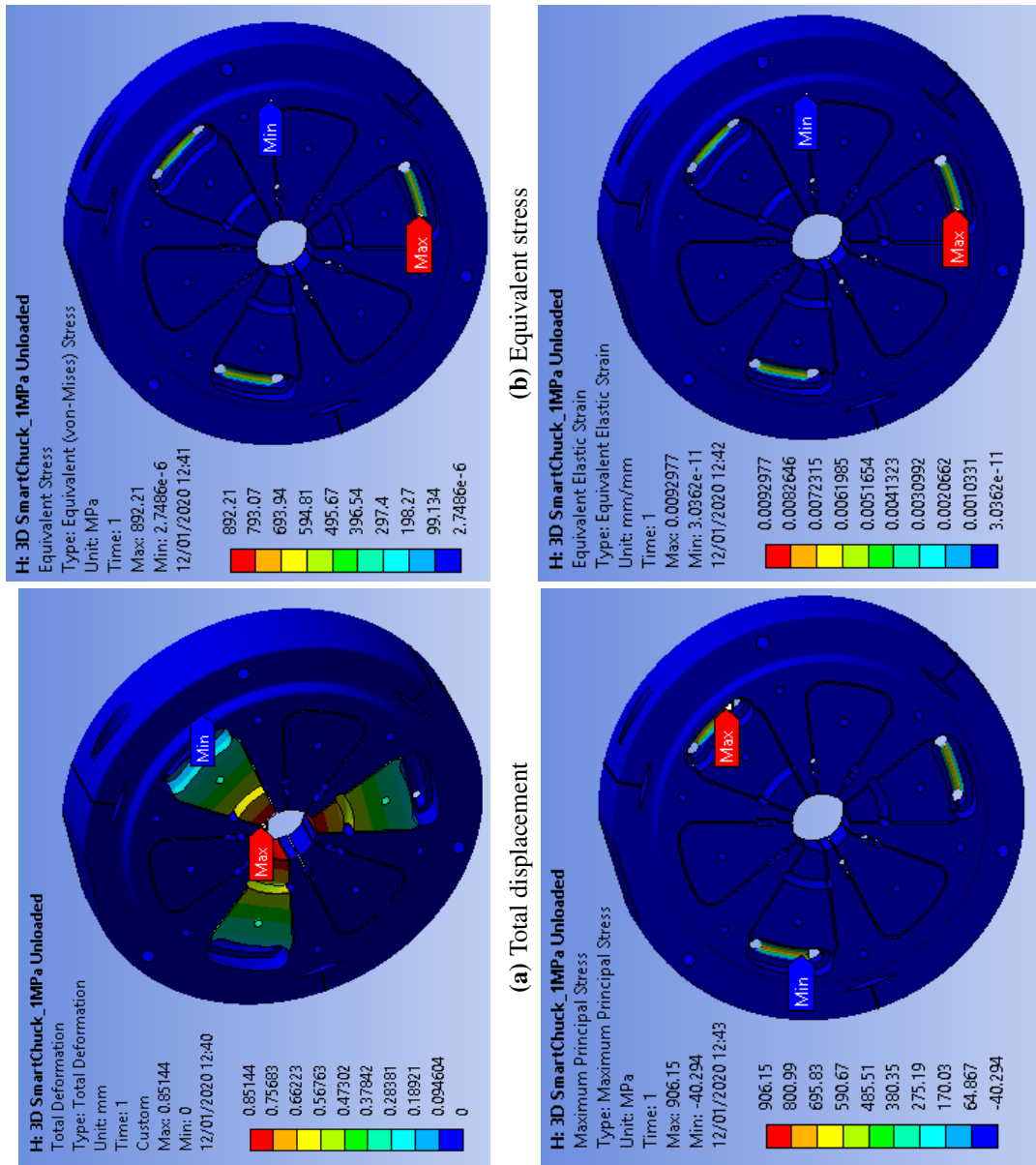

(b) Principal elastic strain

(c) Principal stress vs equivalent stress

(d) Principal strain vs equivalent strain

Fig. B.4 Flexure FL2,FL4 3D FEM analysis, loaded condition, results data Sheet 02

(a) Total displacement

(b) Equivalent stress

(c) Principal stress

(d) Equivalent elastic strain

Fig. B.5 3D FEM unloaded FL2,FL4 result figures, sheet 01

A: 3D SmartChuck_1MPa Loaded
Total Deformation
Type: Total Deformation
Unit: mm
Time: 1
Custom
Max: 0.029075
Min: 0
12/01/2020 12:55

0.029075
0.025844
0.022614
0.019383
0.016153
0.012922
0.0096916
0.0064611
0.0032305
0

(a) Total displacement

A: 3D SmartChuck_1MPa Loaded
Equivalent Stress
Type: Equivalent (von-Mises) Stress
Unit: MPa
Time: 1
Max: 90.02
Min: 1.3271e-6
12/01/2020 12:56

90.02
80.018
70.016
60.014
50.011
40.009
30.007
20.005
10.002
1.3271e-6

(b) Equivalent stress

A: 3D SmartChuck_1MPa Loaded
Maximum Principal Stress
Type: Maximum Principal Stress
Unit: MPa
Time: 1
Max: 57.372
Min: -15.974
12/01/2020 12:57

57.372
49.223
41.073
32.924
24.774
16.624
8.4749
0.32532
-7.8242
-15.974

(c) Principal stress

A: 3D SmartChuck_1MPa Loaded
Equivalent Elastic Strain
Type: Equivalent Elastic Strain
Unit: mm/mm
Time: 1
Max: 0.00093774
Min: 2.5595e-11
12/01/2020 12:57

0.00093774
0.00083354
0.00072995
0.00062516
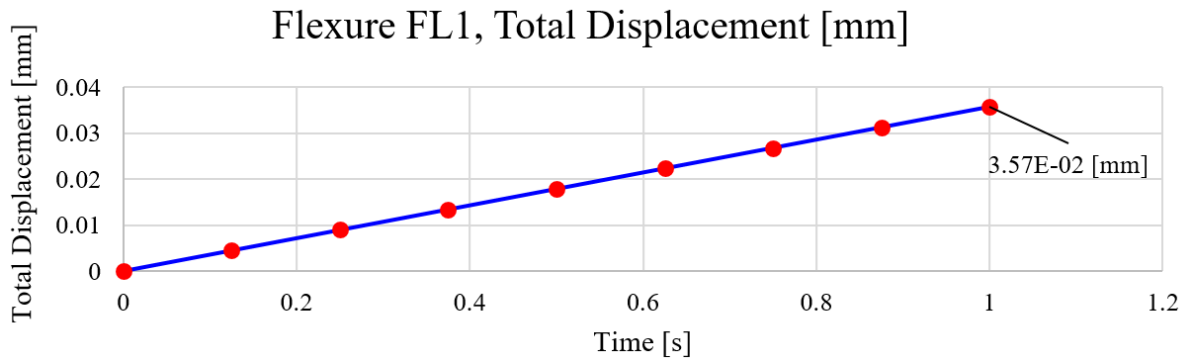0.00052096
0.00041677
0.00031258
0.00020839
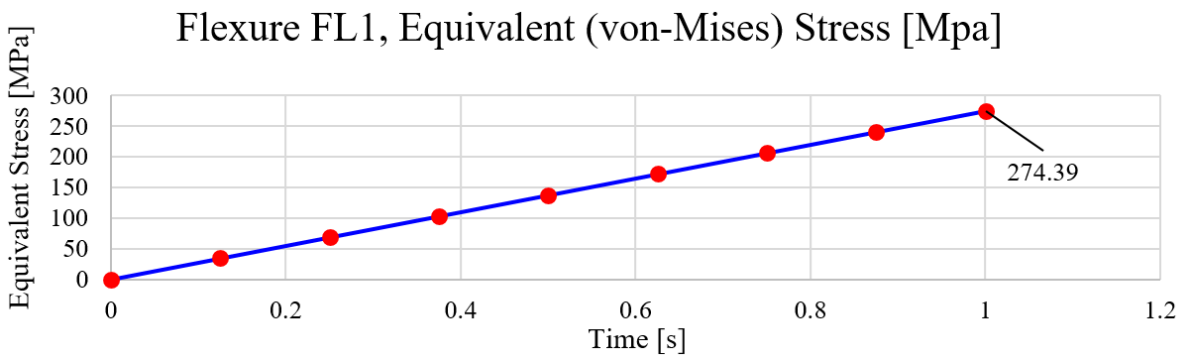0.00010419
2.5595e-11

(d) Equivalent elastic strain

Fig. B.6 3D FEM loaded FL2,FL4 result figures, sheet 02
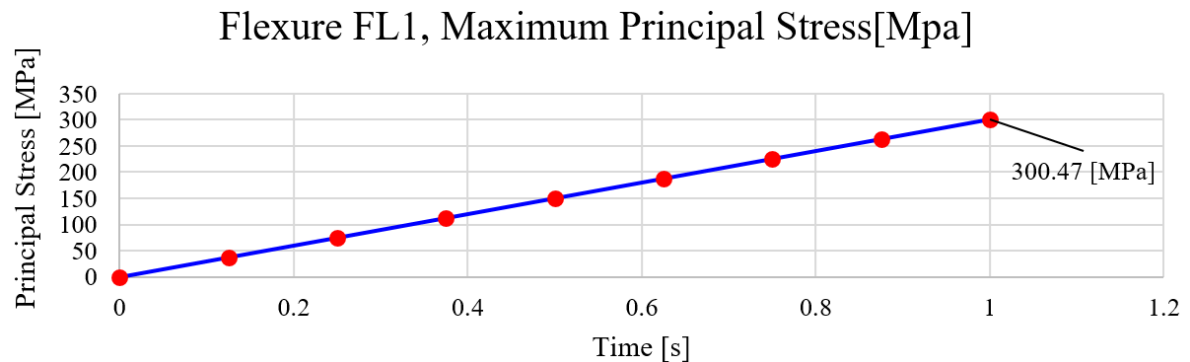
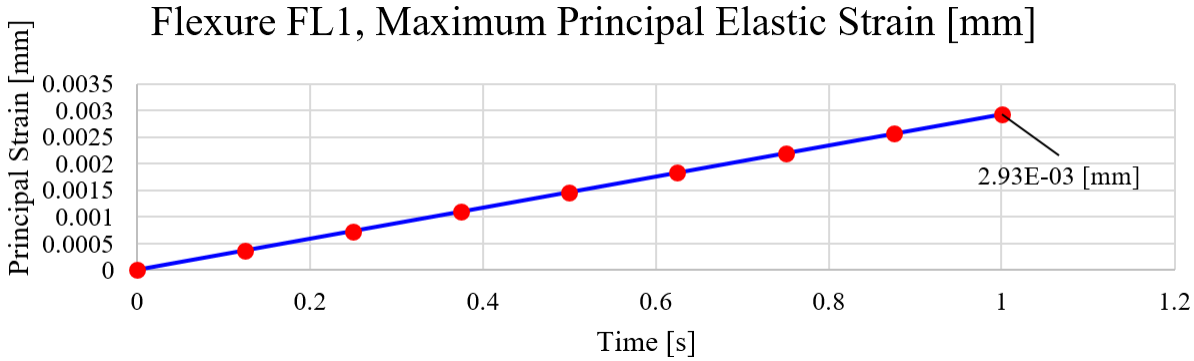# B.3 FL1 3D FEM Result Diagrams and Figures

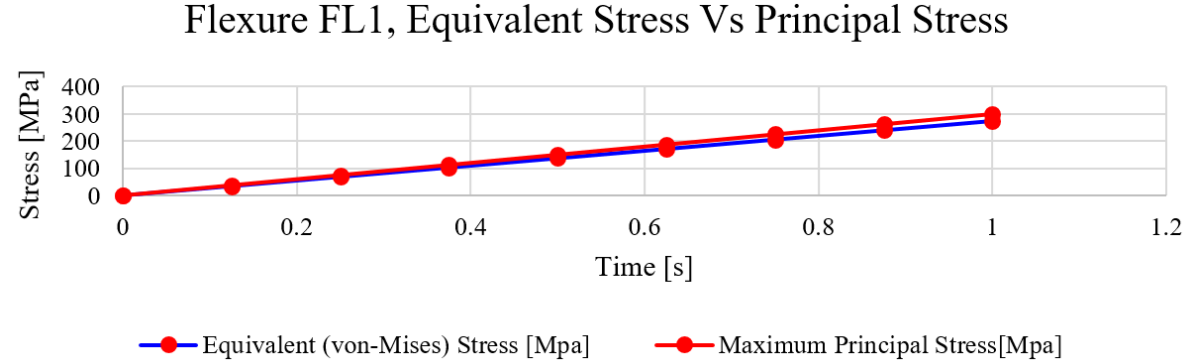**(a)** Total displacement

(b) Equivalent stress

(c) Maximum principal stress

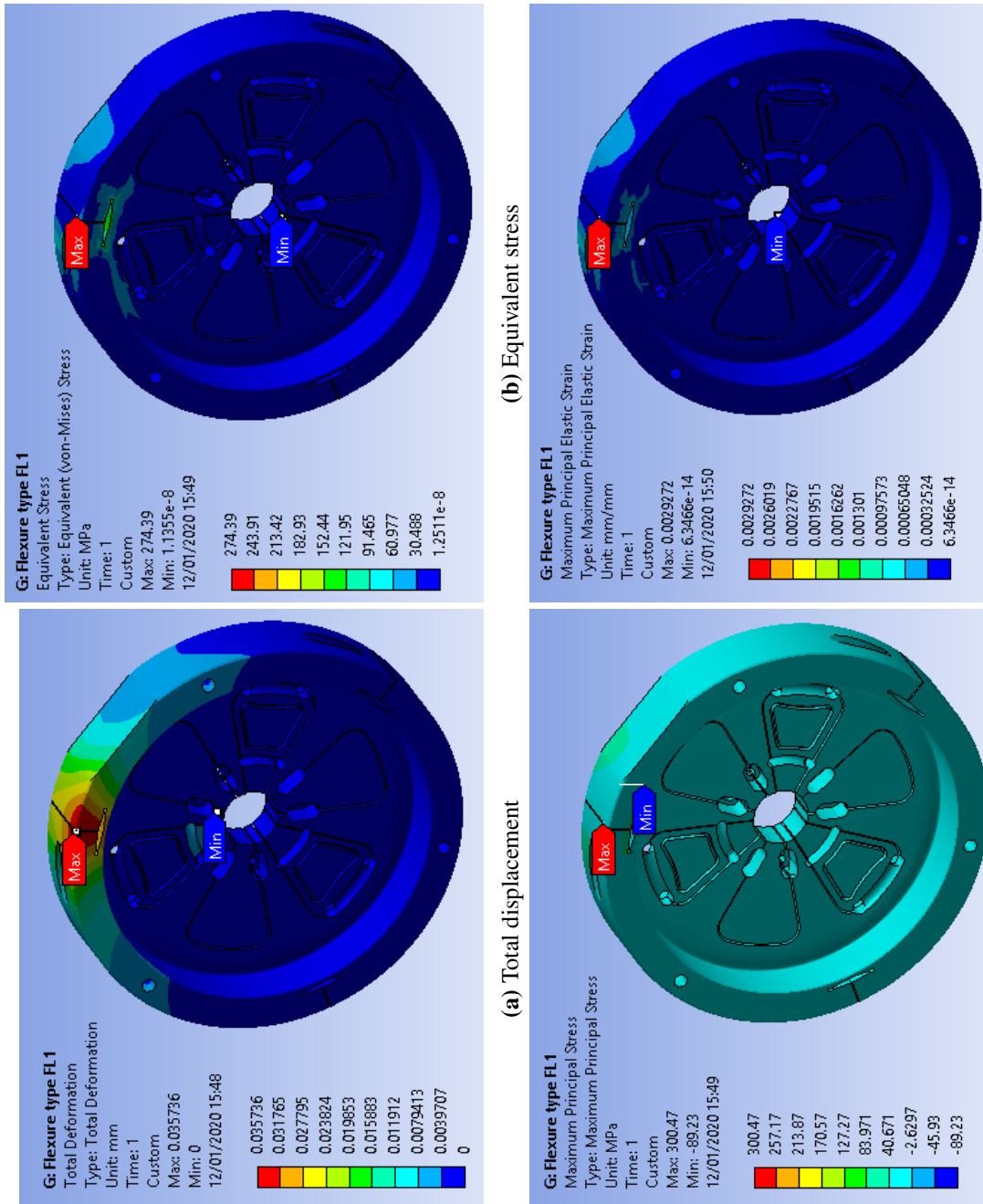**Fig. B.7** Flexure FL1, 3D FEM analysis results data sheet 01

Flexure FL1, Maximum Principal Elastic Strain [mm]

(a) Principal elastic strain

Flexure FL1, Equivalent Stress Vs Principal Stress

(b) Principal stress vs equivalent stress

Fig. B.8 Flexure FL1, 3D FEM analysis results data sheet 02

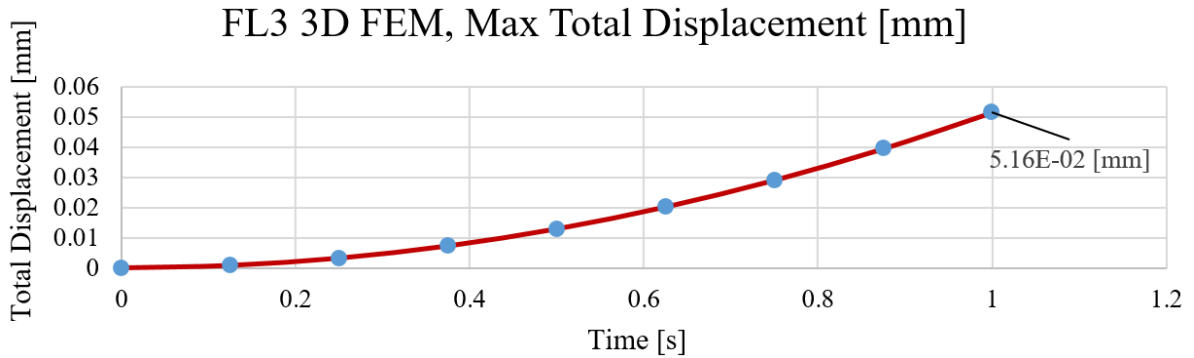**(a)** Total displacement

(b) Equivalent stress

(c) Principal stress

(d) Principal elastic strain

Fig. B.9 3D FEM FL1 result figures

B.4   FL3 3D FEM Result Diagrams and Figures

FL3 3D FEM, Max Total Displacement [mm]

(a) Total displacement

FL3 3D FEM, Max Equivalent (von-Mises) Stress [Mpa]

(b) Equivalent stress

FL3 3D FEM, Maximum Principal Stress [Mpa]
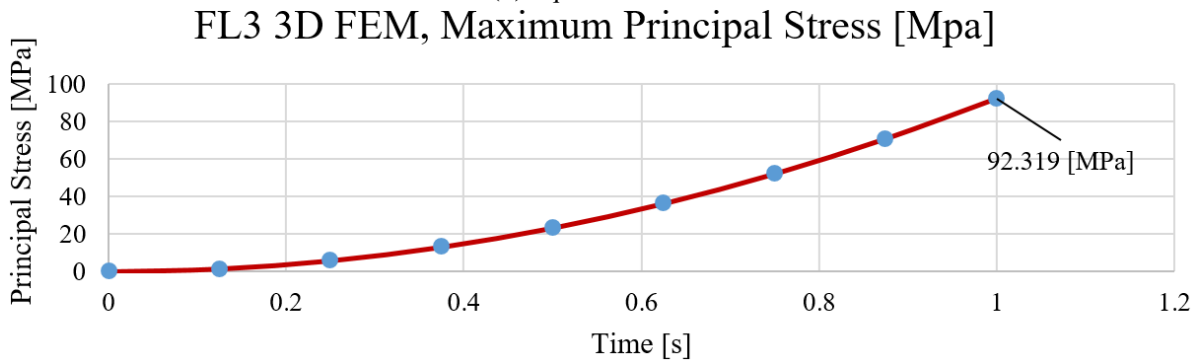
(c) Maximum principal stress

Fig. B.10 Flexure FL3, 3D FEM analysis results data sheet 01

FL3 3D FEM, Maximum Principal Elastic Strain [mm]

(a) Principal elastic strain

FL3 3D FEM, Equivalent Stress Vs Principal Stress
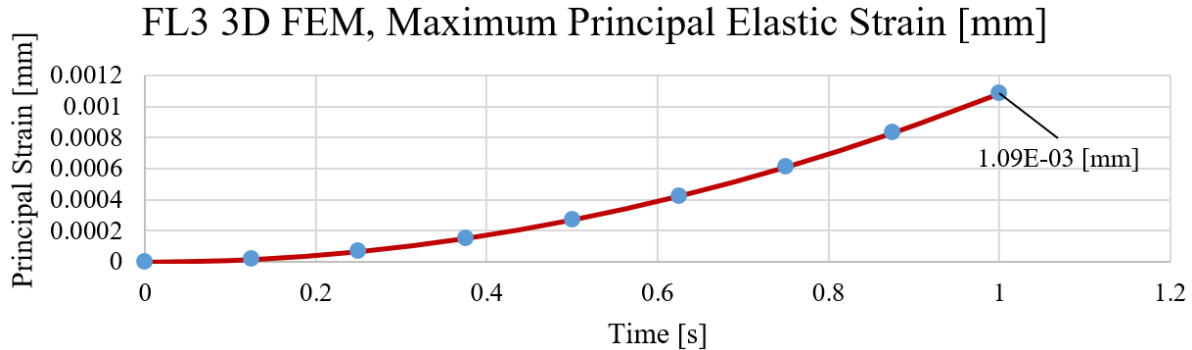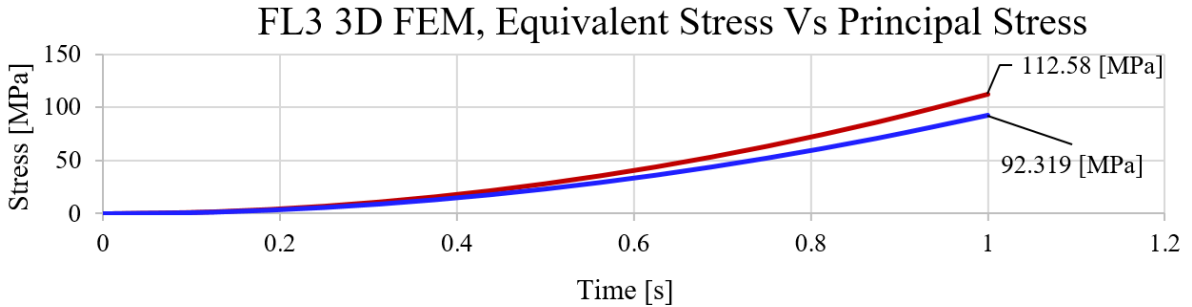
Max Equivalent (von-Mises) Stress [Mpa]   Maximum Principal Stress [Mpa]

(b) Principal stress vs equivalent stress

Fig. B.11 Flexure FL3, 3D FEM analysis results data sheet 02

(a) Total displacement

(b) Equivalent stress
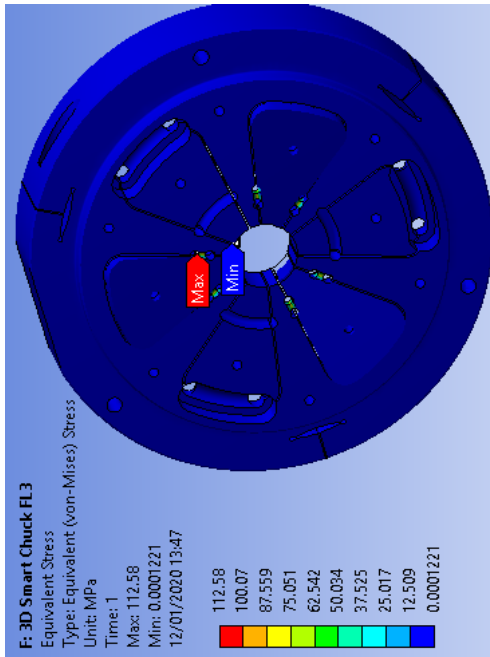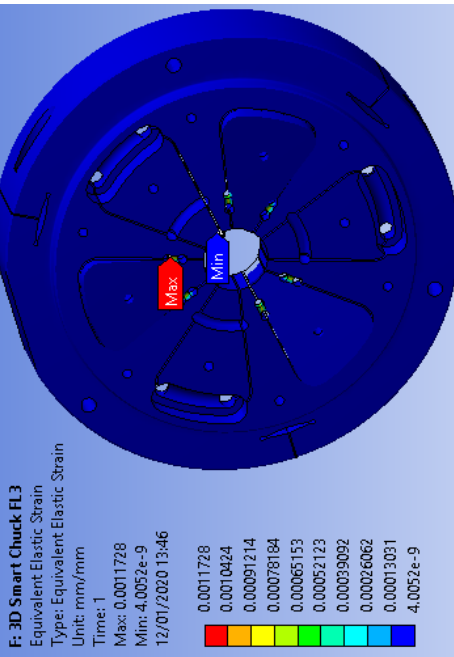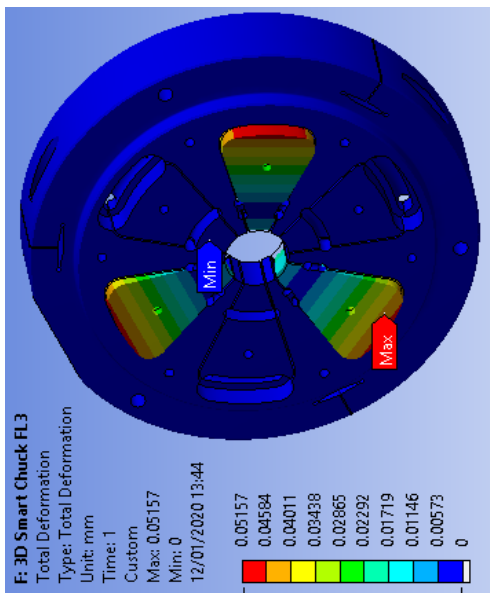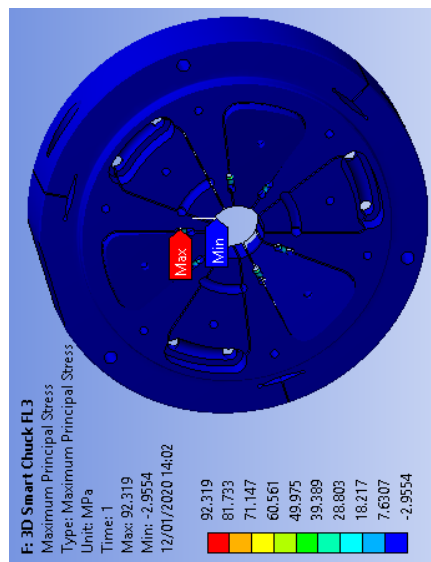
(c) Principal stress

(d) Equivalent elastic strain

Fig. B.12 3D FEM FL1 result figures

B.5 Validation of Positioning at Stage 01

validation of linear Vs angular displacement in stage 01

$A := 9.400 \ mm \qquad B := 32.650 \ mm \qquad b := .002 \ mm$

$R := \sqrt{A^2 + B^2} \qquad R = 33.976 \ mm \quad \alpha := \text{atan}\left(\dfrac{A}{B}\right) = 16.061 \ deg$

$\beta := 90 \ deg - \alpha = 73.939 \ deg$

$a_1 := \dfrac{\sin(\alpha) \cdot b}{\sin(\beta)} \qquad\qquad a_1 = 0.0006 \ mm \qquad L_1 := \sqrt{b^2 + a_1{}^2} = 0.002 \ mm$

$c1 := b \cdot \sin(\alpha) \qquad\qquad c1 = 0.0006 \ mm$
$c2 := b \cdot \cos(\alpha) \qquad\qquad c2 = 0.0019 \ mm$

$\alpha_2 := \text{asin}\left(\dfrac{\sin(\alpha) \cdot c2}{c1}\right) = 73.939 \ deg$

$\beta_2 := 90 \ deg - \alpha_2 = 16.061 \ deg$

$a_2 := \tan(\alpha_2) \cdot b = 0.0069 \ mm$

$\tan(0.288) = 0.296$

$\alpha := 33.35 \ deg \qquad c1 := 0.334 \ mm \qquad c2 := 0.219 \ mm$

$\alpha_2 := \text{asin}\left(\dfrac{\sin(\alpha) \cdot c2}{c1}\right) = 21.129 \ deg$

Fig. B.13 Validation of the positioning at stage 01

Appendix C

Metrology Validation of Accuracy

C.1   Concave Mould Insert

(a) Concave-Item-01

(b) Concave-Item-02

(c) Concave-Item-03

(d) Concave-Item-04

(e) Concave-Item-05
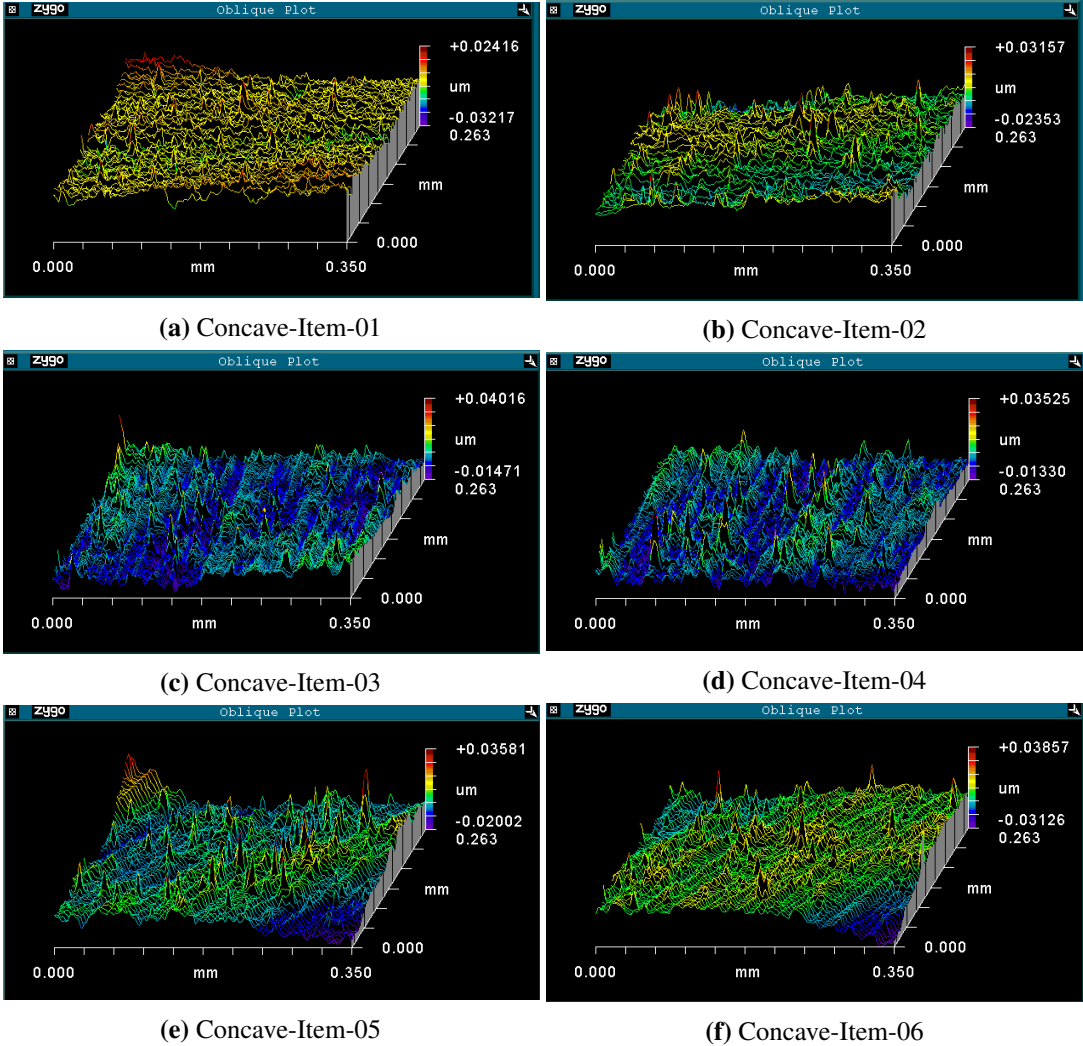
(f) Concave-Item-06

Fig. C.1 Metrology of concave insert moulds

C.2   Convex Mould Insert

(a) Convex-Item-01

(b) Convex-Item-02

(c) Convex-Item-03

(d) Convex-Item-04

(e) Convex-Item-05

(f) Convex-Item-06

(g) Convex-Item-07

(h) Convex-Item-08
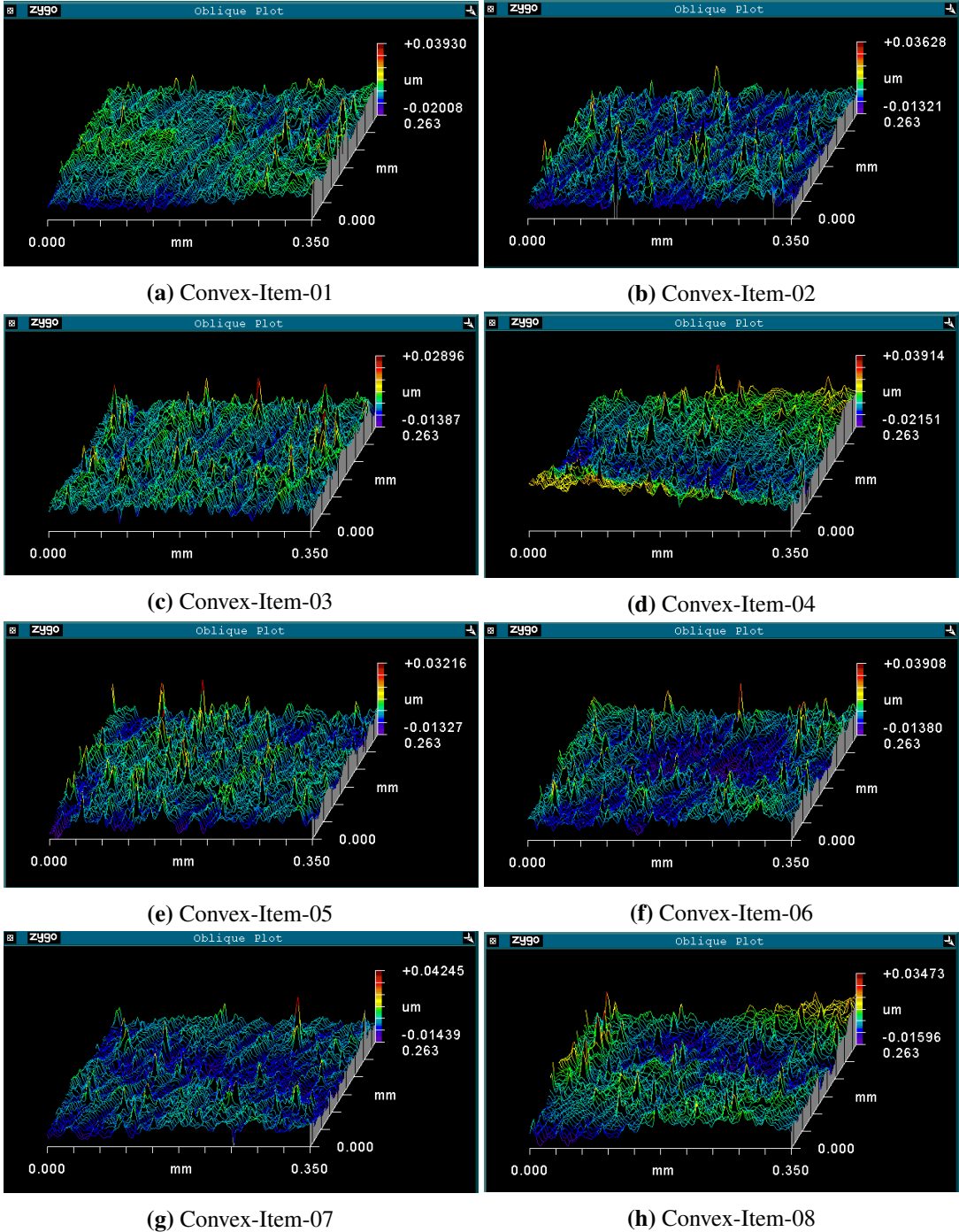
Fig. C.2 Metrology of convex insert moulds items 1-8

(a) Convex-Item-09

(b) Convex-Item-10

(c) Convex-Item-11

(d) Convex-Item-12

(e) Convex-Item-13

(f) Convex-Item-14

(g) Convex-Item-15

(h) Convex-Item-16
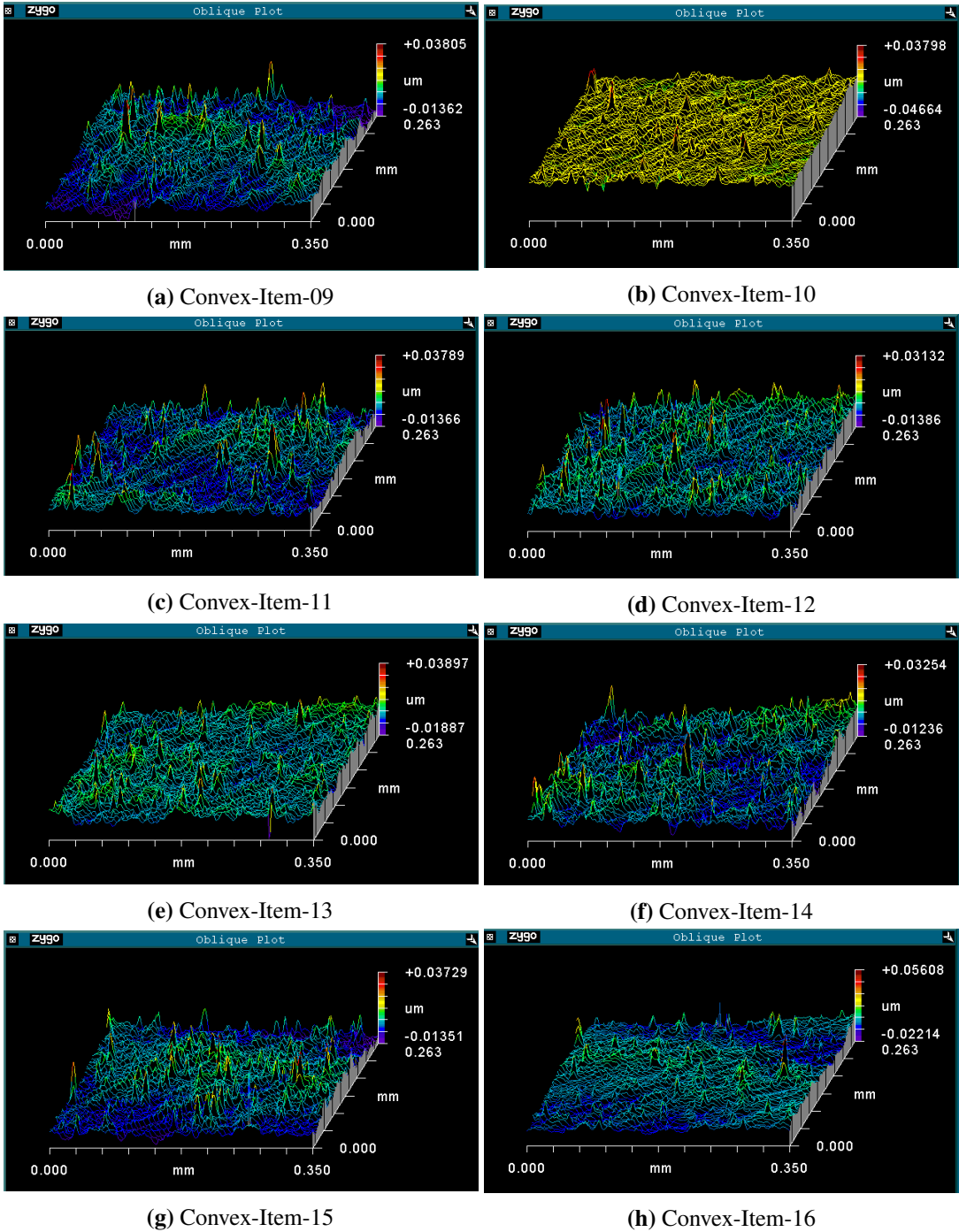
Fig. C.3 Metrology of convex insert moulds items 9-16

(a) Convex-Item-17

(b) Convex-Item-18

(c) Convex-Item-19

(d) Convex-Item-20
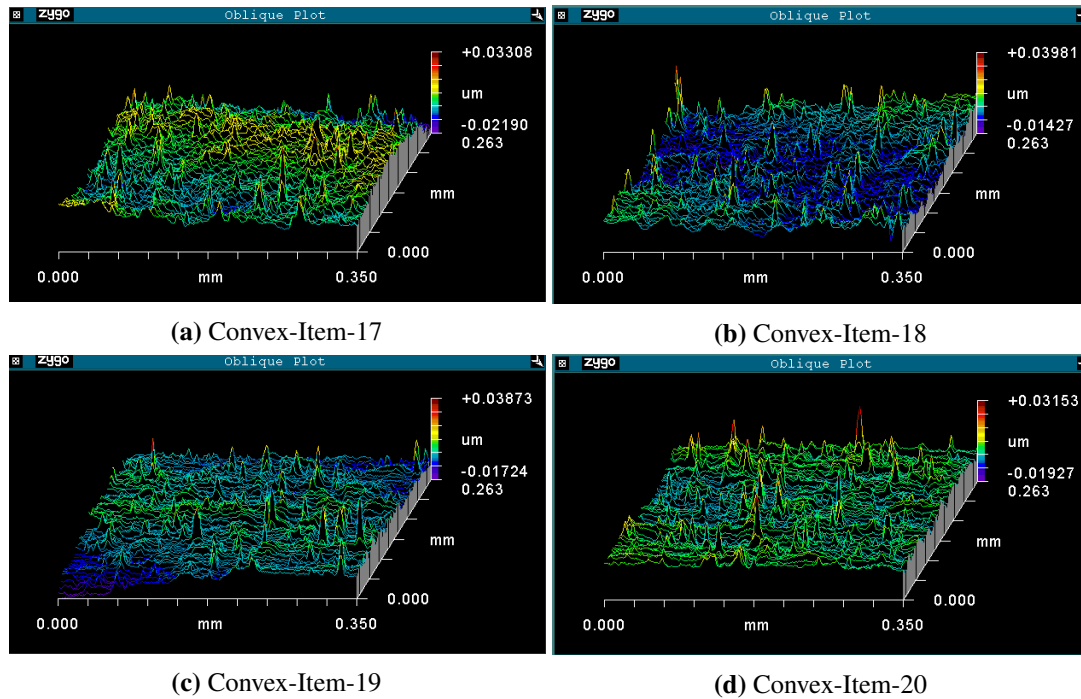
Fig. C.4 Metrology of convex insert moulds items 17-20

C.3   Diamond Tool Geometry

```
C0.195mLECi/0.50µm x CS1419_2 (Controlled Waviness Finishing Tool)
```

```
Tool Type   : C0.195mLECi/120°/0.50µm

Drawing number    : CS1419_2

Quantity (Pcs) : TBA

CFT Code for Internal Use Only   : N.02.N01.I17

Shank (wxhxl)   (mm) : I17, 55° Insert - Tungsten

Nominal Cutting Height (mm) : 3.20mm

Diamond (Natural / Sumitomo or Mono-die)   : Natural N01

Controlled or Standard Waviness   : Controlled Waviness

Radius (R1) (mm) : 0.195mm +0.0mm -0.020mm When New
```

Included angle (Top Angle) (A2) (°) : 52°

Front Clearance (C1) Conical/Cylindrical (°) : 15° Conical (in 0° pocket toolholder)

Arc / Window (A1) (°) : 120°

Rake angle ''R'' (°) : 0° (in 0° pocket toolholder)

Waviness < (Peak to Valley) (0.03µm - 2µm) (µm) : <0.50µm over 120° of arc

Notes:

50   20

5.7 ± 0.10

8

Ø2.5

3.2   Step height

9.3

Shank clearance 10°

Front Clearance 45°

Front View

Fig. C.5 Diamond toolholder

TITLE Standard 55° Insert - Non Controlled For 0° Toolholder

DRAWING NO. CS1763

Ø2.8mm

Radius size

60° Included

Radius see list

55°

3.2mm nominal dependant upon diamond depth

Rake (see list)

0.5mm

Serial number

XXXXX

2.38mm

5° - 15° Front Clearance

7°

12.8mm

13.3mm nominal dependant upon diamond

PLEASE STATE WHEN ORDERING

Standard radius sizes	Standard rake angles
0.25mm (.010")	+2½°
0.3mm (.012")	0°
0.5mm (.020")	-2½°
0.75mm (.030")	-5°
1.0mm (.040")	-7½°

ISSUE 1
CHANGE
DATE 22/03/2010
DRAWN BSR

NOTE:
To be used in a 0° Toolholder.

DIAMOND TYPE	Natural, Sumitomo, Mono Die
RADIUS	See list
FRONT CLEARANCE	5° - 15°
RAKE ANGLE	See list (see note)
SHANK	55° Insert - Tungsten
BRAZE	VB

GENERAL TOLERANCE
LINEAR +/- 0.1   ANGULAR +/- 0.5
DIMENSIONS IN MILLIMETRES

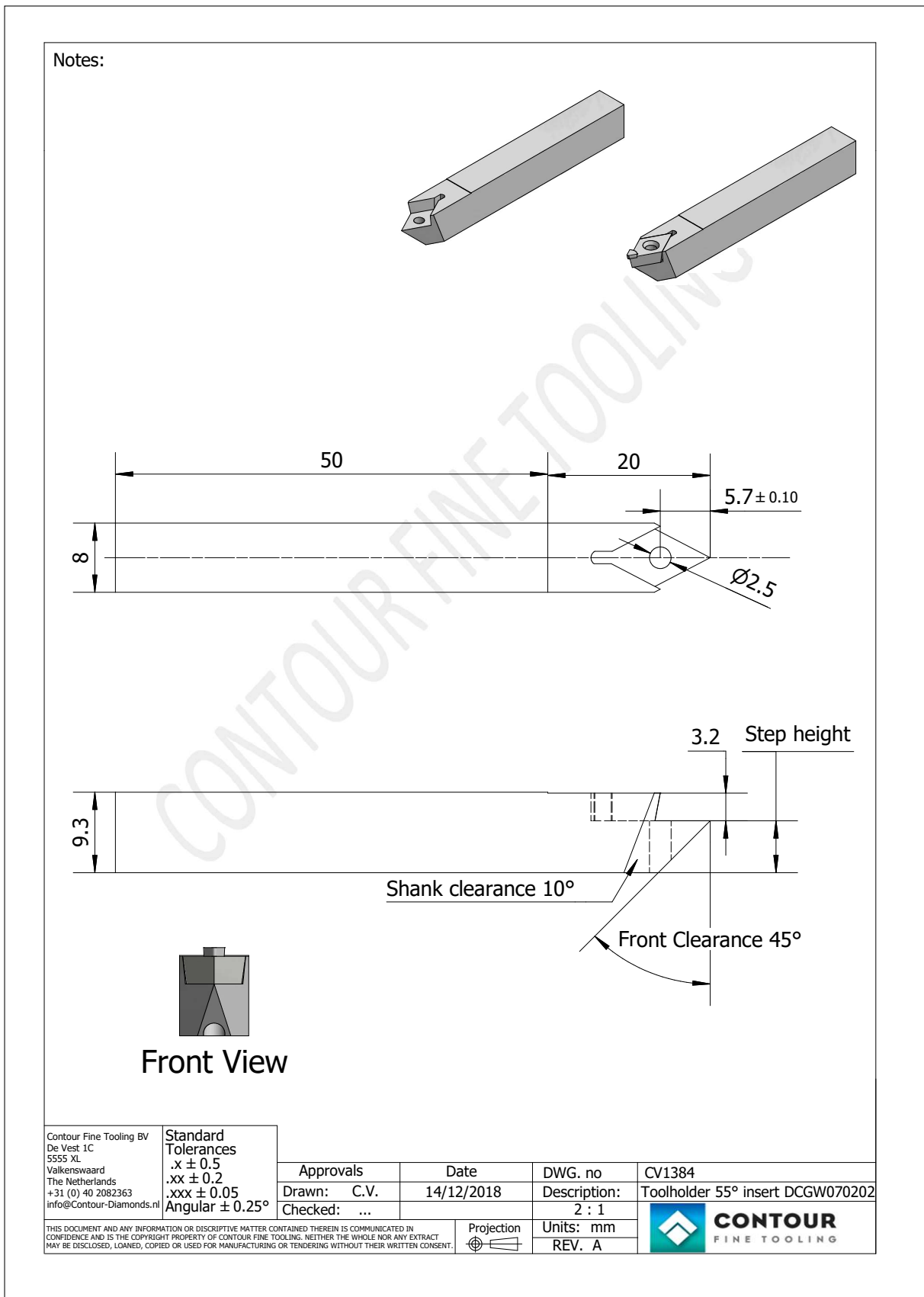ENGRAVE:
Lathe x Radius x insert
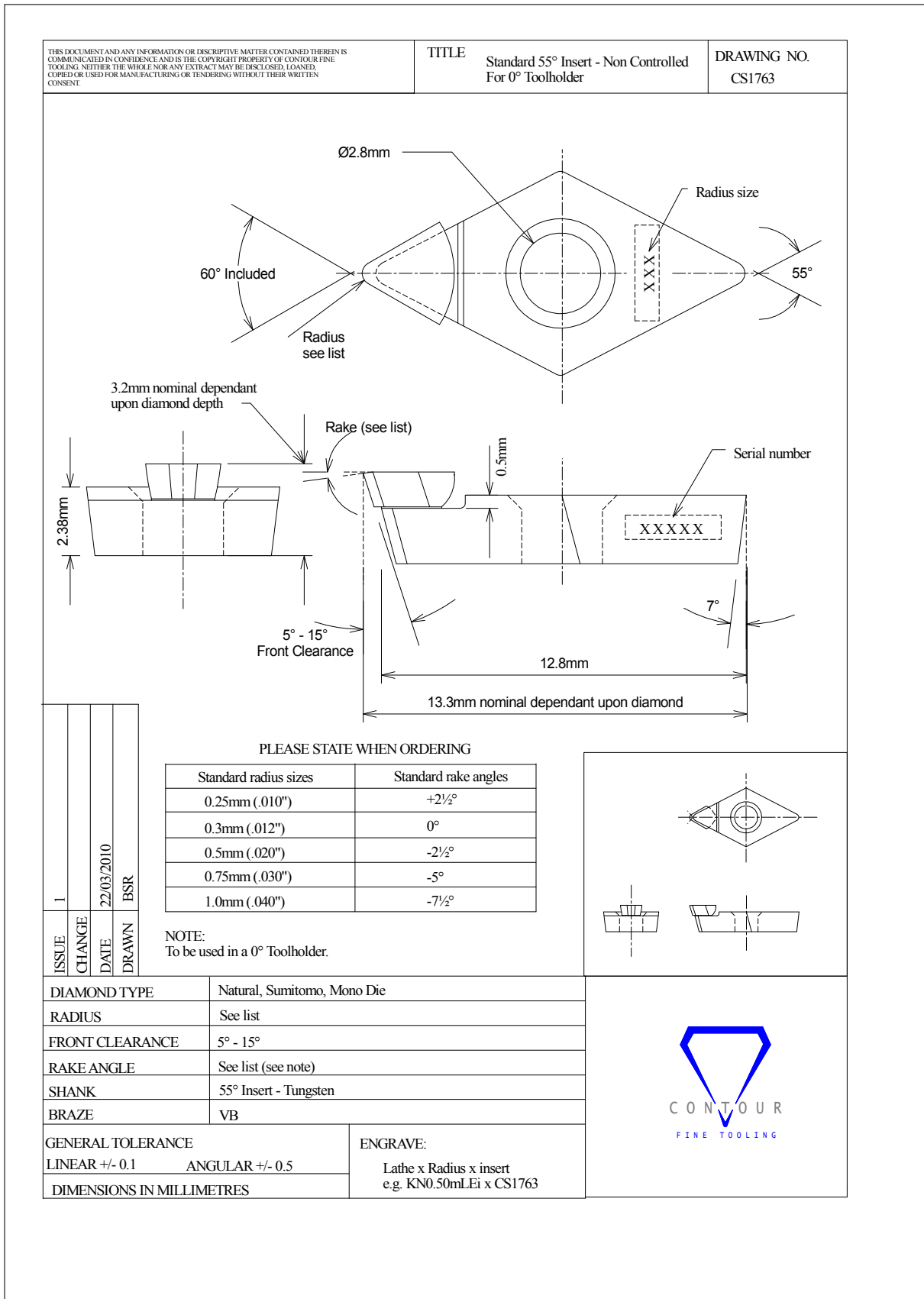e.g. KN0.50mLEi x CS1763

CONTOUR
FINE TOOLING

Fig. C.6 Diamond tool insert

C.4   Contact Lenses Machining NC Files

(NanoCAM 2D - Version 1.55)

(CREATED : Thursday 5/2/2019 12:31:15 PM)

(INPUT FILE : die_Ali_01.mntl)

(========== SECTION INITIALIZATION ==========)

(--- RESET 5XX VARIABLES ---)

#506 = 0

#547 = 0

(========== ROUGH CUT PARAMETERS ==========)

#521 = 2   (NUMBER OF LOOPS)

#522 = 0.02   (DEPTH OF CUT)

#523 = 20   (FEEDRATE)

#524 = 500   (SPINDLE SPEED)

(========== SEMI-FINISH CUT PARAMETERS ==========)

#531 = 2   (NUMBER OF LOOPS)

#532 = 0.01   (DEPTH OF CUT)

#533 = 10   (FEEDRATE)

#534 = 1000   (SPINDLE SPEED)

(========== FINISH CUT PARAMETERS ==========)

#541 = 2   (NUMBER OF LOOPS)

#542 = 0.005   (DEPTH OF CUT)

#543 = 3   (FEEDRATE)

#544 = 2000   (SPINDLE SPEED)

#506 = 0   (LOOP COUNT)

#547 = 0   (CUT OFFSET VARIABLE)

```
( ========== SECTION COMMANDS ========== )

G71 G01 G18 G40 G63 G90 G94 G54

T0000                    ( DEACTIVATE ALL TOOL OFFSETS )

G53 Z0.0 F500            ( PARKING POSITION - NO TOOL ACTIVE )


Y0.0                     ( SET Y AXIS TO ZERO )


( ========== SUBROUTINE CALL ROUGH  CUT ========== )

T0101                    ( ACTIVATE TOOL OFFSET )

WHILE[#506LT#521]DO 2

#502 = #522

#503 = #523

#504 = #524

M98(die_Ali_01_RC.nc)

END 2

#506 = 0                 ( RESET PASS COUNTER )

G04 P.4                  ( DWELL )

T0000                    ( DEACTIVATE ALL TOOL OFFSETS )

G53 Z0.0 F500            ( PARKING POSITION - NO TOOL ACTIVE )


( ========== SUBROUTINE CALL SEMI-FINISH  CUT ========== )

T0101                    ( ACTIVATE TOOL OFFSET )

WHILE[#506LT#531]DO 2

#502 = #532

#503 = #533

#504 = #534
```

```
M98(die_Ali_01_SC.nc)

END 2

#506 = 0                RESET PASS COUNTER )

G04 P.4             ( DWELL )

T0000               ( DEACTIVATE ALL TOOL OFFSETS )

G53 Z0.0 F500       ( PARKING POSITION - NO TOOL ACTIVE )


( ========== SUBROUTINE CALL FINISH  CUT ========== )

T0101               ( ACTIVATE TOOL OFFSET )

WHILE[#506LT#541]DO 2

#502 = #542

#503 = #543

#504 = #544

M98(die_Ali_01_FC.nc)

END 2

#506 = 0            ( RESET PASS COUNTER )

G04 P.4             ( DWELL )

T0000               ( DEACTIVATE ALL TOOL OFFSETS )

G53 Z0.0 F200       ( PARKING POSITION - NO TOOL ACTIVE )


( ========== SECTION END ========== )

G52 Z0.0            ( SHIFT THE LOCAL COORDINATE SYSTEM TO 0.0 )

G53 Z0.0 F500       ( PARKING POSITION - NO TOOL ACTIVE )

M30                 ( RESET PROGRAM )


( NanoCAM 2D - Version 1.55 )
```

```
( CREATED : Thursday 5/2/2019 12:12:57 PM )

( INPUT FILE : punch_Ali_01.MNTL )

( ========== SECTION INITIALIZATION ========== )

( --- RESET 5XX VARIABLES --- )

#506 = 0

#547 = 0



( ========== ROUGH CUT PARAMETERS ========== )

#521 = 2                ( NUMBER OF LOOPS )

#522 = 0.02             ( DEPTH OF CUT )

#523 = 20               ( FEEDRATE )

#524 = 500              ( SPINDLE SPEED )

( ========== SEMI-FINISH CUT PARAMETERS ========== )

#531 = 2                ( NUMBER OF LOOPS )

#532 = 0.01             ( DEPTH OF CUT )

#533 = 10               ( FEEDRATE )

#534 = 1000              ( SPINDLE SPEED )

( ========== FINISH CUT PARAMETERS ========== )

#541 = 2                ( NUMBER OF LOOPS )

#542 = 0.005            ( DEPTH OF CUT )

#543 = 3                ( FEEDRATE )

#544 = 2000             ( SPINDLE SPEED )

#506 = 0                ( LOOP COUNT )

#547 = #521*#522 + #531*#532 + #541*#542 ( CUT OFFSET VARIABLE )

( ========== SECTION COMMANDS ========== )

G71 G01 G18 G40 G63 G90 G94 G54
```

```
T0000                  ( DEACTIVATE ALL TOOL OFFSETS )

G53 Z0.0 F500          ( PARKING POSITION - NO TOOL ACTIVE )


Y0.0                   ( SET Y AXIS TO ZERO )


( ========== SUBROUTINE CALL ROUGH  CUT ========== )

T0101                  ( ACTIVATE TOOL OFFSET )

WHILE[#506LT#521]DO 2

#502 = #522

#503 = #523

#504 = #524

M98(punch_Ali_01_RC.nc)

END 2

#506 = 0               ( RESET PASS COUNTER )

G04 P.4                ( DWELL )

T0000                  ( DEACTIVATE ALL TOOL OFFSETS )

G53 Z0.0 F500          ( PARKING POSITION - NO TOOL ACTIVE )


( ========== SUBROUTINE CALL SEMI-FINISH  CUT ========== )

T0101                  ( ACTIVATE TOOL OFFSET )

WHILE[#506LT#531]DO 2

#502 = #532

#503 = #533

#504 = #534

M98(punch_Ali_01_SC.nc)

END 2
```

```
#506 = 0                ( RESET PASS COUNTER )

G04 P.4                 ( DWELL )

T0000                   ( DEACTIVATE ALL TOOL OFFSETS )

G53 Z0.0 F500           ( PARKING POSITION - NO TOOL ACTIVE )


( ========== SUBROUTINE CALL FINISH  CUT ========== )

T0101                   ( ACTIVATE TOOL OFFSET )

WHILE[#506LT#541]DO 2

#502 = #542

#503 = #543

#504 = #544

M98(punch_Ali_01_FC.nc)

END 2

#506 = 0                ( RESET PASS COUNTER )

G04 P.4                 ( DWELL )

T0000                   ( DEACTIVATE ALL TOOL OFFSETS )

G53 Z0.0 F200           ( PARKING POSITION - NO TOOL ACTIVE )


( ========== SECTION END ========== )

G52 Z0.0                ( SHIFT THE LOCAL COORDINATE SYSTEM TO 0.0 )

G53 Z0.0 F500           ( PARKING POSITION - NO TOOL ACTIVE )

M30                     ( RESET PROGRAM )
```

Appendix D

Hydrostatic Bearing Design with MMC Material
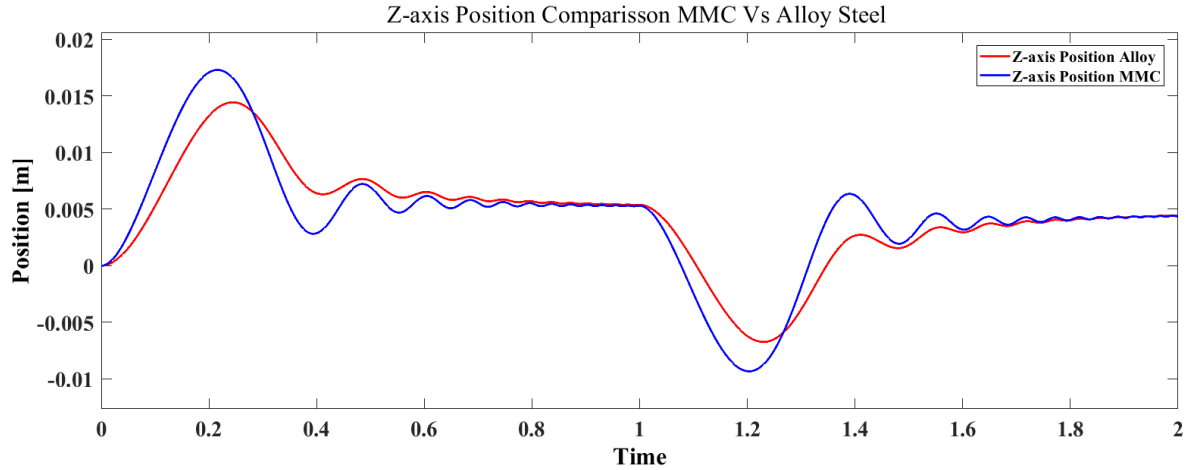
D.1   MBD Results Comparison: MMC vs Steel Alloy

D.1.1 Z axis MMC vs Steel Alloy
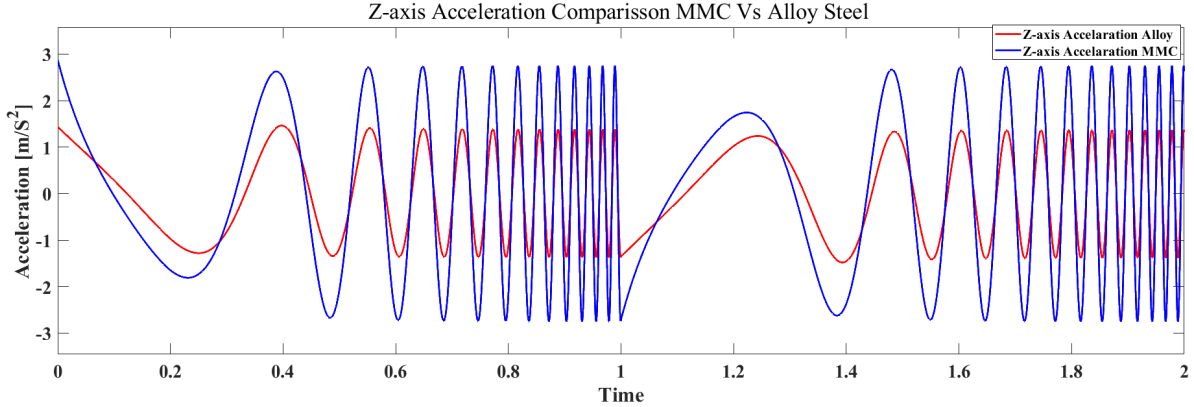
(a)
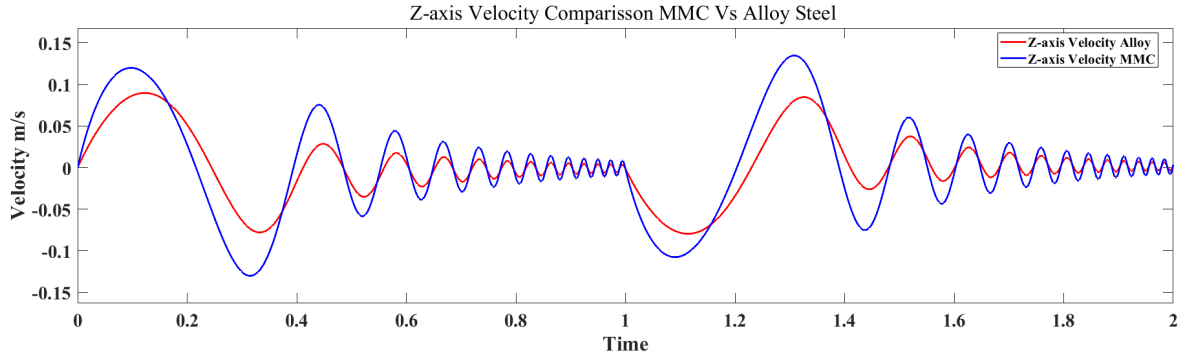
(b)

(c)

Fig. D.1 Simscape MBD result Z-axis: (a) Z-axis acceleration; (b) Z-axis velocity; (c) Z-axis position

D.1.2   X axis MMC vs Steel Alloy
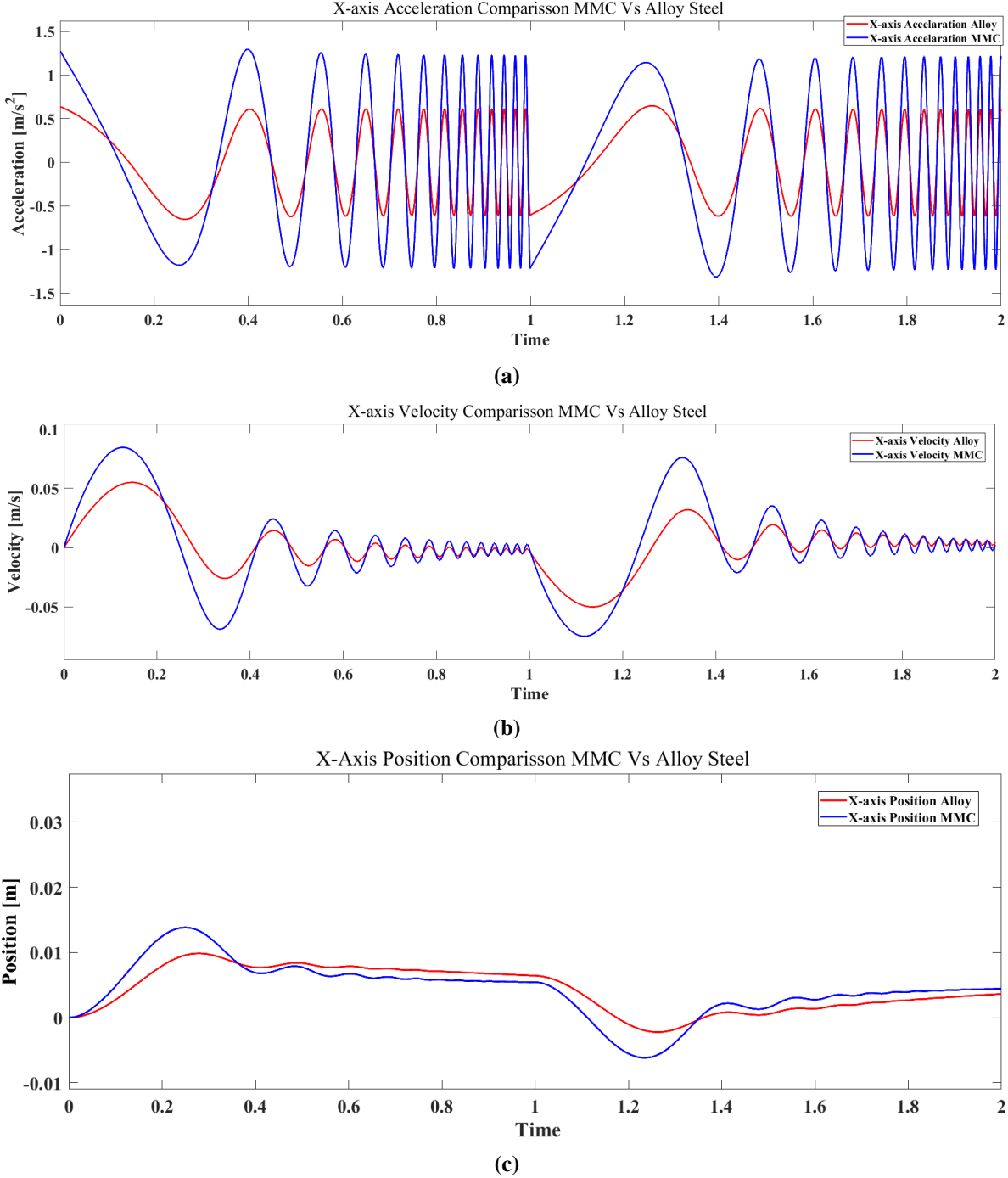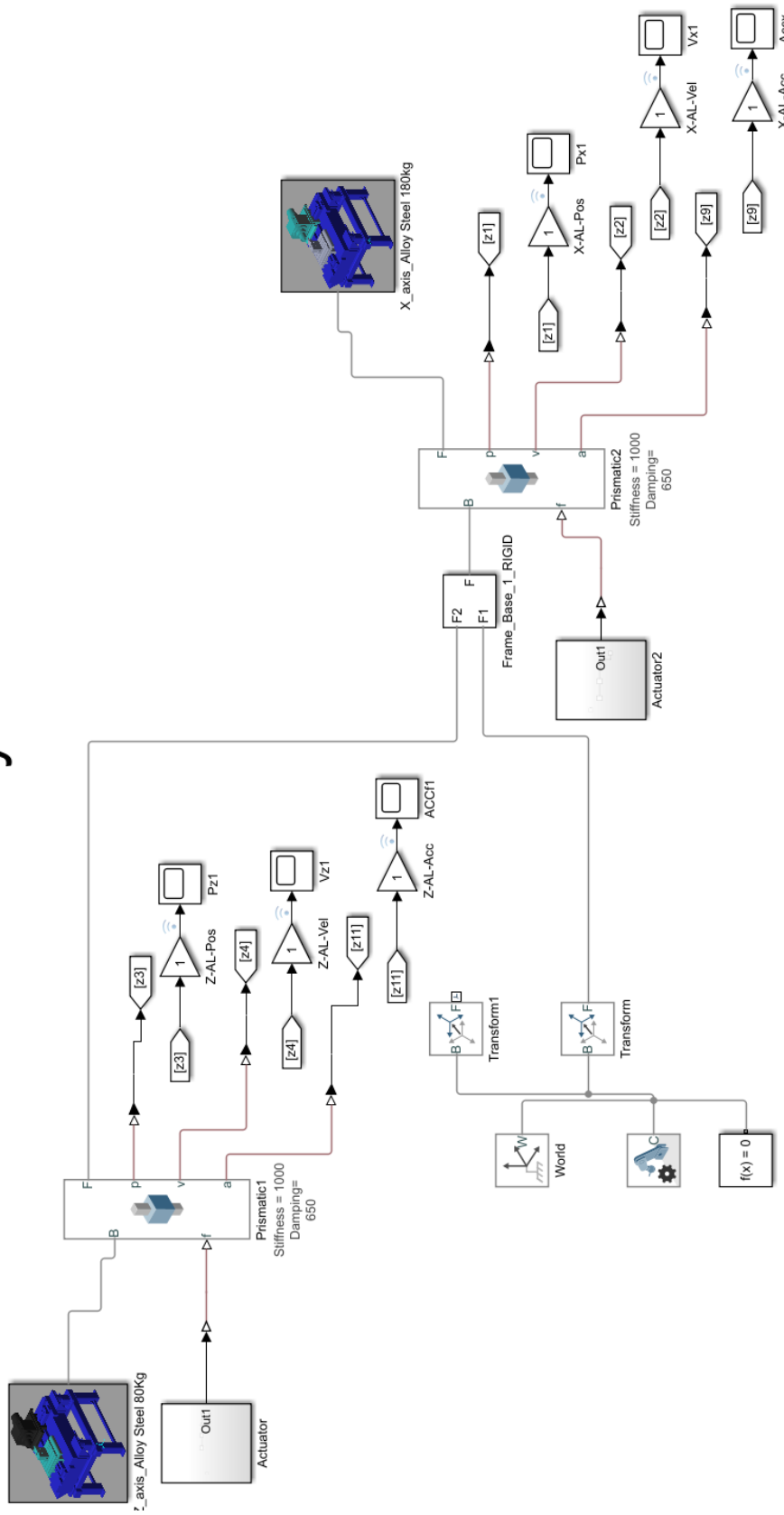

(a)

(b)

(c)

Fig. D.2 Simscape MBD result X axis: (a) X-axis acceleration; (b) X-axis velocity; (c) X-axis position

MBD Simscape Models

(a) Simscape alloy model
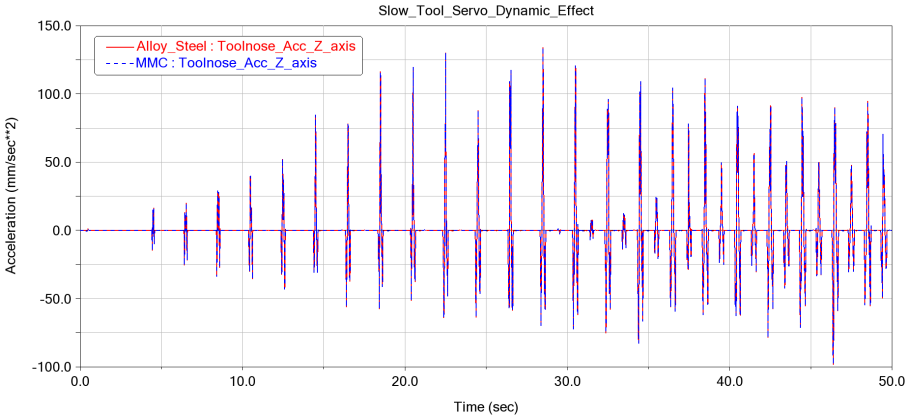
Fig. D.3 MBD Simscape alloy steel model
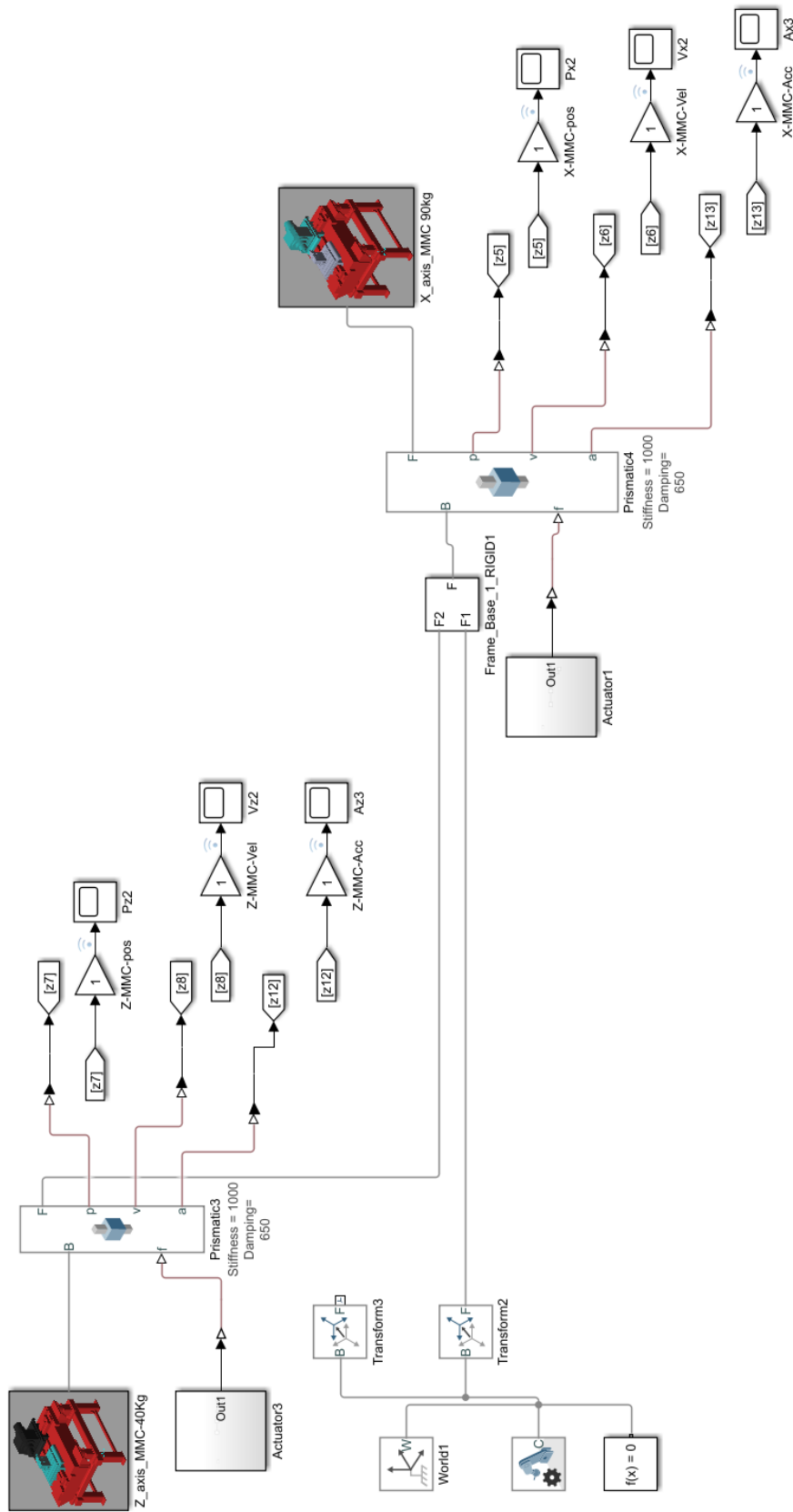
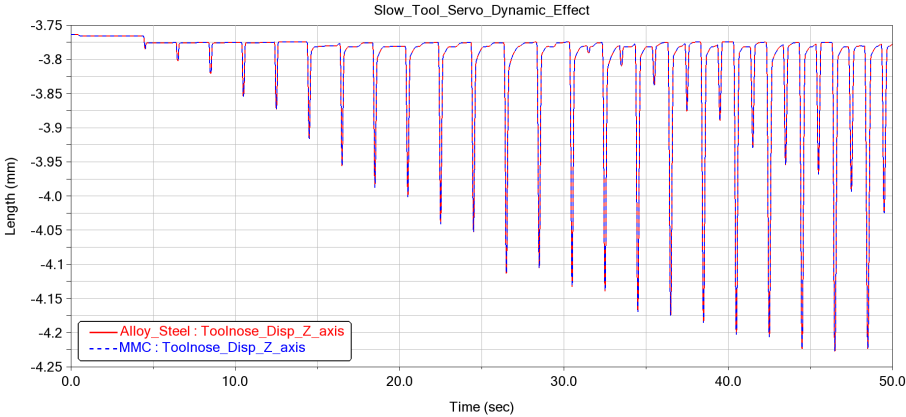(a) Simscape MMC model

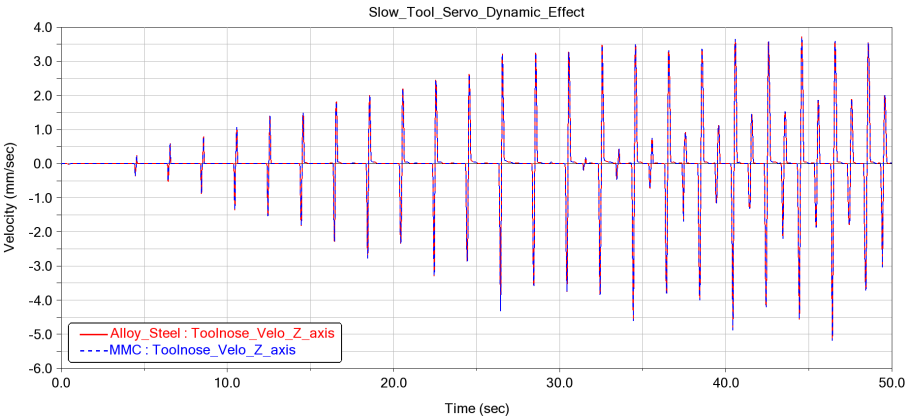**Fig. D.4** MBD Simscape MMC model

Appendix E

Hydrostatic Dynamics

E.1 Prismatic Constraint Slideways

(a)

(b)

(c)

Fig. E.1 ADAMS model, kinematic effects, MMC vs alloy steel: (a) Z-axis acceleration; (b) Z-axis velocity; (c) Z-axis position